# APPLICATIONS OF ADDITIVE MANUFACTURING TECHNOLOGIES TO AMBIENT ENERGY HARVESTERS FOR MICROWAVE AND MILLIMETER-WAVE AUTONOMOUS WIRELESS SENSING NETWORKS AND 3D PACKAGING INTEGRATION

A Dissertation
Presented to
The Academic Faculty

By

Tong-Hong Lin

In Partial Fulfillment
of the Requirements for the Degree
Doctor of Philosophy in the
School of Electrical and Computer Engineering

Georgia Institute of Technology

December 2020

Copyright © Tong-Hong Lin 2020

**APPLICATIONS OF ADDITIVE MANUFACTURING TECHNOLOGIES TO AMBIENT ENERGY HARVESTERS FOR MICROWAVE AND MILLIMETER-WAVE AUTONOMOUS WIRELESS SENSING NETWORKS AND 3D PACKAGING INTEGRATION**

Approved by:

Dr. Manos M. Tentzeris, Advisor
School of Electrical and Computer Engineering
*Georgia Institute of Technology*

Dr. Andrew F. Peterson
School of Electrical and Computer Engineering
*Georgia Institute of Technology*

Dr. Gregory D. Durgin
School of Electrical and Computer Engineering
*Georgia Institute of Technology*

Dr. Madhavan Swaminathan
School of Electrical and Computer Engineering
*Georgia Institute of Technology*

Dr. Pulugurtha M. Raj
Department of Electrical and Computer Engineering
*Florida International University*

Date approved: September 18, 2020

To my parents,

*Yi-Feng Lin* and *Mei-Hua Yang*,

and my sister,

*You-Ru Lin*,

whose unconditionally love, support, and encouragement make this work possible.

Knowing is not enough; we must apply.

Willing is not enough; we must do.

*Johann Wolfgang von Goethe*

# ACKNOWLEDGMENTS

I would like to express my greatest appreciation to my advisor, Dr. Manos M. Tentzeris. His support, encouragement, and guidance got me through the bumpy starting of my Ph.D. journey and paving the way to my final achievements. In addition to the research, he also shared his wisdom about life, work, and how to market me and my works. The most important thing I learned from Dr. Tentzeris is the spirit of challenging new things and that is the most important lesson as a researcher and a technology developer.

I would like to thank Dr. Rao R. Tummala and Dr. Madhavan Swaminathan for giving me the chance to cooperate with the PRC group and support the resources. The close relationship and connection between PRC and the industry benefit me a lot. I would like to thank Dr. Pulugurtha Markondeya Raj and Dr. Venky Sundaram for their motoring during my cooperation with PRC. The organized method to present my works, writing proposals, and interact with industrial researchers are useful even after my graduation. I would like to thank my committee members Dr. Andrew F. Peterson and Dr. Gregory David Durgin for their great feedback and suggestions.

I would like to thank ATHENA members, Dr. Jo Bito, Bijan Tehrani, Ryan Bahr, Dr. Jimmy Hester, Dr. John Kimionis, Dr. Yunnan Fang, Dr. Soyeon Jeong, Dr. Valentina Palazzi, Dr. Syed Abdullah Nauroze, Shicong Wang, Yepu Cui, Aline Eid, and Xuanke He for their help and contribution to my researches. I would like to thank PRC members, Dr. Atom Watanabe, Dr. Muhammad Ali, and Kimiyuki Kanno from the JSR Corporation for the fabrication of test samples. I would also like to thank the industry consortium of PRC for all support and feedbacks.

Finally, I would like to thank my family for always being there and support my decisions. None of this will be possible without their help and support.

**TABLE OF CONTENTS**

**Acknowledgments** . . . . . . . . . . . . . . . . . . . . . . . . . . . . . . v

**List of Tables** . . . . . . . . . . . . . . . . . . . . . . . . . . . . . . xiii

**List of Figures** . . . . . . . . . . . . . . . . . . . . . . . . . . . . . . xv

**List of Acronyms** . . . . . . . . . . . . . . . . . . . . . . . . . . . . . . xxviii

**Summary** . . . . . . . . . . . . . . . . . . . . . . . . . . . . . . xxxi

**Chapter 1: Introduction** . . . . . . . . . . . . . . . . . . . . . . . . . . . . . . 1

1.1 Research Objectives . . . . . . . . . . . . . . . . . . . . . . . . . . . . . . 1

1.2 Dissertation Outline . . . . . . . . . . . . . . . . . . . . . . . . . . . . . . 3

**Chapter 2: Review of Energy Harvesting Technologies** . . . . . . . . . . . . . . . 6

2.1 Overview of Energy Harvesting Technologies . . . . . . . . . . . . . . . . . 6

2.1.1 Comparisons of Energy Sources . . . . . . . . . . . . . . . . . . . . 6

2.1.2 History of Energy Harvesting Technologies . . . . . . . . . . . . . 9

2.2 Rectenna Operation Principles . . . . . . . . . . . . . . . . . . . . . . . . 12

2.2.1 Rectifier Introduction . . . . . . . . . . . . . . . . . . . . . . . . 13

2.2.2 Losses During Rectifications . . . . . . . . . . . . . . . . . . . . . 17

2.2.3 Rectifier Topologies . . . . . . . . . . . . . . . . . . . . . . . . . 20

2.2.4 Power Management Circuit . . . . . . . . . . . . . . . . . . . . . . . 23
2.3 Applications of RF Energy Harvesting Technologies . . . . . . . . . . . . . 24
2.3.1 Evaluate Available RF and mm-wave Power with Friis Equation . . 25
2.3.2 Backscatter Sensors and RFID . . . . . . . . . . . . . . . . . . . . . 26
2.4 Energy Harvesting Design Trends . . . . . . . . . . . . . . . . . . . . . . 30
2.4.1 Rectenna Performance Improvement . . . . . . . . . . . . . . . . . . 31
2.4.2 Harvested Power Level Enhancement . . . . . . . . . . . . . . . . . 32
2.4.3 Advanced Applications . . . . . . . . . . . . . . . . . . . . . . . . 34

**Chapter 3: Review of Additive Manufacturing Technologies . . . . . . . . . . . 35**
3.1 Introduction . . . . . . . . . . . . . . . . . . . . . . . . . . . . . . . . 35
3.2 Inkjet Printing Technology . . . . . . . . . . . . . . . . . . . . . . . . 37
3.2.1 Resolution . . . . . . . . . . . . . . . . . . . . . . . . . . . . . . 37
3.2.2 Printable Materials and Applications . . . . . . . . . . . . . . . . . 38
3.3 3D Printing Technology . . . . . . . . . . . . . . . . . . . . . . . . . . 40
3.3.1 FDM Printing . . . . . . . . . . . . . . . . . . . . . . . . . . . . . 40
3.3.2 DLP and SLA Printing . . . . . . . . . . . . . . . . . . . . . . . . . 40
3.3.3 Available Materials . . . . . . . . . . . . . . . . . . . . . . . . . . 41
3.4 Semi-additive Glass Packaging Technology . . . . . . . . . . . . . . . . . 42
3.5 Printing Material Characterization . . . . . . . . . . . . . . . . . . . . . 42
3.5.1 Resonator-based Method . . . . . . . . . . . . . . . . . . . . . . . . 44
3.5.2 Transmission-based Method . . . . . . . . . . . . . . . . . . . . . . 44

**Chapter 4: On-Body Long-Range Sensor Networks Using RF Energy Harvester 46**

4.1 Objectives and Design Ideas . . . . . 47
4.1.1 Objectives, Challenges, and Solutions . . . . . 47
4.1.2 System Architecture . . . . . 49
4.2 Energy Harvester Design . . . . . 51
4.2.1 Receiving Antenna Design . . . . . 51
4.2.2 Rectifier/Frequency Doubler Design . . . . . 53
4.2.3 Re-emitting Antenna Design . . . . . 56
4.3 Multiple Uses of Harvester DC Output . . . . . 59
4.4 Backscatter Sensor Tag Design . . . . . 62
4.4.1 Sensor Tag Design . . . . . 62
4.4.2 Integration With Ammonia Sensor . . . . . 67
4.5 System Field Operation Test . . . . . 69
4.5.1 Received Power Level Test . . . . . 69
4.5.2 Operating Range Test . . . . . 70
4.5.3 Multiple Tags Test . . . . . 73
4.5.4 Ammonia Sensor Test . . . . . 74
4.5.5 Comparison with Previous Works . . . . . 75
4.6 Design Process Including Human Tissue Effects . . . . . 77
4.6.1 Simulation Process . . . . . 78
4.6.2 Receiving Antenna . . . . . 83
4.6.3 Rectifier Design . . . . . 92
4.6.4 Energy Harvesting Rectenna Measurement . . . . . 93
4.7 Summary . . . . . 96

**Chapter 5: Energy-autonomous Micropump System to Expand Horizons of Microfluidic Applications** . . . 98

5.1 Objectives and Design Ideas . . . 99

5.1.1 Objectives, Challenges, and Solutions . . . 99

5.1.2 System Architecture . . . 102

5.2 Energy Harvester Powered Micropump System Design . . . 104

5.2.1 Receiving Antenna Design . . . 104

5.2.2 Broadband Rectifier Design . . . 106

5.2.3 System Performance Evaluation . . . 108

5.3 Duty Cycling with Power Management Circuits . . . 111

5.3.1 Power Management Circuits . . . 111

5.3.2 Rectifier Design for Power Management Circuits . . . 113

5.4 Microfluidic Sweat Sensor . . . 116

5.4.1 Sweat Conductivity . . . 116

5.4.2 Fabrication Process . . . 118

5.4.3 Microfluidic Sweat Sensor Performance . . . 121

5.5 Energy-autonomous Backscatter Microfluidic Sensing System . . . 122

5.5.1 RF Switch Design . . . 122

5.5.2 Energy Harvester Design . . . 125

5.5.3 Microfluidic Sweat Sensor . . . 129

5.5.4 Backscattering Sensing System Performance Evaluation . . . 132

5.6 Summary . . . 138

**Chapter 6: Broadband 5G Package Integrated Energy Harvester Using Glass Packaging Technologies** . . . 141

6.1 Objectives and Design Ideas . . . 142

6.2 Glass SAP Process for Package Fabrication . . . 144

6.2.1 Glass Packaging Method . . . 144

6.2.2 SAP Process . . . 147

6.3 Broadband 5G Antenna-in-Package Design . . . 148

6.3.1 Broadband Yagi Design . . . 148

6.3.2 UWB Yagi Design . . . 154

6.4 Broadband 5G Energy Harvester . . . 167

6.4.1 Modified UWB Yagi Design . . . 167

6.4.2 Broadband 5G Rectifier Design . . . 169

6.4.3 Broadband 5G Energy Harvester Design . . . 173

6.5 Summary . . . 175

**Chapter 7: Energy Autonomous 5G System-in-Package Module Using Additive Manufacturing 3D Packaging Technologies** . . . 177

7.1 Objectives . . . 178

7.2 Additive Manufacturing 3D System-in-Package Module . . . 179

7.3 Parasitic Characterization Using Tunnel Diode . . . 180

7.3.1 Motivation and Design Idea . . . 180

7.3.2 Fabrication Process . . . 182

7.3.3 Tunnel Diode Characterization . . . 186

7.3.4 Parasitic Comparisons . . . 195

7.4 Fully Additive Manufacturing Fabrication Process Characterization . . . . . 196
7.4.1 Motivation and Design Idea . . . . . . . . . . . . . . . . . . . . . . . 196
7.4.2 3D Printing Flexible Material Characterization . . . . . . . . . . . . 197
7.4.3 3D Printing Core Substrate . . . . . . . . . . . . . . . . . . . . . . . 198
7.4.4 Inkjet Printing Polymer and Conductor . . . . . . . . . . . . . . . . 200
7.4.5 Fabrication Process . . . . . . . . . . . . . . . . . . . . . . . . . . 202
7.4.6 Broadband 5G Antenna-in-Package Design . . . . . . . . . . . . . . 204
7.4.7 System-in-Package Design . . . . . . . . . . . . . . . . . . . . . . . 208
7.5 Energy-autonomous 5G System-in-Package Design . . . . . . . . . . . . . 211
7.5.1 Motivation and Design Idea . . . . . . . . . . . . . . . . . . . . . . . 211
7.5.2 3D Printer Characterization . . . . . . . . . . . . . . . . . . . . . . . 213
7.5.3 Fabrication Process . . . . . . . . . . . . . . . . . . . . . . . . . . 218
7.5.4 Antenna-in-Package Design And Measurement . . . . . . . . . . . 221
7.5.5 Embedded 5G Energy Harvester Design and Measurement . . . . . 222
7.5.6 Energy Harvester Operation Test . . . . . . . . . . . . . . . . . . . 224
7.6 Inkjet-printed Low-loss Polymer for Millimeter-wave Applications . . . . . 227
7.6.1 Motivation and Design Idea . . . . . . . . . . . . . . . . . . . . . . . 227
7.6.2 Layer Thickness Characterization . . . . . . . . . . . . . . . . . . . 229
7.6.3 Via Holes Characterization . . . . . . . . . . . . . . . . . . . . . . . 232
7.7 Summary . . . . . . . . . . . . . . . . . . . . . . . . . . . . . . . . . . . 232

**Chapter 8: Conclusion and Contribution . . . . . . . . . . . . . . . . . . . . . . . 237**

8.1 Conclusion . . . . . . . . . . . . . . . . . . . . . . . . . . . . . . . . . . 237

8.2 Contribution . . . . . . . . . . . . . . . . . . . . . . . . . . . . . . . . 239
8.2.1 Innovative Energy Harvester Topologies . . . . . . . . . . . . . . . . 240
8.2.2 Increase Harvested Power Level . . . . . . . . . . . . . . . . . . . . . 240
8.2.3 Novel Energy Harvester Applications . . . . . . . . . . . . . . . . . 241
8.2.4 Advancement in Additive Manufacturing Process . . . . . . . . . . . 243
8.3 Publications . . . . . . . . . . . . . . . . . . . . . . . . . . . . . . . . 244
8.3.1 Journals . . . . . . . . . . . . . . . . . . . . . . . . . . . . . . . . 244
8.3.2 Conference Proceedings . . . . . . . . . . . . . . . . . . . . . . . . 246
8.3.3 Book Chapters . . . . . . . . . . . . . . . . . . . . . . . . . . . . . 249
**References** . . . . . . . . . . . . . . . . . . . . . . . . . . . . . . . . . . . 250
**Vita** . . . . . . . . . . . . . . . . . . . . . . . . . . . . . . . . . . . . . . 263

# LIST OF TABLES

1.1 The novelty of the works presented in each chapter. . . . . . . . . . . . . . 2

2.1 Comparisons of ambient energy sources . . . . . . . . . . . . . . . . . . . . 8

4.1 The dimensions of the Artificial Magnetic Conductor (AMC) design. . . . . 57

4.2 The power levels for link budget estimation. . . . . . . . . . . . . . . . . . 69

4.3 The performance comparison between the energy harvesters with and without an RF amplifier. . . . . . . . . . . . . . . . . . . . . . . . . . . . . . 71

4.4 The Comparison between this work and previous related works . . . . . . . 77

4.5 The measured results for loop and segmented loop antenna while transmitter and receiver distance is 5 cm. . . . . . . . . . . . . . . . . . . . . . . . 86

4.6 The comparison between simulated and measured results for loop and segmented loop antenna while transmitter and receiver distance is 7 cm. . . . . 91

4.7 The measured output voltage, power, and efficiency at 5 cm separation distance. . . . . . . . . . . . . . . . . . . . . . . . . . . . . . . . . . . . 95

5.1 The highest efficiency of different frequencies. . . . . . . . . . . . . . . . . 115

5.2 The conversion of NaCl concentration to conductivity. . . . . . . . . . . . . 117

5.3 The highest efficiency of different frequencies for the energy harvester with switch. . . . . . . . . . . . . . . . . . . . . . . . . . . . . . . . . . . . 128

5.4 The charging and discharging time of the system while using a 20 dBm 464.5 MHz input signal. . . . . . . . . . . . . . . . . . . . . . . . . . . . 135

5.5 The charging and discharging time of the system while using a 0 dBm input signal and a 47 mF super-capacitor. . . . . . . . . . . . . . . . . . . . . . . . 136

6.1 The frequency bands of the Fifth Generation (5G) New Radio (NR) wireless communication. . . . . . . . . . . . . . . . . . . . . . . . . . . . . . . 142

6.2 Physical dimensions of the proposed Ultra-wideband (UWB) Antenna-in-Package (AiP) element design. . . . . . . . . . . . . . . . . . . . . . . . . 156

6.3 The Comparisons between the proposed UWB and miniaturized AiP element design and previous related works . . . . . . . . . . . . . . . . . . . . 166

7.1 Parameter comparison between the inkjet-printed package and the traditional package. . . . . . . . . . . . . . . . . . . . . . . . . . . . . . . . . 195

7.2 Physical dimensions of the proposed broadband AiP design. . . . . . . . . 204

7.3 Measured surface roughness. . . . . . . . . . . . . . . . . . . . . . . . . 215

7.4 Measured thickness for cavities. . . . . . . . . . . . . . . . . . . . . . . 216

7.5 Measured via holes. . . . . . . . . . . . . . . . . . . . . . . . . . . . . . 217

7.6 Measured substrate thickness at the edge. . . . . . . . . . . . . . . . . . 218

7.7 Measured substrate thickness when printing with a 30° tilt angle. . . . . . . 218

7.8 Summary of different characteristics. . . . . . . . . . . . . . . . . . . . . . 219

## LIST OF FIGURES

2.1 Demonstration of ambient energy sources . . . . . . . . . . . . . . . . . . . . 7

2.2 Timeline of researches on power transmission using radio waves . . . . . . 10

2.3 The block diagram of a typical RF energy harvester . . . . . . . . . . . . . 12

2.4 The I-V curve of a common diode. . . . . . . . . . . . . . . . . . . . . . . . 13

2.5 The rectification principles of a (a) half-wave rectifier at (b) the positive half cycle and (c) the negative half cycle. . . . . . . . . . . . . . . . . . . . . 14

2.6 The rectification principles of a (a) half-wave rectifier with a smoothing capacitor at (b) the positive half cycle and (c) the negative half cycle. . . . . 15

2.7 The circuit model of a Schottky diode. . . . . . . . . . . . . . . . . . . . . . 16

2.8 The parameters of off-the-shelf diodes. . . . . . . . . . . . . . . . . . . . . . 17

2.9 The relationship between the efficiency and losses. . . . . . . . . . . . . . . 18

2.10 (a) Time-domain waveforms and (b) frequency-domain waveforms of a 500 MHz sinusoidal signal and the respective half-wave rectified results. . . . . 18

2.11 The circuit diagram of a (a) series rectifier and (b) parallel rectifier. . . . . . 21

2.12 The circuit diagram of a full-wave bridge rectifier. . . . . . . . . . . . . . . 22

2.13 The circuit diagram of a (a) voltage doubler and a (b) Cockcroft-Walton voltage multiplier. . . . . . . . . . . . . . . . . . . . . . . . . . . . . . . . 23

2.14 General received power for different spectrum when the receiving antenna gain is 0 dBi. . . . . . . . . . . . . . . . . . . . . . . . . . . . . . . . . . 25

2.15 Backscatter topology with waveform generator. . . . . . . . . . . . . . . . 27

2.16 Energy-autonomous backscatter sensors with an energy harvester. . . . . . 28

2.17 Energy-autonomous backscatter Radio-Frequency Identification (RFID) using Amplitude-Shift Keying (ASK) modulation. . . . . . . . . . . . . . . . 29

2.18 Energy autonomous backscatter RFID using Quadrature Phase Shift Keying (QPSK) modulation. . . . . . . . . . . . . . . . . . . . . . . . . 30

3.1 Comparisons between subtractive and additive manufacturing processes. . . 36

3.2 (a) The custom-build Digital Light Processing (DLP) Three-Dimensional (3D) printer. (b) The Stereolithography (SLA) 3D printer from FormLabs. . 41

3.3 Material characterization using commercially available dielectric resonator. 43

3.4 Material characterization using waveguides. . . . . . . . . . . . . . . . . . 44

4.1 The summarizing table of the objectives, challenges, and solutions of the proposed on-body long-range sensing network. . . . . . . . . . . . . . . 49

4.2 Wearable energy-autonomous on-body wireless sensor network system . . . 50

4.3 Block diagram of the proposed on-body wireless sensor network system . . 51

4.4 Measured power spectrum of the off-the-shelf two-way talk radio . . . . . . 52

4.5 (a) Prototype of the 464.5 MHz antenna (b) "On-body emulating" setup of the coupling test for the 464.5 MHz antenna. . . . . . . . . . . . . . . . . 53

4.6 (a) Time-domain waveforms and (b) frequency-domain waveforms of a 464.5 MHz sinusoidal signal and the respective full-wave rectified results. . 54

4.7 (a) The circuit diagram and (b) the prototype of the proposed full-wave rectifier / frequency doubler. . . . . . . . . . . . . . . . . . . . . . . . . 54

4.8 (a) Simulated and measured $S_{11}$ and (b) output Direct Current (DC) and Radio Frequency (RF) power levels from the proposed rectifier/frequency doubler with respect to the input power. . . . . . . . . . . . . . . . . . . 55

4.9 Side view of the wearable 929 MHz antenna. . . . . . . . . . . . . . . . . 56

4.10 Prototype of the FSS. . . . . . . . . . . . . . . . . . . . . . . . . . . . 56

4.11 (a) The single cell AMC structure and (b) the simulated phase of the reflected wave. . . . . . 57

4.12 Prototype of the (a) unfolded and (b) folded 929 MHz antenna. . . . . . . . 58

4.13 Measured $S_{11}$ of the folded and unfolded 929 MHz wearable antenna. . . . 59

4.14 Block diagram of the proposed energy harvester with enhanced RF output by driving an RF amplifier using DC output power. . . . . . 60

4.15 Proof-of-concept prototype of the proposed rectifier/frequency doubler including a DC power enabled amplifier. . . . . . 61

4.16 Simulated and measured output DC and RF power levels from the proposed rectifier/frequency doubler with an RF amplifier . . . . . . 62

4.17 Circuit diagram of the custom-made backscattering sensor tag. . . . . . . . 63

4.18 Prototype of the custom-made backscattering sensor tag. . . . . . 64

4.19 Measured S-parameters of 929 MHz with each expected input power and MOSFET bias voltage. . . . . . 65

4.20 Measured output voltage from the voltage regulator connected with the voltage doubler with 464.5 MHz RF input signal at each input power and MOSFET bias voltage. . . . . . 65

4.21 Measured $S_{11}$ of the 929 MHz antenna. . . . . . 66

4.22 Received 464.5 MHz power from the hand-held two-way radio by the tag antenna. . . . . . 66

4.23 Prototype of the custom backscattering sensor tag with a printed ammonia sensor. . . . . . 67

4.24 Prototype of the energy harvesting circuit without an RF amplifier. . . . . . 68

4.25 Prototype of the energy harvesting circuit with an RF amplifier. . . . . . . . 68

4.26 Experimental setup for the testing of the link budget . . . . . . 69

4.27 Measurement setup for the long-range on-body wireless sensing network. . 70

4.28 Measured signal to noise ratio at different distances. . . . . . 71

4.29 Measurement setup for the multiple sensors test. . . . . . . . . . . . . . . . . 74
4.30 Measured result for multiple sensors test. . . . . . . . . . . . . . . . . . . . . 75
4.31 Measured result for the ammonia sensor tag before exposure to ammonia. . 76
4.32 Measured result for the ammonia sensor tag after exposure to ammonia. . . 76
4.33 The block diagram of the wearable energy harvesting system. . . . . . . . . 77
4.34 The circuit model of the energy harvester. . . . . . . . . . . . . . . . . . . . 78
4.35 The equivalent Thevenin circuit model of the energy harvester. . . . . . . . 78
4.36 The flow chart of energy harvester simulation and the output power estimation. . . . . . . . . . . . . . . . . . . . . . . . . . . . . . . . . . . . . . 80
4.37 (a) The harmonic balance setup in Advanced Design System (ADS) and (b) the simulated open-circuit voltage. . . . . . . . . . . . . . . . . . . . . . . . 81
4.38 Two-way talk radio model in High-Frequency Structure Simulator (HFSS) . 82
4.39 The electric field around the two-way radio . . . . . . . . . . . . . . . . . 82
4.40 The magnetic field around the two-way radio . . . . . . . . . . . . . . . . 82
4.41 (a) Loop type wearable receiving antenna and (b) Segmented loop type wearable receiving antenna. . . . . . . . . . . . . . . . . . . . . . . . . . . 83
4.42 (a) Simulation model for the loop antenna, two-way radio, and human hand and (b) Simulated scattering parameters. . . . . . . . . . . . . . . . . . . . 84
4.43 Fabrication process using inkjet printed masks. . . . . . . . . . . . . . . . 84
4.44 Fabricated prototypes of the (a) loop antenna and (b) segmented loop antenna. 85
4.45 The (a) simulation model and (b) measurement setup of the loop antenna. . 86
4.46 Measured scattering parameters of the loop antenna. . . . . . . . . . . . . . 87
4.47 The (a) simulation model and (b) measurement setup of the segmented loop antenna. . . . . . . . . . . . . . . . . . . . . . . . . . . . . . . . . . . . . 87
4.48 Measured scattering parameters of the segmented loop antenna. . . . . . . . 88

4.49 The measured (a) $S_{22}$ and (b) received power under different distances. . . . 89

4.50 The angle definition for the dynamic motion measurement. . . . . . . . . . 90

4.51 The measured $S_{22}$ under different angles. . . . . . . . . . . . . . . . . . . . . 90

4.52 The measurement setups of the open-circuit voltages for the (a) loop antenna and (b) segmented loop antenna. . . . . . . . . . . . . . . . . . . . . . . 91

4.53 The measured waveforms of open-circuit voltages. . . . . . . . . . . . . . . 92

4.54 (a) The circuit model of the rectifier and (b) The fabricated prototypes. . . . 92

4.55 The measured output powers from the rectifier. . . . . . . . . . . . . . . . . 93

4.56 The prototypes of the rectenna with the (a) loop and (b) segmented loop receiving antenna. . . . . . . . . . . . . . . . . . . . . . . . . . . . . . . . 94

4.57 The definition of angles for dynamic measurements of (a) loop rectenna and (b) segmented loop rectenna. . . . . . . . . . . . . . . . . . . . . . . . 94

4.58 The measured output power at different angles. . . . . . . . . . . . . . . . 95

5.1 The summarizing table of the objectives, challenges, and solutions of the proposed energy-autonomous long-range microfluidic sensing network. . . 100

5.2 Block diagram of the proposed energy-autonomous microfluidic system . . 103

5.3 Block diagram of the proposed energy-autonomous microfluidic backscatter sensing system. . . . . . . . . . . . . . . . . . . . . . . . . . . . . . . 104

5.4 Broadband antenna in (a) flat and (b) folded conditions. . . . . . . . . . . . 105

5.5 Measured $S_{11}$ in flat and folded condition. . . . . . . . . . . . . . . . . . . 105

5.6 (a) The circuit diagram and (b) the prototype of the proposed broadband rectifier . . . . . . . . . . . . . . . . . . . . . . . . . . . . . . . . . . . . 106

5.7 Measured $S_{11}$ of the proposed broadband rectifier. . . . . . . . . . . . . . . 107

5.8 (a) The simulated and measured (a) output DC voltage and (b) output DC power of the proposed broadband rectifier at different frequencies. . . . . . 107

5.9 (a) The simulated and measured (a) output DC voltage and (b) output DC power of the proposed broadband rectifier at different input powers. . . . . 108

5.10 The measurement setup of the proposed energy-autonomous microfluidic system. . . . . . . . . . . . . . . . . . . . . . . . . . . . . . . . . . . 109

5.11 Output voltage at the output pin of the driver Integrated Circuit (IC). . . . . 110

5.12 Measured $S_{21}$ of a liquid-tunable band-stop filter. . . . . . . . . . . . . . . 110

5.13 The definitions of output voltages form the power management circuit (BQ 25570). . . . . . . . . . . . . . . . . . . . . . . . . . . . . . . . . . . 111

5.14 The input impedances of the power management circuit (BQ 25570). . . . . 112

5.15 The circuit diagram of the proposed rectifier with power management circuit (BQ 25570) load. . . . . . . . . . . . . . . . . . . . . . . . . . . . . 113

5.16 The fabricated prototype of the proposed rectifier with power management circuit load. . . . . . . . . . . . . . . . . . . . . . . . . . . . . . . . . 113

5.17 (a) The measured (a) output DC voltage and (b) output DC power of the proposed rectifier with BQ 25570 load at different frequencies. . . . . . . . 114

5.18 (a) The measured (a) output DC voltage and (b) output DC power of the proposed rectifier with BQ 25570 load at different input powers. . . . . . . 114

5.19 (a) The measured RF-DC efficiency of the proposed rectifier with BQ 25570 load (a) at different frequencies and (b) at different input powers. . . . . . . 115

5.20 (a) The conductivity of NaCl under different concentrations [95] and (b) the conversion of NaCl concentration to conductivity. . . . . . . . . . . . . 117

5.21 (a) The topology of a microfluidic sensor and (b) its electrodes. . . . . . . . 118

5.22 The fabrication process of an additive manufacturing mold for microfluidic sensor. . . . . . . . . . . . . . . . . . . . . . . . . . . . . . . . . . . . 118

5.23 (a) The fabricated prototypes of the mold and (b) microfluidic channel. . . . 119

5.24 The fabrication process of an additive manufacturing microfluidic sensor. . 120

5.25 (a) The topology of the microfluidic sensor test vehicle and (b) the flexibility of the proposed microfluidic sweat sensor. . . . . . . . . . . . . . . . . 120

5.26 (a) The measured resistances of the microfluidic sweat sensor (b) the stability and repeatability test of the microfluidic sweat sensor. . . . . . . . . . 121

5.27 The circuit diagram of the RF switch design using MOSFET BF 1118. . . . 123

5.28 The measured $S_{21}$ of the RF switch using MOSFET BF 1118. . . . . . . . . 123

5.29 (a) The circuit diagram and (b) prototype of the RF switch design using pin diode SMP 1340. . . . . . . . . . . . . . . . . . . . . . . . . . . . . 124

5.30 The measured $S_{21}$ of the RF switch using pin diode SMP 1340. . . . . . . . 124

5.31 The circuit diagram of the proposed rectifier with switch and power management circuit load. . . . . . . . . . . . . . . . . . . . . . . . . . . 125

5.32 The fabricated prototype of the proposed rectifier with switch and power management circuit load. . . . . . . . . . . . . . . . . . . . . . . . . 125

5.33 (a) The measured (a) output DC voltage and (b) output DC power of the proposed rectifier with switch and power management circuit load at different frequencies. . . . . . . . . . . . . . . . . . . . . . . . . . . . . 126

5.34 The measured RF-DC efficiency of the proposed rectifier with switch and power management circuit load at different frequencies from (a) 400 MHz to 1000 MHz and (b) from 850 MHz to 950 MHz. . . . . . . . . . . . . . . 126

5.35 (a) The measured (a) output DC voltage and (b) output DC power of the proposed rectifier with switch and power management circuit load at different input powers. . . . . . . . . . . . . . . . . . . . . . . . . . . 127

5.36 The measured RF-DC efficiency of the proposed rectifier with switch and power management circuit load at different input powers. . . . . . . . . . . 127

5.37 The measured input impedances of the rectifier while the switch is on different states. . . . . . . . . . . . . . . . . . . . . . . . . . . . . . . 128

5.38 (a) The design schematic of the sweat sensor, (b) the inkjet printed electrodes, (c) the 3D printed flexible microchannel, and (d) the sweat sensor test sample . . . . . . . . . . . . . . . . . . . . . . . . . . . . . . . 130

5.39 The measured resistance of the microfluidic sweat sensor while the microchannel is filled with (a) distilled water (b) 30.8 mmol/L NaCl, and (c) 71.9 mmol/L NaCl . . . . . . . . . . . . . . . . . . . . . . . . . . . . 130

5.40 The prototypes of the microfluidic sweat sensor with a default resistor. . . . 131

5.41 The measured resistance of the microfluidic sweat sensor with default resistor while the microchannel is filled with (a) 30.8 mmol/L NaCl and (b) 71.9 mmol/L NaCl . . . . . . . . . . . . . . . . . . . . . . . . . . . . . . 131

5.42 The prototypes of all components of the proposed Energy Harvester (EH) powered backscattering sensing system. . . . . . . . . . . . . . . . . . . . . 132

5.43 The output voltage waveforms of the power management circuit. . . . . . . 133

5.44 The output voltage waveforms of the micropump driving IC in (a) large time scale and (b) small time scale. . . . . . . . . . . . . . . . . . . . . . . . 133

5.45 The output voltage waveforms of the oscillator. . . . . . . . . . . . . . . . 134

5.46 The voltages across energy storage devices (super-capacitor) while charging and discharging using a 20 dBm 464.5 MHz input signal. . . . . . . . . 135

5.47 The voltages across a 47 mF super-capacitor while charging and discharging using 0 dBm input signals. . . . . . . . . . . . . . . . . . . . . . . . . . 136

5.48 The measurement setup of the proposed EH powered backscattering sensing system. . . . . . . . . . . . . . . . . . . . . . . . . . . . . . . . . . . 137

5.49 The measured wireless backscattered signals when the sweat sensor is filled with (a) 30.8 mmol/L NaCl and (b) 71.9 mmol/L NaCl . . . . . . . . . . . 137

6.1 The 3D System-in-Package (SiP) module with AiP designs for 5G applications. . . . . . . . . . . . . . . . . . . . . . . . . . . . . . . . . . . . . . 142

6.2 The summarizing table of the objectives, challenges, and solutions of the proposed 5G UWB AiP and energy harvester design. . . . . . . . . . . . . 144

6.3 The dielectric constant and loss tangent of the AGC EN-A1 glass substrate. 145

6.4 The comparisons between the glass packaging and other packaging methods. 146

6.5 Fabrication process of glass Semi-Additive Patterning (SAP) packaging technology. . . . . . . . . . . . . . . . . . . . . . . . . . . . . . . . . . . 147

6.6 The stackup for the proposed broadband AiP design. . . . . . . . . . . . . 148

6.7 The geometry of the proposed broadband AiP element design. . . . . . . . 149

6.8 The design idea to realize broadband Yagi AiP Design. . . . . . . . . . . . 149

6.9 The fabricated prototype of the proposed broadband AiP element design. . . 150

6.10 The measured and simulated $S_{11}$ of the proposed broadband AiP element. . 151

6.11 The measured and simulated realized gain of the proposed broadband AiP element. . . . . . . . . . . . . . . . . . . . . . . . . . . . . . . . . . 152

6.12 The measured and simulated normalized E-plane radiation patterns at (a) 24 GHz and (b) 30 GHz. . . . . . . . . . . . . . . . . . . . . . . . . . 153

6.13 The measured and simulated normalized H-plane radiation patterns at (a) 24 GHz and (b) 30 GHz. . . . . . . . . . . . . . . . . . . . . . . . . . 153

6.14 The stackup for the proposed UWB AiP element design. . . . . . . . . . . 154

6.15 The geometry of the proposed UWB AiP element design. . . . . . . . . . . 155

6.16 The geometry of the proposed UWB AiP array design. . . . . . . . . . . . 156

6.17 The fabricated prototypes of the UWB AiP (a) element design and (b) array design. . . . . . . . . . . . . . . . . . . . . . . . . . . . . . . . . . 157

6.18 The comparisons of measured and designed dimensions for the UWB AiP (a) element and (b) 2-by-1 array design. . . . . . . . . . . . . . . . . . . 158

6.19 The measured and simulated (a) $S_{11}$ and (b) gain of the proposed UWB and miniaturized AiP element design. . . . . . . . . . . . . . . . . . . . . . 159

6.20 Measured and simulated normalized E-plane radiation patterns of the UWB AiP element at (a) 24.25 GHz (b) 29.5 GHz (c) 37 GHz and (d) 40 GHz. . . 160

6.21 Measured and simulated normalized H-plane radiation patterns of the UWB AiP element at (a) 24.25 GHz (b) 29.5 GHz (c) 37 GHz and (d) 40 GHz. . . 161

6.22 The measured and simulated (a) $S_{11}$ and (b) gain of the proposed UWB and miniaturized AiP 2-by-1 array design. . . . . . . . . . . . . . . . . . . 163

6.23 Measured and simulated normalized E-plane radiation patterns of the UWB AiP array at (a) 24.25 GHz (b) 29.5 GHz (c) 37 GHz and (d) 40 GHz. . . . 164

6.24 Measured and simulated normalized H-plane radiation patterns of the UWB AiP array at (a) 24.25 GHz (b) 29.5 GHz (c) 37 GHz and (d) 40 GHz. . . . 165

6.25 (a) The geometry of the modified UWB AiP element design and (b) the fabricated proof-of-concept sample. . . . . . . . . . . . . . . . . . . . . 167

6.26 The measured (a) $S_{11}$ and (b) gain of the modified UWB and miniaturized AiP design. . . . . . . . . . . . . . . . . . . . . . . . . . . . . . . . . 168

6.27 The geometry of the proposed broadband rectifier design for 5G lower bands. 169

6.28 The geometry of the proposed broadband rectifier design for 5G upper bands. 169

6.29 The simulated (a) output voltage and (b) RF-DC efficiency of the lower-band rectifier with respect to different frequencies. . . . . . . . . . . . . . . 170

6.30 The simulated (a) output voltage and (b) RF-DC efficiency of the lower-band rectifier with respect to different input powers. . . . . . . . . . . . . 170

6.31 The simulated (a) output voltage and (b) RF-DC efficiency of the upper-band rectifier with respect to different frequencies. . . . . . . . . . . . . . . 171

6.32 The simulated (a) output voltage and (b) RF-DC efficiency of the upper-band rectifier with respect to different input powers. . . . . . . . . . . . . 171

6.33 The fabricated rectifiers for the (a) lower-band operation and (b) higher-band operation. . . . . . . . . . . . . . . . . . . . . . . . . . . . . . . 172

6.34 The measured and simulated output power levels for the proposed (a) lower-band rectifier design and (b) higher-band rectifier design. . . . . . . . . . . 173

6.35 The fabricated broadband 5G energy harvester for the (a) lower-band operation and (b) higher-band operation. . . . . . . . . . . . . . . . . . . . . . 174

6.36 The measurement setup for the proposed broadband 5G energy harvester. . 174

7.1 The summarizing table of the objectives, challenges, and solutions of the proposed energy-autonomous SiP module. . . . . . . . . . . . . . . . . . . 178

7.2 The additive manufacturing 3D SiP module for Millimeter-Wave (mm-wave) applications. . . . . . . . . . . . . . . . . . . . . . . . . . . . . 179

7.3 The general I-V curve of a tunnel diode. . . . . . . . . . . . . . . . . . . . 181

7.4 Side-view schematic of inkjet-printed interconnect fabrication process: (1) inkjet print SNP die attach, (2) attach diode die, (3) inkjet print SU-8 dielectric ramp, (4) inkjet print SNP interconnect. . . . . . . . . . . . . . . . 183

7.5 Inkjet-printed interconnect fabrication process with tunnel diode die: (a) Silver Nanoparticle (SNP) die attach patterning, (b) die placement, (c) SU-8 ramp patterning, (d) final SNP interconnect patterning, and (e) perspective micrograph. . . . . . . . . . . . . . . . . . . . . . . . . . . . . . . . . . 184

7.6 Profilometer scan of inkjet-printed ramp interconnect to diode die. . . . . . 185

7.7 The equivalent circuit model of the tunnel diode with packaging. . . . . . . 186

7.8 The photo of the (a) die with inkjet printed package and (b) die with traditional package. . . . . . . . . . . . . . . . . . . . . . . . . . . . . . . . . . 187

7.9 The TRL calibration circuits. . . . . . . . . . . . . . . . . . . . . . . . . . 188

7.10 The measured $S_{21}$ of the TRL calibration. . . . . . . . . . . . . . . . . . . 189

7.11 The measured $S_{21}$ of the original and TRL de-embedded tunnel diode with (a) inkjet printing package and (b) traditional package. . . . . . . . . . . . 190

7.12 The measured DC I-V Curves of the tunnel diodes. . . . . . . . . . . . . . 191

7.13 The extraction of $R_s$ for the tunnel diode with the inkjet-printed package. . . 192

7.14 The extraction of $R_s$ for the tunnel diode with the traditional package. . . . 193

7.15 The comparisons between the equivalent model and the measured $S_{21}$ of the tunnel diode with the inkjet-printed package. . . . . . . . . . . . . . . . 194

7.16 The comparisons between the equivalent model and the measured $S_{21}$ of the tunnel diode with the traditional package. . . . . . . . . . . . . . . . . 195

7.17 The measured dielectric constant of the 3D printing material, Flexible FLGR02. 198

7.18 The measured loss tangent of the 3D printing material, Flexible FLGR02. . 199

7.19 The effects of exposure time on the 3D-printed substrates. . . . . . . . . . . 200

7.20 Demonstration of large-scale fabrication. . . . . . . . . . . . . . . . . . . . 200

7.21 Flexibility of the 3D-printed substrate. . . . . . . . . . . . . . . . . . . . . 201

7.22 Ink adhesion while (a) no surface treatment is applied and (b) exposure to ultraviolet (UV) ozone before inkjet printing. . . . . . . . . . . . . . . . . 201

7.23 Inkjet printing results (a) without SU-8 coating and (b) with SU-8 coating. . 202

7.24 Fully additive manufacturing SiP process with surface treatment. . . . . . . 203

7.25 The geometry of the proposed broadband AiP design. . . . . . . . . . . . . 203

7.26 The fabricated prototype of the proposed broadband AiP design. . . . . . . 204

7.27 Measured and simulated (a) $S_{11}$ and (b) gain of the proposed broadband AiP design. . . . . . . . . . . . . . . . . . . . . . . . . . . . . . . . . . 205

7.28 Measured normalized radiation patterns of the proposed broadband AiP design at (a) 22 GHz (b) 24 GHz (c) 28 GHz and (d) 30 GHz. . . . . . . . . 206

7.29 Fully additive manufacturing SiP Process with an embedded IC. . . . . . . 208

7.30 3D- and inkjet-printed SiP design with an embedded IC. . . . . . . . . . . . 209

7.31 Fabricated prototypes of 3D- and inkjet-printed SiP design with an embedded IC. . . . . . . . . . . . . . . . . . . . . . . . . . . . . . . . . . . . 210

7.32 SiP design (a) with an embedded IC attached and (b) sealed with flexible material. . . . . . . . . . . . . . . . . . . . . . . . . . . . . . . . . . . 210

7.33 Miniaturized 3D- and inkjet-printed SiP design with an embedded IC. . . . 211

7.34 The embedded-in-package energy harvester within 3D-printed multilayer packaging structure. . . . . . . . . . . . . . . . . . . . . . . . . . . . . 212

7.35 The stackup of the test samples for 3D printing material, Flexible FLGR02. 213

7.36 The geometry of the test samples for 3D printing material, Flexible FLGR02.214

7.37 The fabricated prototypes of the test sampless for 3D printing material, Flexible FLGR02 under different printing tilt angles. . . . . . . . . . . . . 214

7.38 The definition of the tilt angle. . . . . . . . . . . . . . . . . . . . . . . . . 215

7.39 The measured positions of the test samples for 3D printing material, Flexible FLGR02. . . . . . . . . . . . . . . . . . . . . . . . . . . . . . . . . 217

7.40 Fabrication process for additive manufacturing multilayer packaging structures. . . . . . . . . . . . . . . . . . . . . . . . . . . . . . . . . . . . . 220

7.41 (a) 3D printed substrate with cavity, ramps, and vias. (b) Substrate coated with SU-8. . . . . . . . . . . . . . . . . . . . . . . . . . . . . . . . . . 221

7.42 (a) Inkjet printed silver on the top of the 3D-printed substrate (b) The package-integrated energy harvester (c) Filling the cavity with flexible material and (d) Inkjet-printed antenna array on the top layer. . . . . . . . . . . 222

7.43 The prototypes of ramp interconnections. . . . . . . . . . . . . . . . . . . . . 223

7.44 The geometry of the package-integrated antenna array design. . . . . . . . . 223

7.45 The prototype of the package-integrated antenna array design. . . . . . . . 224

7.46 The measured (a) $S_{11}$ and (b) normalized radiation pattern at 26 GHz of the package-integrated antenna array design. . . . . . . . . . . . . . . . . . . . . 225

7.47 Measured and simulated (a) output voltage of the embedded energy harvester with respect to different input powers at 26 GHz and (b) $S_{11}$ of the embedded energy harvester after filling. . . . . . . . . . . . . . . . . . . . . 226

7.48 The wireless performance evaluation setup for the 5G package-integrated energy harvester. . . . . . . . . . . . . . . . . . . . . . . . . . . . . . . . 227

7.49 Fully autonomous SiP backscattering sensor topology. . . . . . . . . . . . . 228

7.50 Prototype for fully autonomous SiP backscattering sensor. . . . . . . . . . . 228

7.51 The inkjet-printed Bisbenzocyclobutene (BCB) patterns. . . . . . . . . . . 229

7.52 The inkjet printing BCB squares for layer thickness characterization. . . . . 230

7.53 The profilometer measurement of the inkjet-printed BCB with (a) 1-layer, (b) 3-layer, (c) 5-layer, (d) 7-layer, and (e) 9-layer printing. . . . . . . . . . 231

7.54 The thickness comparisons between different numbers of layer. . . . . . . . 232

7.55 The profilometer measurement of the inkjet-printed BCB with 12-layer printing and the pattern is a larger 8 mm square. . . . . . . . . . . . . . . . 233

7.56 The inkjet-printed via holes with different dimensions using BCB ink. . . . 233

7.57 The measured sizes of 12-layer via holes under microscope with diameter equals (a) 400 µm, (b) 500 µm, and (c) 600 µm. . . . . . . . . . . . . . . . . 234

## LIST OF ACRONYMS

**3D** Three-Dimensional

**3G** Third Generation

**5G** Fifth Generation

**ADC** Analog to Digital Converter

**ADS** Advanced Design System

**AiP** Antenna-in-Package

**AMC** Artificial Magnetic Conductor

**ASK** Amplitude-Shift Keying

**BCB** Bisbenzocyclobutene

**CPW** Coplanar Waveguide

**CTE** Coefficient of Thermal Expansion

**DC** Direct Current

**DLP** Digital Light Processing

**DTV** Digital Television

**EH** Energy Harvester

**EIRP** Effective Isotropically Radiated Power

**EM** Electromagnetic

**FBW** Fractional Bandwidth

**FCC** Federal Communications Commission

**FDM** Fused Deposition Modeling

**FSS** Frequency Selective Surface

**GSM** Global System for Mobile Communications

**HFSS** High-Frequency Structure Simulator

**IC** Integrated Circuit

**IoT** Internet-of-Things

**LCP** Liquid Crystalline Polymer

**LTCC** Low Temperature Co-fired Ceramic

**MCU** Micro-controller Unit

**MIMO** Multi-input Multi-output

**mm-wave** Millimeter-Wave

**MPPT** Maximum Power Point Tracking

**NR** New Radio

**PCB** Printed Circuit Board

**PEC** Perfect Electrical Conductor

**PV** Photovoltaic

**QPSK** Quadrature Phase Shift Keying

**RF** Radio Frequency

**RFIC** Radio Frequency Integrated Circuit

**RFID** Radio-Frequency Identification

**SAP** Semi-Additive Patterning

**SDR** Software Defined Radio

**SiP** System-in-Package

**SLA** Stereolithography

**SNP** Silver Nanoparticle

**SNR** Signal-to-Noise Ratio

**SoP** System-on-Package

**SPS** Solar Power Satellite

**UHF** Ultra High Frequency

**UV** ultraviolet

**UWB** Ultra-wideband

**VNA** Vector Network Analyser

**WPT** Wireless Power Transfer

**WSN** Wireless Sensor Network

# SUMMARY

The objectives of my researches are developing new RF and mm-wave energy harvester topologies and realizing them with new additive manufacturing fabrication processes. The proposed energy harvester topologies are utilized to achieve energy-autonomous wireless sensing networks for 5G communication and Internet-of-Things (IoT) solutions. The developed additive manufacturing fabrication process is adopted to realize not only energy harvesters but also mm-wave IC packaging process.

Ambient energy harvesting techniques collect ambient energy such as solar, RF, heat, and vibration and convert them into DC power sources to support the energy requirement of electronics. Since the energy is provided autonomously and constantly, maintenance or replacement for the batteries inside wireless electronics is not necessary resulting in enormous cost reduction. The researches of energy harvester focus on three categories, new topologies to enhance the performances, increased harvested power levels, and applied energy harvester to find new killer applications. This work proposes new designs and improvements in all three categories. Various proof-of-concept backscatter sensing systems with integrated RF energy harvesters for 5G and IoT applications are demonstrated. In this research, high-efficiency and broadband rectifiers are proposed to support high-performance rectifications as well as increase harvested energy. New topologies to utilize both DC and harmonics are demonstrated to increase the reading range of on-body wireless sensing networks. Furthermore, energy-autonomous microfluidic sensing systems are demonstrated to unleash the potential of microfluidic applications. 5G energy harvester is proposed and integrated inside the multi-layered additive manufacturing IC packages to achieve fully-functional SiP modules.

While determining the fabrication methods, low-cost, fast-prototyping, and scalable methods with great material and structural flexibilities are preferable, and thus, additive manufacturing technologies including inkjet printing, 3D printing, and glass SAP pro-

cess are adopted. This research utilizes inkjet-printed masks, substrates, and metal traces to simplify the conventional fabrication process. The new low-loss inkjet-printable ink is developed to push the additive manufacturing technologies to mm-wave ranges. The flexible 3D-printed materials are characterized and used for wearable sensor designs, microfluidic channels, and flexible packaging topologies. The 3D features are included inside the IC packages to achieve high-performance multi-layer packaging structures with shorter lengths, lower loss, and smaller parasitics. The high-precision glass SAP process is used to realized AiP and SiP designs with great performances. Furthermore, through combining inkjet and 3D printing, this work proposes a fast, cost-effective, scalable, and environmentally-friendly fabrication process for various high-performance and compact antenna designs, microwave/mm-wave components, microfluidic channels, RF energy harvesters, and SiP designs.

In summary, this work utilizes additive manufacturing processes to realize various innovative topologies of energy harvesters to harvest more power and achieve higher rectification efficiency with smaller sizes. Additive manufacturing processes and energy harvesting techniques are also used to demonstrate new applications including the first on-body long-range sensing network, the first energy-autonomous long-range microfluidic sensing system, and the first fully-functional energy-autonomous 5G SiP module design. The proposed topologies are suitable for smart cities, smart skin, and IoT applications.

# CHAPTER 1
# INTRODUCTION

## 1.1 Research Objectives

My researches focus on two main objectives. The first one is to develop new energy harvester topologies to achieve better performances, harvest more power, and apply to new applications. The second one is to develop new additive manufacturing procedures with better physical and electrical properties.

The energy harvesting technologies collect ambient energy from the environment and convert it to electrical power to drive applications. The RF energy harvester has attracted more and more attention in recent years because this kind of energy can be accessed all day and the ability to bypass the obstacles make RF energy ubiquitously available. However, the weakness of the RF ambient energy compared with other kinds of energy sources is the lower power density. Thus, two of the main research directions of RF energy harvesters are developing topologies that improving the performances and establishing methods that harvesting more power. To improve the performance, numerous topologies are proposed to increase the RF-DC conversion efficiency, reduce the effects of load variation, increase the sensitivities, and expand the operating power range. On the other hand, technologies such as broadband and multi-band energy harvesters are proposed to collect more power simultaneously to overcome the low RF power density. In addition to these two research focuses, some researchers focus on applying the energy harvesters to new applications to find the "killer" applications of energy harvesting technologies. Such applications include IoT, smart skins, and smart cities.

The additive manufacturing process is a relatively young technology compared with subtractive manufacturing processes. However, numerous advantages including complex

Table 1.1: The novelty of the works presented in each chapter.

| Novelty | Chapter 4 | Chapter 5 | Chapter 6 | Chapter 7 |
|---|---|---|---|---|
| EH improved performance | o | | | |
| EH harvested more power | o | o | o | |
| EH new applications | o | o | o | o |
| AM process improvement | o | o | o | o |

EH: Energy Harvester
AM: Additive Manufacturing
o: Contains improvements in this field

3D structures, non-orthogonal structures, lower cost, lesser waste, faster prototyping, and more material choices are provided by using the additive manufacturing process. The drawbacks of the additive manufacturing process are that since it is relatively immature, the resolution is lower, the fabrication equipment has to be improved, large-scale fabrication method needs to be perfected, printable materials with better properties are still desired, and the integration of different additive manufacturing methods also remains under development.

In my researches, both advancements in energy harvester topologies and additive manufacturing processes are proposed and demonstrated. The novelties of each chapter are summarized as in Table 1.1. For the performance enhancement, in chapter 4, commonly waste harmonics are utilized as a carrier emitter to increase the reading range of backscattering on-body sensing systems. For the power level enhancement, energy from the near-field hand-held devices is harvested to overcome the low RF power density in chapter 4. In chapter 5, the near-field energy is integrated with far-field RF energy sources with a power management circuit to achieve advantages of both types of energy sources. In chapter 6, the UWB designs are proposed to increase the received power level.

For the novel applications, in chapter 4, the first energy-autonomous on-body wireless sensing network is proposed and can be applied to smart skins. In chapter 5, the energy-autonomous microfluidic sensor is built to move microfluidic and bio-sensing from in-lab application to ubiquitous applications. Designs that harvested high-power 5G mm-wave

energy are demonstrated in chapter 6 and chapter 7.

The additive manufacturing methods used in my researches include inkjet printing, 3D printing, and glass SAP processes. In chapter 4, a new 3D and inkjet printed AMC structure is proposed to isolate the human tissue effects. A new additive manufacturing process to realize micro-channels for microfluidic sensors is proposed in chapter 5. In chapter 6, the high-precision glass SAP packaging process is developed with a new low-loss material. The inkjet and 3D printing are integrated to develop a fully additive manufacturing IC packaging fabrication process in chapter 7. Furthermore, low-loss inkjet printable material is developed to push the proposed additive manufacturing packaging process to mm-wave applications.

## 1.2 Dissertation Outline

The outline of the dissertation is as the following:

1. Chapter 1 introduces the objectives of my researches and the outline of the rest of the content.

2. Chapter 2 provides background knowledge and the history of the energy harvester. The operation principles of the rectenna are introduced with detailed discussions of the diodes and rectifier topologies. The calculations of available RF power levels are included. Furthermore, as an important application of energy harvesting technologies, the background knowledge of the backscatter sensors and RFID is introduced. The literature survey of the energy harvester in performance enhancement, received power enhancement, and new applications are also included.

3. Chapter 3 reviews the additive manufacturing technologies. Current statuses of both inkjet printing and 3D printing will be provided.

4. Chapter 4 proposes an on-body long-range sensing network. The high-power energy from hand-held two-way talk radio is harvested. The new flexible energy harvester

topology to utilize both the rectified DC power and the commonly wasted harmonics is demonstrated. The reading range of the sensing network is extended to more than 270 m due to the use of the harmonics as the carrier emitter. The human body effects on energy harvester are investigated. The 3D printed AMC structure is adopted to isolate the circuit and the human body.

5. Chapter 5 demonstrates an energy-autonomous microfluidic sensing system. The near-field energy from two-way radio and far-field energy from the Ultra High Frequency (UHF) RFID reader are harvested simultaneously and integrated with a power management circuit. Both advantages from the near-field and far-field energy sources are achieved using the proposed system. The energy-autonomous micropump system is used to drive the microfluidic applications and expand the applications of microfluidic from lab-use only to ubiquitous applicable. A new fast-prototyping additive manufacturing microfluidic fabrication process is proposed and a sweat sensor is realized as a proof-of-concept test vehicle. The microfluidic sweat sensor detects the conductivity change in the fluid so that the effects of the clutters can be minimized. The backscatter topology is used to expand the reading range of the microfluidic sensor to more than 22 m.

6. Chapter 6 illustrates a 5G SiP energy harvester realizing using the glass packaging process. The UWB AiP designs with reduced size and bandwidth large enough to cover all three main operating bands of the 5G communication. The AiP design is then utilized to realize broadband energy harvesters. The new low-loss polymer is also utilized to ease the fabrication of the semi-additive glass packaging process and improve the performance.

7. Chapter 7 depicts a fully additive manufacturing packaging process as well as an energy-autonomous SiP module. The fabrication process integrating both inkjet and 3D printing is proposed. The new low-loss printable material is used to push the

proposed process to mm-wave applications. The energy-autonomous SiP does not need to connect to any exterior boards since it is fully functional with a power supply from the embedded energy harvester. Thus, the functional system size can be shrunk from the board level to the packaging level.

8. Chapter 8 discusses the novelties and contributions of my works and concludes.

# CHAPTER 2

# REVIEW OF ENERGY HARVESTING TECHNOLOGIES

In this chapter, a full review of energy harvesting technologies will be provided. This chapter begins with the introduction and comparisons of different energy resources for energy harvesting technologies. Each energy source has its pros and cons and the RF and mm-wave frequency Electromagnetic (EM) waves are chosen as the main focusing energy source due to its magnificent potential. Then the history of the RF and mm-wave frequency EM waves energy harvesting technologies starting from where the ideas come from to the current important research status will be introduced. The differences between energy harvest and wireless power transfer will be discussed.

Since the key enabling technologies for RF and mm-wave energy harvesting is the rectenna system, the operation principles, as well as each building blocks including antenna, rectifier, and power management circuit will be introduced thoroughly. The estimations of the available RF power levels are calculated. The applications of RF and mm-wave energy harvest on backscatter sensors and RFID will be addressed. This chapter ends with the discussion of current and future design trends of RF and mm-wave energy harvesting technologies.

## 2.1 Overview of Energy Harvesting Technologies

### 2.1.1 Comparisons of Energy Sources

As shown in Figure 2.1, there are different types of ambient energy sources around us such as solar, heat (thermal), vibration, and electromagnetic waves. The idea of energy harvest is to collect energy from the ambient environment and converts it into DC power to drive load applications. Although the term "energy harvest" is relatively new terminology,

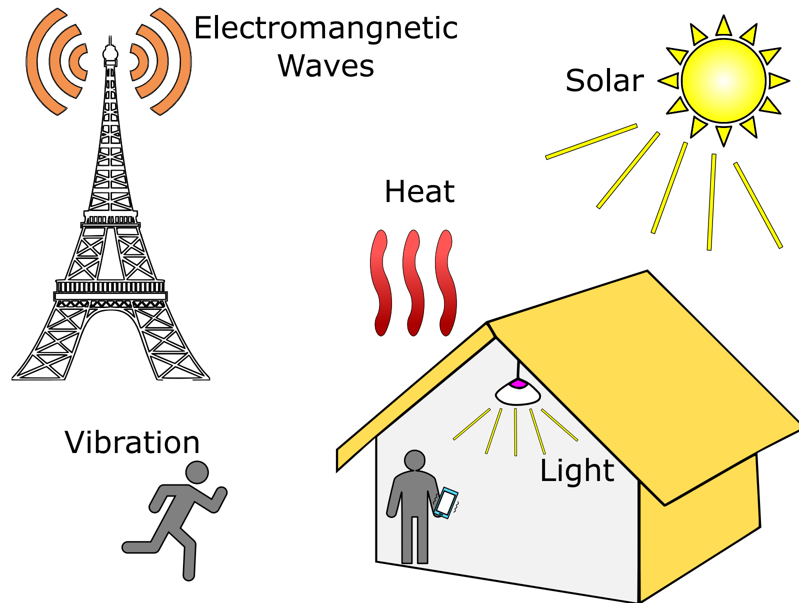


Figure 2.1: Demonstration of ambient energy sources.

the first successful example can be dated back to 1826 when Thomas Johann Seebeck successfully created a current using two metals at different temperature [1]. This was the first demonstration of energy harvesting from thermal energy. Later in 1839, Edmund Becquerel discovered the photovoltaic effect which made harvesting from solar energy possible. In 1880, piezoelectricity which comes from vibration was first predicted and proven by Pierre and Jacques Curie. The idea of harvesting energy from radio waves started in 1899 while Nikola Tesla demonstrated the wireless power transfer through resonant Tesla coils. It then slowly evolve to energy harvest technologies using rectennas. The detailed evolution and history will be introduced in subsection 2.1.2. Until today, solar, thermal, RF, and vibration are still four main ambient energy sources and researchers has been working hard to build systems that can extract the energy and converted them into DC power efficiently.

The four main ambient energy sources are summarized and compared in Table 2.1 [6–9]. The pros and cons of different energy sources are included for trade-off and decision making. One example is also included for each type of energy source to provide ideas of the real-life applications of harvesting from these energy resources. For the solar energy,

Table 2.1: Comparisons of ambient energy sources.

| | **Solar** | **Thermal** | **RF** | **Vibration** |
|---|---|---|---|---|
| Power Density (mW/cm$^2$) | 15 - 100 | 0.06 | $10^{-5}$ - 0.1 | 0.2 |
| Output Voltage | 0.5 - 4 V | - | 3 - 4V (Open Circuit) | 2 - 10 V |
| Available Time | Day Time (4-8 Hours) | Any Time | Any Time | Activity Dependent |
| Harvester | PV Cell | Thermocouple | Rectenna | Piezoelectric |
| Pros | • Large amount of energy<br>• Well developed tech.<br>• High output voltage | • Always available | • Ubiquitously available<br>• Small size and light weight<br>• Easy to integrate | • Light weight<br>• Well developed tech. |
| Cons | • Large area<br>• Non-continuous<br>• Orientation issue | • Large area<br>• Low power<br>• Brittle<br>• Low efficiency | • Distance dependent<br>• Low power density<br>• Low output voltage | • Large area<br>• Variable output |
| Example Work | [2] | [3] | [4] | [5] |

the power density varies from 15 - 100 mW/cm$^2$ depends on different environment. For example, high power densities can be expected outdoor under sunny days while much lower values are obtained indoor [7]. The output voltage is around 0.5 - 4 V. The available time is during the daytime which is about 4-8 hours depends on the weather. The harvester used to extract solar power and convert it into electricity is the Photovoltaic (PV) cell or also known as the solar cell. As an example, in [2], a solar-powered sensor network is demonstrated. Solar power can offer a large amount of power and high output DC voltages. The technologies are well developed since 1839. However, there are still some drawbacks. To begin with, the sizes of solar panels are large which makes it different to integrate with other applications. The solar panel also only be used during the daytime and the weather takes an important factor in the received power. The orientation also plays a critical role

which makes the integration with moving objects harder.

For the thermal energy, the power density is 0.06 mW/cm$^2$ which is relatively low [8]. Thermal energy can be gathered continuously using thermoelectric materials [10] and a thermoelectric micro-converter is proposed to support low-power electronics in [3]. Nevertheless, it also required a large area and the efficiency is generally low. The vibration due to human or mechanical movement can be converted into electricity through piezoelectric devices [11]. The power density is 0.2 mW/cm$^2$ [7] and can be used to support wireless sensor applications as demonstrated in [5]. However, it also requires a large area, and the output power is very unstable because of the variation in the amplitude of vibration.

Recently, RF energy harvesting utilizing antennas and rectifiers has attracted lots of attentions [12]. RF signals can be accessed all day at any place due to the ability to bypass the obstacles. Hence, RF energy is a suitable source to provide stable and constant output power. The rectenna size is much smaller compared with other methods and the orientation doesn't matter once beam-tracking is applied. Thus, it is perfect to be integrated with moving objects like wearable applications and small objects like IoT applications. Furthermore, when integrating the RF energy harvester with wireless applications, the same antenna can be used to perform both communication and energy harvesting and thus, making the size even more compact. Although the energy density is lower, enough power can be obtained by broadband or multi-band RF energy harvesting. Furthermore, massive antenna arrays or phased arrays can also be used to boost the received power. Therefore, in this work, the focus is on the RF energy harvesting technology.

#### 2.1.2 History of Energy Harvesting Technologies

The precursor of RF energy harvesting technology is Wireless Power Transfer (WPT) using radio waves. Therefore, the introduction will begin with the history of power transmission using radio waves. The timeline of important years, works, and authors are shown in Figure 2.2. Transmitting power using radio waves was first demonstrated in 1890 when Hein-

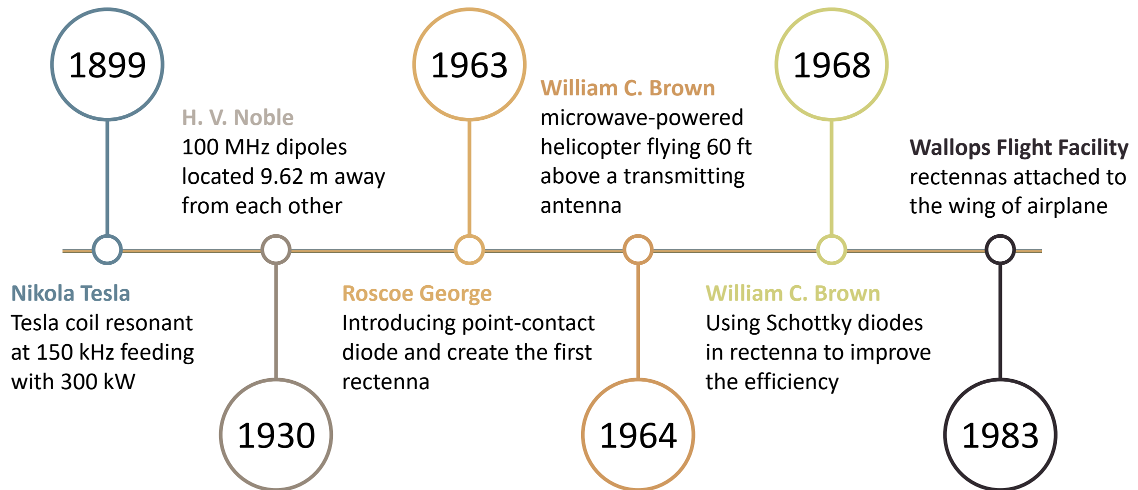


Figure 2.2: Time line of researches on power transmission using radio waves.

rich Hertz utilized spark gap to create high-frequency power and received at some distance away [13]. Later in 1899, Nikola Tesla used huge Tesla coils resonated at 150 kHz fed with 300 kW to build up extremely high voltage and shoot out lightning-like bolts to receiving coils. Tesla's work was the inspiration and can be viewed as the earliest demonstration of WPT through radio waves [14]. Then in the early 1930s, H. V. Noble experimented in the Westinghouse Laboratory using 100 MHz dipoles located 7.62 m from each other to realize WPT.

In 1963, Roscoe George introduced diodes into the WPT and built the first "rectenna" at Purdue University. The system was composed of 28 half-wave dipoles each terminated in a bridge rectifier operated at 2-3 GHz with 7 W output. The diode used is 1N82G point-contact semiconductor diodes and the estimated efficiency is 40 %. This work is very important since the rectenna is widely adopted in today's energy harvesting researches. In 1964, another great pioneer, William C. Brown, adopted the rectenna topology and demonstrated a microwave-powered helicopter flying 18 m above a transmitting antenna. The rectenna for the helicopter is 0.37 $m^2$ composed of 4480 point-contact diodes. The maximum DC power was 270 W. Four years later (1968), William C. Brown switched from point-contact semiconductor diodes to Schottky diodes HPA 2900 in rectenna and significantly improved the efficiency. Until then, the foundation of a high-efficiency topology

through rectenna and Schottky diodes was established.

In 1983, Wallops Flight Facility proposed rectennas attached to the wing of airplane capable of handling 1 kW/kg under the fund received from Lewis Research Center. In the 1990s, huge interests are renewed in the concept of Solar Power Satellite (SPS) which was first proposed by Dr. Peter Glaser in 1968. The idea is to collect solar power in geosynchronous orbit and then converted it into 2.45 GHz microwaves. The microwave power is transmitted down to the receiver rectenna on earth [15].

Another close technology is the RFID. The RFID tags receive power from the reader through radio waves and convert it into DC power, most likely using rectenna, to drive the load IC and then transmit the signals with modulated information back to reader [16].

The RFID and WPT technologies are all very close to energy harvest. However, there is still a major difference between them. The transmitters for WPT and RFID can be co-designed and optimized with the receivers. In other words, both the transmitters and receivers are designed by the same group of people to achieve the same goal. However, the transmitters of the energy harvest can not be controlled by the designers of the receivers, and most of the time, those transmitters are not made for energy harvest. For example, in [12], an energy harvester harnessing energy from Digital Television (DTV) signal to drive load is presented. Those authors can not control the design of the DTV transmitter. Furthermore, the DTV transmitters are designed to broadcast the DTV signal for audiences rather than designing for energy harvest. Since the developers of energy harvest can only control the receiving side, it is more difficult to optimize the system compared with WPT or RFID.

The following are some previous researches about energy harvester designs. In [17], Vyas demonstrated energy harvesting from ambient DTV at Atlanta using the rectenna topology. The frequency range is from 512 MHz to 566 MHz and the distance is 6.3 km. The work successfully charge a 100 μF capacitor from 2 V to 2.5 V which is 112.5 μJ within 10 seconds. In [18], a rectenna harvesting Global System for Mobile Communica-

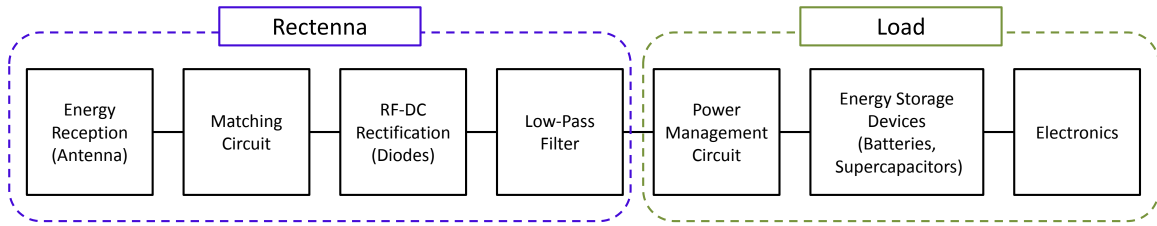


Figure 2.3: The block diagram of a typical RF energy harvester.

tions (GSM)900 signals was demonstrated. The work harvested energy from a 10-second cell-phone call at 0.5 m away and charge the load capacitor to 2.5 V. In [12], the authors measured the power levels of DTV, GSM900, GSM1800, and Third Generation (3G) wireless communication in London. Then, they harvested energy from each source and the best they got is harvesting from GSM900. They successfully charged a 100 µF capacitor from 2.4 V to 2.84 V which is 115.28 µJ within 14 seconds.

There are two observations worth noting. First, most of the works harvested energy in µJ level. Although the power level looks small, this is enough for most of the low-power electronics. The applications of energy harvest consuming this level of power will be introduced later in section 2.3. Second, most of the works using the rectenna topology due to its high efficiency and simple structure. Thus, the next section will be focused on the rectenna operation principles.

## 2.2 Rectenna Operation Principles

The block diagram of a typical RF energy harvester is shown in Figure 2.3. It is composed of two main blocks: the rectenna and the load. The RF energy is received by energy reception components where antennas are widely used here. The matching circuit is inserted to match the impedance between the antenna and the RF-DC rectification unit. Then, the received RF energy is rectified into DC energy through RF-DC circuits where Schottky diodes are mainly used in this stage. The low-pass filters are used to mitigate higher order harmonics to obtain pure DC energy. Once clean DC energy is obtained, it is passed to the power management circuit to boost the voltage level or to switch between the charging and

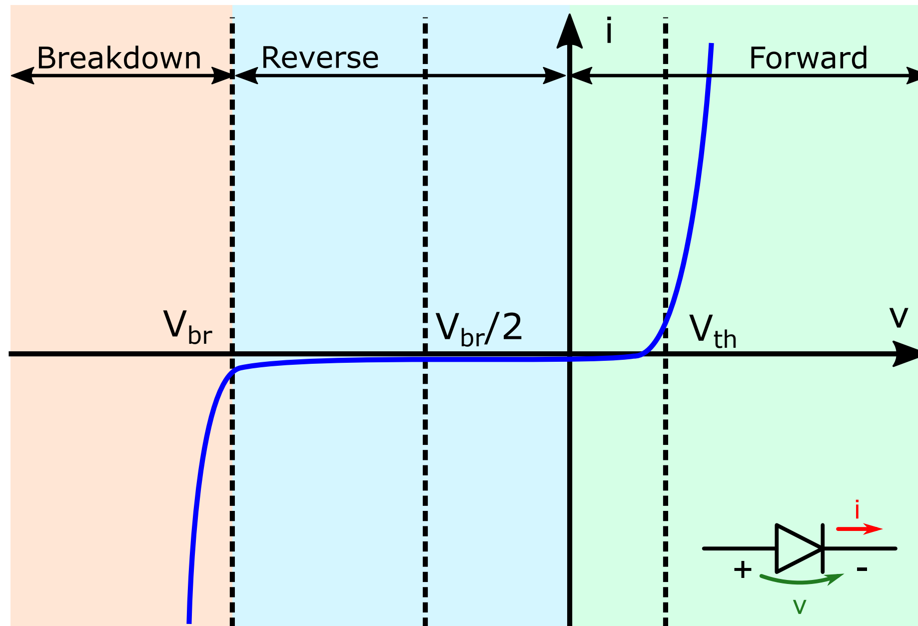


Figure 2.4: The I-V curve of a common diode.

discharging. Finally, the energy is stored in the energy storage devices such as batteries and supercapacitors to meet the energy requirement of the electronics.

### 2.2.1 Rectifier Introduction

Since most of the load applications are driven with DC power, the rectifier is necessary to convert the received RF energy to DC energy. Here, the brief rectification principles of using diodes and the losses during rectifications are introduced. Furthermore, the circuit models of commonly used Schottky diodes are built. The SPICE parameters of some off-the-shelf Schottky diodes are included for comparisons.

*Rectification Principles*

The I-V curve of a typical diode is shown in Figure 2.4 and a half-wave rectifier using single series diode is shown in Figure 2.5a. The input and output waveforms are also included in Figure 2.5a. As shown in Figure 2.4, for a diode, the forward biasing has to be larger than a threshold value ($V_{th}$) to turn on the diode and the diode can be viewed as a small resistor under this condition. On the other hand, the diode can be viewed as a

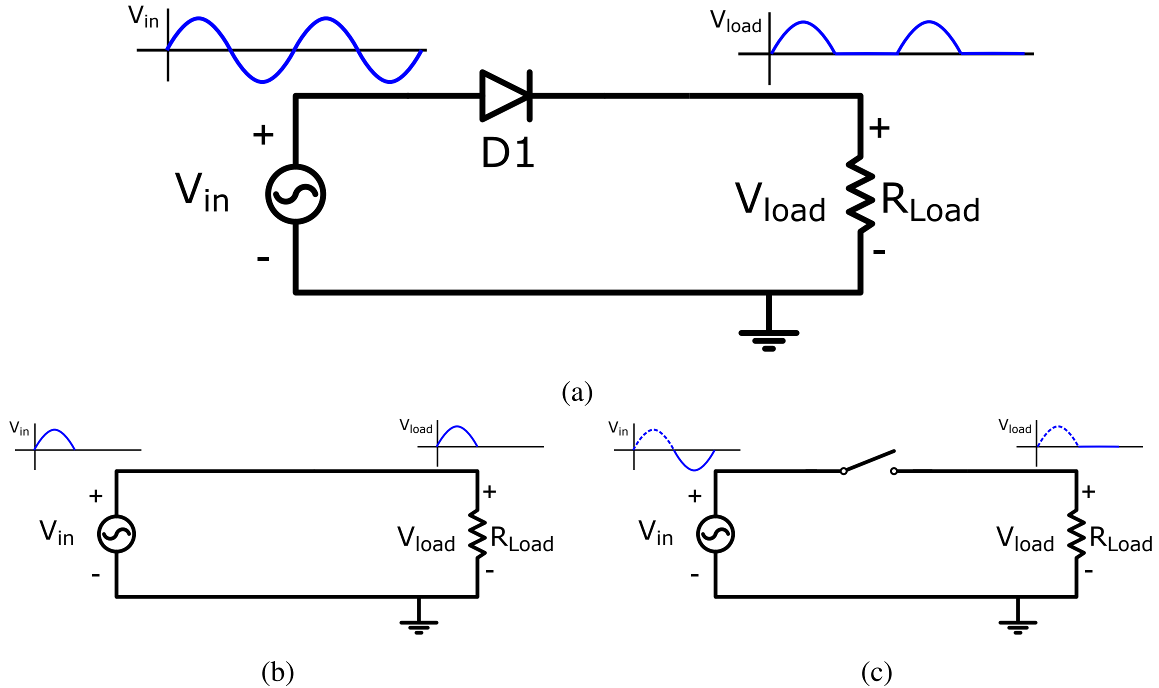


Figure 2.5: The rectification principles of a (a) half-wave rectifier at (b) the positive half cycle and (c) the negative half cycle.

large resistor under reverse biasing. While the reverse bias is larger than the breakdown voltage ($V_{br}$), the diode becomes highly conductive again. For an ideal diode, the threshold voltage ($V_{th}$) is 0 V. Furthermore, the diode can be viewed as short-circuit under forward biasing and open-circuit under reverse biasing as shown in Figure 2.5b and Figure 2.5c, respectively.

With these basic ideas in mind and assuming the diode is ideal, the diode is replaced with a short circuit under the positive half cycle and thus, the input and output waveforms are the same as shown in Figure 2.5b. Under the negative half cycle, as shown in Figure 2.5c, the diode is replaced as an open circuit. Therefore, the output waveform is kept at 0 voltage. The complete output waveform is a half-rectified sinusoidal wave as shown in Figure 2.5a. The output waveform is composed of both DC power and harmonics and thus, it is not a steady DC energy yet. The way to smooth the output waveform is to eliminate the harmonics by using low-pass filters.

As shown in Figure 2.6a, a capacitor at the load is used to smooth the output waveform.

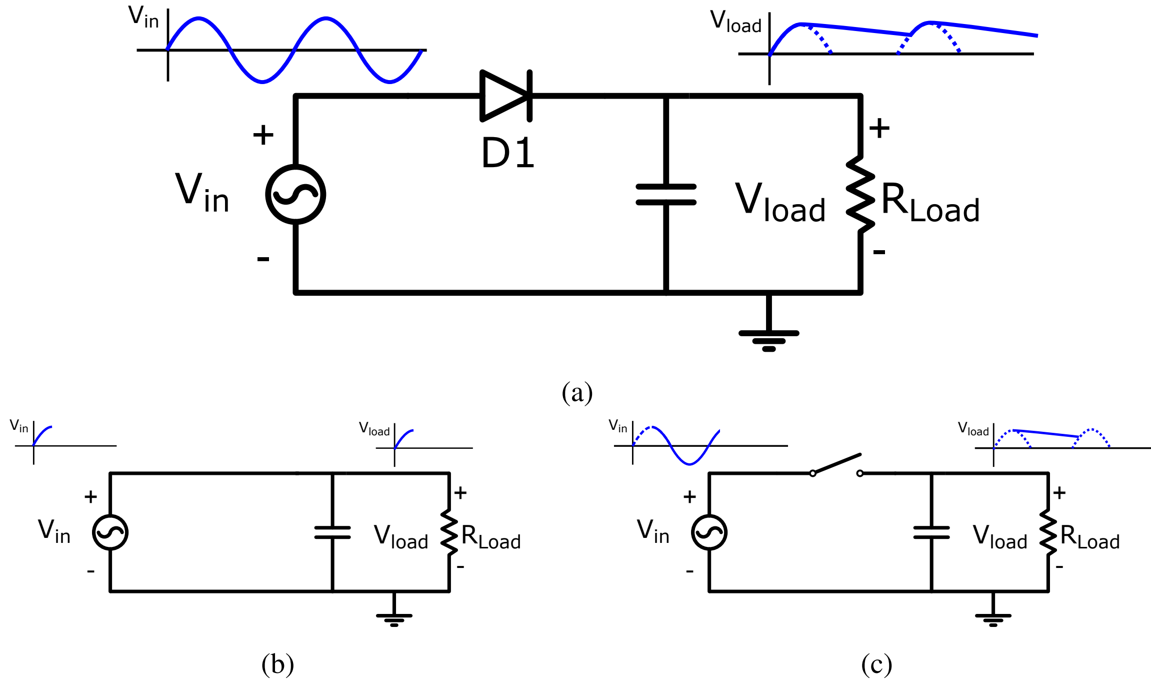


Figure 2.6: The rectification principles of a (a) half-wave rectifier with a smoothing capacitor at (b) the positive half cycle and (c) the negative half cycle.

When the input voltage started from 0 V to the peak of the amplitude, the diode is under forward biasing. Therefore, it is replaced with a short circuit, the capacitor is charging until the output waveform is the same as the input as shown in Figure 2.6b. When the input voltage is decreasing from the peak value, the diode is under reverse biasing since the capacitor is charged to the peak value. The diode is viewed as an open circuit and the capacitor is discharging as shown in Figure 2.6c. The final output waveform is demonstrated in Figure 2.6a and it is much smoother compared with the one in Figure 2.5a.

*Schottky Diode*

Schottky diode is one of the most commonly used diodes for performing RF-DC rectification. The I-V curve of the Schottky diode is shown in Figure 2.4. The mathematical form can be represented as

$$I = I_s(\exp(\frac{qV}{nkT}) - 1) \tag{2.1}$$

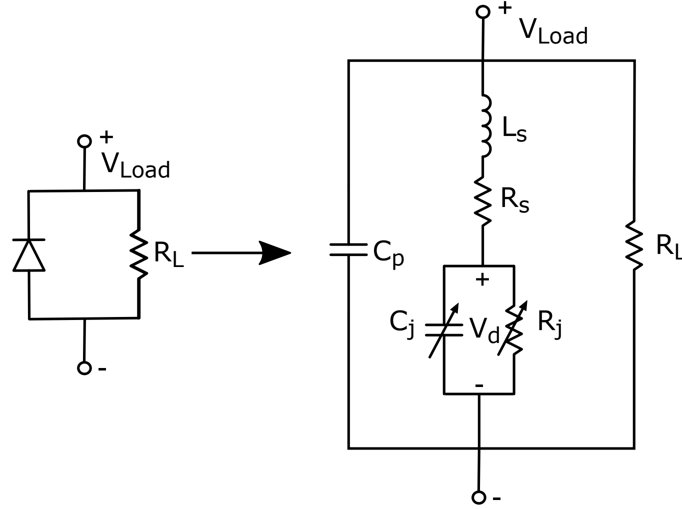


Figure 2.7: The circuit model of a Schottky diode.

where $I_s$ is the saturation current, q is the electronic charge $(1.6 \times 10^{-19} C)$, n is the ideality factor, k is Boltzman's constant $(1.37 \times 10^{-23} J/K)$, and T is the absolute temperature in K. The equivalent circuit model of a Schottky diode is shown in Figure 2.7. The equivalent model is composed of a series resistor $(R_s)$, a variable resistor $(R_j)$ for junction resistance, a variable capacitor $(C_j)$ for junction capacitance, a parasitic inductor $(L_s)$, and a parasitic capacitor $(C_p)$. The junction resistance and junction capacitance varied with respect to the different applied voltage. The parasitic inductor and capacitor are associate with the package of the diode. The parameters of some off-the-shelf diodes are summarized in Figure 2.8. The HSMS-282 diode has a high breakdown voltage which makes it suitable for high RF input power applications. On the other hand, the SMS7630 has the lowest threshold voltage and thus, it is suitable for low input power applications. The junction capacitance is also an important parameter and is closely related to the cut-off frequency which is the highest frequency where the diode can be operated. The cut-off frequency is higher when the junction capacitance is smaller. The MA4E2038 and MA4E1317 diodes can operate up to 80 GHz which covers all the 5G NR bands. Therefore, they are suitable to be applied in harvesting 5G power.

| Parameter | Description | HSMS-282 | SMS7630 | MA4E2038 | MA4E1317 |
|---|---|---|---|---|---|
| Is (A) | Saturation Current | 2.2E-8 | 5E-6 | 9E-14 | 1.7E-14 |
| Rs (Ω) | Slope Resistance | 6 | 20 | 5.1 | 1.7 |
| N | Ideality Factor | 1.08 | 1.05 | 1.16 | 1.08 |
| Ikf (A) | Knee Current | - | - | 0.001 | 0.016 |
| Bv (V) | Breakdown Voltage | 15 | 2 | 8 | 7 |
| Ibv | Current at Bv | 1E-4 | 1E-4 | 1E-5 | 1E-5 |
| Cj0 (pF) | Zero-bias Junction Capacitance | 0.7 | 0.14 | 0.046 | 0.047 |
| Vj (V) | Junction Potential | 0.65 | 0.34 | 1.07 | 0.86 |
| M | Grading Coefficient | 0.5 | 0.4 | 0.5 | 0.38 |
| Fc | Forward-bias Depletion Capacitance | - | 0.5 | 0.78 | 0.99 |
| Xti | Saturation-current Temperature | 2 | 2 | 2 | 2 |
| Eg (eV) | Energy Gap | 0.69 | 0.69 | 1.424 | 1.424 |
| fc (GHz) | Cut-off Frequency | 6 | 24 | 80 | 80 |
| Vth (V) | Forward Threshold Voltage | 0.34 | 0.18 | 0.7 | 0.7 |

Figure 2.8: The parameters of off-the-shelf diodes.

### 2.2.2 Losses During Rectifications

One of the objectives of using different rectifier topologies or components is to achieve as high efficiency as possible. However, there are inevitable losses during rectifications. As shown in Figure 2.9, theses losses includes the threshold voltage effect ($V_T$ effect), breakdown voltage effect ($V_{br}$ effect), and harmonic effects. In addition to these losses, the impedance mismatch between the antenna and the rectifier and the device parasitics also contribute to the efficiency degradation. The detailed introduction of these effects and losses during rectification is discussed in this section.

*Threshold and Breakdown Voltage Effects*

As mentioned in subsection 2.2.1, the input voltage has to be larger than the threshold voltage to overcome the barrier and turn on the diode so that the current can flow through. Thus, when the input power is low, the key limiting factor for the efficiency is the threshold (turn-on) voltage. This effect is described as the $V_T$ effect in Figure 2.9. Under low input power, the efficiency will increase when the input power increase. The efficiency is

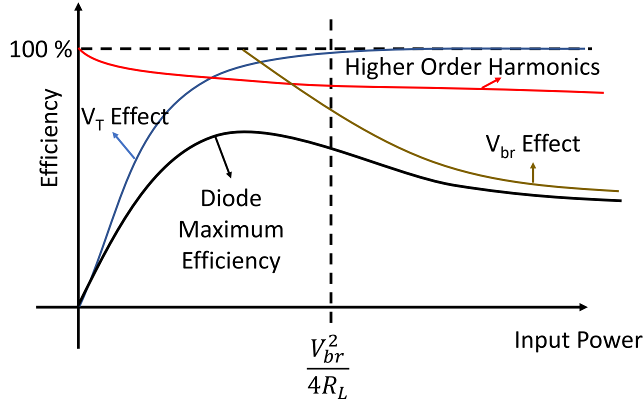


Figure 2.9: The relationship between the efficiency and losses.

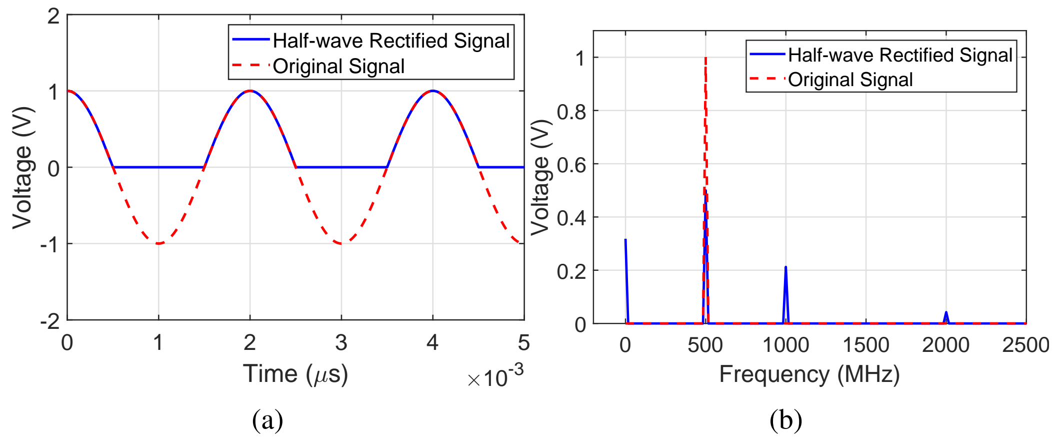


Figure 2.10: (a) Time-domain waveforms and (b) frequency-domain waveforms of a 500 MHz sinusoidal signal and the respective half-wave rectified results.

saturated while the input power is large enough to fully overcome the barrier.

When the input power is high, the breakdown voltage starts to affect efficiency. The reason is that the reverse leakage current increases when the input power increases. As shown in Figure 2.9, the $V_{br}$ effect curve is at high efficiency when input power is low but starting to decrease when the input power approaches to $V_{br}^2/4R_L$ [19]. Therefore, the input power where the highest efficiency occurs depends on the load impedance, and the selection of the load impedance should be careful to maximize the RF-DC conversion efficiency.

*Harmonic Effects*

Since the diodes are non-linear components, the higher-order harmonics are generated while rectification. The higher-order harmonics are one of the main sources of the loss. As an example, the time-domain waveforms and frequency-domain waveforms of a 500 MHz sinusoidal signal and the respective half-wave rectified results are shown in Figure 2.10. Although the desired DC is generated, the unwanted higher-order harmonics at other frequencies are generated simultaneously. From the Fourier series of the half-wave rectified signal

$$f(t) = \frac{A}{\pi} + \frac{A}{2} sin(\omega_0 t) - \frac{2A}{\pi} \sum_{n=1}^{\infty} \frac{cos(2n\omega_0 t)}{4n^2 - 1} \tag{2.2}$$

where $A$ is the amplitude of the voltage which is 1 V in Figure 2.10. When the voltage is 1 V, by Equation 2.2, the DC amplitude is 0.32 and two largest harmonic values are 0.5 and 0.21, respectively. In this example, the powers in high order harmonics are not desired and are wasted during rectification. One design that can recycle and utilize the higher-order harmonics is presented in chapter 4. The power lost in higher harmonics will increase when the input power increases as shown in Figure 2.9. Therefore, the optimal conversion efficiency is obtained by trading off between the threshold voltage, breakdown voltage, and harmonics.

*Impedance Matching*

As shown in Figure 2.3, there is a matching circuit block between the antenna and the rectification circuit. If the rectification circuit is not properly matched to the antenna, the incident power collected by the antenna is not fully absorbed by the rectifier. Therefore, this matching circuit block is very important to prevent the degradation of efficiency. The matching design for the rectifier is more difficult than other passive circuits since the diodes are non-linear components. The input power, load impedance, and frequency will change

the input impedance and thus, all aspects need to be considered. The harmonic balance and large scale S parameter simulation provided by Keysight ADS are used to help the matching circuit design and estimate the conversion efficiency.

*Device Parasitics and RF Circuit Loss*

The parasitics in diodes are also an important source of the loss. As shown in Figure 2.7, the series resistance ($R_s$) reduces the efficiency since partial of the input power is dissipated because of it. The junction capacitance ($C_j$) will limit the cut-off frequency which is the highest operating frequency of the diode. As shown in Figure 2.8, the diode model with smaller junction capacitance has a higher cut-off frequency. Once exceed the cut-off frequency, the conversion efficiency drops severely. The package parasitics also affect efficiency.

*RF Circuit Loss*

The RF circuit loss including the conductor loss, dielectric loss, and radiation loss also plays an important role. The conductor loss due to finite conductivity and surface roughness becomes more important at higher frequencies. Furthermore, the dielectric loss is also important at higher frequencies. Therefore, both the conductor and the dielectric have to be chosen carefully.

### 2.2.3 Rectifier Topologies

The basic principle of a rectifier using a series diode is described in subsection 2.2.1. In addition to a series diode rectifier, numerous rectifier topologies are proposed to meet different requirements such as high conversion efficiency, high output power, and harmonic control for different applications. In this section, three categories of rectifiers based on the diodes will be introduced. These categories include the half-wave rectifier, the full-wave rectifier, and the voltage multiplier. The advantages and applications of each rectifier are

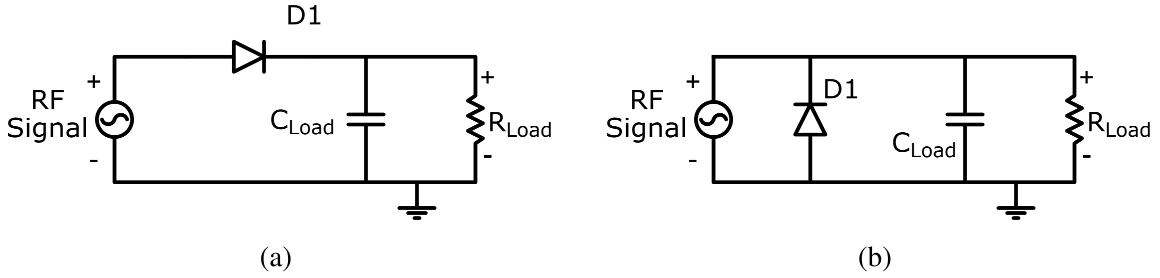


Figure 2.11: The circuit diagram of a (a) series rectifier and (b) parallel rectifier.

introduced.

*Half-wave Rectifier*

Two half-wave rectifier topologies are shown in Figure 2.11. A single series or parallel diode is used to perform the RF-DC conversion. The mechanism of a half-wave rectifier is already discussed in subsection 2.2.1. This type of topology is called the half-wave rectifier because they can only rectify either positive or negative half cycle as shown in Figure 2.10a. The selection of using series or parallel topology depends on the circuit layout. For microstrip line circuits, the series topology is better, since there is no need for vias to connect the diode to the ground. On the other hand, the parallel topology can be used if Coplanar Waveguide (CPW) is adopted for the circuit. The advantages of the half-wave rectifier are lower cost, fewer components, and easy to design. Furthermore, since the wave only passes one diode, the dissipation loss and parasitic effects are minimized. Therefore, half-wave rectifiers are suitable for low input power applications. However, the output voltage is typically low and a low-power high-efficiency DC-DC converter is required to boost the output voltage value.

*Full-wave Rectifier*

The circuit diagram of a full-wave bridge rectifier is shown in Figure 2.12. This type of rectifier is called the full-wave rectifier since it can rectify both the positive and negative half-cycles. Therefore, the theoretical RF-DC conversion efficiency is higher than the

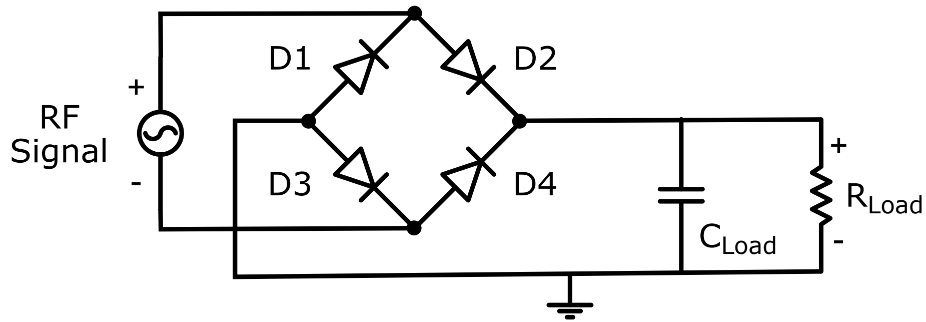


Figure 2.12: The circuit diagram of a full-wave bridge rectifier.

half-wave rectifier. However, since each half-cycle will need to pass through two diodes, the series resistance is double and the dissipation loss from the diode is increased. The parasitic is also larger compared with the half-wave rectifier. This topology can be used as a frequency doubler since the odd-order harmonics are eliminated. The application of full-wave rectifier as both rectifier and frequency doubler is discussed detailed in chapter 4.

*Voltage Multiplier*

The voltage multipliers cascade multiple unit cells to generate high output voltages. For example, a voltage doubler as shown in Figure 2.13a can double the output voltage value. The Cockcroft charge pump as shown in Figure 2.13b cascades multiple cells to boost the output voltage. Theoretically, the output voltage can be multiplied by the number of cascading cells. However, the dissipation loss increases with the increase of the cells. Therefore, the increased voltage will be smaller than the additional dissipation loss at some point and the number of the cell can be optimized to maximize the output voltage. Since the charge pump topologies normally have higher dissipation loss, they are suitable to be used when the input power is high. On the other hand, the parasitics also increase with the increase of cells. Thus, the charge pump topologies are not suitable for high-frequency applications.

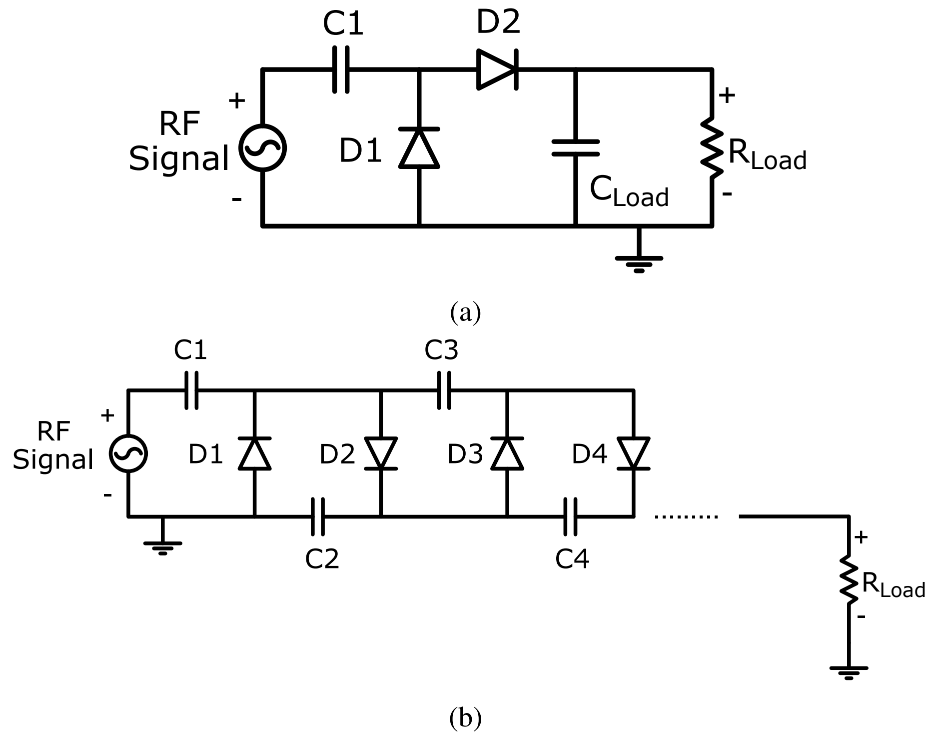


Figure 2.13: The circuit diagram of a (a) voltage doubler and a (b) Cockcroft-Walton voltage multiplier.

### 2.2.4 Power Management Circuit

As shown in Figure 2.3, the power management circuit block is followed after the rectifier to adjust the rectified power so that it can better meet the requirement of the application. Most of the power management circuit can provide two critical functions including DC-DC converter and duty cycling the power supply. Both functions will be introduced in this section.

*DC-DC Converter*

To maximize the conversion efficiency, the input power has to be optimized. Therefore, the voltage at the output of the rectifier might not be the best value for the load applications. The DC-DC converter in the power management circuit can be used to adjust the output voltage to meet the requirement of the applications. For example, since the output voltage from the RF energy harvester is normally low and can not be used to overcome the IC

cold start barrier, the DC-DC boost converter can be used to increase the voltage value and successfully overcome the barrier. On the other hand, the output voltage might be too large when the voltage multiplier topology is used. In this case DC-DC buck converter can be used to step down the voltage and protect the application IC. Moreover, complex DC-DC converter with Micro-controller Unit (MCU) can be used to keep the output voltage steady at a certain level to minimize the power integrity issue for IC driven source. In summary, the DC-DC converters in the power management circuit are used to adjust the output voltage at the rectifier to a certain steady value so that it can be used to safely drive the applications.

*Duty Cycling*

The other key function of the power management circuit is duty cycling. Since the harvested RF power is generally not large enough to turn on applications instantaneously, the power is first stored in the power storage elements such as batteries or super-capacitors rather than directly connect to the applications. The charging step will maintain for a period until the battery voltage exceeds a certain value or in other words until the stored power is large enough. Once the power is large enough, the power management circuit will switch to discharging mode where the applications are driven with the energy stored in the power storage elements. The duty cycle between charging and discharging has to be determined based on the power requirements of the load applications. For example, if low-power applications such as sensors are used, the duty cycle can be close to 50 %. On the other hand, the charging period can be much longer than the discharging period to sustain high power applications. A more detailed discussion can be found in chapter 5.

## 2.3 Applications of RF Energy Harvesting Technologies

There is a wide range of radio spectrum existing around us such as UHF reader, cellular, wifi, and 5G signals. The frequency band, Effective Isotropically Radiated Power (EIRP), and regulations are all different for various signal sources. Therefore, in this section, the

| | FCC Regulations | | Distance (m) | | |
|---|---|---|---|---|---|
| **Name** | Frequency (GHz) | EIRP (dBm) | 1 | 3 | 10 |
| **UHF RFID** | 0.86 | 36 | 4.9 dBm | -4.7 dBm | -15.1 dBm |
| **wifi** | 2.40 | 36 | -4.1 dBm | -13.6 dBm | -24.1 dBm |
| **5G** | 24.25 | 75 | 14.9 dBm | 5.3 dBm | -5.1 dBm |

Figure 2.14: General received power for different spectrum when the receiving antenna gain is 0 dBi.

available radio power is first evaluated to determine if they are suitable as an energy source for energy harvesters. Then, the step-by-step evolution to construct an energy harvester powered backscatter sensing network and RFID system is introduced. The advantages of the backscattered topology and the compatibility with energy harvesting techniques are also introduced.

### 2.3.1 Evaluate Available RF and mm-wave Power with Friis Equation

One of the most important pieces of information for designing the energy harvester is the estimation of the received power. As mentioned in subsection 2.2.1, the received power level is crucial for optimizing the conversion efficiency. Furthermore, it can also affect the duty cycle for the charging and discharging time. For far-field applications, the received power can be estimated using the Friis equation

$$P_r = P_t G_t G_r (\frac{\lambda}{4\pi R})^2 \tag{2.3}$$

where $P_r$ is the received power, $P_t$ is the transmitted power, $G_t$ is the transmitted antenna gain, $G_r$ is the received antenna gain, $\lambda$ is the wavelength, and $R$ is the distance between the transmitted and the receiver.

The received powers at 1,3, and 10 meters distances for UHF RFID, wifi, and 5G signals are summarized in Figure 2.14. The Federal Communications Commission (FCC) regulations about the operating frequency and the maximum allowed EIRP are also included. Only the lowest frequency within the operating band is included. For example, the UHF RFID band is from 860 to 960 MHz and only 860 MHz is included in the figure. The received powers are calculated using maximum EIRP with receiving antenna gain 0 dBi. Therefore, the received power will increase when high gain receiving antennas are used.

For low power applications, the power required is normally around hundreds of μW. As shown in Figure 2.14, although 5G signals induce higher path loss due to high operating frequency, the high EIRP makes it suitable for energy harvesting applications. The UHF RFID is also a good candidate for energy harvesting applications according to the received power as shown in Figure 2.14.

### 2.3.2 Backscatter Sensors and RFID

In this section, the applications of energy harvesting on backscatter sensors and backscatter RFID are introduced. The section begins with the principle of backscatter topology and then move to energy-autonomous backscatter sensor and RFID using energy harvesting techniques.

#### *Principal of Backscatter RFID*

A backscatter topology is demonstrated in Figure 2.15, the receiver is an antenna with two states of loads. A PMOS is used as a switch to switch between two different states and a waveform generator is used to generate square waves to control the switch. In this example, the reader generates a 900 MHz carrier signal and illuminates the receiver. The time domain and frequency domain waveform of a 900 MHz signal is also included in Figure 2.15. For the receiver, when the switch is open, the antenna is connected to the matched 50 Ω load. When the switch is closed, the antenna is connected to the capacitor to the ground.

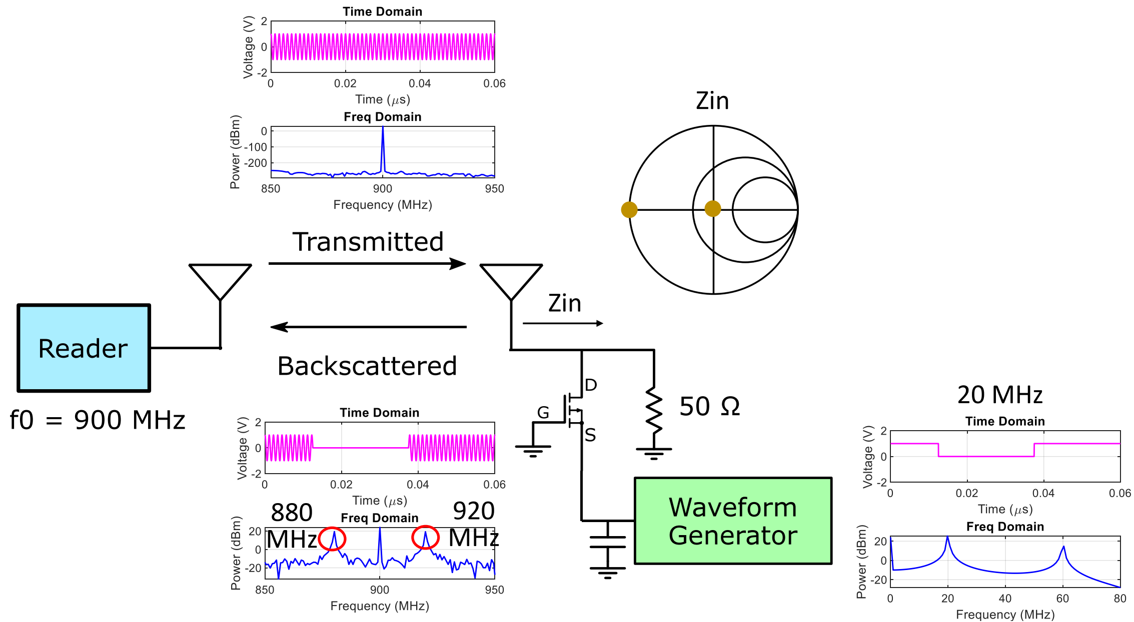


Figure 2.15: Backscatter topology with waveform generator.

The capacitor value can be chosen carefully so that the high-frequency 900 MHz signal is connected to the ground. Therefore, the two states of the receiver are matched and short as shown in the Smith chart.

When the 900 MHz carrier signal transmitted by the reader illuminated the receiver, it will be modulated and backscattered back to the reader. The modulation mechanism is simple. When the antenna is connected to a matched load, the backscattered signal amplitude is close to 0. On the other hand, when the antenna is connected to the short, the backscattered signal amplitude is maximized. As shown in Figure 2.15, when the waveform generator outputs a 20 MHz square waveform, the waveform will be super-composed to the 900 MHz carrier signal and generated modulated backscattered signals. The time domain and frequency domain of the backscattered signal waveforms are also included in the figure. To make a RFID using this topology, the information can be encoded within the square waveform using high voltage as 1 and low voltage as 0. By detecting the amplitude-modulated backscattered waveforms, the information can be decoded and transmitted wirelessly.

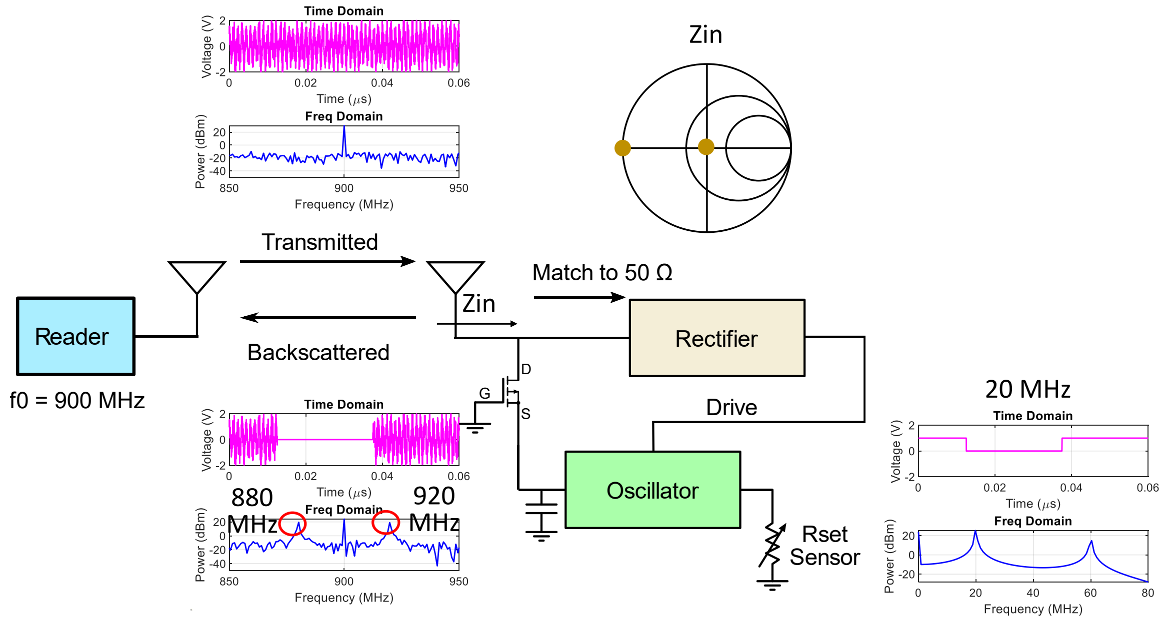


Figure 2.16: Energy-autonomous backscatter sensors with an energy harvester.

*Energy Autonomous Backscatter Sensor*

An energy-autonomous backscatter sensor is shown in Figure 2.16. Compared with the topology shown in Figure 2.15, the matched 50 Ω load is replaced with a matched rectifier and the waveform generator is replaced with a low-power oscillator. The two states of the receiver are still matched and short as shown in the Smith chart in Figure 2.16. However, at a matched state, the power now is rectified and used to drive the oscillator. In this topology, no exterior power supply is required and energy-autonomous is realized. The oscillator will output a square wave to control the switch. Furthermore, the frequency of the square wave depends on the load impedance. As shown in Figure 2.16, the load of the oscillator is a sensor that can change impedance depends on the sensing status.

As shown in Figure 2.16, the reader is still broadcasting a 900 MHz carrier signal. The time and frequency domain waveforms including random noises are included in Figure 2.16. The carrier signal will be received by the receiver sensor tag and then be rectified since the oscillator is not driven yet. Once the rectified power is large enough to drive the oscillator, the oscillator will generate a square waveform depending on the sensor sensing

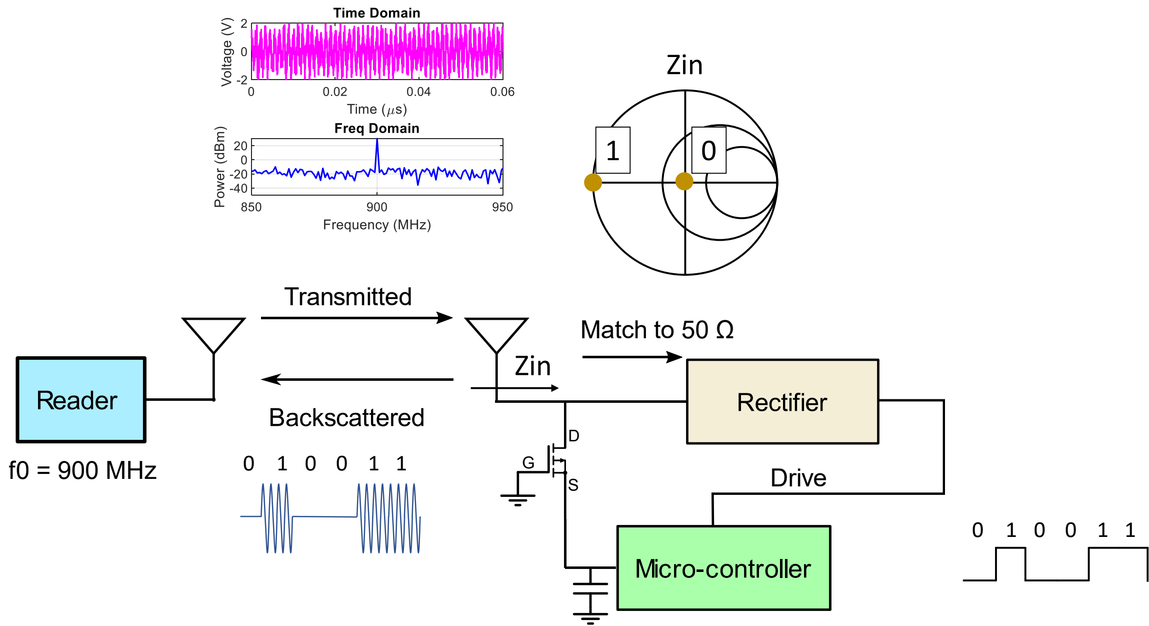


Figure 2.17: Energy-autonomous backscatter RFID using ASK modulation.

status. Assuming the frequency of the square waveform is 20 MHz in this example, the square wave is super-composed to the carrier and backscattered to the reader. The time domain and frequency domain waveforms of the backscattered signal are also included in Figure 2.16. As shown in the frequency domain signal, there are three spikes, one is the carrier frequency at 900 MHz and the other two are the backscattered signals at 920 (900+20) MHz and 880 (900-20) MHz. By detecting the frequency of the backscattered signals, the oscillated frequency of the oscillator can be determined. Furthermore, by checking the oscillator specifications, the sensor impedance can be obtained. Finally, by checking the sensor specifications, the sensing status can be determined. Thus, the sensing status can be transmitted wirelessly.

*Energy Autonomous Backscatter RFID*

The energy-autonomous backscattered RFID topology is shown in Figure 2.17. Compared with Figure 2.16, the only difference is that the oscillator is replaced with a MCU. There are still two states as shown in the Smith chart in Figure 2.17. The matched state is used to

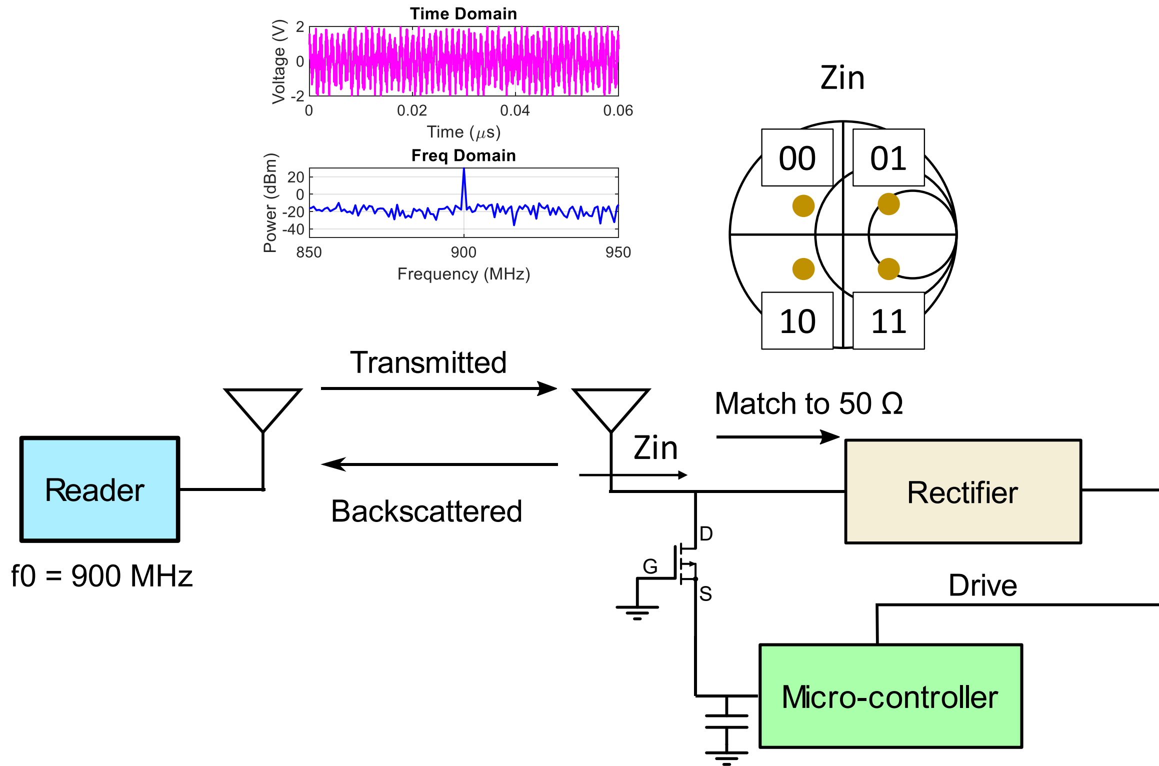


Figure 2.18: Energy autonomous backscatter RFID using QPSK modulation.

modulated bit '0' and the short state is used to modulated bit '1'. The MCU can generate a square waveform based on the pre-coded ID. The ASK backscattered signals can be picked up and decoded by the reader. It is worth noting that the topology is still energy-autonomous since the MCU is powered by the RF energy harvesting techniques.

To send more information, a more complex modulation can be achieved by using more than two states as shown in Figure 2.18. A QPSK modulation can be achieved by creating four states on the Smith chart. This can be achieved by using multiple switches. The backscattered signals can be demodulated by calculating the respective amplitudes and phases.

## 2.4 Energy Harvesting Design Trends

Current researches about energy harvesting technologies can be classified into three categories. The first one is to improve the performance of the rectenna. New rectenna and

rectifier topologies are explored and advanced components are used to achieve rectenna with better RF-DC efficiency. Besides, new topologies that can withstand the variances in the load are proposed to enhance the capability of the rectenna. The second category is to increase the harvested power level to overcome the low RF energy density problem. Researches in this area include broadband or multi-band energy harvesters which harness RF energy at different bands and combine them to provide a higher received power level. Moreover, hybrid energy harvesters that harvest more than one type of energy source are proposed to combine the advantages of different energy sources and alleviate all drawbacks. The third category is focusing on applying energy harvester to new applications such as IoT, 5G, smart skin, and smart cities. The previous achievements and related researches will be introduced in the following sections. Furthermore, all related works will be classified into three categories as mentioned earlier.

### 2.4.1 Rectenna Performance Improvement

One of the key components in the rectenna is the rectifier which can convert the RF signals into DC energy. The roadmap history and evolution of techniques to convert electromagnetic energy since 1900 are summarized in [20]. Until today, one of the commonly used techniques which is suitable for the RF energy harvesters is the rectifier built with Schottky diodes. In [19], lots of different commercial available Schottky diodes and typical rectifier topologies with respective RF-DC conversion efficiency are summarized. In order to break the efficiency barrier posed by Schottky diodes, new rectifier topologies using tunnel diodes have been proposed [21–23]. Since the turn-on voltage for the Schottky is around 300 mV, the RF-DC efficiency will drop severely while the input power is small. Compared with Schottky diodes, the turn-on voltages for tunnel diodes are around 100 mV and thus, they can support higher RF-DC conversion efficiency at low input power.

In addition to perusing high conversion efficiency, rectennas which can keep high efficiency at different load values and different input power levels are also critical. This is

difficult since the diodes are non-linear components and the input impedance of the RF-DC rectifier is sensitive to input power levels and loads. Thus, methods to reduce the variation or matching circuits that can adapt to the variation are significant. Resistance compression networks are proposed to smooth the variation in the load circuit and successfully compress the load variation from 5 Ω - 500 Ω to 50 Ω - 290 Ω [24]. This method is then adopted to design a dual-band rectifier which can resist the variation in the load resistance [25]. In [26], a buck-boost DC-DC converter is inserted between the rectifier and the load reducing the changes in the load from 100 Ω - 5000 Ω to 90 Ω - 140 Ω.

To accommodate a wide input power range, modified rectifier topology integrating with a p-type high-electron-mobility transistor (pHEMT) is proposed in [27]. One of the popular techniques to solve this problem is to integrate the Maximum Power Point Tracking (MPPT) algorithm and reconfigure the rectifier to adapt to different input levels [28].

### 2.4.2 Harvested Power Level Enhancement

*Broadband and Multi-band Energy Harvesters*

One way to collect more RF energy is to harvest RF energy at different frequency bands simultaneously. Therefore, various broadband and multi-band energy harvesters have been developed. There are generally two different categories to achieve the objective: RF combining and DC combining. DC combining general means different sets of rectennas harness energy at different frequencies separately and combines the DC voltage at the end of each rectenna. For example, in [29], two sets of energy harvesters are used to harvest RF energy at 900 MHz and 1800 MHz and DC combining techniques are utilized to combine the DC voltage at the output to obtain higher output power.

RF combining utilize one antenna to peak up RF signals at different frequencies and they are passed to the matching circuit and the RF-DC rectifier at the same time. Hence, the antennas, matching circuit, and the RF-DC rectifier need to be taken into consideration at the same time to achieve broadband or multi-band energy harvesters. In [30], a dual-

band energy harvester operated at 1.85 GHz and 2.15 GHz is proposed. It is composed of a broadband Yagi antenna and a dual-band matching circuit. Since the matching circuit is matched only at 1.85 GHz and 2.15 GHz, only RF signals at correct frequencies are passed to the RF-DC rectifier. A similar idea is adopted in [31, 32] to accomplish triple-band and six-band energy harvester. Moreover, multi-band antennas and multi-band matching circuits are also used to increase the total output power [33, 34].

In addition to multi-band energy harvesters, broadband energy harvesters attract more attention recently, since the new 5G communication occupies a broad operating band. In order to realize broadband energy harvesters, broadband antennas, matching circuits, and rectifiers are essential. In [35], an octave rectifier with non-uniform broadband matching circuit is proposed. In [36], another octave rectifier is realized with diode arrays to rectify RF energy at different frequencies.

*Hybrid Energy Harvesters*

As mentioned in section subsection 2.1.1, there are pros and cons for different energy sources. By harvesting from different energy sources simultaneously and combining the output power at the end, we can obtain advantages from these sources while mitigating all disadvantages. This type of energy harvesters that harness energy from more than one type of source is known as hybrid energy harvesters. In [37, 38], solar cell and RF energy harvester are integrated together to form hybrid energy harvesters. The solar cell can provide high open-circuit voltage but can only obtain energy during the daytime. The voltage of RF energy harvester is relatively low but it can be accessed all day. Hence, by combining both energy sources, we can have both advantages while alleviating the drawbacks. Hybrid energy harvesters harness thermal energy and RF energy are proposed and it was proven that the hybrid energy harvesters can obtain higher output power compared with using only RF energy harvesters [39, 40].

### 2.4.3 Advanced Applications

By integrating energy harvesters with wireless platforms such as RFID and wireless sensing platforms, battery-free devices with longer sensing range can be achieved [17, 41–43]. Thus, from an energy perspective, the devices with energy harvesters can operate forever without the requirement to replace or recharge batteries manually. This characteristic makes energy harvesting one of the most significant enabling technologies to realize IoT networks because IoT networks are composed of hundreds or even thousands of sensors and devices and it is impossible to replace the batteries one by one manually [44, 45]. In addition to IoT networks, energy harvesting is also crucial to achieving smart skins where numerous sensors are integrated inside clothes to perform constant human body monitoring [46]. Finally, energy harvesting can be combined with 5G communication networks to enhance energy efficiency eminently [47, 48]. In the meantime, 5G networks with high EIRP, around 75 dBm [49], is a good candidate to provide enough harvested power. Applications of energy harvesters to new areas that can completely change the game and can only be realized utilize energy harvesting technologies are still being explored and remain a popular topic.

# CHAPTER 3

# REVIEW OF ADDITIVE MANUFACTURING TECHNOLOGIES

In this chapter, an introduction of different additive manufacturing technologies including inkjet printing and 3D printing technologies is addressed in section 3.1. The inkjet printing technologies are discussed in section 3.2 and the 3D printing technologies are addressed in section 3.3. The glass SAP packaging process is introduced in section 3.4. The material characterization methods will be included in section 3.5.

## 3.1 Introduction

Additive manufacturing technologies [50] are emerging fabrication methods and expanding rapidly both in industrial applications and academic research. Compared with traditional subtractive manufacturing technologies which remove materials in unwanted regions, additive manufacturing technologies only deposit materials at desired regions. Due to the reduction of materials used, additive manufacturing can reduce the costs by two main vectors: it significantly reduces material usage during structural formation, and it reduces waste materials such as etchants, solvents, and coolants. The most common subtractive fabrication method for electronics is photolithography, as shown in Figure 3.1. The process begins with copper cladding a substrate and then adhering a thin layer of photoresist onto that copper. A mask needs to be fabricated, which is then used in the light exposure process to either weaken or strengthen bonds via exposed light, depending on if it is a positive or negative resist, respectively. Thereafter, chemical etching is utilized to remove unwanted materials (in this case, the copper pattern), and finally, one more chemical wash is used to remove the remaining photoresist to achieve a patterned circuit. While the process has been utilized successfully for countless years, the advancement of digital fabrication, the so-called 'fourth industrial revolution' has enabled the exploration of alternative technologies that

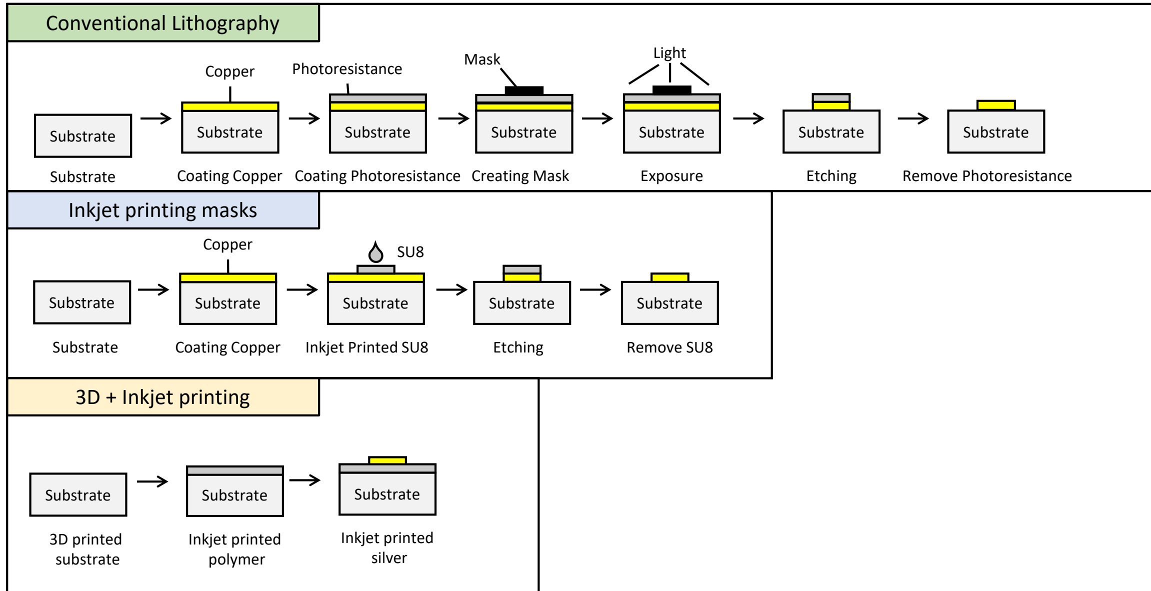


Figure 3.1: Comparisons between subtractive and additive manufacturing processes.

would have previously been determined as too complex.

The most popular additive manufacturing technologies are inkjet printing and 3D printing. Inkjet printing utilizes liquid materials or "inks" with different properties for a wide range of applications. The nozzles or the substrate are moving while inks are jetting out so that the inks can be deposit on desired regions. Extensive research on how to use different inks to print components such as sensors, passives, origami, microfluidics, flexible electronics, transistors, and solar cells have been proposed [51–53]. For 3D printing, the most popular two methods for RF and mm-wave components are SLA 3D printing and DLP 3D printing since they can achieve smoother surface and thus, reducing the surface roughness and the conductor loss. Furthermore, different additive manufacturing techniques can be combined together to realize a fast and large-scale prototyping method with higher material and structural flexibility. As demonstrated in Figure 3.1, ideally, the circuit fabrication process can be reduced to only three steps by using both inkjet and 3D printing. The first step is to 3D printed the substrate, the second step is to inkjet print the polymer to smooth the surface roughness, and the final step is to inkjet print conductive patterns for electronics.

Recently, the emerging high-frequency 5G and mm-wave wireless communications re-

sult in the size reduction of the RF components and give rise to the high interests in System-on-Package (SoP) and SiP designs which incorporates ICs with RF peripheral components such as filters, couplers, and antennas in one package [54]. Thus, research involving exploiting additive manufacturing techniques to achieve 3D structures for performance improvement and fully additive manufacturing SiP modules has seen drastic increases of interest. In [55], inkjet-printed ramp structures with transmission lines on the top are used as the die-to-package interconnects. It has been proved that the structure can support lower parasitics and better physical reliability [56]. In [57], 3D-printed ramp structures are used as inter-layer interconnects with lower parasitics compared with vias.

## 3.2 Inkjet Printing Technology

Inkjet printing may not be the first thought coming to mind when additive manufacturing is discussed. However, 3D structures can be formed by repeatedly inkjet printing layers over and over, on the same area. An advantage of inkjet printing is that it has demonstrated its scalability through centuries of use. The large-scale fabrication is achieved by utilizing multiple cartridges and each cartridge contains over a thousand drop-on-demand nozzles dispensing material of pico-liter volume at a rate that can exceed 10,000 times per second. With the ability to utilize multiple cartridges of different materials, similar to how a consumer inkjet printer utilizes multiple color cartridges, it can be readily utilized to print multiple materials simultaneously. Therefore, inkjet printing is ideal for fabricating anything between circuit boards and interconnected multichip modules.

### 3.2.1 Resolution

The resolution of inkjet printing technology is relevant to the printer, ink, and structures. For the inkjet printer such as a Dimatix DMP-2831 printer, typical cartridges are in the 1-10 pL range, corresponding to a drop diameter size of roughly 30 µm, with a layer thickness between 0.5 to 2 µm. Inkjet printable materials need to be within a certain viscosity

(often between 1-30 cPs) and surface energy. Therefore, different solvents are used to adjust the viscosities of different materials such as metallic nanoparticles, surfactants, and polymers [58]. When the droplet hits the surface of the substrate, it spreads depending on the material surface energy and the solvent used. Furthermore, multilayer printing with thicker thickness might cause coffee-ring at the edge or extrusion at the center depends on the sintering process and the structure. Taking all aspects into consideration, the typical x and y resolution of the Dimatix DMP-2831 printer is from 20 µm to 50 µm.

### 3.2.2 Printable Materials and Applications

Numerous inkjet-printable materials are developed and most of them can be classified into three categories: dielectric, conductive, and reactive ink. The dielectric inks are typically composed of organic polymers and can be applied to realize masks for the photolithography process or substrate for the circuit. Two dielectric inks including SU-8 and BCB are introduced in this section. The conductive ink is composed of metallic nanoparticles and solvent. This type of ink normally required to be sintered at a temperature higher than 120° to vapor the solvent and cross-link the metallic nanoparticles. A typical example of the conductive ink is SNP which can be used to realize conductive traces. The final type of ink is the reactive ink which will change properties while exposing to certain environmental stimuli such as humidity, targeted gas, or temperature. This type of ink is a good candidate for sensor realization and a commonly used example is solvent with carbon nanotubes (CNTs). The focus of this thesis will be on the dielectric and conductive inks and their applications to energy harvester and packaging designs.

*Silver Nano-particle*

The SNP ink introduced here is EMD-5730 developed by Sun Chemical Corporation. The SNP ink has to be sintered at 120° for 2 hours. If the substrate can withstand higher temperature, the SNP ink can be sintered at 180° for 1 hour, and a higher conductivity can be

realized. The resistivity of the SNP ink after proper thermal sintering is from 5 μΩ cm to 30 μΩ cm. The thickness of each layer is about 0.5 μm and at least 3 to 5 layers are used each time. The SNP ink is used to realize conductive traces in energy harvester designs, sensor designs, and packaging structures in chapter 5 and chapter 7.

*SU-8*

SU-8 is a commonly used polymer ink. The SU-8 used for inkjet printing is a blend of 35% SU-8 2005 and 65% SU-8 2002 from Microchen Corporation. The mixing ratio is optimized to realize the best viscosity for the Dimatix DMP-2831 inkjet printer. The layer thickness of each printing process is about 4-6 μm. The SU-8 can be used for two different applications. The first one is to act as the photoresist and realize masks for the photolithography process. The process steps of using SU-8 ink as photoresist is demonstrated in Figure 3.1. The first step is to inkjet print the desired pattern using SU-8 ink. Generally, 2-3 layers of the SU-8 printing are required. The substrate with printing masks is soft-baked under 95 °C for 10 minutes. The printed SU-8 mask is then crosslinked with a 600 mJ/cm$^2$ exposure of 365 nm UV light. The sample is then hot baked under 95 °C for 10 minutes. Etching of the board is then performed using $FeCl_3$ at a temperature of 55 °C. Finally, acetone is used to strip the printed SU-8 mask from the board. The inkjet-printed mask method is adopted for the fabrication of multiple energy harvester designs in chapter 4 and chapter 5. In addition to the mask, the SU-8 can be used as a substrate. The detailed applications of using SU-8 as substrate are included in chapter 7. At 25 GHz, the dielectric constant is 2.85 and the loss tangent is 0.04 [59]. The multilayer circuits can be realized by repeatedly printing the SU-8 as the substrate layers and SNP as the metal layers.

*BCB*

Although the SU-8 ink can be used as the substrate, the high loss tangent will induce serious performance degradations at high-frequency applications such as 5G and mm-wave applications. Furthermore, most of the 3D-printed materials are based on the resin which also has high loss tangents (around 0.03). Therefore, a low-loss inkjet-printable ink is necessary to push the additive manufacturing process to high-frequency applications. BCB is a commonly used substrate and is well-known for its low loss tangent at 0.002 (10 GHz) [60]. Thus, an inkjet-printable BCB ink is developed and characterized. The detailed characterizations are included in section 7.6.

## 3.3 3D Printing Technology

### 3.3.1 FDM Printing

For the thermal extrusion method, the solid materials are extruded and heated to become soft and sticky so that they can be adhered together on the plate to form the desired 3D structures. One of the representative techniques is Fused Deposition Modeling (FDM) 3D printing. FDM printed 3D passives including capacitors, inductors, and resistors are realized by first 3D-printed molds and filled them with liquid metal [61]. However, the surfaces of samples fabricated using the thermal extrusion method are generally rough [62]. Since the surface roughness will increase the conductor loss, it is not suitable to apply to high-frequency applications.

### 3.3.2 DLP and SLA Printing

For UV polymerization, the build plate is first submerged inside liquid materials. Then the UV light is exposed to solidify materials at desired places. Then the build plate is lifted a little for the next layer. Typical UV polymerization methods are SLA 3D printing and DLP 3D printing. A custom-build DLP 3D printer is shown in Figure 3.2a. A white light

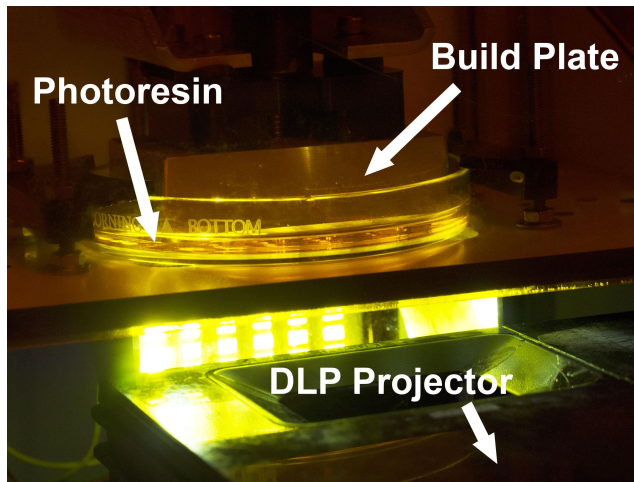


(a)

(b)

Figure 3.2: (a) The custom-build DLP 3D printer. (b) The SLA 3D printer from FormLabs.

projector is used to project the images of designs and cure the material layer by layer. The x and y resolution is about 36 µm and the thickness resolution can be adjusted from 10 to 50 µm. As shown in Figure 3.2b, an off-the-shelf 3D printer utilized SLA method is built and sold by FormLabs. The latest version of the 3D printer, FormLabs Form 3, can offer x and y resolution at 25 µm using 85 µm laser spot size. The thickness resolution is 50 µm. These two techniques can achieve much smoother surfaces compared with FDM printing. Therefore, they can be used in high-frequency applications such as 5G and mm-wave devices.

### 3.3.3 Available Materials

One of the advantages of using 3D printing technologies is the wide variety choices of off-the-shelf materials. The high-temperature material which can withstand 238 °C is suitable for integration with inkjet printing since SNP ink has to be cured at 180 °C. The flexible material can be used to realize wearable designs or shock abortion inside packaging designs. Although most of the physical parameters of these materials can be found in the

datasheet, the electrical properties have to be characterized. The characterization method for dielectric constant and loss tangent is discussed in section 3.5 and an example can be found in section 7.4.

## 3.4 Semi-additive Glass Packaging Technology

The glass SAP packaging process is proposed and used to realize high-quality and high-resolution packaging structures. Compared with subtractive manufacturing, the conductor patterns using copper is plated only on desired locations. However, some of the commonly used subtractive manufacturing processes and machines are still adopted rather than printing technologies. For example, the substrate layers are spin-coated on the core glass and the masks are used to selectively plat the copper. This fabrication method falls in between additive manufacturing and subtractive manufacturing and thus, it is called a semi-additive manufacturing process. This process provides both advantages of additive and subtractive manufacturing processes. Since the plating technique is used to realize the conductor traces, the conductivity is much higher than SNP ink and the resolution is also much higher compared with printing technologies. Furthermore, the spin-coating method is used to deploy low-loss materials and achieve extremely low surface roughness. The material consumption is less and the cost is lower due to the selective conductor plating. This method is used to built high-performance AiP and SiP modules in chapter 6. The detailed fabrication steps of the glass SAP packaging process is introduced in section 6.2. Besides, the comparisons of the glass SAP packaging process and other commonly used processes are also discussed.

## 3.5 Printing Material Characterization

As mentioned before, the developers of printing materials often focus on the specifications related to printability, strength, flexibility, temperatures, and a wide variety of other features. However, RF parameters such as the dielectric constant and loss tangent are typ-

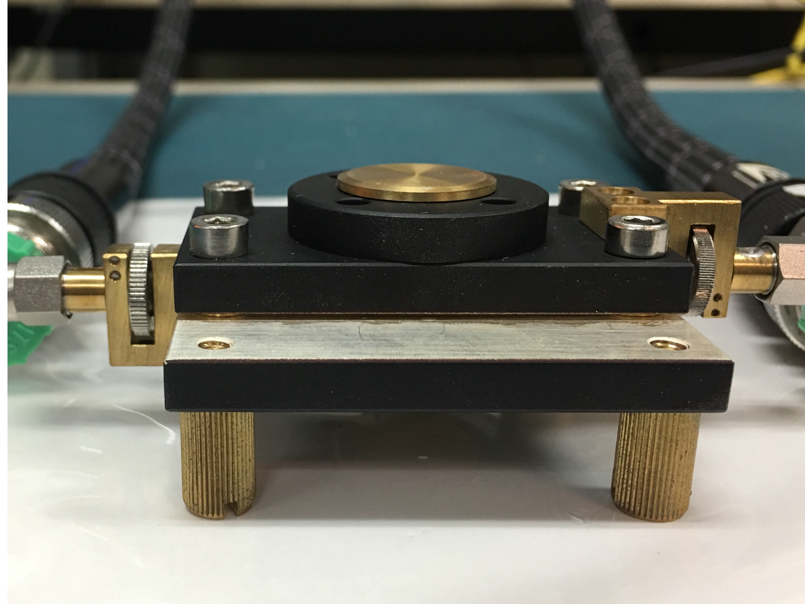

Figure 3.3: Material characterization using commercially available dielectric resonator.

ically not included in the datasheet because of the significant disconnect between the RF and material science engineers. An advantage to 3D printing techniques that utilize relatively bulk materials, such as FDM is that the RF material properties are relatively known. Other printing techniques that require specially formulated materials such as inkjet printing, aerosol jet printing, and SLA have evolving materials with novel properties, and often require constant characterization for every variation of material.

There are generally two types of material characterization methods. The first one is based on resonator or resonating structures. To characterize inkjet printing dielectrics, T-resonator or ring-resonator structures are commonly used. The off-the-shelf dielectric resonator can be used to characterize 3D printing materials. The other one is to characterize materials with transmission structures. For example, the two-line method extracting the dielectric constant and loss tangent of inkjet printing substrates by comparing the performance differences between two transmission lines with different lengths. The waveguides are also used to extract the properties of 3D printing materials. Resonator-based methods can only extract properties at discrete resonant frequencies, but the accuracy of loss tangent measurements is higher compared with transmission-based techniques. On the other hand,

Figure 3.4: Material characterization using waveguides.

transmission-based techniques are suitable for broadband characterization with a finer frequency step.

### 3.5.1 Resonator-based Method

One methodology is the utilization of a dielectric resonator as shown in Figure 3.3. This enables measurements of thin sheets, up to 600 μm thick for 15 GHz structures, where the resonant frequency variation and quality factor determine the dielectric constant and loss tangent, respectively. If the 3D printed substrate can be metalized, resonating structures can be patterned directly onto the substrate, offering an integrable approach where characterization structures can be included during fabrication of circuit designs.

### 3.5.2 Transmission-based Method

A commonly used broadband transmission-based characterization technique is waveguides as shown in Figure 3.4. The 3D-printed samples are fitted into waveguide shim, and the scattering parameters are measured. The same measurement are also recorded when the shim is empty or in other words filled with air. The reflection and transmission values are

utilized to calculate the dielectric properties by the Nicholson-Ross-Weir derivations. As samples are ideally near a quarter wavelength in thickness and need to fill a waveguide, this can lead to large samples at low frequencies. Overmoding, avoiding half wavelengths, and reducing or preventing any air gaps in the shim must also be accounted for, which may be difficult depending on the tolerances of a 3D printer at higher frequencies [63]. Regardless of whichever method is utilized, any characterization technique should be verified to satisfy the Kramers-Kronig relation.

# CHAPTER 4
# ON-BODY LONG-RANGE SENSOR NETWORKS USING RF ENERGY HARVESTER

On-body sensor networks is one of the key enabling technologies to achieve health monitoring. One of the key challenges for wearable sensors is the power supply. Customers don't want to replace batteries all the time, and the wearable sensors are moved with humans which makes stationary RFID reader-powered technology difficult to cover all wearable sensors all the time. Hence, EH is a good candidate to solve the problem and realize real-time health monitoring. Among all types of sensors, backscattering sensors are known for their low power requirement which makes them perfect applications for energy harvesters.

The hand-held devices such as cell phones or two-way talk radios are good energy sources for the RF EH to power on-body sensors for two critical reasons. First, the hand-held device is close to all on-body sensors. Thus, the low RF power density problem can be solved. Second, the hand-held devices will move with users so that tracking the position of users is not necessary and the power level can be kept at the maximum at all times.

In this chapter, an on-body long-range sensor network using RF EH harnessing energy from a hand-held two-way talk radio is proposed. The objectives and the design ideas will be addressed in section 4.1. The design and test of the EH will be introduced in section 4.2. The applications of the harvested DC power is in section 4.3. The on-body backscatter sensor tag design is in section 4.4. The system range test and the system field test will be included in section 4.5. Finally, the simulation, design, and measurement of the EH including the effects of human tissue are discussed in section 4.6.

## 4.1 Objectives and Design Ideas

### 4.1.1 Objectives, Challenges, and Solutions

The idea of applying IoT and Wireless Sensor Network (WSN) to build smart cities and smart skins has become extremely popular in the last decade [64], [65]. These technologies expect to deploy hundreds or even thousands of sensors in the cities or on the clothes and collect multiply sensing data to analyze and monitor the security of the cities or the health status in real-time. However, conventional sensor devices are mostly relying primarily on batteries, which require replacement after a few years of operation. Due to the large number of sensors, it is nearly impossible to change the batteries of the sensor nodes one by one because of the excessive cost. Hence, one of the biggest challenges is to realize energy-autonomous sensing systems eliminating the use of conventional batteries.

Ambient energy harvesting is a good solution to power these sensing devices by harnessing ambient energy from existing ambient energy sources such as solar, heat, and vibration. Among all sources, RF energy sources are popular since they can be accessed all day while their inherent ability to bypass or penetrate walls makes them ubiquitously available. There are many different types of RF energy sources such as UHF communication, WiFi, and DTV signals, especially in urban environments [12, 17]. The challenges associated with the relatively low energy density of ambient RF energy sources [8] have been commonly addressed using high gain antennas and broadband or multi-band antennas [12, 32, 66] for low energy far-field RF energy harvesting applications. However, in addition to those RF energy sources with relatively low energy density, there are numerous "hotspots" where RF energy is fairly high, which can generate very high DC voltage and power and alleviate the issues of low energy density and ICs' "cold start" [67]. As an example, the two-ways talk radio, which is a typical communication device, is a great energy source with large near-field RF power density.

In most of the previously reported ambient RF energy harvesters in literature, the main

focus of harvester design is to maximize the output DC power [19, 42, 68]. Therefore, output filters are used in the designs of typical energy harvesting circuits to eliminate harmonics created during rectification. However, for wireless sensing applications, wireless communication of sensing data is another important aspect in the system and these commonly wasted harmonics can be utilized for communication. The conventional approach for wireless communication is to utilize a transceiver IC and to transmit the sensing data obtained by utilizing Analog to Digital Converter (ADC), but this approach requires power-hungry DC-RF conversion and RF signal amplification processes and is not suitable for ambient RF energy harvesting, which has limited power supply. Another approach is to utilize conventional passive RFID and backscattering for sensing, but the reading range of conventional RFID sensor networks is about only 3 m [64]. The reading range is so small that multiple RFID readers need to be arranged to collect the data, resulting in a dramatically increased implementation cost. Thus, another key challenge is to significantly increase the reading range of the RFID sensor tags.

To extend the reading range of the passive RFID tags, it has been proven that multiple carrier emitters can be used to illuminate nearby RFID in bi-static RFID reader configurations [69]. However, these carrier emitters are not energy-autonomous which means there is additional maintenance cost. Moreover, especially for smart skin applications, the sensors worn on users change their location following body movements. Thus, carrier emitters with fixed positions might not be able to cover them all the time and mobile/portable carrier emitters are necessary. Since the two-way talk radio is utilizing analog modulated signals [70], harmonics from the energy harvester include continuous RF signals, which can be used to realize a carrier emitter for passive RFIDs.

In this chapter, a novel wearable energy-autonomous on-body wireless sensor network system is proposed. The objectives, challenges, and the solutions are summarized as shown in Figure 4.1. The system diagram is demonstrated in Figure 4.2. To realize this system, a wearable and flexible energy harvester which harnesses near-field energy from a Motorola

| Metrics | Objectives | Prior Art | Challenges | Solutions |
|---|---|---|---|---|
| **Performance** | • On-body real-time sensing<br>• Wearable and flexible<br>• Energy autonomous<br>• EH power and efficiency improvement<br>• Reading range > 50 m | • Harvested RF power is low<br>• Wasted the higher-order harmonics<br>• Reading range < 20 m | • Isolated human effects<br>• Harvested enough RF power<br>• Tracked the energy source<br>• Improved the EH efficiency<br>• Increased reading range<br>• Designed with human effects | • AMC design to isolate human effects<br>• Harvested energy from two-way radio<br>• Harvested energy from hand-held devices<br>• New EH topology to utilize higher-order harmonics<br>• New system topology to increase range<br>• New design process to include the human body effects |
| **Fabrication** | • Additive manufacturing process<br>• AMC design with optimize thickness | • AMC design with limiting thickness | • 3D printing flexible substrate<br>• AMC design with optimize thickness | • Utilized flexible material “NinjaFlex”<br>• 3D printing substrate with optimize thickness |

Figure 4.1: The summarizing table of the objectives, challenges, and solutions of the proposed on-body long-range sensing network.

RDU4100 464.5 MHz two-way talk radio is proposed using inkjet and 3D printing techniques for its fabrication. In the proposed energy harvester circuit, both DC power and the second harmonic at 929 MHz are utilized for different applications. The RF second harmonic signal output can be used as a wearable mobile carrier emitter to simultaneously illuminate multiple on-body sensing capable backscattering RFID tags and extend their reading ranges. Meanwhile, the DC power output can be used to drive a RF amplifier to further extend the operating range. Similarly, the oscillator in the tags is powered by an integrated energy harvester harnessing the 464.5 MHz signals from the two-way talk radio. Thus, this energy harvester is the first-ever demonstration of an energy-autonomous system that enables three different functions simultaneously to establish an on-body autonomous sensing network by utilizing a single ambient RF energy source.

### 4.1.2 System Architecture

The detailed block diagram of the proposed system is shown in Figure 4.3. The system is composed of one energy harvester and multiple on-body sensing tags. The only energy source for the entire system is a 464.5 MHz two-way talk radio with the measured power spectrum shown in Figure 4.4. The output powers are 34.3 dBm and -29 dBm at 464.5 and 929 MHz, respectively.

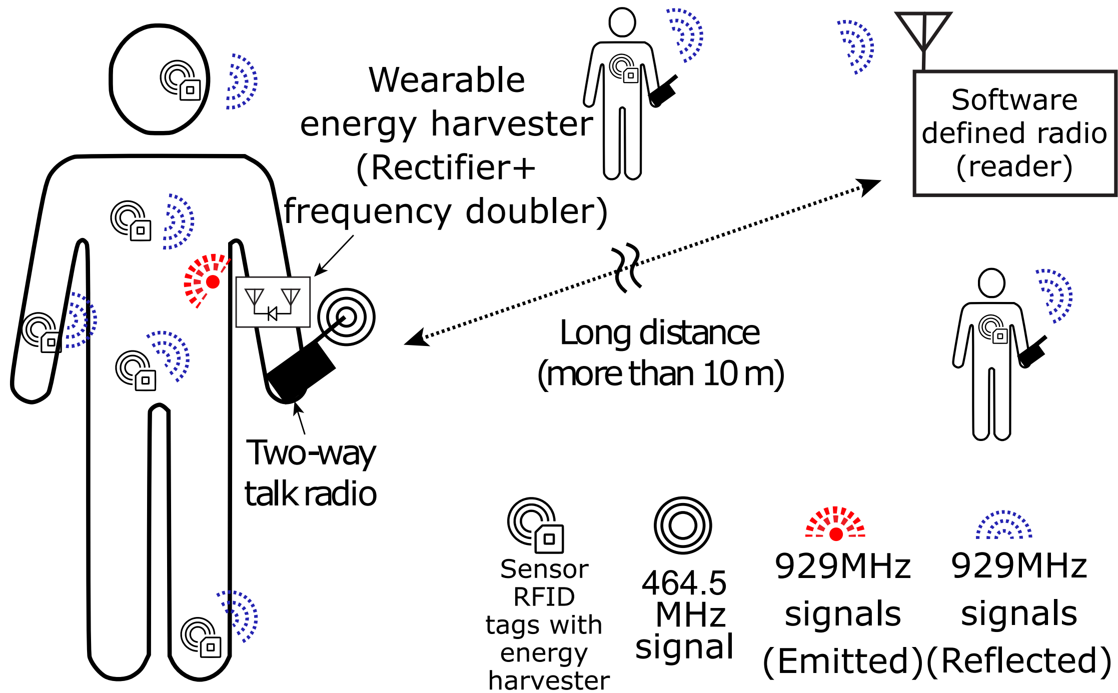


Figure 4.2: Wearable energy-autonomous on-body wireless sensor network system.

The energy harvester section is composed of three main components; a 464.5 MHz receiver, a proposed rectifier/frequency doubler, and a 929 MHz antenna. The 464.5 MHz near-field receiver is used to harness the power radiated from the radio, which is later sent to the rectifier/frequency doubler that generates the following outputs: the DC power is used to drive a DC applications and the RF output is fed to a 929 MHz antenna.

For the interrogated tag design, the 464.5 MHz signal that comes from the two-way radio is harvested by the integrated energy harvester which is composed of a matching circuit, a rectifier circuit, and a voltage regulator. The harvested power is used to drive the oscillator. While the oscillator is properly driven by the rectifier, it is used to control the MOSFET switch to create the modulated backscattered signals using the 929 MHz signal generated by the energy harvesting circuit as the carrier.

In summary, the 464.5 MHz two-way talk radio is used as an energy source to serve three different purposes.

- To power RF amplifier IC as an DC application

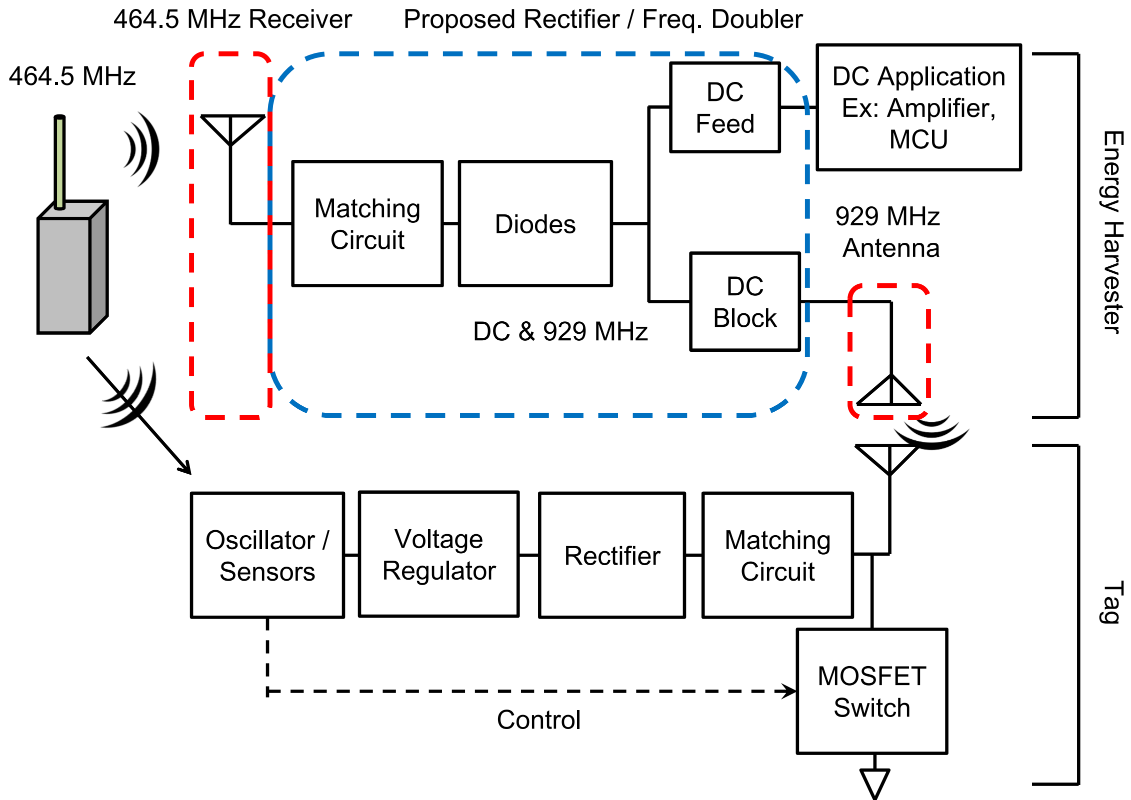


Figure 4.3: Block diagram of the proposed on-body wireless sensor network system.

- To create carrier emitter signals for the interrogated tag/sensor
- To power the oscillator IC in backscattering tags

Besides, since the carrier emitter is wearable, mobile, and capable of moving with the user, the relative distances between the wearable RFID tags and the carrier emitter would not change dramatically. Thus, all wearable RFID tags are in the proximity of the carrier emitter all the time significantly enhancing their readability.

## 4.2 Energy Harvester Design

### 4.2.1 Receiving Antenna Design

A proof-of-concept prototype of 464.5 MHz near-field receiver/antenna fabricated utilizing inkjet printing masking technique and its physical dimensions are shown in Figure 4.5a.

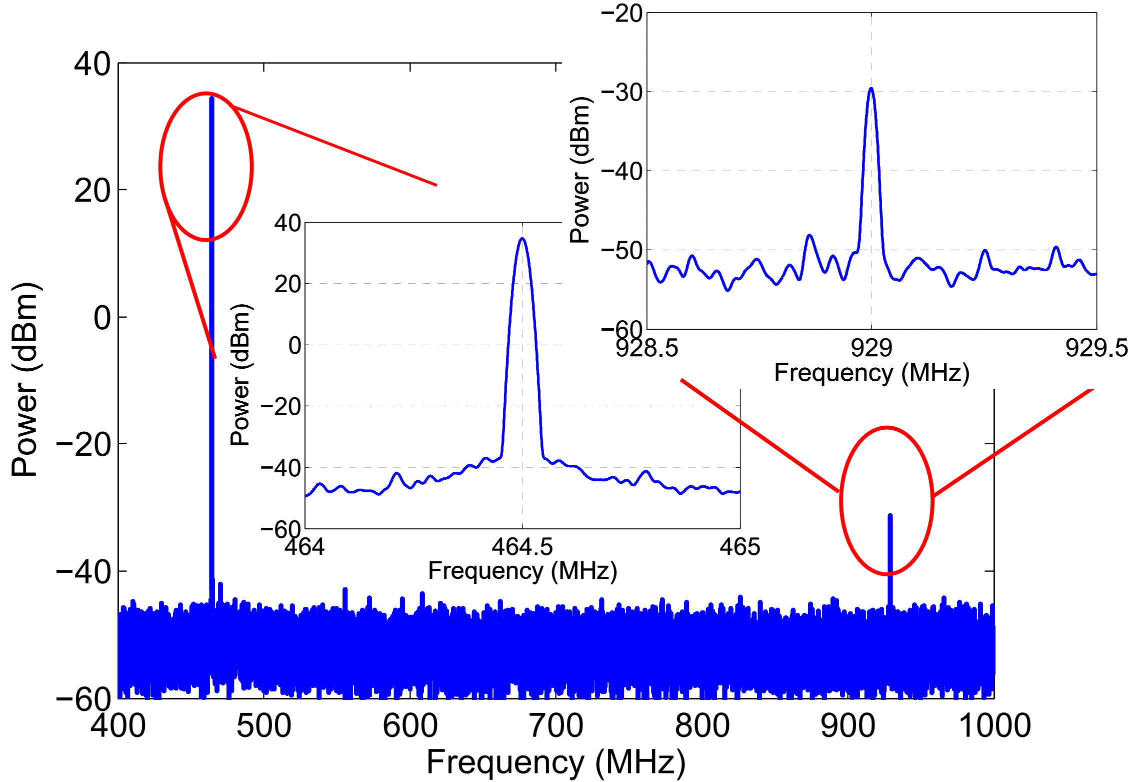


Figure 4.4: Measured power spectrum of the off-the-shelf two-way talk radio.

This receiver is designed with an open-type helical coil structure to enhance coupling between the two-way talk radio and the 464.5 MHz receiver. The "on-body emulating" setup of the coupling test for this 464.5 MHz antenna is shown in Figure 4.5b. The distance between the two-way talk radio and the 464.5 MHz antenna is 9 cm. Moreover, since the stationary measurement is preferred for the first estimation and the human phantom is not available at the time of this study, the circuit is mounted on a water bottle filled with water. The dielectric constant and the conductivity of the water are 82 and 0.01 S/m, respectively. Although the electric properties of water are different from the human tissue, it can serve as a good start. In section 4.6, a new design procedure which considers the real human body effects is proposed and the procedure is used to improve the receiving antenna design.

The 464.5 MHz antenna is connected to the spectrum analyzer to measure the received power level, which is found to be around 20 dBm. The power supply from the two-way talk radio is 36 dBm and about 2.5 % of the power is harvested by the 464.5 MHz near-field

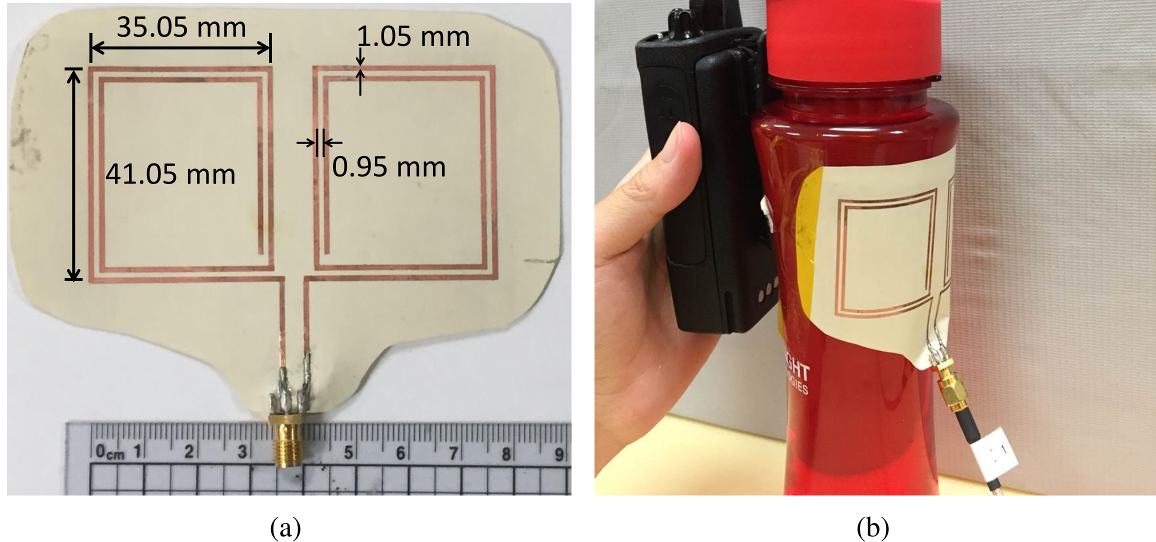


(a) (b)

Figure 4.5: (a) Prototype of the 464.5 MHz antenna (b) “On-body emulating” setup of the coupling test for the 464.5 MHz antenna.

coupling antenna. The harvested energy is large enough to drive all components but not too large to significantly affect the quality and performance of the overall communication.

### 4.2.2 Rectifier/Frequency Doubler Design

Since one of the most commonly used frequency bands for RFID tags is 860-960 MHz, the second harmonic of 929 MHz signals would be a good choice for the carrier emitter. Thus, the main goal of the proposed rectifier/frequency doubler is to generate as large power as possible at the DC and the second harmonic frequencies. The time-domain waveforms and frequency-domain waveforms of a 464.5 MHz sinusoidal signal with amplitude 1 and the respective full-wave rectified results are shown in Figure 4.6. As demonstrated in Figure 4.6b, the first order harmonic is eliminated in the full-wave rectified signal, and the two largest tunes after full-wave rectifying are the DC and the second harmonic at 929 MHz. Therefore, a full-wave rectifier topology is adapted since it can generate the signals that

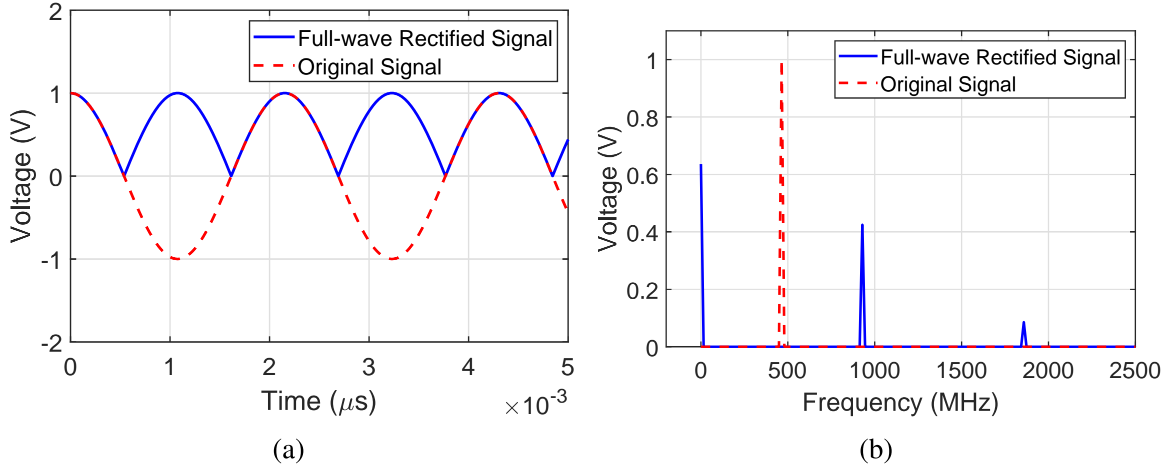


Figure 4.6: (a) Time-domain waveforms and (b) frequency-domain waveforms of a 464.5 MHz sinusoidal signal and the respective full-wave rectified results.

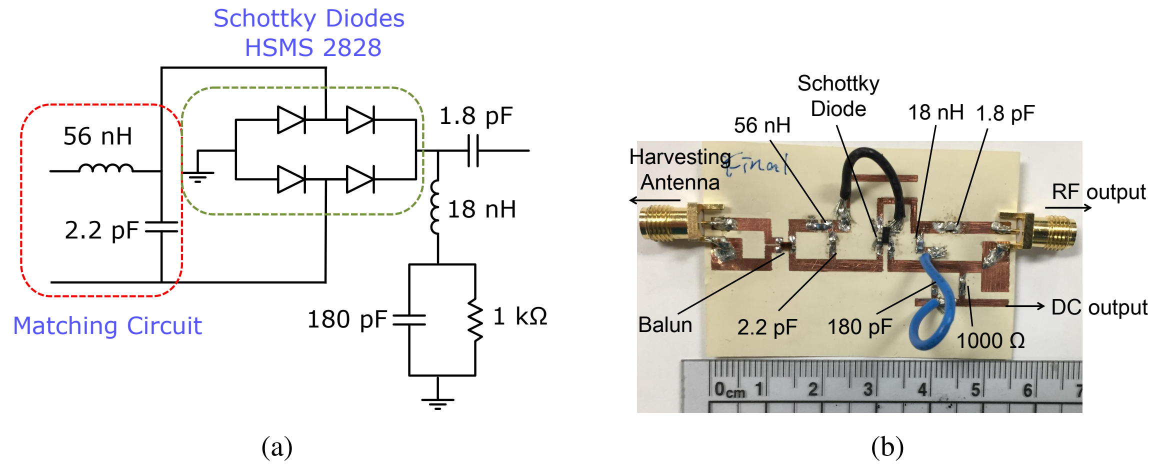


Figure 4.7: (a) The circuit diagram and (b) the prototype of the proposed full-wave rectifier / frequency doubler.

meet the requirement.

The circuit diagram and the prototype of the proposed full-wave rectifier/frequency doubler are shown in Figure 4.7a and Figure 4.7b, respectively. A balun is used, as demonstrated in Figure 4.7b, to guarantee the differential feeding of the full-wave rectifier. The matching circuit is composed of a 56 nH series inductor and a 2.2 pF parallel capacitor. The HSMS 2828 Schottky diode package is used to perform the full-wave rectification. The 1.8 pF capacitor and the 18 nH inductor are serving as a DC block and a DC feed, respectively. Finally, a 180 pF capacitor is used to eliminate higher-order harmonics while

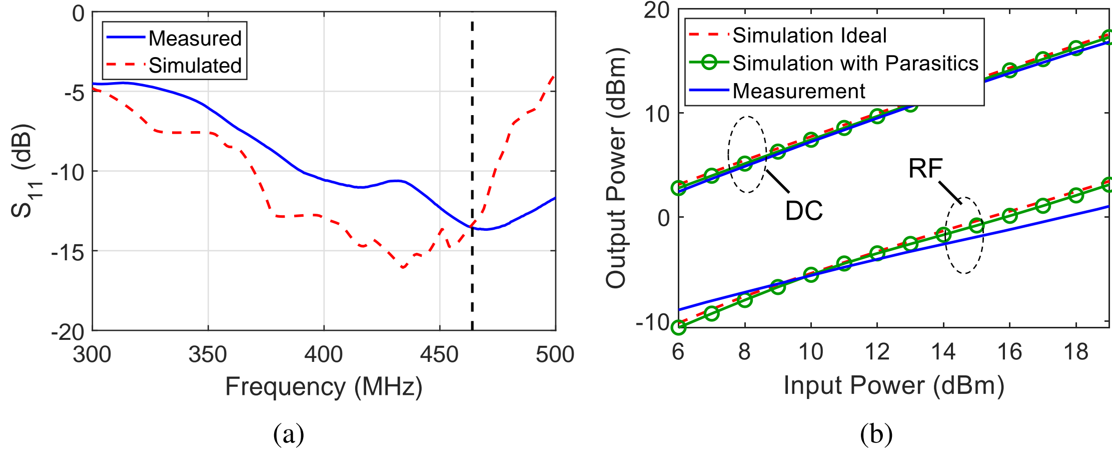


Figure 4.8: (a) Simulated and measured $S_{11}$ and (b) output DC and RF power levels from the proposed rectifier/frequency doubler with respect to the input power.

a 1 kΩ resistor acts as the load. This 1 kΩ resistor is chosen because the RF-DC conversion efficiency of the rectifier is the highest under this load value.

The measured and simulated $S_{11}$ of the proposed rectifier is shown in Figure 4.8a. The black vertical dash line is at 464.5 MHz. Although there is a slight frequency shift between the measured and simulated results due to the parasitics of the lump components, the overall results agree with each other. Furthermore, the measured $S_{11}$ at 464.5 MHz is -13.5 dB which demonstrates a good matching. The measured DC and RF output power levels from the proposed rectifier with respect to the input power are shown in Figure 4.8b. The simulated results using ADS harmonic balance simulator are also included for comparison. As shown in Fig. Figure 4.8b, good agreements between the simulated and measured results can be observed. The maximum RF-DC conversion efficiency is about 61 % and the maximum RF(464.5 MHz)-RF(929 MHz) conversion efficiency is about 3.8 %. The maximum total conversion efficiency is 63.1% when 19 dBm RF input power is provided. The maximum output DC and RF power levels are 17.27 and 1.41 dBm when the input power is about 19 dBm.

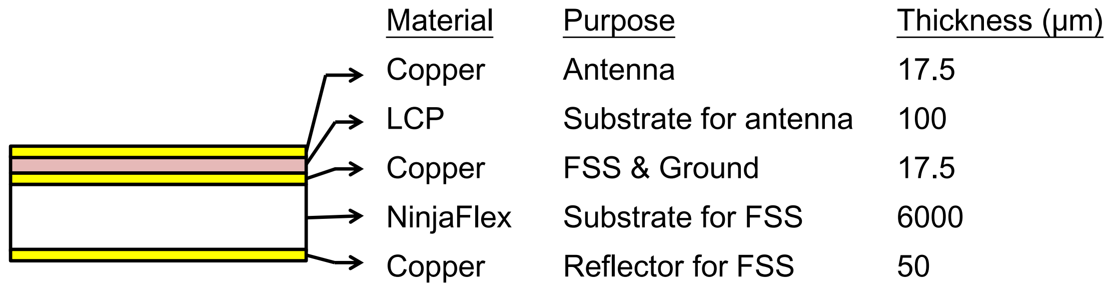


Figure 4.9: Side view of the wearable 929 MHz antenna.

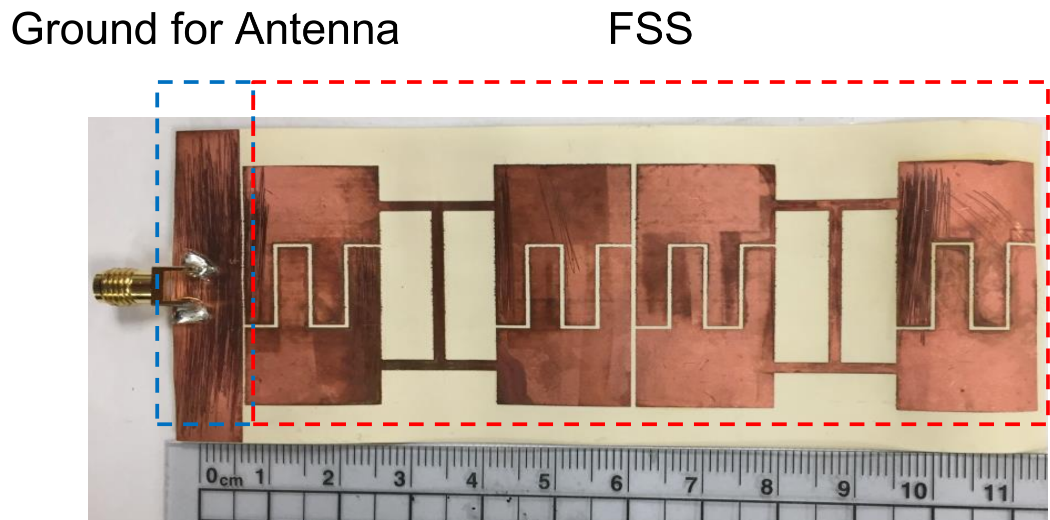


Figure 4.10: Prototype of the FSS.

### 4.2.3 Re-emitting Antenna Design

The 929 MHz antenna is a Z-shaped monopole antenna with an AMC on the back that is used to eliminate the effects of the human body on the antenna [71]. The side view of this antenna is shown in Figure 4.9. It is composed of 5 layers. The top copper layer is used for the Z-shaped monopole antenna. The second layer is the LCP substrate. The AMC structure is composed of a Frequency Selective Surface (FSS), a spacer, and a metal reflector which are corresponding to the third, fourth, and fifth layer, respectively. The thickness and the purpose of each layer are also included in Figure 4.9. The pattern of the FSS and the ground plane for the monopole are contained in the third layer as shown in Figure 4.10. The single cell AMC structure is shown in Figure 4.11a while the physical dimensions

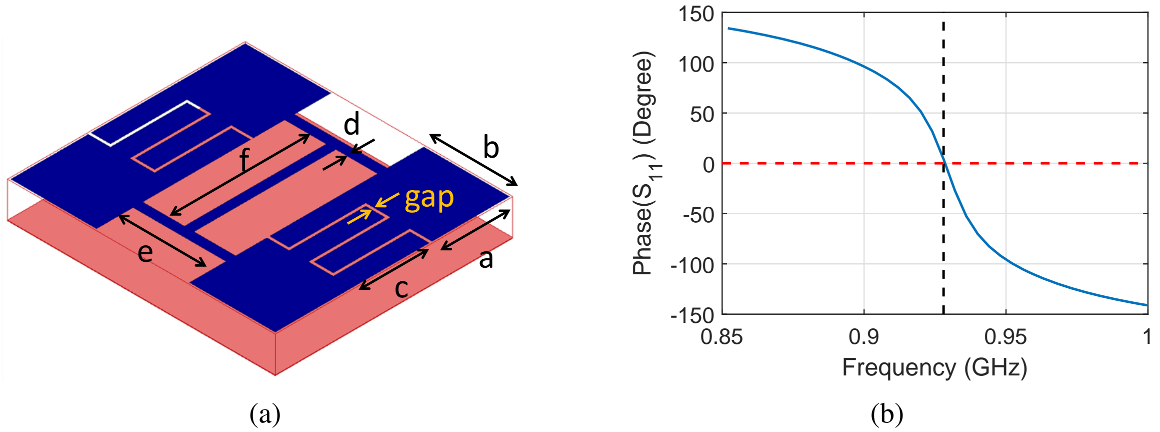


(a) (b)

Figure 4.11: (a) The single cell AMC structure and (b) the simulated phase of the reflected wave.

Table 4.1: The dimensions of the AMC design.

| Parameter | Size (mm) | Parameter | Size (mm) |
|---|---|---|---|
| a | 12.5 | e | 15.8 |
| b | 18.5 | f | 24.1 |
| c | 13 | gap | 0.5 |
| d | 1.6 | | |

are summarized in Table 4.1. The simulated results using Ansys HFSS periodic boundary conditions are shown in Figure 4.11b. The incident wave is from the top and the phase of the return wave is 0° at 929 MHz which means the reflected wave is fully constructive on the surface of the AMC structure. Although the Z-shape monopole is located 100 µm above the AMC structure as shown in Figure 4.9 rather than directly on the surface of the AMC, the thickness is extremely small compared with the wavelength at 929 MHz. Thus, a very good constructive wave can be obtained. Moreover, since there is a complete metal plane on the bottom as the reflector for FSS, the effects of human tissue can be isolated. If a single metal plane is used to isolate the human tissue effects, the phase of the reflected wave will be 180° at 929 MHz similar to Perfect Electrical Conductor (PEC) which means the reflected wave is fully destructive on the surface of the AMC structure. Thus, the AMC structure is necessary to achieve good performance.

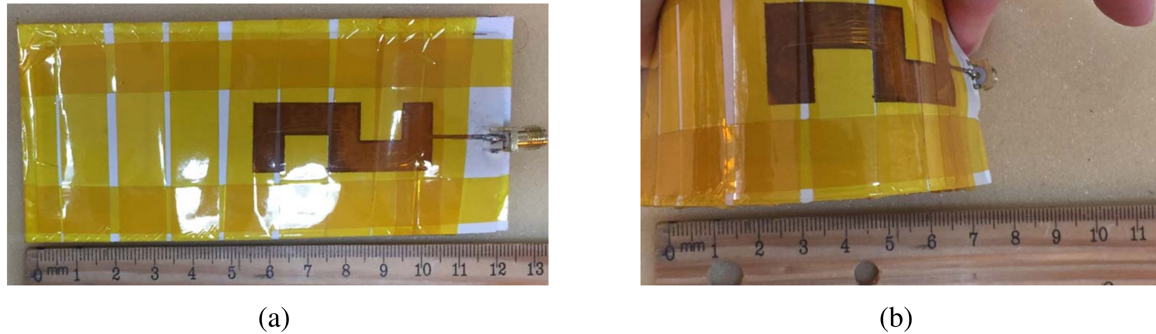

(a) (b)

Figure 4.12: Prototype of the (a) unfolded and (b) folded 929 MHz antenna.

The fourth layer is a spacer between the metal reflector and the FSS. The thickness of this layer is extremely important since it significantly affects the bandwidth and the operating frequency of the AMC plane [71]. However, the thickness of this layer can not be designed arbitrarily if off-shelf substrates are used. The reason is that the thicknesses of off-shelf substrates are limited to specific discrete values and it is hard to realize substrates with custom/optimized thicknesses. The 3D printing technique offers a good solution to this problem. The minimum and maximum thickness that can be realized using Printrbot Metal Plus 3D printer are 127 µm and 25 cm, respectively. Thus, by 3D printing flexible thermoplastic polyurethane NinjaFlex [72], almost any arbitrary thickness values can be realized and a more optimal design of the AMC plane can be achieved. The final layer is a reflector fabricated using copper tape.

The prototype of the 929 MHz antenna is shown in Figure 4.12a. Furthermore, since the 929 MHz antenna is wearable and flexible, the prototype under the folded condition is also shown in Figure 4.12b demonstrating very good flexibility. The length of the unfolded one is about 12.5 cm and can be folded to about 8 cm. The measured scattering parameter values of the wearable 929 MHz antenna are shown in Figure 4.13. Measured results for the folded and the unfolded conditions are included. As demonstrated in Figure 4.13, the return loss values at 929 MHz for folded and unfolded conditions are 14.1 and 14.8 dB, respectively.

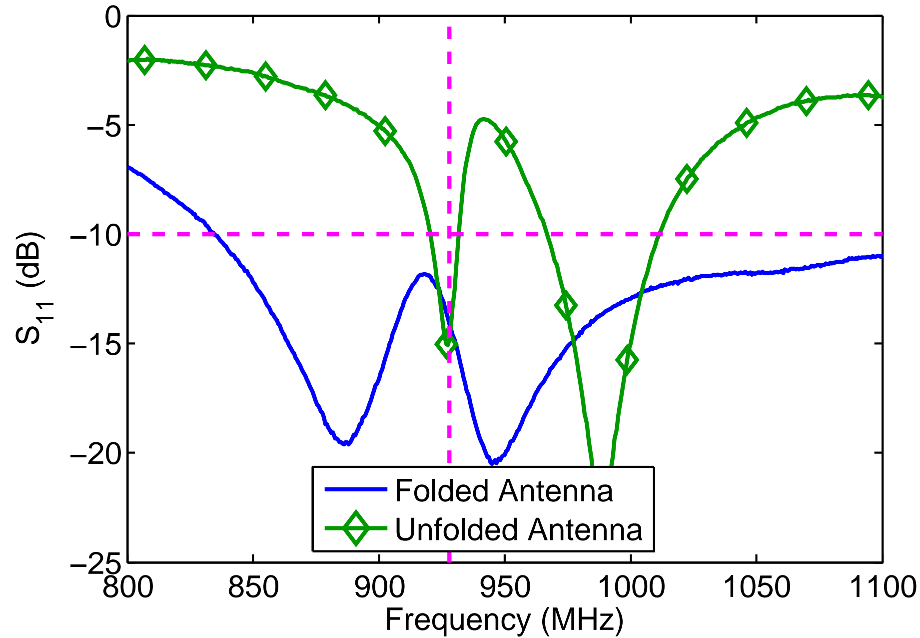


Figure 4.13: Measured $S_{11}$ of the folded and unfolded 929 MHz wearable antenna.

### 4.3 Multiple Uses of Harvester DC Output

Two different output power, DC and 929 MHz continuous RF power, are provided by the proposed energy harvester. The 929 MHz RF output signal is utilized to create a carrier emitter to enhance the reading range of the wearable passive RFID tags. The DC power generated here is a convenient source to drive different applications since the voltage and the power are both high enough to drive most low power applications immediately without requiring a waiting time for charging. There are two potential categories of uses of the DC power. The first one is to achieve a function that is uncorrelated with the carrier emitter. For example, the DC power can be used to drive an RFID reader chip, and thus, a wearable reader can be realized. The other one is to be appropriately combined with the RF power to achieve more complex functions or further range extension. For example, the DC power can be used to drive an MCU to achieve modulated carrier emitter signals or drive an RF amplifier to enhance the carrier emitter power thus leading to a further range extension.

Here, the RF amplifier IC was added as a DC-power enabled component to increase

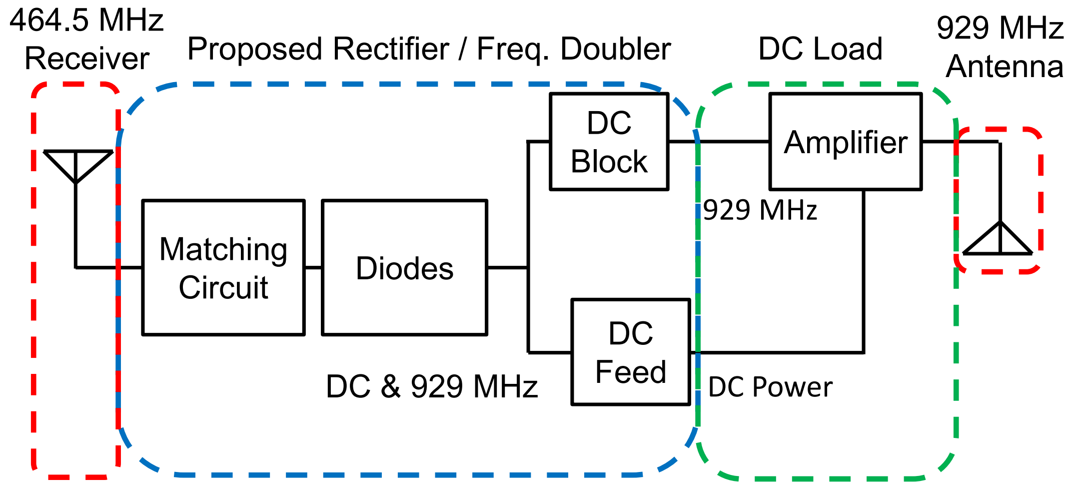


Figure 4.14: Block diagram of the proposed energy harvester with enhanced RF output by driving an RF amplifier using DC output power.

the 929 MHz RF output power level extending the range of backscattering communication and sensing. The new block diagram of the proposed energy harvester with the amplifier is depicted in Figure 4.14 with a proof-of-concept prototype as shown in Figure 4.15. The difference between the prototype shown in Figure 4.15 and Figure 4.7 is that the DC load in Figure 4.7 is a resistor which is replaced by an amplifier in Figure 4.15. As shown in Figure 4.15, the matching circuit is composed of a 16 nH series inductor and a 1.8 pF parallel capacitor. The HSMS 2828 Schottky packaged diode is used to perform the full-wave rectification. The 2.7 pF capacitor and the 16 nH inductor are serving as a DC block and a DC feed, respectively. A 180 pF capacitor is used to eliminate higher-order harmonics. The 929 MHz signal is then fed to the input matching circuit of the amplifier which is composed of a series 6.8 nH inductor and a series 100 pF capacitor and then fed to the input pin of the MGA-68563 RF amplifier chip. On the other hand, the DC power is connected to the amplifier bias circuit which is composed of a 4.3 k$\Omega$ resistor, a 10 nF capacitor, a 68 pF capacitor, and a 43 nH inductor.

The measured DC and RF output levels from the proposed rectifier including an RF amplifier with respect to the input power are shown in Figure 4.16a. The simulated results are also included for comparison and a good agreement between the simulated and mea-

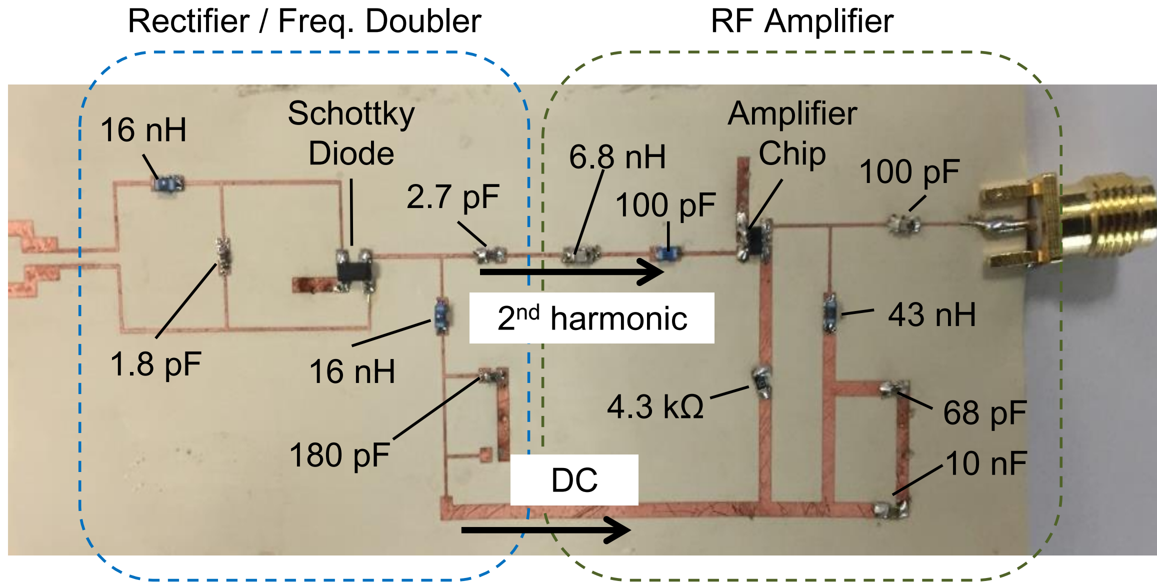


Figure 4.15: Proof-of-concept prototype of the proposed rectifier/frequency doubler including a DC power enabled amplifier.

sured results can be observed. As shown in Figure 4.16a, the maximum RF-DC conversion efficiency is about 33 % and the maximum RF(464.5 MHz)-RF(929 MHz) conversion efficiency is about 14.8 %, thus leading to the maximum total efficiency of 47.8% when 19 dBm RF input power is provided. The RF-DC conversion efficiency is smaller compared to Figure 4.8b (61 %). The reason is that the resistor used in Figure 4.8b is 1 kΩ which is the optimal load resistance value for the rectifier. In the meantime, the input resistance of the RF amplifier IC is only about 0.2 kΩ which is much smaller than the optimal value. Although the DC power is smaller, it can be still used to successfully drive the RF amplifier. Moreover, the comparison of the 929 MHz output between the harvesters with and without the amplifier is shown in Figure 4.16b. The output 929 MHz power is much larger with the help of the amplifier and the effect is more significant when the input power is larger. The 929 MHz output power is about 9 dB larger when the input 464.5 MHz signal is about 19 dBm. Since the carrier emitter is much stronger, a significantly enhanced interrogation range is expected. Furthermore, as shown in Figure 4.4 the second harmonic noise generated by the two-way radio is only -29 dBm. Thus, a much larger carrier signal can be

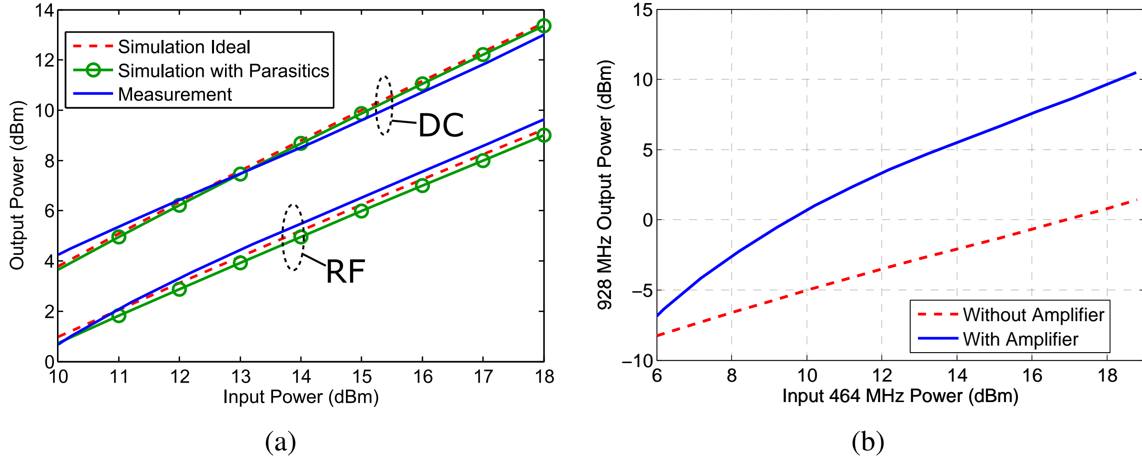


Figure 4.16: (a) Simulated and measured output DC and RF power levels from the proposed rectifier/frequency doubler with an RF amplifier (Figure 4.15) and (b)Comparison of the 929 MHz output power between the harvesters with and without an RF amplifier.

provided utilizing our proposed energy harvester.

## 4.4 Backscatter Sensor Tag Design

### 4.4.1 Sensor Tag Design

For on-body communication and sensing applications, a custom backscatter tag was designed and fabricated. The circuit diagram is shown in Figure 4.17 and the prototype photo is shown in Figure 4.18. The power received by the Z-shaped antenna of the tag is rectified by the voltage doubler. Then a 3.3 V voltage regulator (Linear technology LT3009) is connected between the voltage doubler and the oscillator to protect the oscillator. The output signal from the Silicon Labs TS3006 oscillator is applied to trigger an RF switching MOSFET (NXP BF1118) to create modulated backscattered signals. The modulation frequency (output frequency of the oscillator IC) varies depending on the impedance value of the sensing element connected to the oscillator thus enabling wireless sensing [73]. A P-MOSFET is used as the switch to create two different load impedances for the antenna so that binary modulation can be achieved. The switch design was based on the MOSFET front-end from [74], used in cut-off and saturation regions.

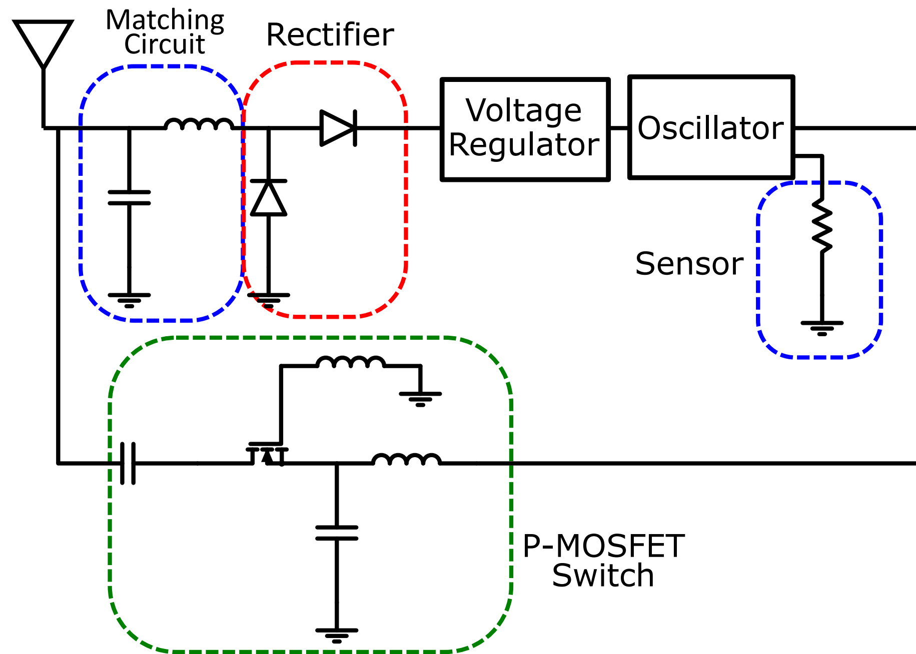


Figure 4.17: Circuit diagram of the custom-made backscattering sensor tag.

The 929 MHz signal is used as the carrier by the custom-made backscattering tag to send the modulated signals. Performing measurements utilizing a Vector Network Analyser (VNA), the input impedance of each input power level of 929 MHz signal (-5, -10, and -20 dBm) and MOSFET bias voltage condition (0 and 1.55 V) is obtained as depicted in Figure 4.19. These bias conditions are chosen because the MOSFET is "Off" when the bias condition is 0 V and "On" when the bias condition is 1.55 V. As shown in Figure 4.19, the impedance values while the MOSFET is on and off are very different. Hence, they can be used to binary modulate bits with the values "0" and "1". At 929 MHz for -20 dBm of RF input power, the difference in the magnitude of the normalized input impedance between 0 V and 1.55 V bias voltage conditions is 0.775 and the phase difference is 112.3° as shown in the measurements.

The 464.5 MHz signal which comes from the two-way radio is harvested and used to drive the oscillator. Figure 4.20 depicts the measured output voltage from the voltage regulator that is connected to the voltage doubler with respect to RF input power (464.5 MHz) at each MOSFET bias voltage condition when a 824 kΩ resistor, which is the expected

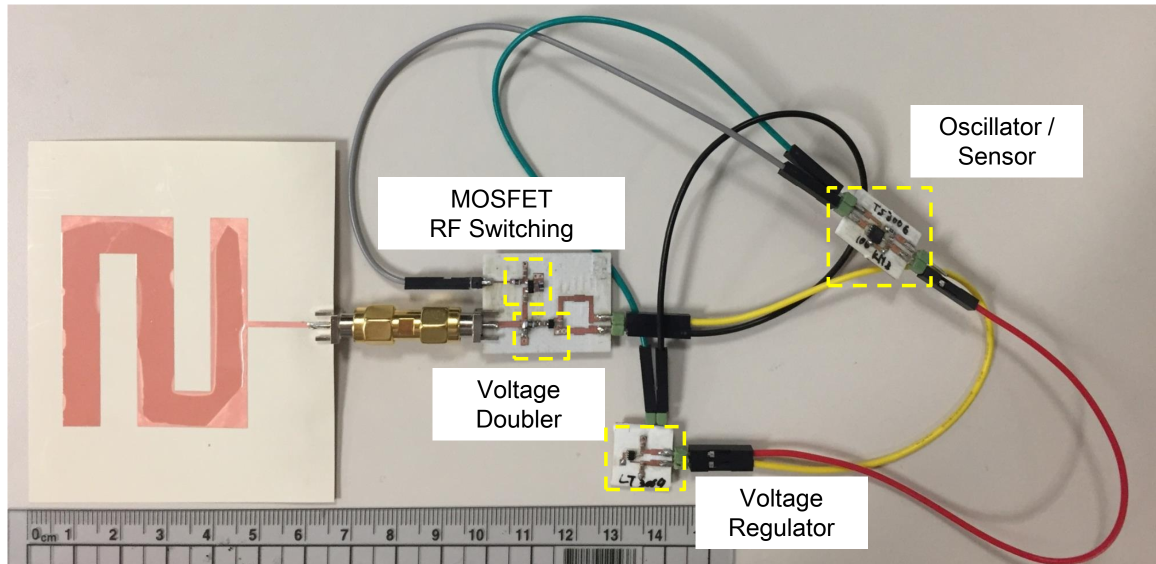


Figure 4.18: Prototype of the custom-made backscattering sensor tag.

equivalent DC resistance of the oscillator IC, is connected as a load. According to the measured results, the tag requires about −5 dBm of input power to achieve 1.55 V to turn on the operation of the oscillator IC.

The operation goals of the tag antenna are to harvest 464.5 MHz power from the handheld two-way radio and backscatter the modulated signal to the reader. However, a dual-band antenna is not suitable for wearable design due to its large size. Since only a small amount of power is required to drive the tag, an antenna which is operated at 929 MHz is sufficient because of the high transmitted power from the two-way talk radio. The measured $S_{11}$ of the proof-of-concept antenna prototype is shown in Figure 4.21 and a good matching at 929 MHz can be observed. The received 464.5 MHz power level using the Z-shaped antenna of the tag is shown in Figure 4.22. The tag operation/interrogation range is about 1.2 m, which can cover the entire human body. Thus, even when the $S_{11}$ at 464.5 MHz is only about -1.5 dB, the received power is large enough to drive the oscillator. This demonstrates the inherent flexibility of the proposed tag to operate effectively using practical on-body antennas without the need for high gain and large form-factors.

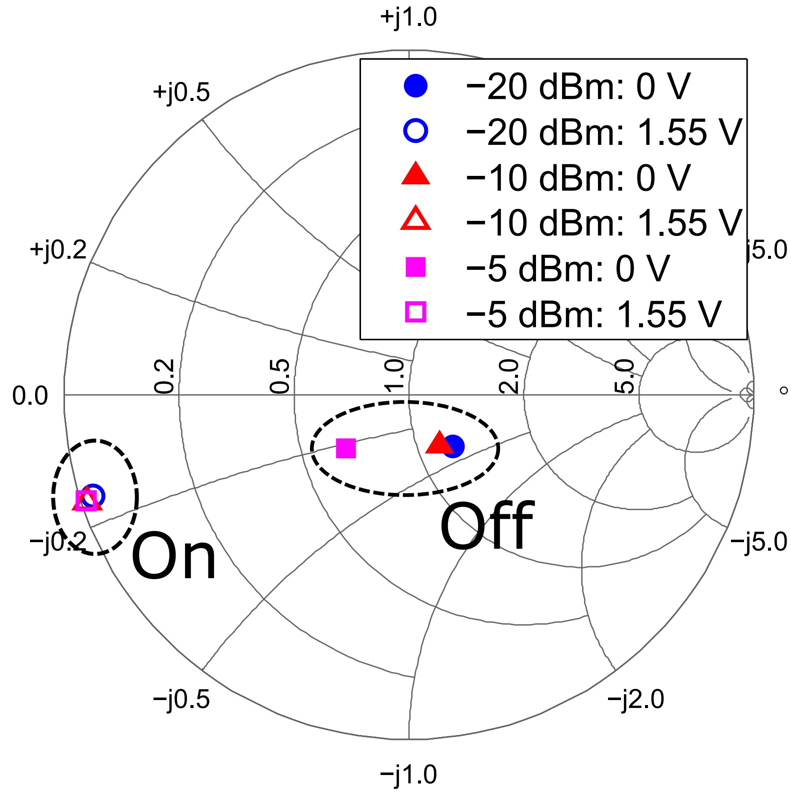


Figure 4.19: Measured S-parameters of 929 MHz with each expected input power and MOSFET bias voltage.

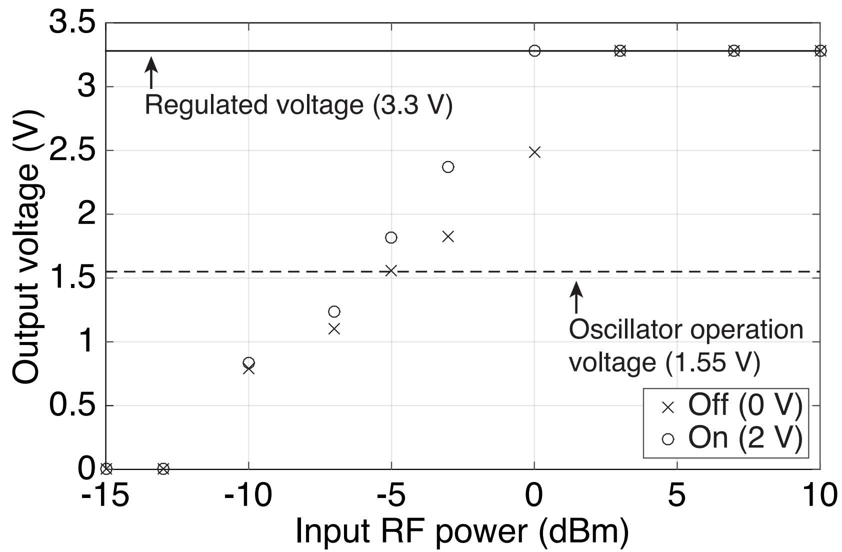


Figure 4.20: Measured output voltage from the voltage regulator connected with the voltage doubler with 464.5 MHz RF input signal at each input power and MOSFET bias voltage.

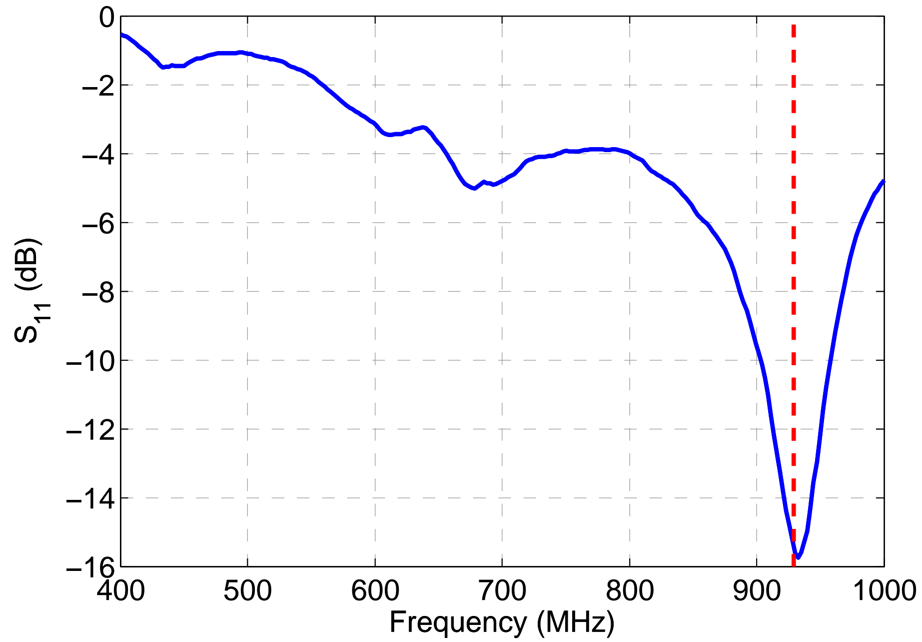


Figure 4.21: Measured $S_{11}$ of the 929 MHz antenna.

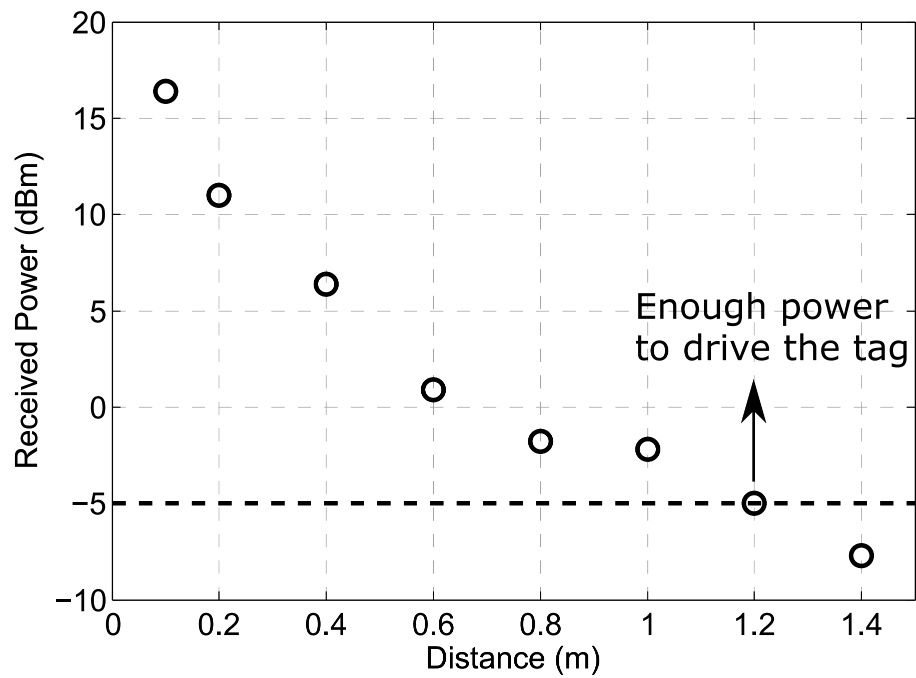


Figure 4.22: Received 464.5 MHz power from the hand-held two-way radio by the tag antenna.

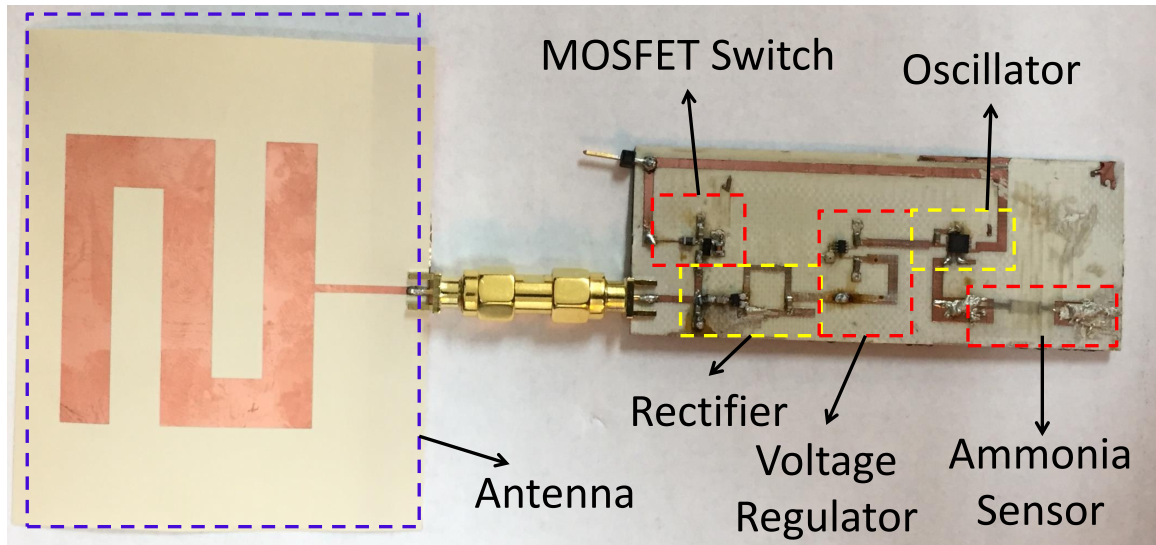


Figure 4.23: Prototype of the custom backscattering sensor tag with a printed ammonia sensor.

### 4.4.2 Integration With Ammonia Sensor

A printed ammonia sensor as reported in [75] is integrated into the custom backscatter tag to detect the existence of the ammonia. The ammonia gas sensor is chosen because of its wide applications including food sensing, environmental sensing, automotive industry, chemical factory safety, and health monitoring [76]. For food sensing, the ammonia sensor can detect the food spoilage since rotten food gives out ammonia [77]. In the farming area, the ammonia sensors can detect the ammonia level to prevent pollution to the environment. As for the automotive industry, the ammonia emission from vehicles has to comply with the regulation. For the fertilizer factory or refrigeration system, since pure ammonia is used, it will be extremely harmful if leakage happened. Thus, the ammonia gas sensor can serve as a great leakage alarm in the factories. Finally, the ammonia sensor can serve as health monitoring by breath analysis.

The modulation frequency is determined by the oscillation frequency which varies as a function of the external load resistance value of the oscillator IC. Therefore, it is possible to integrate arbitrary sensors (in this case a gas sensor), that changes its impedance when it is exposed to certain chemicals, into the custom backscattering tag to detect the existence

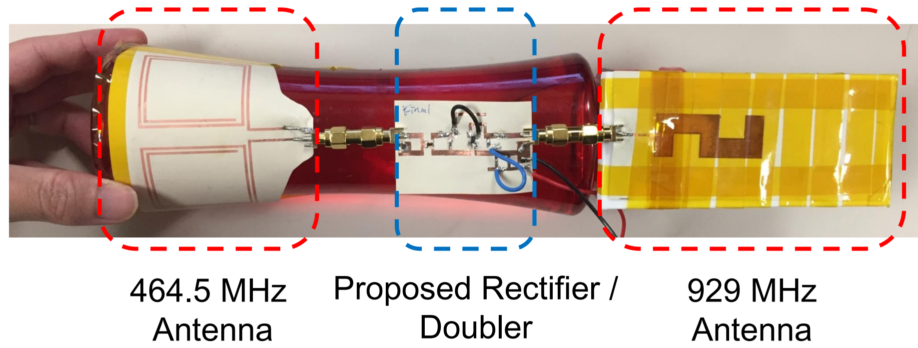


Figure 4.24: Prototype of the energy harvesting circuit without an RF amplifier.

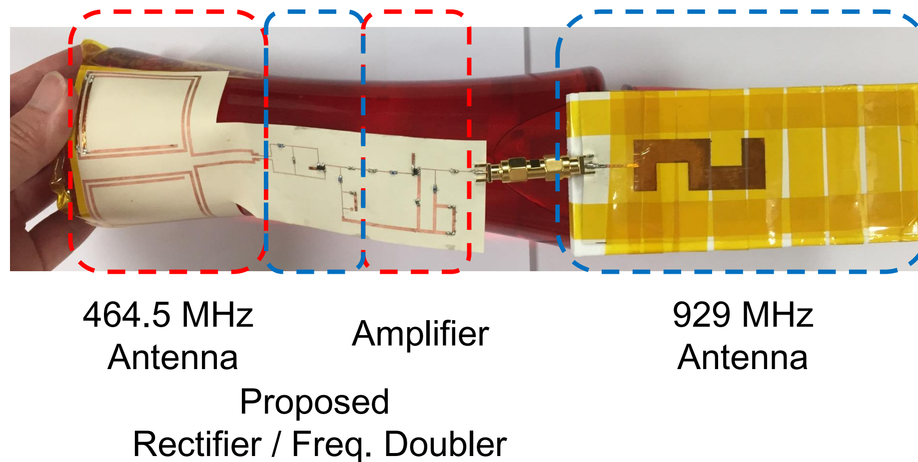


Figure 4.25: Prototype of the energy harvesting circuit with an RF amplifier.

of specific gases by measuring the change in oscillation frequency. Therefore, the resistor in the previous prototype as shown in Figure 4.18 was replaced with a printed ammonia sensor as depicted in Figure 4.23. The impedance of the ammonia sensor increases when it is exposed to ammonia gas and the oscillation frequency is expected to decrease due to the change of the impedance. Experimental results shown in subsection 4.5.4 confirm this assumption.

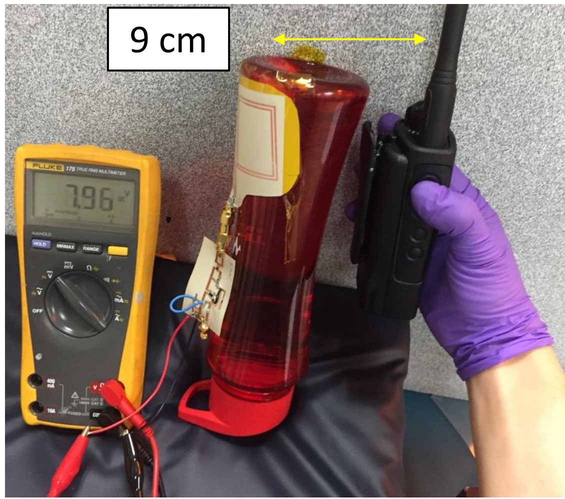


(a)

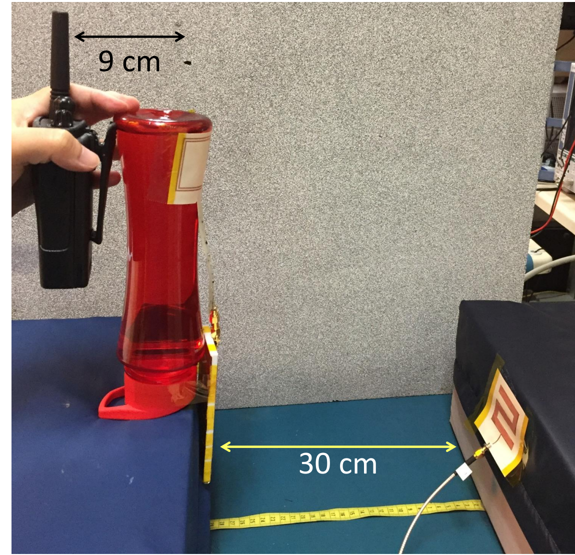


(b)

Figure 4.26: Experimental setup for the testing of the link budget for (a) measured 929 MHz power at the output of the rectifier/frequency doubler and (b) measured received 929 MHz power at the backscatter sensor antenna.

Table 4.2: The power levels for link budget estimation.

| Measured Condition | With Amplifier | Without Amplifier |
|---|---|---|
| 929 MHz at the output of the rectifier | 13.00 dBm | 2.27 dBm |
| Received 929 MHz at tag antenna | -16.54 dBm | -23.00 dBm |

## 4.5 System Field Operation Test

### 4.5.1 Received Power Level Test

The prototypes of the proposed energy harvester without and with an RF amplifier are shown in Figure 4.24 and Figure 4.25, respectively. To evaluate the performance and the link budget of the proposed energy harvester and the tag configuration, two experiments are performed. First, as shown in Figure 4.26a, the ambient RF source (two-way talk radio) is placed at a distance of 9 cm from the proposed energy harvester. The 929 MHz power levels at the output of the proposed rectifier/frequency doubler are measured using a spectrum analyzer. These are the power levels of the carriers and will be input into the

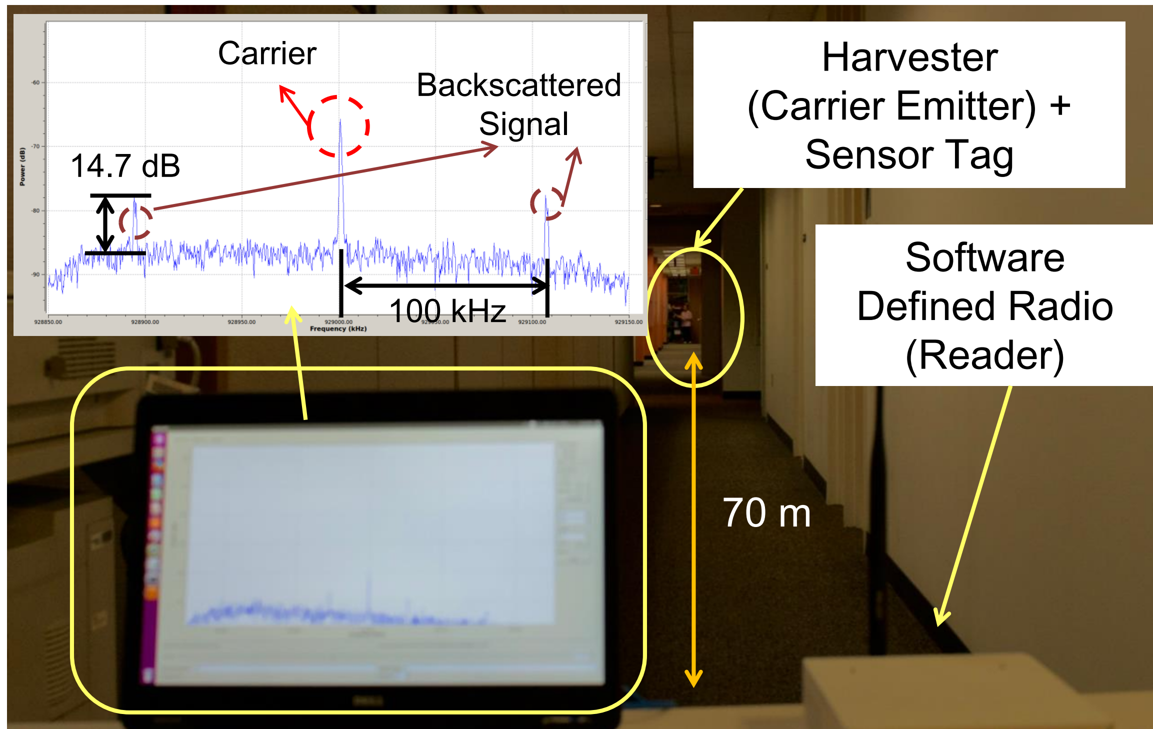


Figure 4.27: Measurement setup for the long-range on-body wireless sensing network.

re-emitting antenna to be radiated out as the carrier emitters. The measured 929 MHz power levels are 13 dBm for the one with the amplifier and 2.27 dBm for the one without the amplifier. Second, the two-way talk radio is placed at a distance of 9 cm from the proposed energy harvester and the antenna of the tag is put 30 cm away from the energy harvester as shown in Figure 4.26b. This experiment is used to evaluate the power level of the interrogating carrier at 929 MHz on the tag. The measured 929 MHz received power level by the antenna of the tag is -22.2 dBm and -16.5 dBm for topologies without and with the amplifier, respectively. The measured results are summarized in Table 4.2.

### 4.5.2 Operating Range Test

The measurement setup of the entire system is shown in Figure 4.27 and the energy harvester utilized is the one with an RF amplifier. The sampling frequency is 250 kHz and the number of Fast Fourier Transform samples is 1024. Thus, the frequency resolution of the

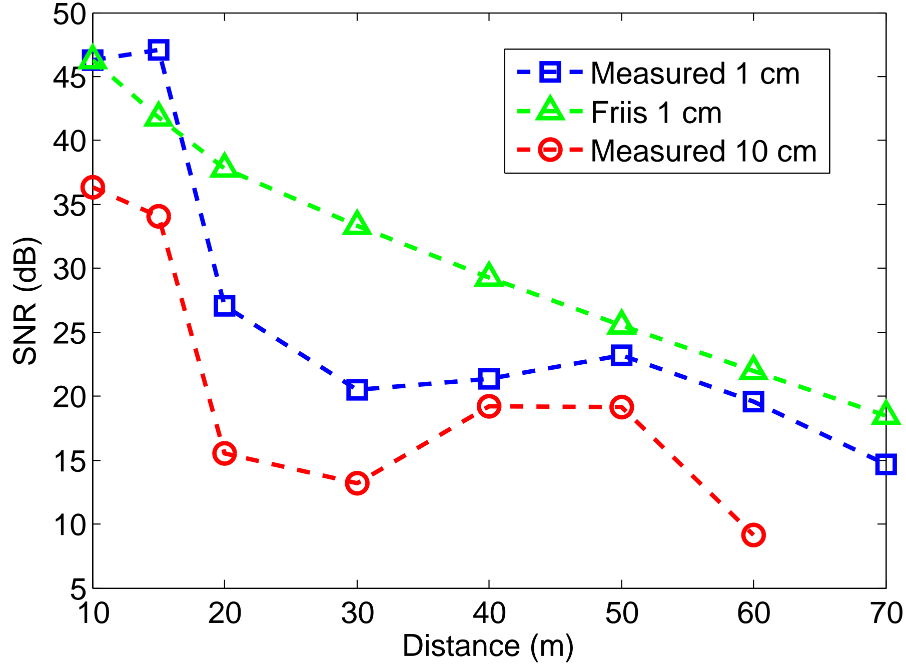


Figure 4.28: Measured signal to noise ratio at different distances.

Table 4.3: The performance comparison between the energy harvesters with and without an RF amplifier.

| | **With Amplifier** | **Without Amplifier** |
|---|---|---|
| Max. Distance Tag-EH | 80 cm | 10 cm |
| Max. Distance Reader-Tag | >70 m | 17 m |

software defined reader is about 244 Hz. Furthermore, Nyquist theorem states that

$$f_s \geq 2B \tag{4.1}$$

where $f_s$ is the sampling frequency and $B$ is the bandwidth. By (Equation 4.1), the bandwidth is about 125 kHz. The channel capacity can be calculated by the Shannon equation

$$C = Blog_2(1 + SNR) \tag{4.2}$$

where $C$ is the channel capacity and $B$ is the bandwidth. Thus, by (Equation 4.2), the channel capacity for the system while the distance between the reader and the tag is 70 m is about 0.6 Mb/s.

As depicted in Figure 4.27, three major spikes are detected by the software-defined reader. The center spike is the carrier and the other two spikes which are symmetric with respect to the carrier are the backscattered signals. Since the modulation frequency is 100 kHz, the distances between the carrier and the backscattered signals are also 100 kHz. The backscattering signals are not drastically affected by the noise generated by the two-way radio. The reason is that the only significant side-band noise from the radio which falls into the operating bandwidth occurs at 929 MHz. However, this is the same frequency as the carrier frequency and there would be no backscattering signals at that frequency. Both the proposed energy harvester with and without the amplifier are measured and the maximum distances between the tag and the proposed energy harvester and between the tag and the software-defined reader are summarized in Table 4.3. As shown in Table 4.3, with the help of the 929 MHz carrier emitted from the proposed energy harvester, the backscattered signal from the proposed sensor tag can be detected by the software-defined reader which is located at 17 m away. Moreover, if the DC power from the proposed energy harvester is utilized to drive the additional RF amplifier, as shown in Figure 4.14, and enhance the carrier emitter signals, the reading range can be significantly extended to 70 m as shown in the measurements. Furthermore, as shown in Figure 4.27, the backscattered signals are 14.7 dB above the noise floor, which means a 14.7 dB Signal-to-Noise Ratio (SNR). As the typically required SNR for detection is 3 dB, there is still a margin of 11.7 dB. According to Friis equation, this implies the reading range can be extended more than 3.8 times, i.e. more than 270 m. Similarly, as depicted in Table 4.3, the maximum distance between the tag and the energy harvester is also extended to 80 cm which is long enough to effectively cover all on-body backscattering sensor tags.

In order to investigate the effects of multipath and nearby clutters on the sensing range,

the SNR of the detected backscattering signals were measured while varying the distance between the reader and the tag and the distance between the proposed energy harvester and the tag. The indoor measured results are demonstrated in Figure 4.28. The horizontal axis is the distance between the reader and the tag. Two different distances (1 cm and 10 cm) between the proposed energy harvester and the tag were tested. Moreover, the theoretical results calculated using the Friis equation are also included for comparison. As shown in Figure 4.28, theoretically the SNR of the 10 cm case is 20 dB lower than 1 cm case. However, since the distance between the proposed energy harvester and the tag is not long, near-field coupling occurs that reduces the SNR drop due to increase distance. For the 1 cm case, the general trend is the same as the Friis equation. However, constructive interference occurs at 15 m and destructive interferences occurs at 20 , 30 , and 40 m. The general trend for the 10 cm case is similar to the 1 cm one. Thus, although the complex interferences due to multipath and ambient clutters cannot be accurately predicted, the Friis equation can serve as a good approximation to predict the SNR at even longer distances.

### 4.5.3 Multiple Tags Test

Since the proposed on-body wireless sensor network typically consists of multiple sensor tags, different modulation frequencies are assigned for each sensor tag to enable simultaneous multiple sensor detection. Therefore, the experimental setup shown in Figure 4.29 was used to demonstrate that multiple tags operating at different modulation frequencies can be detected by the reader at the same time. As shown in Figure 4.29, two tags are placed on the two sides of a sponge and interrogated with the carrier emitter (energy harvester). The software-defined reader is placed around 60 cm away from the tags. The measured results using the software-defined reader is shown in Figure 4.30. As demonstrated in Figure 4.30, two tags with different modulation frequencies (50 kHz and 100 kHz) were successfully detected simultaneously. Moreover, five spikes can be observed. The center spike is the carrier and the two symmetric spikes with 25 dB SNR which are located at 50 kHz away

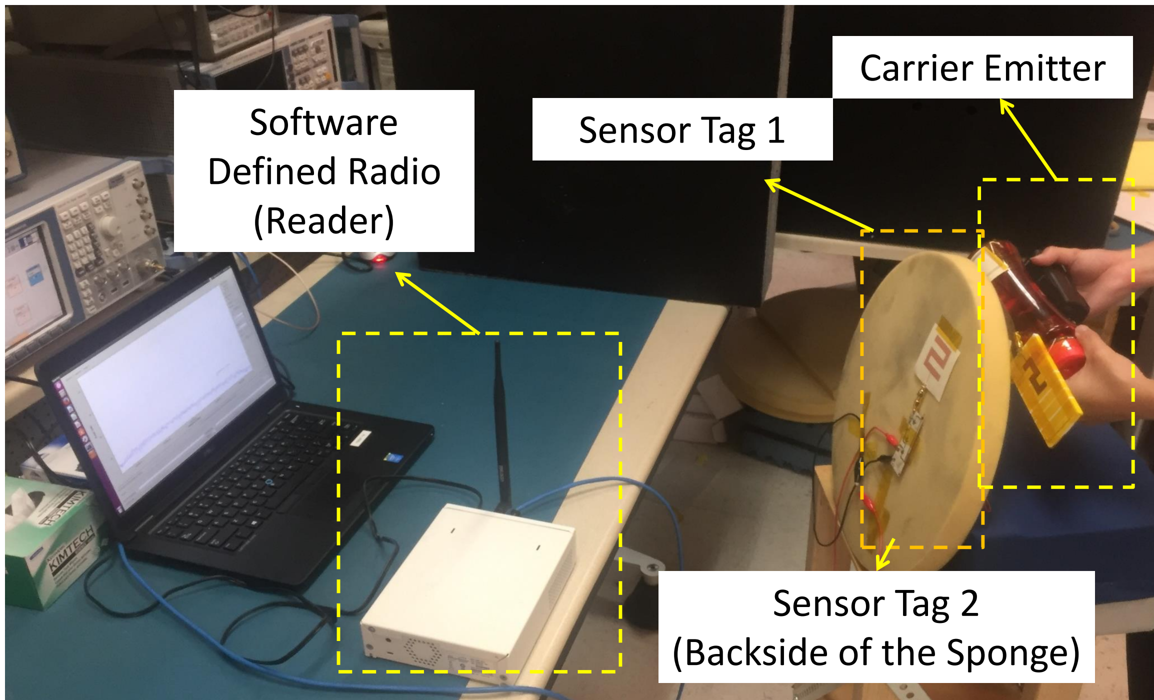


Figure 4.29: Measurement setup for the multiple sensors test.

from the carrier are the backscattered signals from the first tag. The remaining two spikes with 40 dB SNR which are located at 100 kHz away from the carrier are the backscattered signals from the second tag. The difference of the SNR values between the two tags is because the distance between "On" and "Off" resistances on the Smith chart as shown Figure 4.19 are different for two tags.

### 4.5.4 Ammonia Sensor Test

The backscattering tag that was integrated with the ammonia sensor is tested with the similar experimental setup shown in Figure 4.29. The only difference is that there is only one sensor tag and the tag is exposed to ammonia gas during the measurement. The measured results of the tag before and after being exposed to ammonia gas are shown in Figure 4.31 and Figure 4.32, respectively. As shown in Figure 4.31, the modulation frequency of the ammonia sensor tag is 50 kHz before the tag is exposed to the ammonia gas. The impedance of the ammonia sensor is increased after the ammonia gas exposure effectively

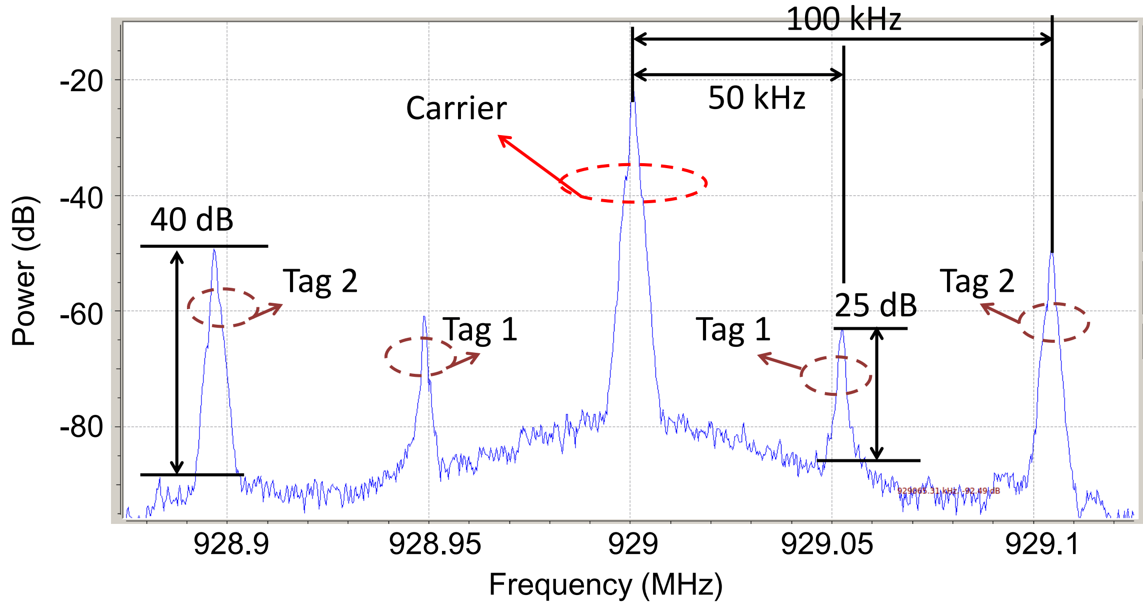


Figure 4.30: Measured result for multiple sensors test.

decreasing the modulation frequency (output oscillated frequency of the oscillator IC) to 7 kHz as shown in Figure 4.32. Due to the frequency change of the backscattered signals, the ammonia gas can be easily detected ("red/green detection") by processing the received data.

### 4.5.5 Comparison with Previous Works

The comparison between this work and previous related research efforts are shown in Table 4.4. As demonstrated in Table 4.4, reading ranges only up to around 10 m can be achieved by purely passive RFID tags. The reading ranges of the active RFID tags are larger than purely passive ones. For example, 46 m reading range is achieved in [83]. In [69], a very long (130 m) reading range is achieved utilizing semi-passive backscattering tags and carrier emitters. However, batteries are used in both tags and carrier emitters. The reading range of this work is much longer compared with other previous works listed in Table 4.4 except [69]. Compared with [69], the energy harvesting techniques utilized in this work support all energy requirements and enable a fully energy-autonomous system,

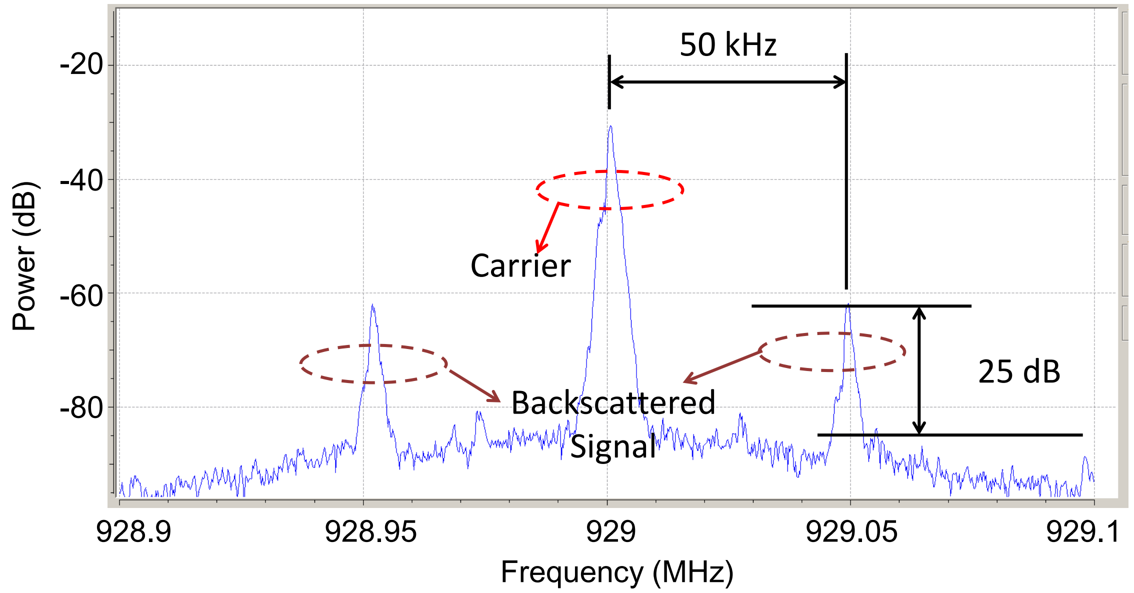


Figure 4.31: Measured result for the ammonia sensor tag before exposure to ammonia.

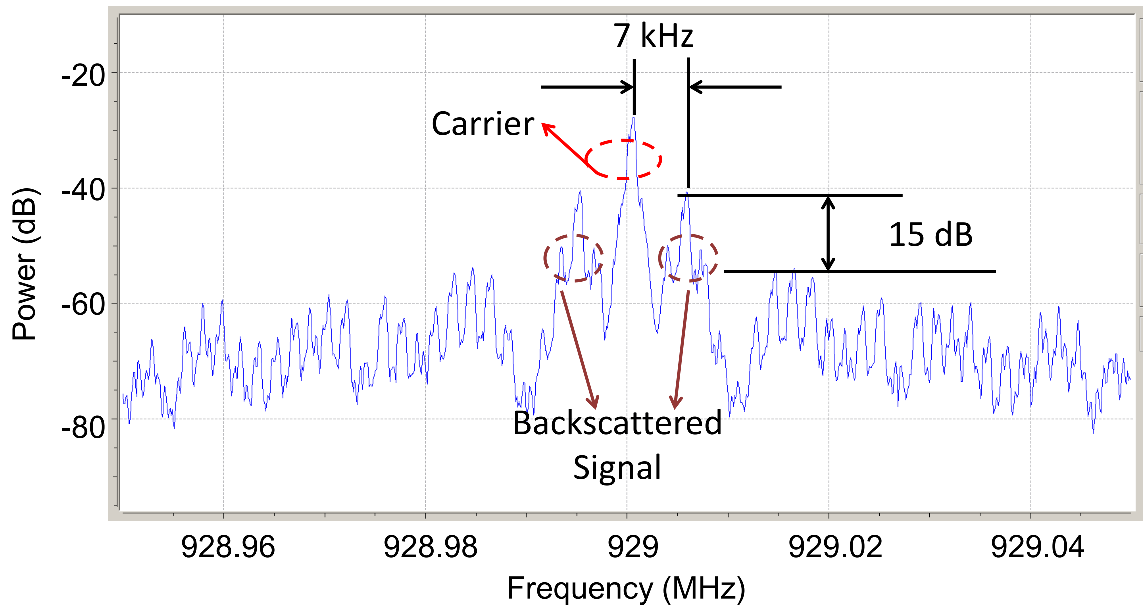


Figure 4.32: Measured result for the ammonia sensor tag after exposure to ammonia.

thus leading to much lower maintenance costs.

Table 4.4: The Comparison between this work and previous related works

| Work | Operating Frequency (MHz) | RFID Type | Energy for Tag | Energy for Carrier Emitter | Reading range(m) |
|---|---|---|---|---|---|
| [78] | 915 | Passive | Harvested | NA | 4 |
| [79] | 868 | Passive | Harvested | NA | 6 |
| [80] | 900 | Passive | Harvested | NA | 9 |
| [81] | 865 - 870 | Passive | Harvested | NA | 14 |
| [82] | 34450 | Active | Battery | NA | 11.5 |
| [83] | 308 | Active | Battery | NA | 46 |
| [69] | 867 | Semi-passive + Carrier Emitter | Battery | Battery | 130 |
| **This Work** | 929 | Passive + Carrier Emitter | Harvested | Harvested | 70 |

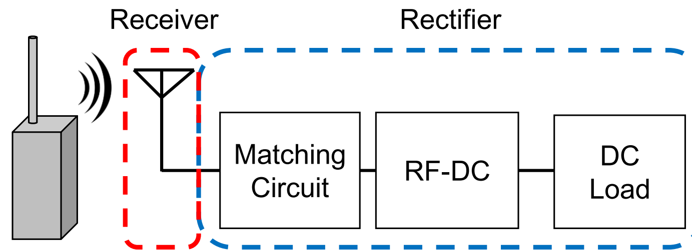


Figure 4.33: The block diagram of the wearable energy harvesting system.

## 4.6 Design Process Including Human Tissue Effects

Harvesting energy from hand-held devices normally involved near-field coupling which can not be estimated using the Friis equation. Furthermore, the human body will have huge impacts on the receiving antenna and has to be include while designing and simulating. Therefore, a new design and simulation process is necessary to estimate the received power. In this section, a simulation process that can estimate the power transfer efficiency for the receiving antenna, predict the optimal matching impedance for the rectifier, and consider the human body effects is proposed. Two types of rectennas using an E-field coupling or an H-field coupling receiving antennas are proposed and the block diagram is shown in Figure 4.33. This simulation process can be used to improve the design proposed

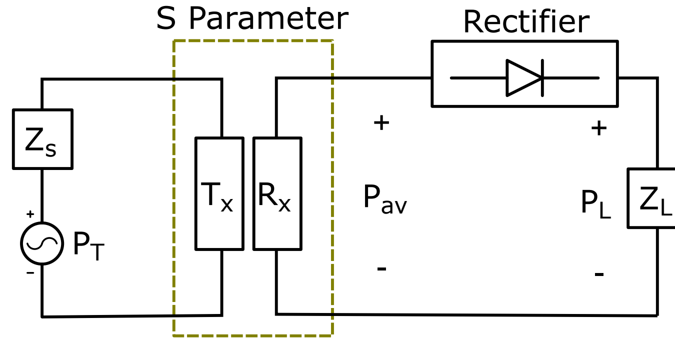


Figure 4.34: The circuit model of the energy harvester.

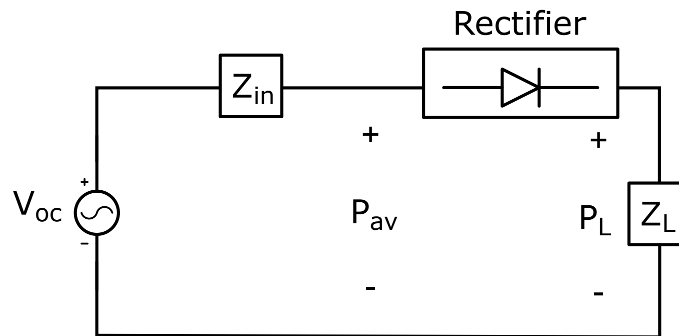


Figure 4.35: The equivalent Thevenin circuit model of the energy harvester.

in subsection 4.1.2 and take the human body effects into consideration.

### 4.6.1 Simulation Process

*Full Simulation Process to Estimate Harvested Power*

The circuit model of the energy harvester is shown in Figure 4.34. The $P_T$ is the transmitted power, $P_{av}$ is the maximum RF available power received at the receiver, and $P_L$ is the rectified DC power measured at the load. The $Z_s$ is the source impedance and the $Z_L$ is the load impedance. The Tx and Rx are the transmitting antenna and receiving antenna, respectively. Assuming the scattering parameters between Tx and Rx can be obtained. One way to simplify the circuit model is building the equivalent Thevenin circuit at the receiving side as shown in Figure 4.35. The receiving antenna can be replaced with the open-circuit voltage source and input impedance, $Z_{in}$. As long as we can find these values, we can derive

the following results

$$Zin = R + jX \tag{4.3}$$

$$P_{av} = \frac{|V_{oc}|^2}{8R} \tag{4.4}$$

$$\eta_{RF} = \frac{P_{av}}{P_T} \tag{4.5}$$

$$\eta_{RF-DC} = \frac{P_L}{P_{av}} \tag{4.6}$$

where R is the real part of the input impedance, X is the imaginary part of the impedance, $\eta_{RF}$ is the RF power transfer efficiency from the transmitter to the receiver, and $\eta_{RF-DC}$ is the rectifier RF-DC efficiency. Furthermore, the maximum available power $P_{av}$ is obtained while complex conjugate matching is achieved. Thus, the matching circuit of the rectifier has to make the input impedance of the rectifier become

$$Zin^* = R - jX \tag{4.7}$$

The flow chart of the energy harvester simulation process is summarized in Figure 4.36. The first step is to simulate the 2-port scattering parameters of the transmitter and receiver antenna in HFSS. The effects of human body effects are taken into consideration in this step and will be discussed in detailed in subsubsection 4.6.1. Then the 2-port scattering parameters are import into ADS and the harmonic balance simulator is used to obtain the open-circuit voltage as demonstrated in Figure 4.37. As an example, a 4 W input power at 464.5 MHz is used as the source and the open-circuit voltage is obtained using the full-wave simulated 2-port scattering parameters. The result is shown in Figure 4.37b. Once the value of open-circuit voltage is obtained, the next step is to find the $Z_{in}$ which is the input impedance of the receiving antenna by Thevenin theorem. Assuming port 1 is the transmitting port and port 2 is the receiving port, $Z_{in}$ can be calculate using $S_{22}$ as the

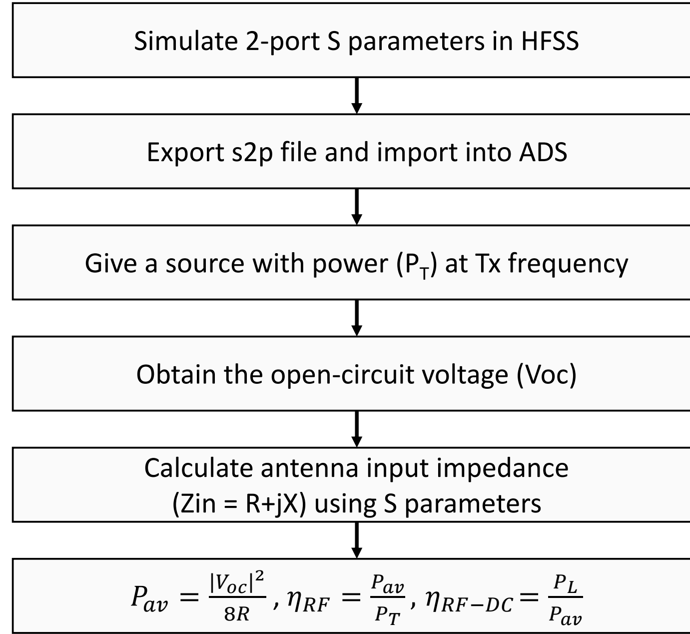


Figure 4.36: The flow chart of energy harvester simulation and the output power estimation.

following

$$Zin = Z_0 \frac{1 + S_{22}}{1 - S_{22}} \tag{4.8}$$

where $Z_0$ is the reference impedance and normally is $50\,\Omega$. Then the maximum available power, RF efficiency, and RF-DC efficiency can all be obtained as shown in Figure 4.36.

*Two-way Talk Radio Model and EM Fields*

The two-way talk radio simulation model is built in HFSS as shown in Figure 4.38a. The simulated and measured $S_{11}$ are compared in Figure 4.38b. The good matching below -10 dB is obtained at 464.5 MHz. Besides, good agreements between the simulated and measured results can be observed. Hence, this model will be used for the 2-port S-parameter simulation in the following content. The E-field and H-field distributions around the two-way radio are shown in Figure 4.39 and Figure 4.40, respectively. The field distributions are helpful to determine the positions and structures of the E-field coupling and H-field coupling receiving antennas.

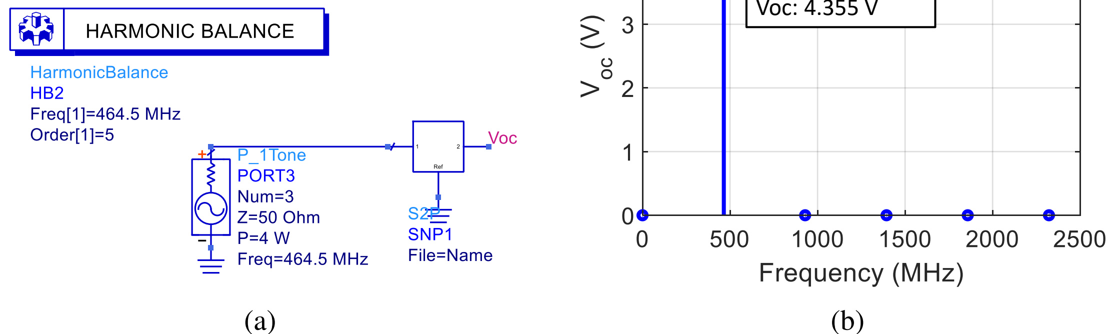


Figure 4.37: (a) The harmonic balance setup in ADS and (b) the simulated open-circuit voltage.

*Human Model Simulation*

In order to include the human body effects into the simulation, the human model is built. Furthermore, to reduce the simulation time, the homogeneous human model is adopted. Both the relative permittivity and conductivity are set to 2/3 of the values of muscle to accurately mimic the human tissue [84]. At 464.5 MHz, the relative permittivity is set to 33.67 and the conductivity is 0.436 S/m. Provided by human phantom company, Schmid & Partner Engineering AG (speag), the relative permittivity and conductivity of their homogeneous human phantom are 33.9 and 0.43 S/m at 450 MHz, respectively. The value used in simulation and the values provided by human phantom are very close to each other which proves setting values to 2/3 of the values of muscle is correct. Only the human hand and wrist are included in the simulation since the wearable energy harvester is worn on the wrist and the two-way radio is holding in the hand.

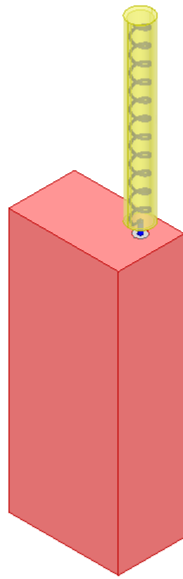

(a)

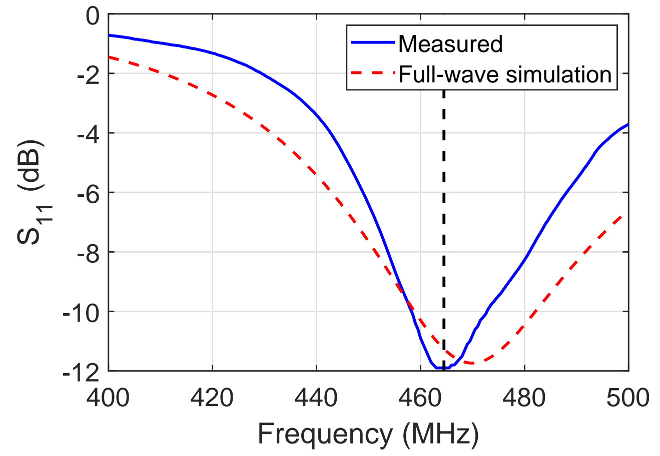


(b)

Figure 4.38: (a) Two-way talk radio model in HFSS and (b) Measured $S_{11}$.

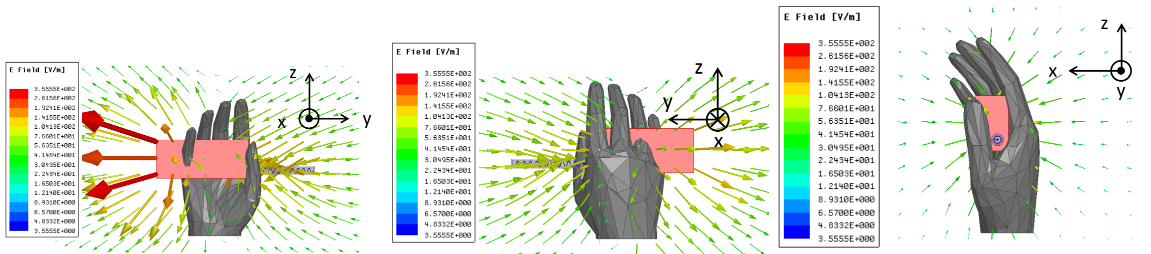

(a) (b) (c)

Figure 4.39: The electric field around the two-way radio on (a) front view (b) back view and (c) side view.

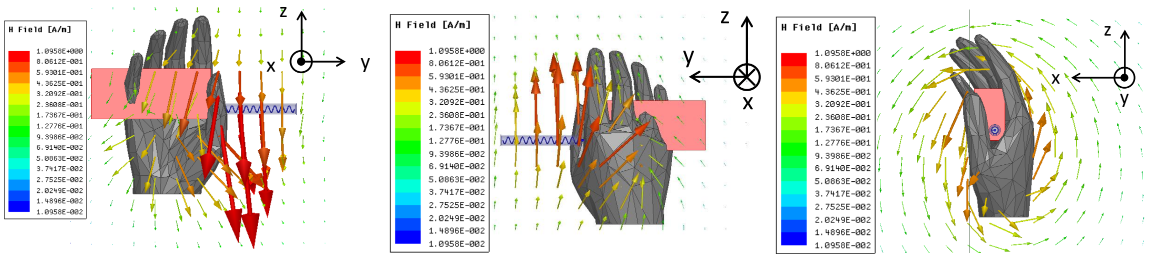

(a) (b) (c)

Figure 4.40: The magnetic field around the two-way radio on (a) front view (b) back view and (c) side view.

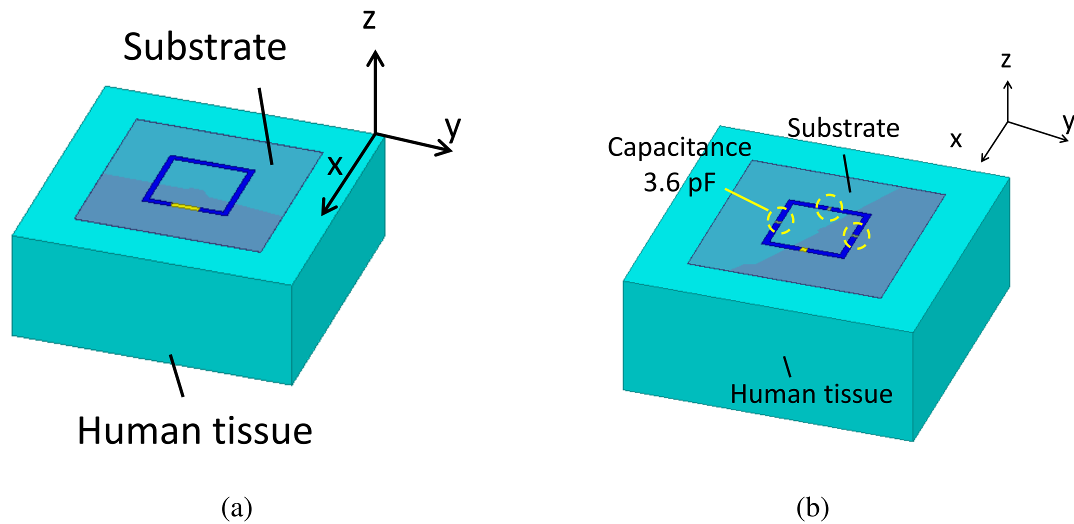


Figure 4.41: (a) Loop type wearable receiving antenna and (b) Segmented loop type wearable receiving antenna.

### 4.6.2 Receiving Antenna

*Design and Simulation*

Two different near-field coupling antennas are designed to receive the power from two-way radio as shown in Figure 4.41. For the electric-coupling receiving antenna, a quarter-wave loop antenna is adopted as shown in Figure 4.41a. The size is 45.625 mm × 45.625 mm. Generally, a full-wave loop is used to provide high radiation efficiency. However, as the loop size becomes larger, the loss due to human tissue becomes larger as well. Therefore, after the trade-off between the coupling efficiency and loss, a quarter-wave loop antenna is adopted. Since it is an E-coupling antenna and the E-field around the radio is depicted in Figure 4.39, the monopole-shape whip antenna of the radio needs to be oriented along the z-axis in Figure 4.41a to achieve the largest coupling factor.

Another magnetic-coupling segmented loop antenna is also used for comparison as shown in Figure 4.41b. The size is 37.5 mm × 37.5 mm. Furthermore, three 3.6 pF capacitors are embedded inside the loop to unify the current distribution and mimic a small loop antenna. Since it is an H-coupling antenna and the H-field around the radio is depicted

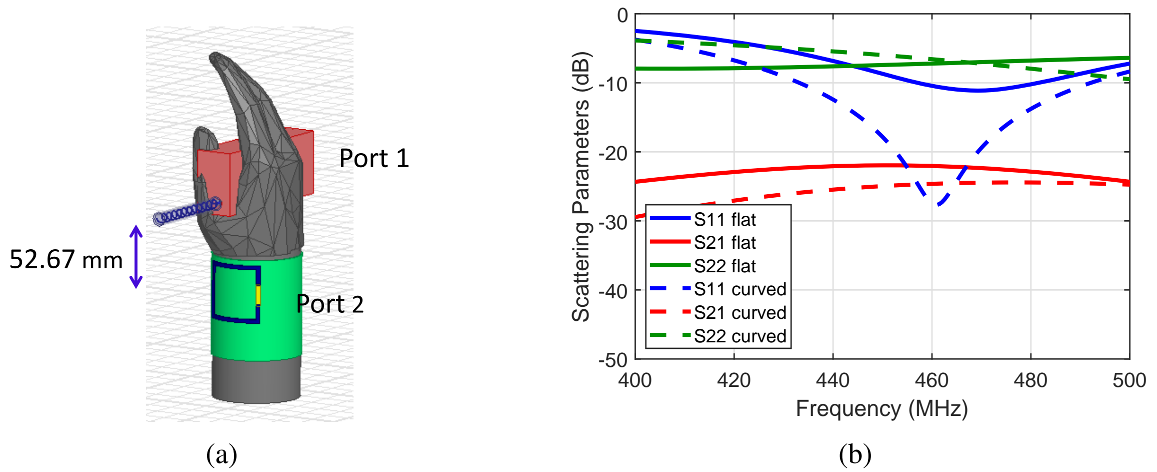


(a) (b)

Figure 4.42: (a) Simulation model for the loop antenna, two-way radio, and human hand and (b) Simulated scattering parameters.

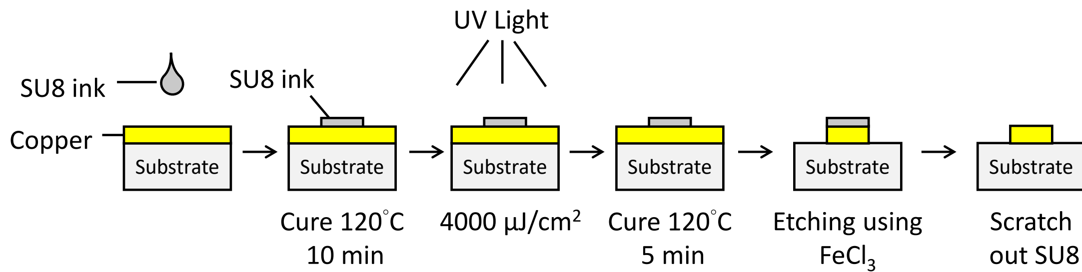


Figure 4.43: Fabrication process using inkjet printed masks.

in Figure 4.40, the monopole-shape whip antenna of the radio needs to be oriented along the y-axis in Figure 4.41b to achieve the largest coupling factor. Both antennas are placed on Rogers Liquid Crystalline Polymer (LCP) and then on a big block of human tissue with dielectric constant 33.67 and conductivity 0.436 S/m. The curved loop antenna on the wrist is also simulated to compare with the flat condition. The final simulation model is shown in Figure 4.42a and the simulated S-parameters are shown in Figure 4.42b. There is a slight difference between the results under flat and curved conditions.

*Fabrication and Measurement*

Both receiving antennas are fabricated with an inkjet-printed masking process and the fabrication steps are shown in Figure 4.43. The copper-clad LCP is used as the substrate. The

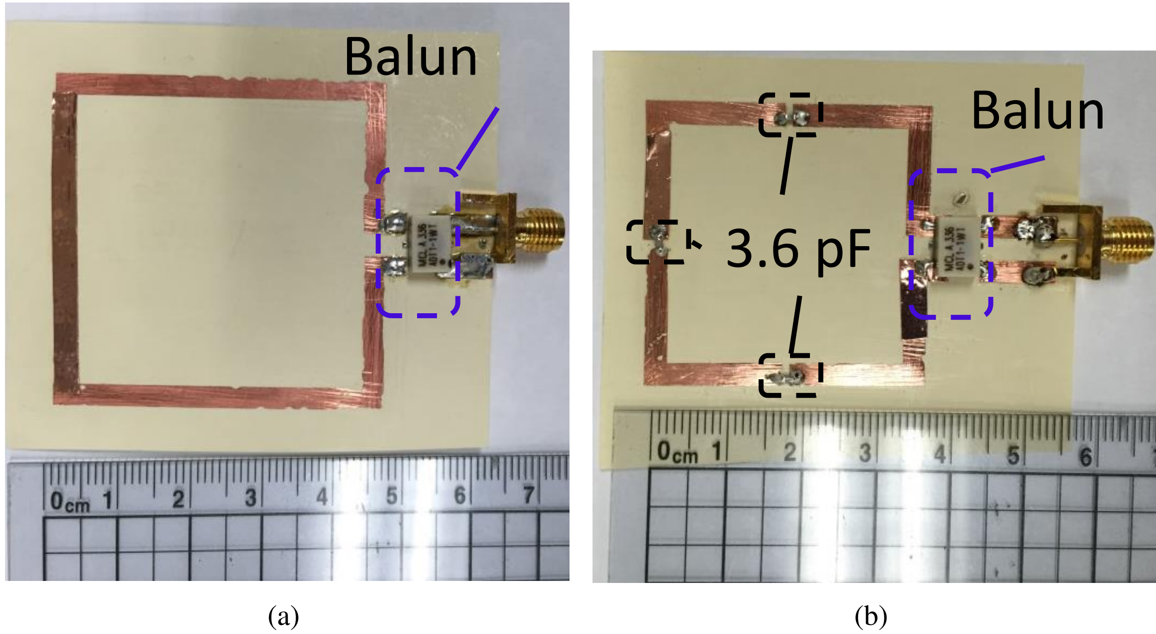


(a) (b)

Figure 4.44: Fabricated prototypes of the (a) loop antenna and (b) segmented loop antenna.

SU-8 ink from MicroChem is used to inkjet print the mask pattern and then cured under UV light. Then the sample is soaked into $FeCl_3$ to remove the copper. Finally, the SU-8 is removed with acetone. The fabricated prototypes are shown in Figure 4.44 and baluns are included.

The simulation model and the measurement setup for the loop antenna are shown in Figure 4.45a and Figure 4.45b, respectively. The antenna of the two-way radio is connected to VNA port 1 and the loop antenna is connected to VNA port 2. The distance between them is 52.67 cm. The measured S parameters are shown in Figure 4.46. The simulated results are also included for comparison and a good agreement can be observed. There is a slight frequency shift on the $S_{11}$ which is the two-way radio antenna because only the antenna is measured without the body of the two-way radio. However, good matching is still obtained.

The segmented loop is also measured and the respective simulation model and measurement setup are shown in Figure 4.47a and Figure 4.47b, respectively. Compared with Figure 4.45b, the relative location between the receiving antenna and two-way radio antenna

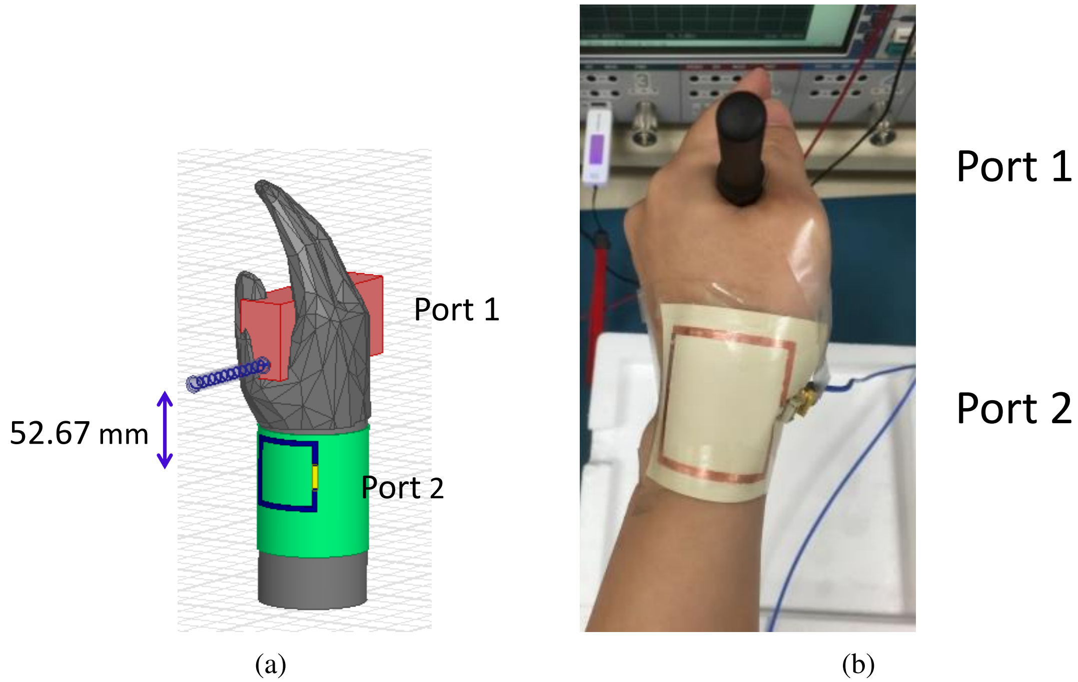

(a) (b)

Figure 4.45: The (a) simulation model and (b) measurement setup of the loop antenna.

Table 4.5: The measured results for loop and segmented loop antenna while transmitter and receiver distance is 5 cm.

| | **Loop** | **Segmented Loop** |
|---|---|---|
| Voc | 3.78 V | 4.33 V |
| Antenna Zin | 33.57-40.02j Ω | 66.68+58.04j Ω |
| Available Power | 53.2 mW | 35.1 mW |

are different because the loop antenna is E-coupling based and the segmented loop antenna is H-coupling based antenna. The distance is 52.47 mm and the measured S parameters are shown in Figure 4.48. The simulated results are also included for comparison and a good agreement can be observed. There is a small $S_{11}$ frequency shift as shown in Figure 4.46 because of the same reason.

The Thevenin parameters, open-circuit voltage, and input impedance are obtained using the process in Figure 4.36 and the measured S parameters. The results are summarized in Table 4.5. Although the open-circuit voltage of the loop antenna (3.78 V) is smaller than the segmented loop antenna (4.33 V), the real part of the antenna input impedance of the

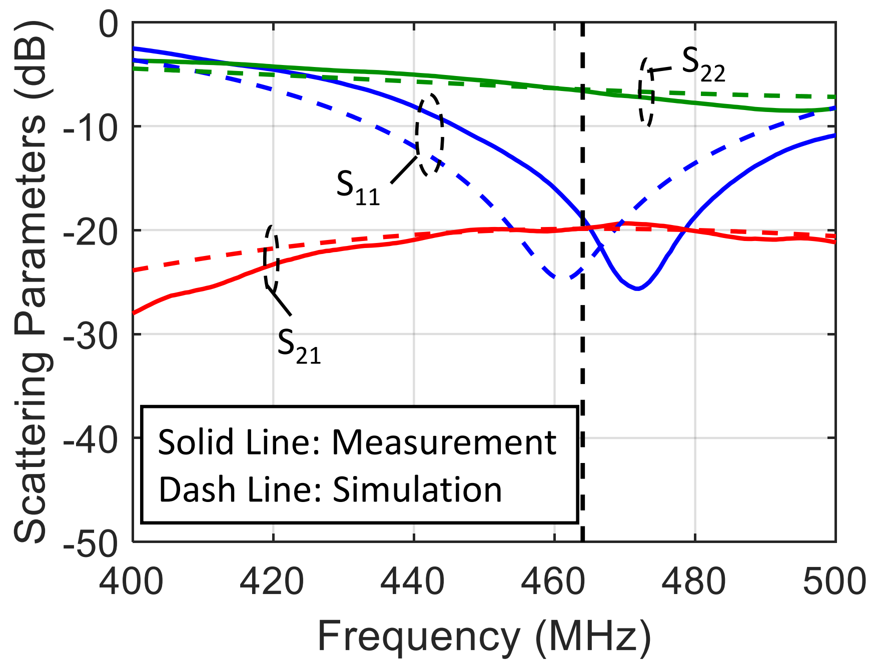


Figure 4.46: Measured scattering parameters of the loop antenna.

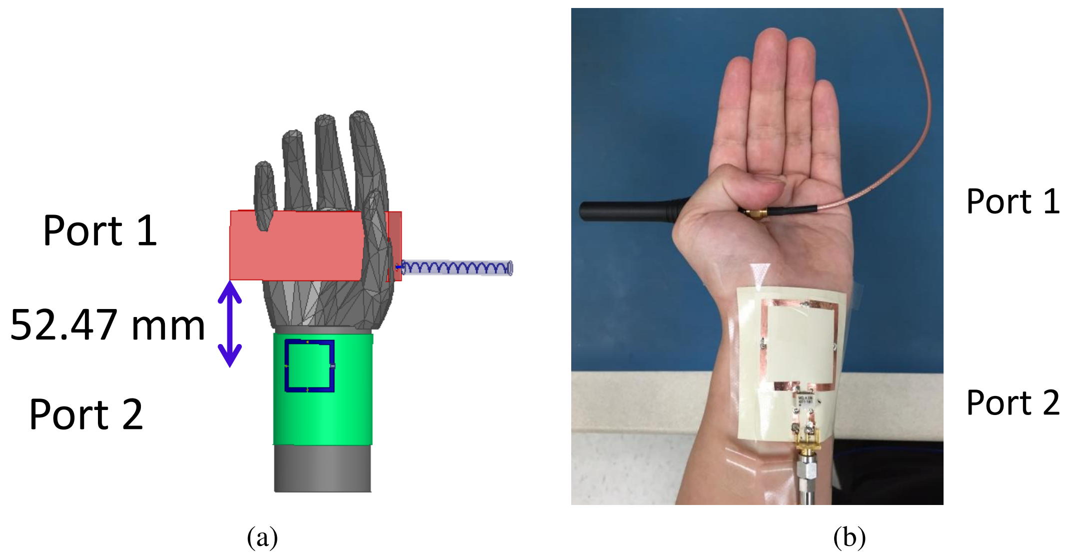


(a) (b)

Figure 4.47: The (a) simulation model and (b) measurement setup of the segmented loop antenna.

loop antenna (33.57 Ω) is also smaller than the segmented loop antenna (66.68 Ω). Under 5 cm and this angle orientation, the maximum available power for the loop antenna is 53.2 mW which is larger than the segmented loop antenna which is 35.1 mW.

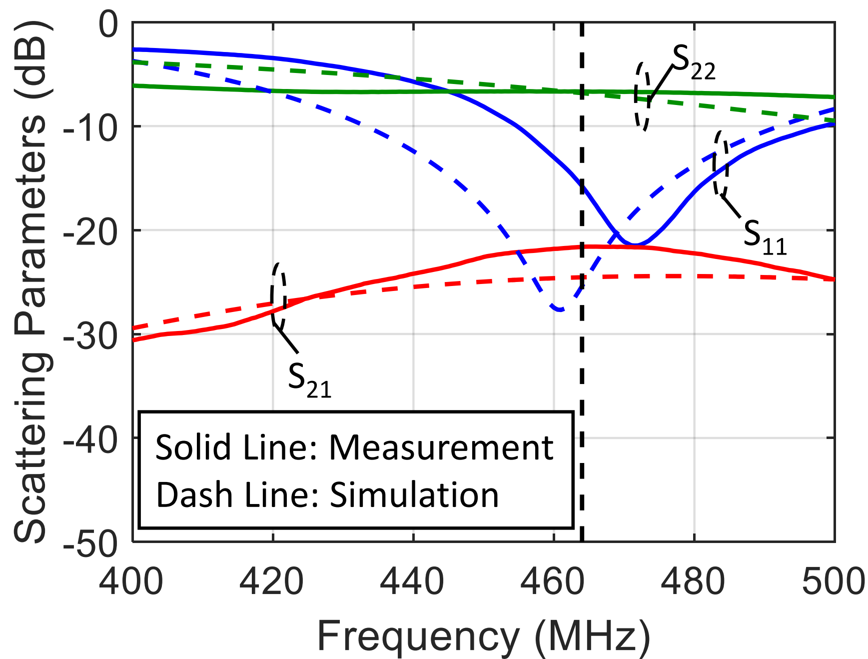


Figure 4.48: Measured scattering parameters of the segmented loop antenna.

*Dynamic Measurement*

In order to determine whether active matching is required under conditions of different angles and distances due to the motion of the hand, the dynamic measurement under different angles and distances are performed. The dynamic measurements under different distances are shown in Figure 4.49a. Since port 2 is connected to the receiving antenna, the smith chart results show that the input impedance of the receiving antennas. As shown in Figure 4.49a, the changes in the input impedance due to different distances are very small. Furthermore, the maximum available power, $P_{av}$, which defined in Figure 4.35 and derived using the measured data under different distances are summarized in Figure 4.49. Two different loads are included for comparison. The first one is the optimal load derived by measured S parameters at different distances. The second one is the fixed load at the optimal load while the distance is 5 cm. As shown in Figure 4.49, the available powers are almost the same for the optimal and the fixed load. Therefore, for different distances, active matching which actively changing the matching circuit to meet the optimal load is not

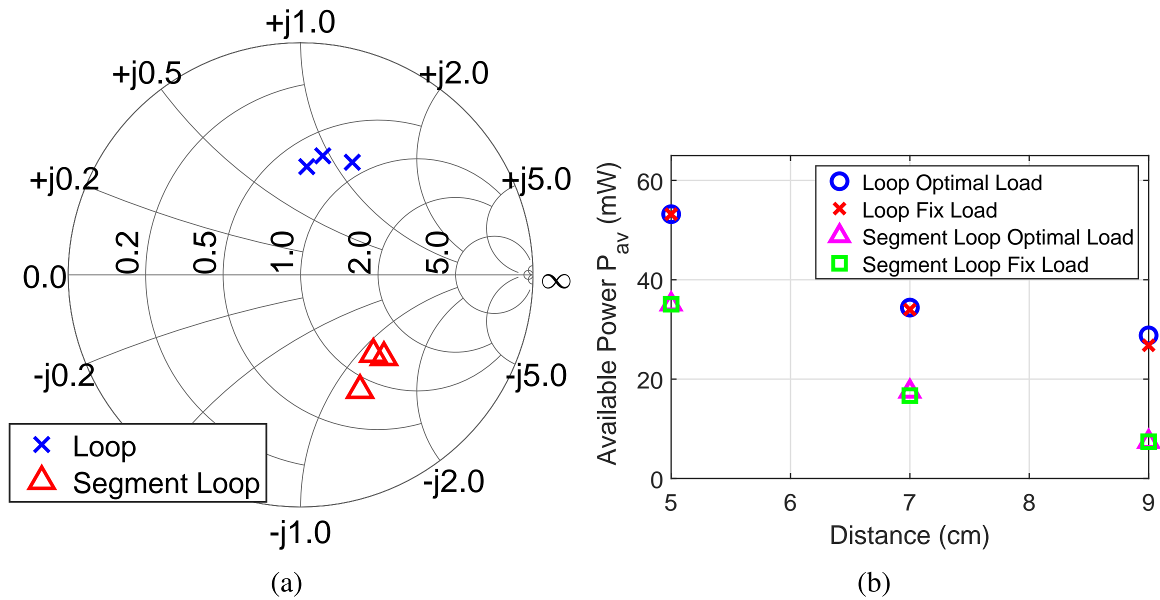


Figure 4.49: The measured (a) $S_{22}$ and (b) received power under different distances.

necessary.

In addition to different distances, different angles are also measured. The angle definition is defined in Figure 4.50. The measured results are shown in Figure 4.51. The measured input impedances do not change significantly due to different angles. Thus, the input impedances of the receiving antennas are similar and thus, active matching is not required.

*Verification of The Proposed Simulation Process*

In order to verify the simulation process proposed in Figure 4.36, both open-circuit voltages of the loop and segmented loop antenna are measured. The simulation setup is shown in Figure 4.52. The loop and segmented loop antenna are open-circuited and connected to the oscilloscope. The two-way radio is located at 7 cm away and turns on to emitting power. The measured open-circuit voltages are demonstrated in Figure 4.53. The 464.5 MHz open-circuit voltages are 3.04 V and 2.45 V for the loop and segmented loop, respectively. The simulated S parameters obtained using HFSS are import into ADS to extract the open-circuit voltages as described in Figure 4.36. The simulated results are 3.16 V

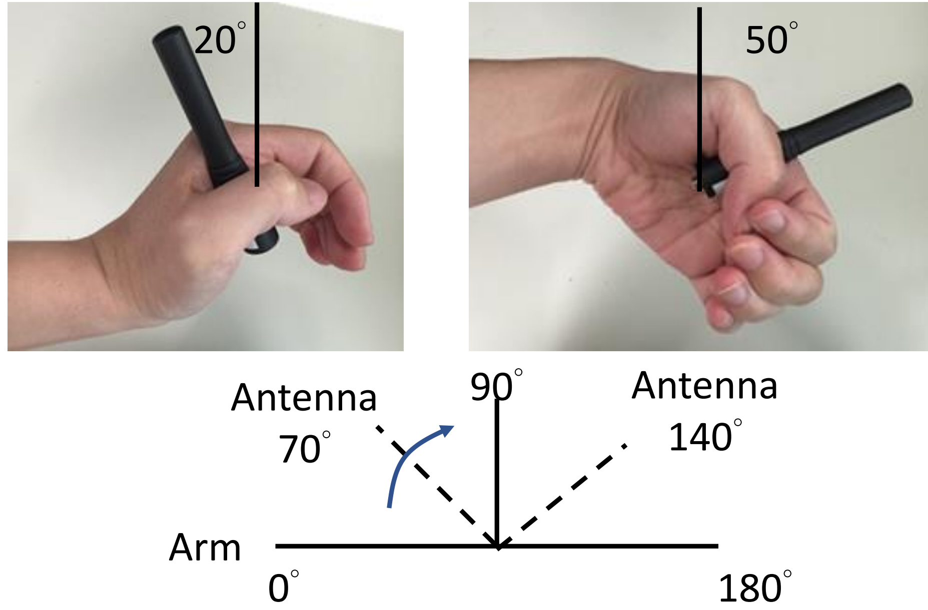


Figure 4.50: The angle definition for the dynamic motion measurement.

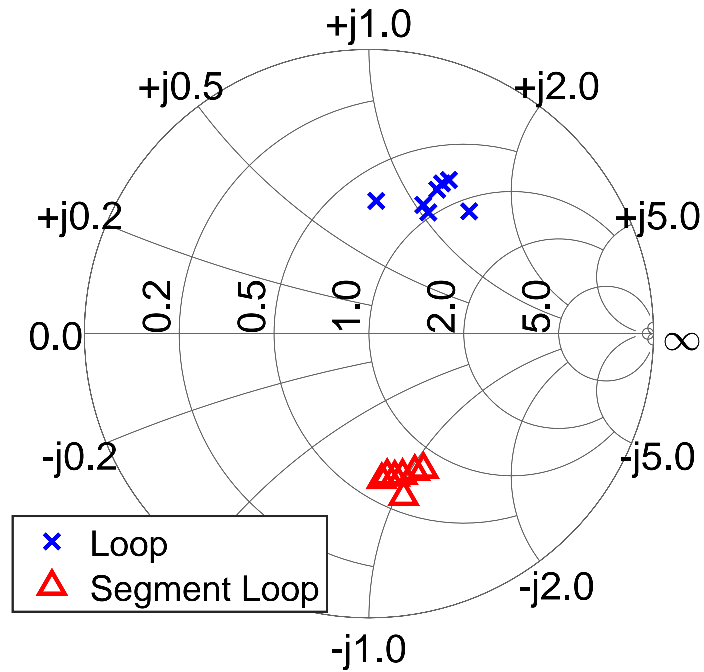


Figure 4.51: The measured $S_{22}$ under different angles.

and 2.44 V for the loop and segmented loop, respectively. The input impedances are also extracted from both the simulation and measurement and maximum available powers are calculated. All results are summarized and compared in Table 4.6. As shown in Table 4.6,

(a)

(b)

Figure 4.52: The measurement setups of the open-circuit voltages for the (a) loop antenna and (b) segmented loop antenna.

Table 4.6: The comparison between simulated and measured results for loop and segmented loop antenna while transmitter and receiver distance is 7 cm.

| | **Loop** | **Segmented Loop** |
|---|---|---|
| Simulated Voc | 3.04 V | 2.45 V |
| Measured Voc | 3.16 V | 2.44 V |
| Voc Error | 3.8 % | 0.4 % |
| Simulated Pav | 34.40 mW | 17.52 mW |
| Measured Pav | 37.00 mW | 17.30 mW |
| Pav Error | 7.0 % | 1.3 % |

the errors between the simulated and measured open-circuit voltage (Voc) are smaller than 3.8% while the errors of maximum available power (Pav) are smaller than7 %. This can serve as proof that the simulation process with human tissue is accurate and can be used to evaluate the design of near-field coupling wearable energy harvesting.

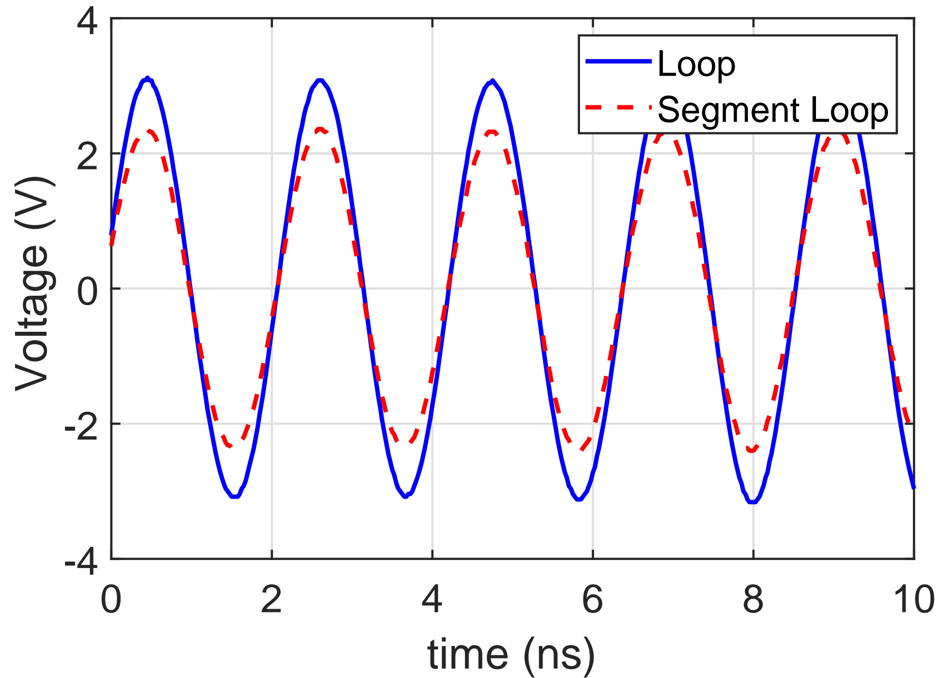


Figure 4.53: The measured waveforms of open-circuit voltages.

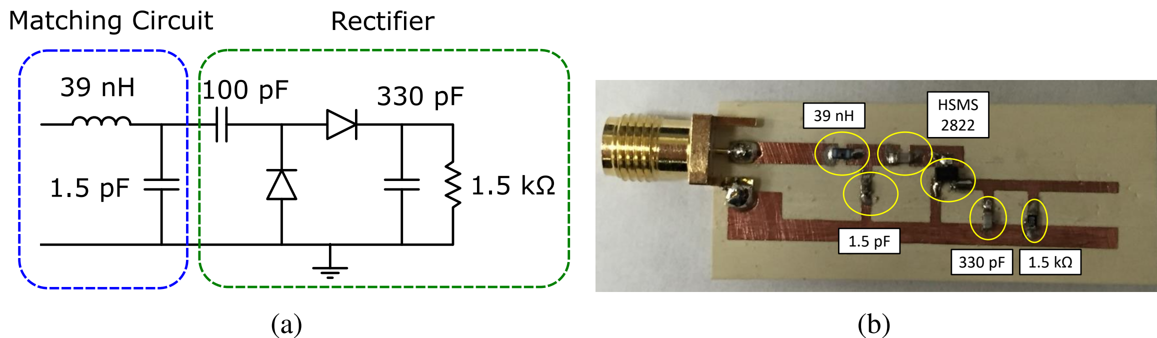


(a) (b)

Figure 4.54: (a) The circuit model of the rectifier and (b) The fabricated prototypes.

### 4.6.3 Rectifier Design

Once the receiving antenna designs are finished, the next step is to design the rectifier. The circuit diagram of the rectifier is shown in Figure 4.54a and the fabricated prototype is shown in Figure 4.54b. The matching circuit is composed of a 39 nH inductor and a 1.5 pF capacitor. For the rectifier design here, the purpose of the matching circuit is to match the rectifier to 50 Ω for measurement. However, while in the rectenna design, different sets of matching circuits are used to match the rectifier to the complex conjugate of the impedance

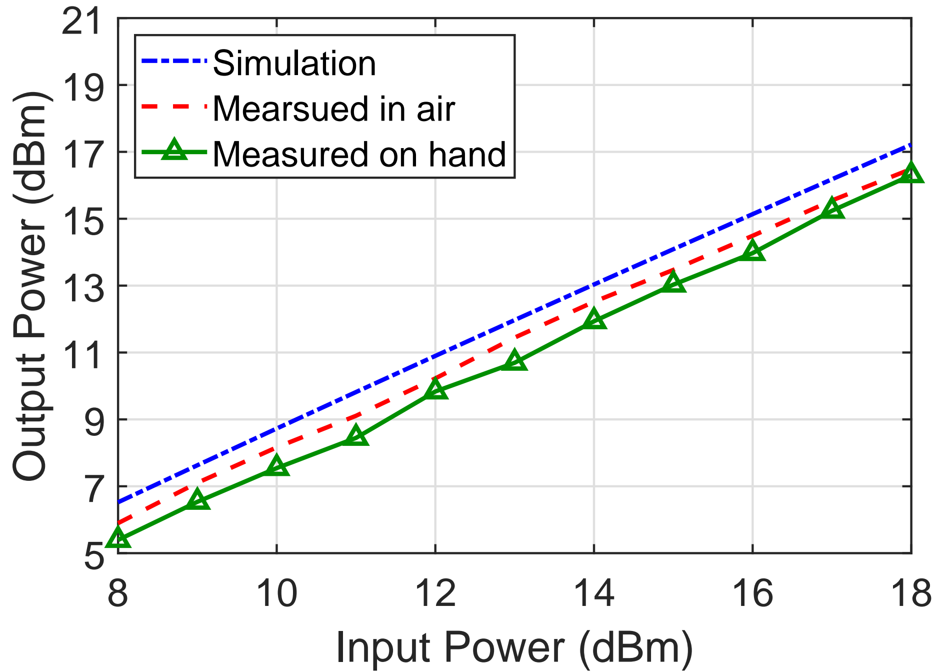


Figure 4.55: The measured output powers from the rectifier.

of the receivers as mentioned in subsection 4.6.1. The rectifier is composed of a voltage doubler using HSMS2828 Schottky diodes and the load is a 330 pF capacitor for removing higher-order harmonics and a 1.5 kΩ resistor. The simulated and measured results of the output powers with different input powers are shown in Figure 4.55 and the maximum DC conversion efficiency is about 68 % while the input power is 18 dBm. Moreover, the effects of the human hand on the rectifier are also taken into consideration. The output powers while measuring on hand are slightly smaller compared with measuring in air. However, they are all very close to the simulated results.

#### 4.6.4 Energy Harvesting Rectenna Measurement

The prototypes of the rectennas by combining the proposed receiving antennas and rectifiers are shown in Figure 4.56. The matching circuits are adjusted to match the input impedance of the respective receiving antennas which are extracted using the measured S parameters of the antennas. Furthermore, the output powers, $P_L$ in Figure 4.35, under different orientations are measured and the results are shown in Figure 4.58. The angle defi-

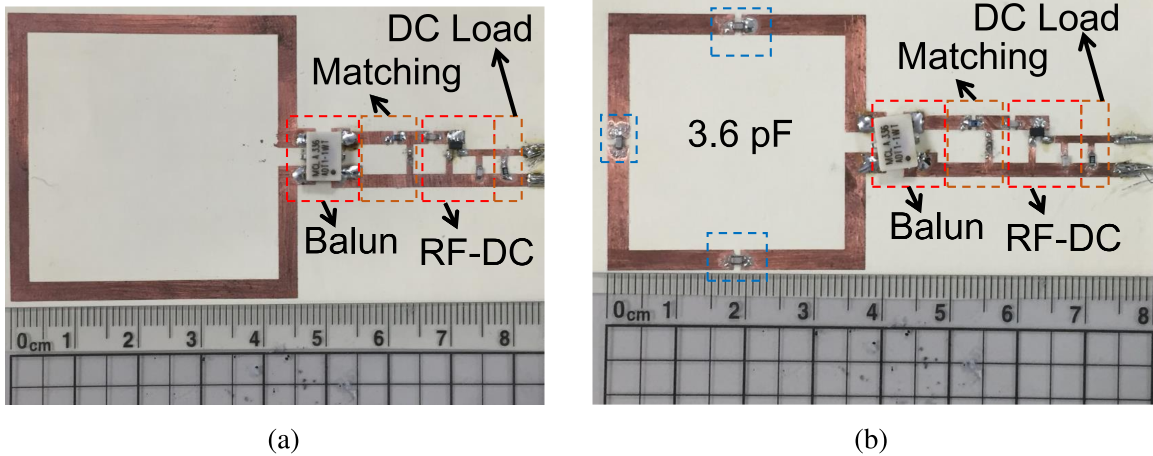


(a) (b)

Figure 4.56: The prototypes of the rectenna with the (a) loop and (b) segmented loop receiving antenna.

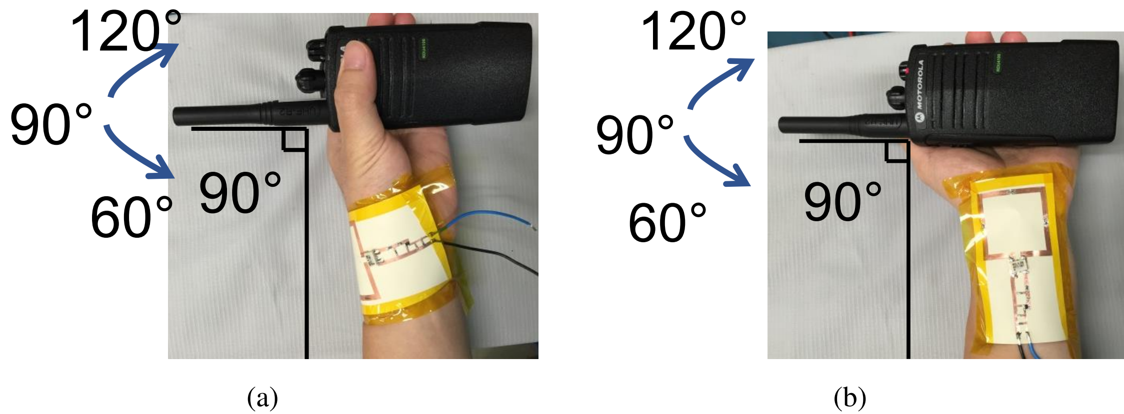


(a) (b)

Figure 4.57: The definition of angles for dynamic measurements of (a) loop rectenna and (b) segmented loop rectenna.

nitions of different types of rectennas are shown in Figure 4.57. As shown in Figure 4.58, the output power of the loop type rectenna will change significantly with the angle and it is larger at smaller angles. On the other hand, the segmented loop rectenna is relatively stable when the orientation angle changes. The reason is that the segmented loop rectenna is an H-field coupling type and the H fields do not change significantly while adjusting the orientation angle.

The measured performances are summarized in Table 4.7. The 110° is also included since it is the most comfortable angle for the hand position. As shown in Table 4.7, the

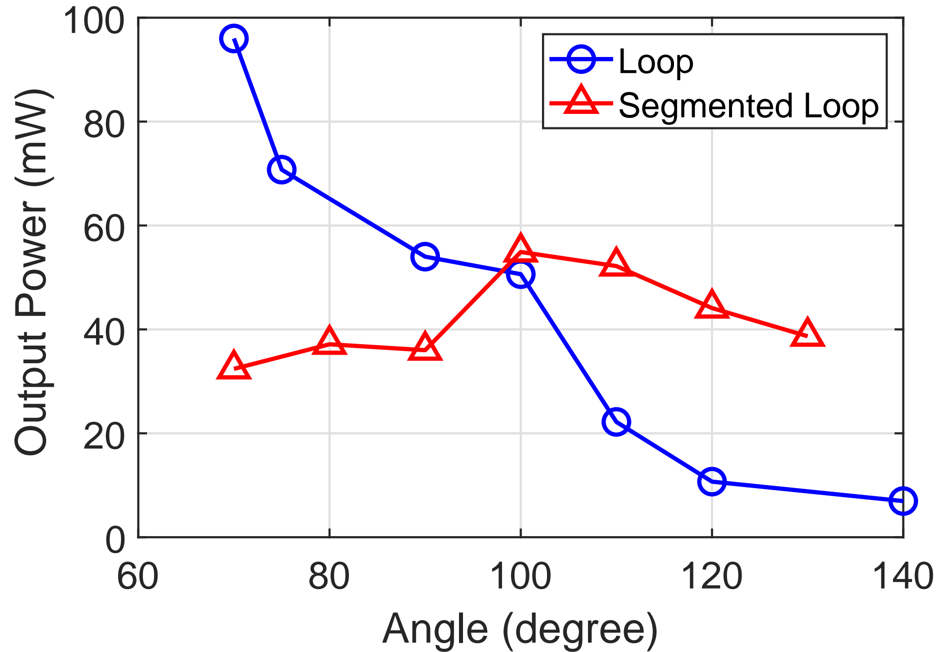


Figure 4.58: The measured output power at different angles.

Table 4.7: The measured output voltage, power, and efficiency at 5 cm separation distance.

| | **Output Voltage (V)** | **RF $P_{av}$ (mW)** | **DC $P_L$ (mW)** | **RF-DC Efficiency (%)** |
|---|---|---|---|---|
| Loop 90° | 8.50 | 53.2 | 48.2 | 90.5 |
| Loop 110° | 5.00 | 22.2 | 16.7 | 75.1 |
| Segmented Loop 90° | 6.72 | 35.1 | 30.1 | 83.6 |
| Segmented Loop 110° | 8.26 | 52.2 | 45.5 | 87.1 |

RF-DC efficiencies are all larger than 75 %. Regarding the choice of using a loop (E-field coupling) or segmented loop (H-field coupling) rectenna, the segmented loop is better for a couple of reasons. First, the segmented loop has better resistant to dynamic angle changes. Although at 90°, the harvested power by loop antenna is larger, it drops seriously when increasing the angle and it is smaller than the segmented loop at 110° which is the most comfortable and possible orientation for most of the time. Second, the magnetic coupling antenna tends to have lower loss induced by the human body and will have less harm to humans [85].

## 4.7 Summary

In this chapter, a novel wearable and flexible energy-autonomous on-body sensing network is proposed featuring full operability through energy harvesting from a hand-held 464.5 MHz two-way talk radio. Three different functions are provided utilizing the hand-held two-way talk radio as the only energy source for our proposed system. There are two types of EHs proposed for the presented system. The first EH that is integrated with backscattering sensor tags harvests the 464.5 MHz signal energy to drive the tags; the second EH that can be worn on hands harvests the same 464.5 MHz signal to produce both the DC power and the carrier signal. The second EH is more efficient than conventional ambient RF energy harvesting architectures because, for the first time, both the DC and the second harmonics generated by the rectifier are utilized to enable two additional functions. The generated second harmonic is used to realize an RF carrier emitter without using an external "power-hungry" RF oscillator and interrogate backscattering sensor tags for on-body sensing. The DC power is used to power an RF amplifier in order to enhance the second harmonic to effectively extend the sensing and communication range. The additive manufacturing technologies including inkjet printing and 3D printing are used to fabricate proof-of-concept prototypes. For the proof-of-concept demonstration, the measured DC and the second harmonic, 929 MHz, output power from the proposed energy harvester are 17.5 dBm and 1.43 dBm, respectively, while a two-way talk radio is 9 cm away. The measured second harmonic output power is increased to 13 dBm utilizing the harvester-powered RF amplifier, and the reading range of the custom backscattering sensor tag is extended to more than 70 m with SNR equals to 14.7 dB. The reading range is expected to extend to more than 270 m with 3 dB SNR. Also, the interrogation of multiple sensor tags and the wireless detection of ammonia gas utilizing an inkjet-printed flexible ammonia sensor is demonstrated showing the wide range of applications of the proposed approach.

A simulation process to accurately predict the coupling power of near-field coupling

energy harvesters is also proposed and verified in this chapter. The human tissue effects are taken into consideration. Two types of rectennas including loop type (E-field coupling) and segmented loop type (H-field coupling) are proposed and the prototypes are realized with the inkjet printing masking method. The measured results on the human body can be used to verify the accuracy of the simulation and design process. Dynamic measurements with different distances and angles are performed to address the effects of misalignment between the radio and the harvesters and determine if active matching is required.

# CHAPTER 5

# ENERGY-AUTONOMOUS MICROPUMP SYSTEM TO EXPAND HORIZONS OF MICROFLUIDIC APPLICATIONS

Microfluidic applications utilize the very little amount of fluid to analyze its properties. They have played an important role in bio-sensing such as sweat, droplet, and blood analysis. They can also be used to perform environmental analysis such as water and rain analysis. However, most of these analyses are done in the laboratory since actuation forces are required to pump the liquid into the small microchannels for analysis. The micropump systems are ideal to provide the actuation forces since they can be used on any type of liquids. Furthermore, energy-autonomous micropump systems powered by EHs can expand the horizons of microfluidic applications. Since now the actuation forces are provided, the microfluidic applications are no longer restricted for in-lab use. That means wireless sensing, wearable health monitoring, real-time environment monitoring, and IoT applications are now all possible.

In chapter 4, a EH harvesting from near-field hand-held devices is proposed. A large amount of energy is provided because of the small distance. However, the drawback is that it only provides energy while the hand-held device is in use. On the other hand, harvesting from far-field signals such as DTV. UHF RFID is complementary to the near-field sources since it provides much smaller but continuous energy. Thus, a EH design which harvests energy from both near-field and far-field energy sources is necessary to combine both advantages without any drawbacks.

In this chapter, an energy-autonomous micropump system is proposed to expand the horizons of microfluidic applications. The micropump system is powered by an energy harvester which harvests energy from both near-field 464.5 MHz two-way radio and far-field UHF (850-950 MHz) RFID reader. The details of the micropump system are intro-

duced in section 5.2 and successfully demonstrate the functionality. In section 5.3, a power management circuit is included in the micropump system to further improve the system and integrating both the large near-field energy and small far-field energy. The duty cycling function is also included by utilizing the power management circuit. In section 5.4, a new fabrication process utilizing only additive manufacturing technologies is proposed to realize microfluidic sensors. The proposed process can realize microchannels with a lower cost, more complex structures, and a shorter time. A proof-of-concept sweat sensor is also demonstrated. Finally, the energy-autonomous micropump system, the power management circuit, and the sweat sensor are combined to built a long-range backscatter microfluidic sensing system in section 5.5.

## 5.1 Objectives and Design Ideas

### 5.1.1 Objectives, Challenges, and Solutions

Microfluidics has been a significant technique for advanced RF components over the last decade. Non-conductive fluids are used to adjust the permittivity and achieve reconfigurable RF components such as resonators, filters, antennas, sensors, and frequency selective surfaces (FSS) [86–88]. In the meantime, conductive fluids are suitable for switches and flexible circuits [89]. For all microfluidic applications, actuation forces are required to move fluids inside microchannels. Typical ways of moving fluids includes manually pressing fluids into the channels using syringes [90], using pumps [91], and using electrochemically controlled capillarity [92]. However, all methods require a certain power or voltage to drive the system which significantly limits their applications.

To expand the usage of microfluidics techniques to modern applications such as IoT and smart skins, it is crucial to provide a battery-less actuation force to reduce the maintenance cost. The energy harvesting techniques combining with a cheap and small micropump which is capable of driving all types of liquids inside microchannels is an appropriate solution to expand the horizon of the microfluidic applications since it has been proven that

| Metrics | Objectives | Prior Art | Challenges | Solutions |
|---|---|---|---|---|
| **Performance** | • Energy-autonomous microfluidic sensing network<br>• Wearable and flexible<br>• Applied to IoT<br>• Harvested more power<br>• Automatically cycling<br>• Sweat sensor for health monitoring<br>• Easy detect and use in cluttered environment<br>• Reading range > 20 m | • Limited to in-lab use<br>• Complex VNA is required for detection<br>• Detected the dielectric constant change of the fluids<br>• Bad in cluttered environment<br>• Reading range < 5 m | • Energy-autonomous actuation force for microfluidic applications<br>• Low-cost reader and easy detection<br>• Reduced effects from clutters<br>• Increased reading range | • Energy-autonomous micro-pump system<br>• Detected the conductivity change of the fluids<br>• Backscatter topology |
| **Fabrication** | • Additive manufacturing system<br>• Fast and easy microfluidic microchannel fabrication | • Multi-process slow fabrication | • Simple, fast, and large-scale microchannel fabrication process | • Inkjet printing electrodes<br>• 3D printing microchannels |

Figure 5.1: The summarizing table of the objectives, challenges, and solutions of the proposed energy-autonomous long-range microfluidic sensing network.

the energy harvesting techniques are suitable to support green and constant energy for low-power electronics [93]. For energy harvesting techniques, there are many different types of ambient energy sources such as solar, RF, heat, and vibration that can be utilized in energy harvesting systems. Among all ambient energy sources, RF sources are particularly popular since they can be accessed all day while their ability to bypass or penetrate walls makes them ubiquitously available. There are two types of RF energy harvesting approaches. The first one is to harvest far-field RF energy such as DTV and communication signals [12]. This type of energy can be accessed all the time but it typically has relatively low energy density [8]. The other type of RF energy harvesting technique is to harvest RF energy from nearby "hot spots" such as hand-held and wearable devices where RF energy is fairly high. With a wearable and flexible energy harvester, this type of energy can generate very high DC voltage and power [94]. However, it might be accessible only a small amount of time when those hand-held and wearable devices are transmitting power.

In this chapter, the main objective is to propose a novel long-range microfluidic sensing network. The detailed objectives, comparisons to prior arts, challenges, and solutions are summarized in Figure 5.1. The microfluidic applications are still limited and not widely adopted because of three main challenges. The first one is to provide energy-autonomous actuation forces so that microfluidic applications will be no longer limited to only in-lab

use. The second one is to come up with a new wireless detection method. Since most of the prior arts detect the changes in the dielectric constants of the fluids, they will need expansive readers such as VNA to detect the resonance frequencies. The detecting range for this method is small and is easily affected by the clutters around the environment. The third one is to reduce the cost of realizing microfluidic channels. The previous fabrication processes required multiple process steps and thus increasing the cost significantly. Furthermore, the structural flexibility is low. Therefore, developing a new fabrication process to realize the microchannels for microfluidic applications is essential.

One of the solutions to the energy-autonomous actuation force is a micropump system solely powered by energy harvesting techniques. The proposed energy harvester harvests near-field and far-field RF energy sources simultaneously. A broadband energy harvester which is composed of a broadband antenna and a broadband rectifier is proposed to simultaneously harvest the far-field UHF RFID reader signals within the range of 860 to 960 MHz and near-field two-way talk radio waves at 464.5 MHz. By combining the two sources, the system would have both advantages from the near-field and far-field energy harvesting. The high power and DC from near-field energy harvesting can be achieved to overcome the cold-start of the driving IC chip for the micropump immediately while the consistently accessed far-field energy can be used to charge the energy storage device continuously to maintain the function of the micropump system. The proposed energy-autonomous micropump system can provide large actuation forces which can be applied to any type of microfluidic applications.

The proposed autonomous micropump system is further improved using a power management circuit (TI BQ 25570) to integrate the harvested near-field high power energy and far-field low power energy and to provide the duty cycling function. Since the input impedance of the power management circuit which is also the load impedance for the rectifier varies depends on the input power, the matching circuit of the rectifier has to be designed carefully. The input impedance of the power management circuit is low (around

200 Ω) at high input power and high (around 5 kΩ) at low input power. Thus, a carefully designed tapered matching circuit is used to match both at 464.5 MHz while the load is around 200 Ω and between 860 MHz to 960 MHz while the load is around 5 kΩ.

To increase the reading range and reduce the effects of the clutters, a backscatter microfluidic sensing topology is proposed. Instead of detecting the dielectric constant changes or the resonance frequencies, the proposed topology detects the conductivity changes in the fluids inside the microchannel. The reader is much simpler and cheaper compared with prior arts since a cheap off-the-shelf Software Defined Radio (SDR) can be used as the reader. Furthermore, since the detecting target is the backscatter signals rather than resonance frequencies, the clutter effects are much smaller.

To reduce the cost of microfluidic applications, a new additive manufacturing microchannel fabrication process for the microfluidic sensor is also proposed. Thanks to the 3D printing technology, microchannels with various shapes and sizes can be realized easily. Furthermore, only two steps are required to realize the microchannels and thus reducing the cost significantly. The fabrication process is used to realize a sweat sensor as a proof-of-concept test vehicle. The proposed micropump system, energy harvester, and microfluidic sweat sensor are integrated to achieve a backscatter microfluidic sensing system to perform real-time on-body health monitoring.

### 5.1.2 System Architecture

The block diagram of the proposed energy-autonomous micropump system is shown in Figure 5.2. As shown in Figure 5.2, the energy sources are a UHF RFID reader (860 MHz-960 MHz) with EIRP equals to 4 W (36 dBm) and a two-way talk radio (464.5 MHz) with output power around 35 dBm at near range. A broadband antenna is used to receive power from both sources while a broadband matching circuit is used to match the antenna with the rectifier within these frequencies. The rectifier would convert the RF signal to DC power and use it to charge a supercapacitor which serves as the power storage circuit. Once the

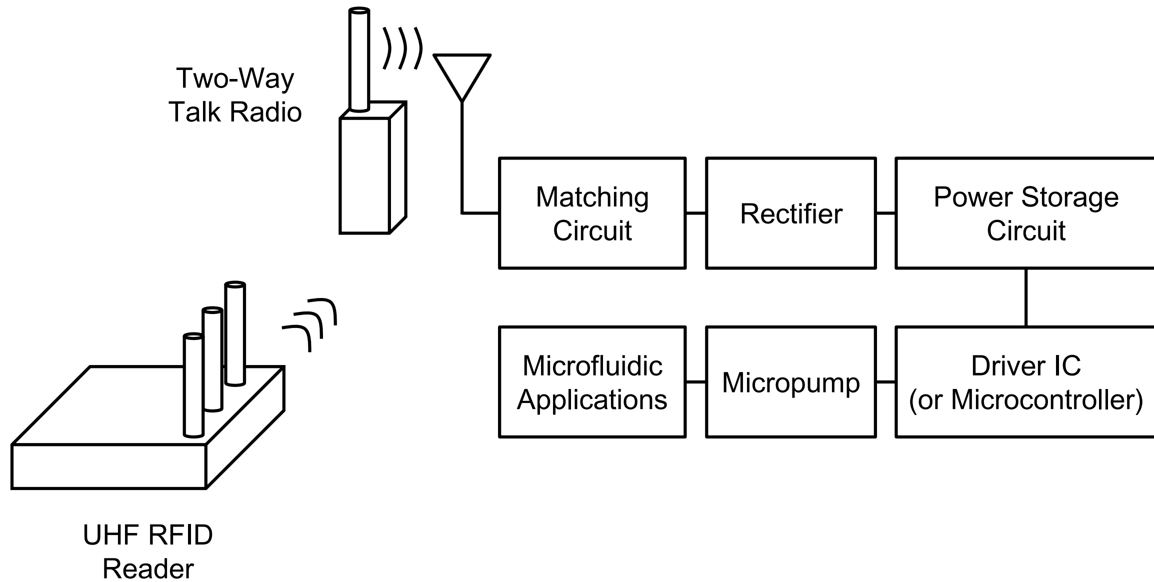


Figure 5.2: Block diagram of the proposed energy-autonomous microfluidic system.

voltage is high enough, the supercapacitor can be used to power up the driving IC or a MCU to generate driving signals for the micropump. A small and cheap micropump that is operated based on a piezoelectric diaphragm is used to support the actuation force for the microfluidic applications.

The block diagram of the proposed energy-autonomous backscatter microfluidic sensing system is shown in Figure 5.3. The broadband antenna is used to receive power from both sources. The matching circuit is designed to meet both low power and high power conditions. The harvested power is used to charge supercapacitors after the voltage is regulated by the power management circuit. Once the voltage at the supercapacitor reaches the designed value, the power management circuit will start the discharging process and drive both the oscillator and the micropump IC. The micropump IC will provide a suitable voltage waveform to drive the micropump and pump the liquid into the microfluidic sensor. The DC resistance of the microfluidic sensor varies depends on the conductivity of the liquid. For example, when the human body dehydrates, the conductivity will increase and change the DC resistance of the microfluidic sweat sensor. The oscillator frequency will change based on the DC resistance and control the RF switch with respective oscillating

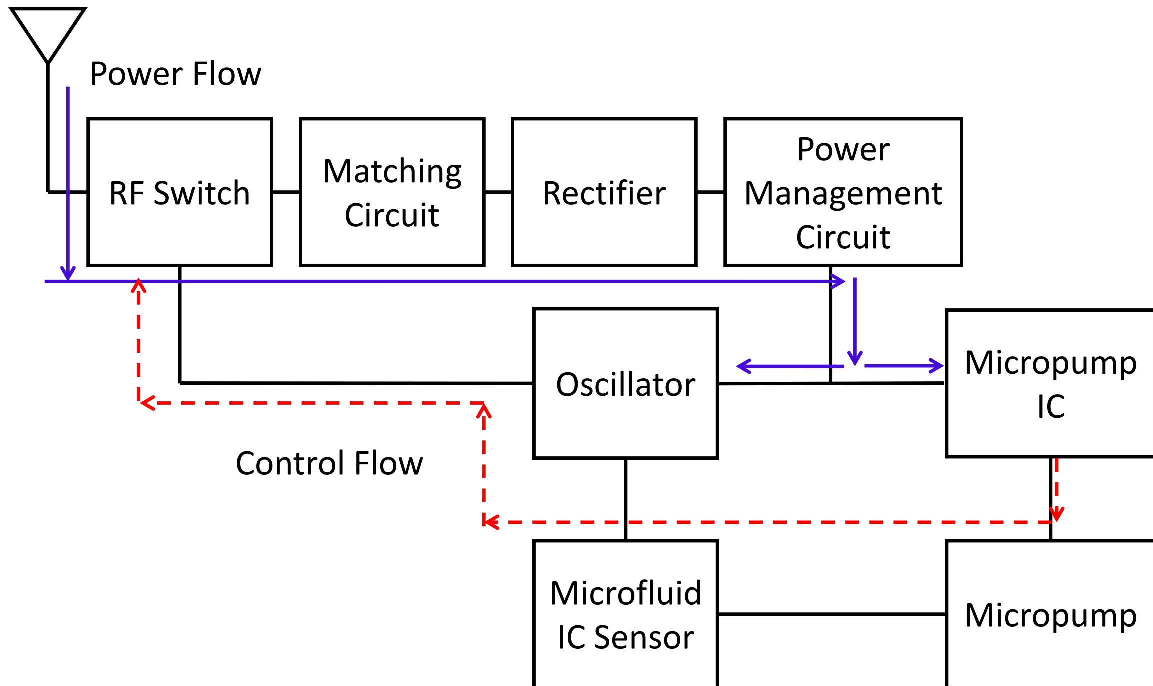


Figure 5.3: Block diagram of the proposed energy-autonomous microfluidic backscatter sensing system.

frequencies. Therefore, the modulated backscatter signals are created and backscatter to the RFID reader or SDR. By monitoring the frequency of the backscattered signals, a wireless, wearable, and real-time health monitoring system using microfluidic sensors can be realized.

## 5.2 Energy Harvester Powered Micropump System Design

### 5.2.1 Receiving Antenna Design

A broadband flexible monopole antenna as shown in Figure 5.4 is used for the collection of energy from multiple ambient sources. As shown in Figure 5.4b, good flexibility can be observed by curving the broadband antenna along with a cylinder with a diameter equals to 10.1 cm. The measured $S_{11}$ of the antenna in the flat and the curved configurations are shown in Figure 5.5. As demonstrated in Figure 5.5, for the flat condition, the measured $S_{11}$ is smaller than -10 dB from 700 MHz to over 1.2 GHz. There is a frequency shift due

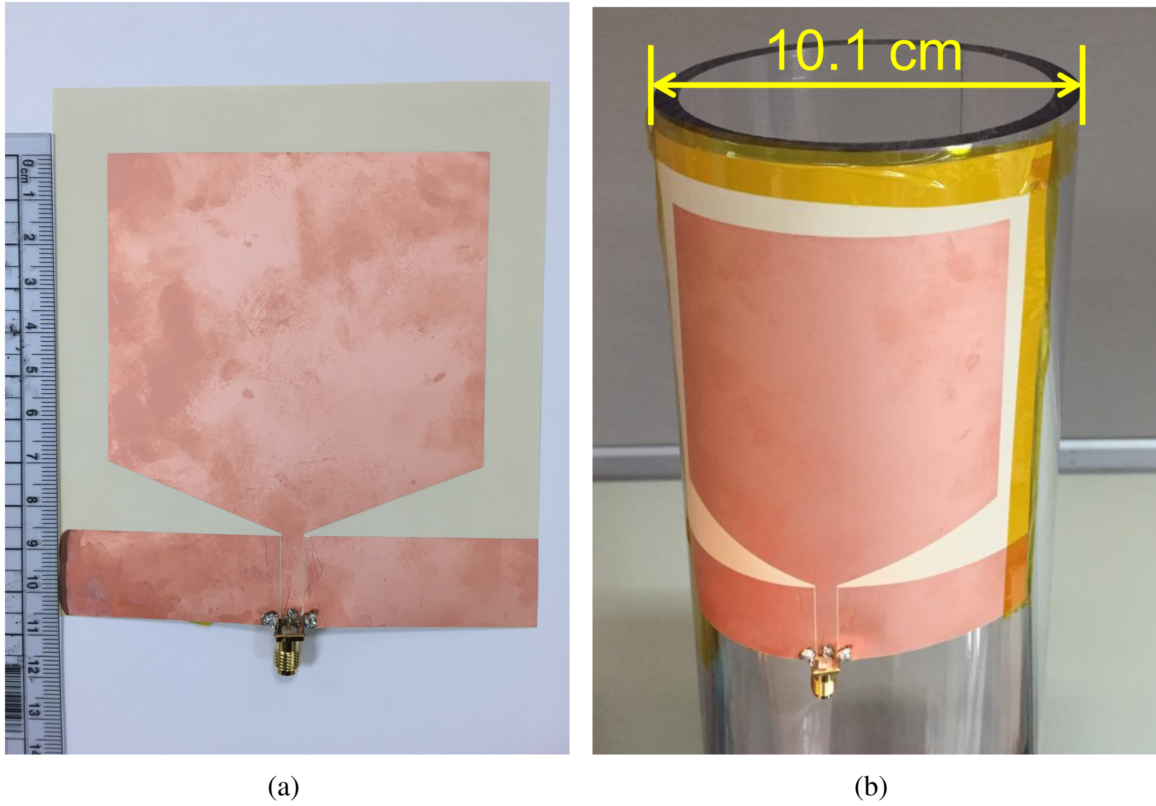


(a) (b)

Figure 5.4: Broadband antenna in (a) flat and (b) folded conditions.

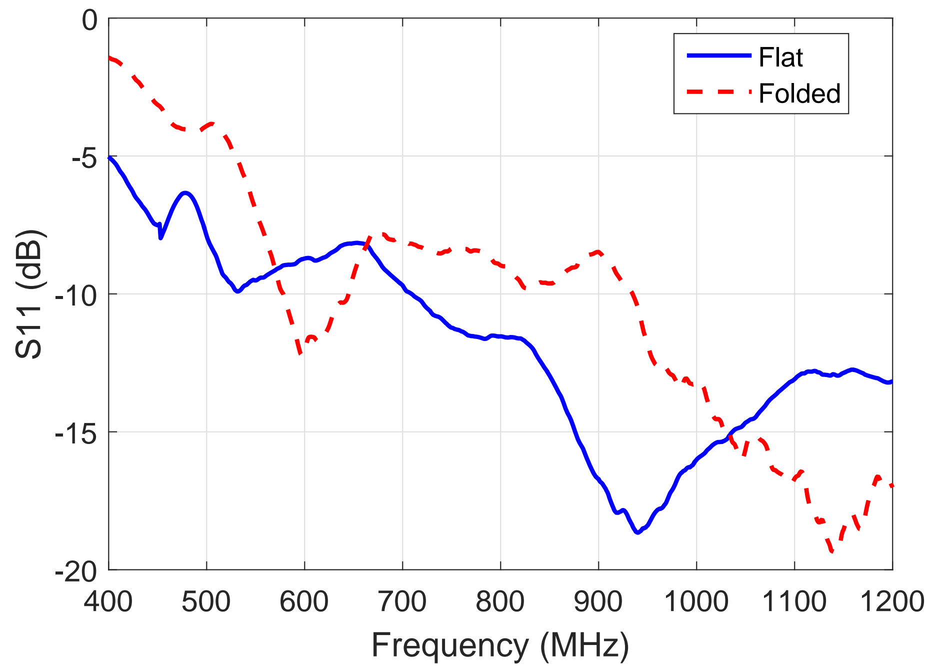


Figure 5.5: Measured $S_{11}$ in flat and folded condition.

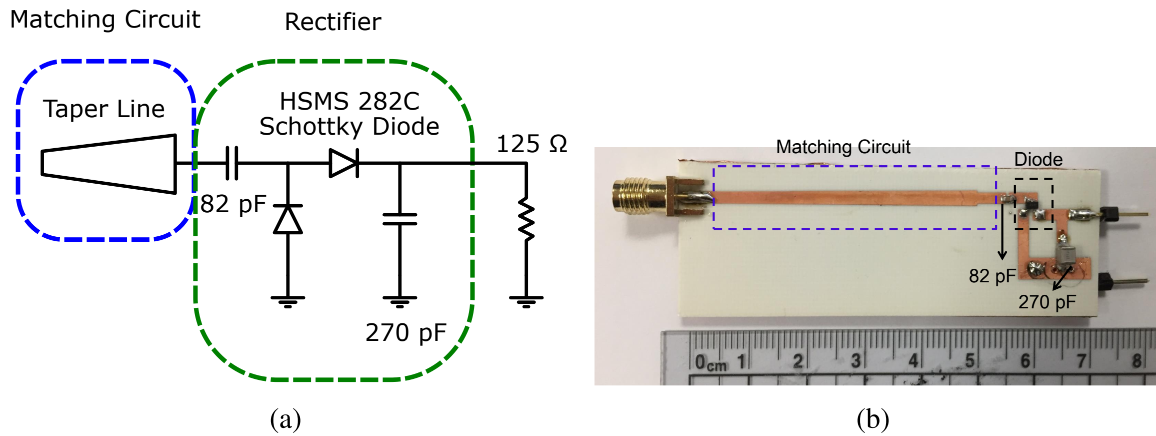


Figure 5.6: (a) The circuit diagram and (b) the prototype of the proposed broadband rectifier

to folding and the $S_{11}$ is kept smaller than -9 dB from 850 MHz to over 1.2 GHz. The UHF RFID band can be covered by this broadband antenna under both conditions. The near-field coupling between the 464.5 MHz two-way radio and the antenna is still good enough as discussed in Section subsection 5.2.3.

### 5.2.2 Broadband Rectifier Design

A broadband rectifier which covers frequencies from 300 MHz to over 1.2 GHz is proposed as shown in Figure 5.6. The circuit diagram is shown in Figure 5.6a and the fabricated prototype is demonstrated in Figure 5.6b. A tapered line with length 50 mm, left width 1.83 mm, and right width 2.58 mm is used to achieve broadband impedance matching. The voltage doubler topology is adopted for the rectification. The voltage doubler is composed of an 82 pF capacitor, an HSMS 282C diode package for rectification, and a 270 pF capacitor to eliminate higher-order harmonics. The load of the proposed rectifier is the driving IC of the micropump which has a resistance equals to 125 Ω. The measured $S_{11}$ values for different input power levels are shown in Figure 5.7. The measured $S_{11}$ are all smaller than -9 dB for different input power levels and a very broadband performance can be proved.

The measured output power levels while using different input power levels at different frequencies are shown in Figure 5.8. The simulated results using harmonic balance pro-

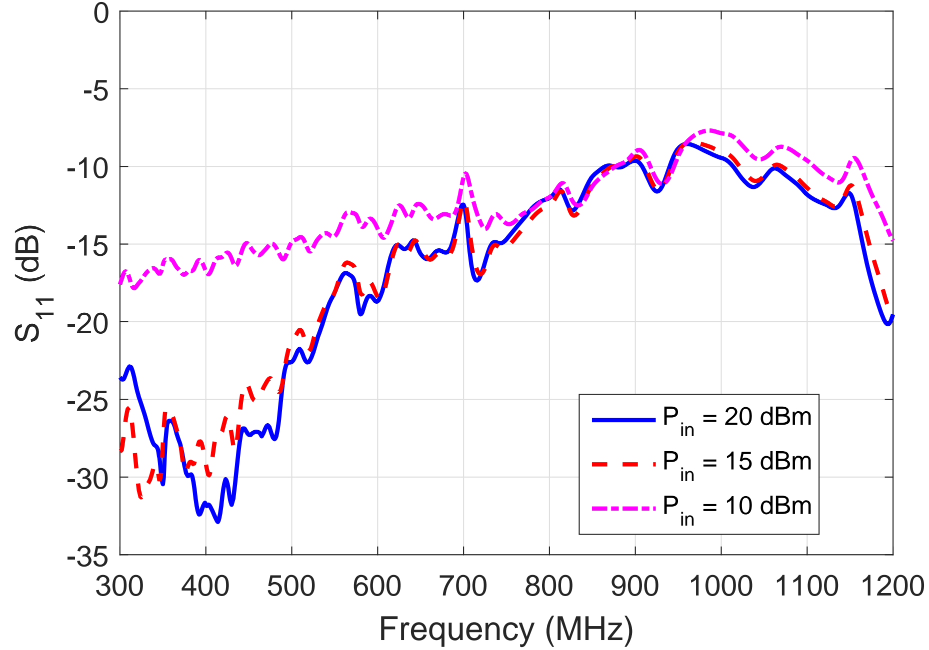


Figure 5.7: Measured $S_{11}$ of the proposed broadband rectifier.

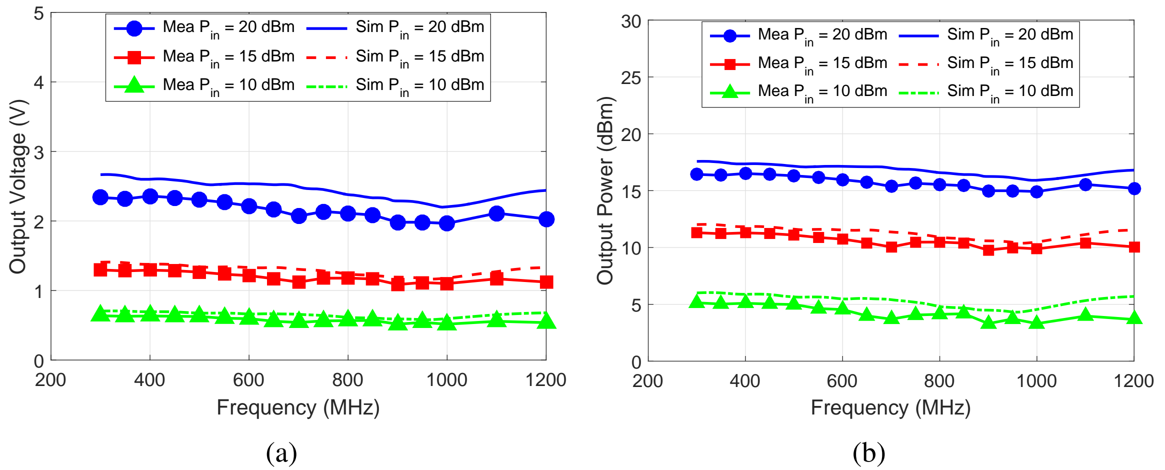


Figure 5.8: (a) The simulated and measured (a) output DC voltage and (b) output DC power of the proposed broadband rectifier at different frequencies.

vided by ADS are also included for comparison and good agreements can be observed. As depicted in Figure 5.8, flat responses at different frequencies can be observed which serves as strong proof of the broadband performance of the proposed broadband rectifier. There is a minor decrease around 1000 MHz due to the higher $S_{11}$ values around that frequency. The simulated and measured output DC voltage and output DC power of the proposed broad-

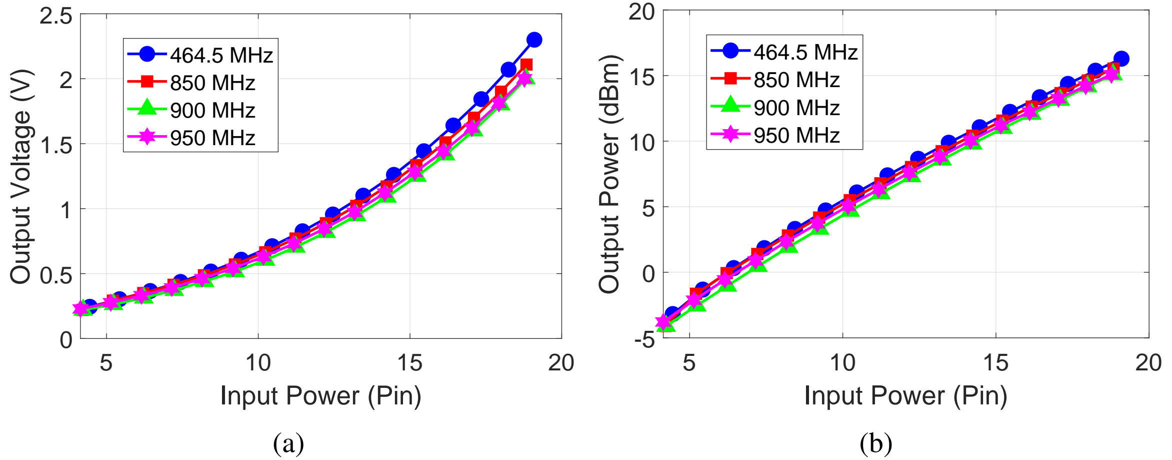


Figure 5.9: (a) The simulated and measured (a) output DC voltage and (b) output DC power of the proposed broadband rectifier at different input powers.

band rectifier at different input powers are shown in Figure 5.9. The RF-DC conversion efficiency is about 50 %, 45 %, and 35 % while the input power levels of 20 dBm, 15 dBm, and 10 dBm, respectively.

#### 5.2.3 System Performance Evaluation

For the near-field energy harvesting, the measured coupling between the two-way talk radio and the final output power at the output of the rectifier at different distances is 21.5 dBm, 16.3 dBm, and 14.6 dBm while the distance is 5 cm, 10 cm, and 15 cm, respectively. The micropump-driving IC can be driven at the power level of at least 14 dBm which means the maximum range is about 15 cm. This can be improved significantly to less than 0 dBm and a much longer reading range by integrating the power management circuit and the automatic duty cycling function. The details will be introduced in section 5.5. For the far-field energy harvesting from UHF RFID reader, to follow FCC regulations, 4 W EIRP is used. The received power by the broadband antenna at 900 MHz and 45 cm away is around 13 dBm. It takes 77 s to fully charge a 47 mF supercapacitor to 3.5 V and the micropump can be operated for 10 s before the voltage drops below the driving point. Thus, the duty cycle is about 13 %. The measurement setup for the entire system is shown in Figure 5.10.

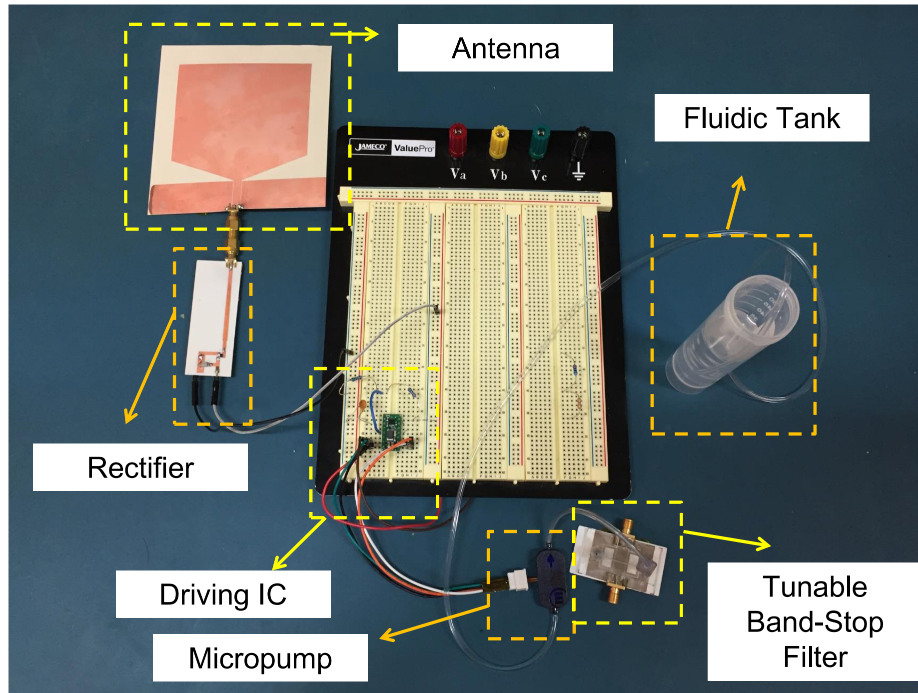


Figure 5.10: The measurement setup of the proposed energy-autonomous microfluidic system.

The voltage at the output of the driving IC is measured and shown in Figure 5.11. As shown in Figure 5.11, three different conditions are measured. The first one is the use of the energy from the two-way radio to turn on the driving IC immediately. The second one is to use a signal generator to generate a 19 dBm 464.5 MHz signal and directly feed to the proposed broadband rectifier. The final one is to harvest UHF signals to charge supercapacitor and use that to drive the IC. Since the micropump is based on piezoelectric principles, the resulting voltage change can be used to induce the vibration while the amplitude of the voltage difference can be used to control the amplitude of the vibration and thus, control the amplitude of the actuated force. As shown in Figure 5.11, since the two-way talk radio can support high energy density, the IC can be turned on immediately with an output voltage of 67.2 V at the output end of the driving IC. The result is similar to that using a signal generator with 19 dBm input power and the output voltage is 56 V. The noise in the two-way talk radio measurement is due to the coupling between the two-way talk radio and the probing cable of the oscilloscope. Moreover, the output voltage is 10.2 V while using

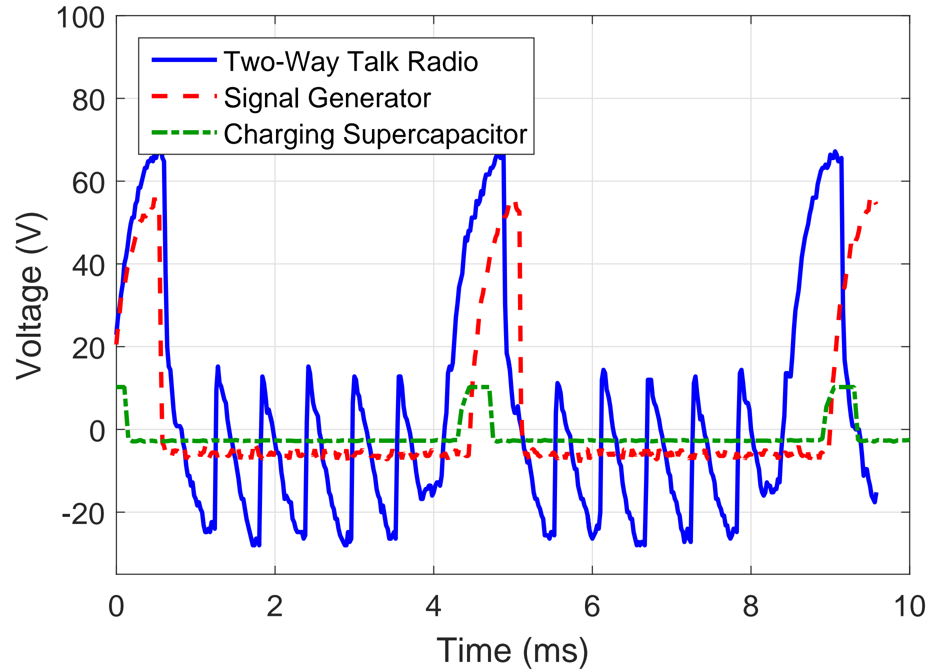


Figure 5.11: Output voltage at the output pin of the driver IC.

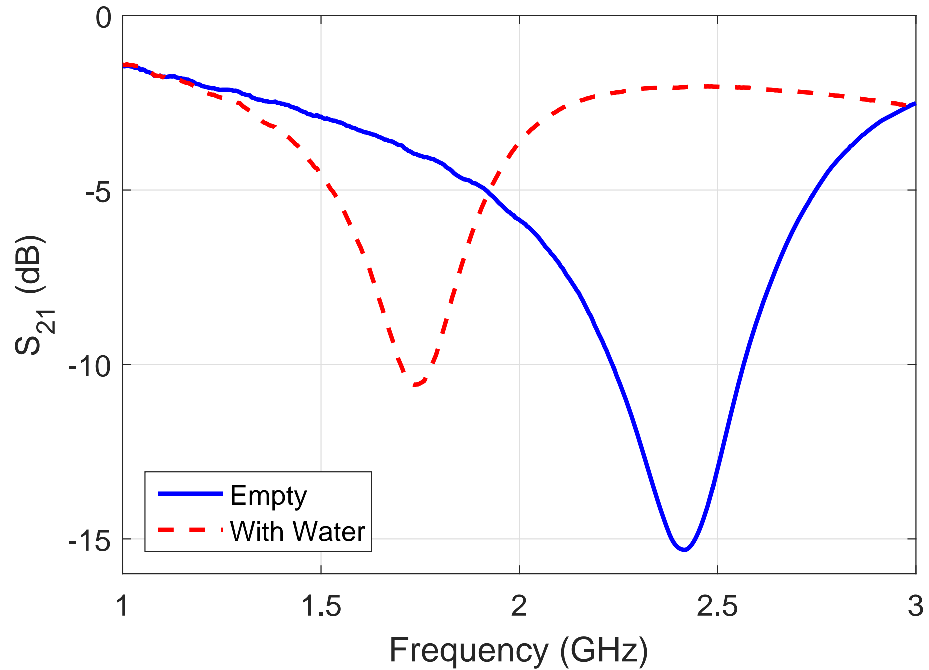


Figure 5.12: Measured $S_{21}$ of a liquid-tunable band-stop filter.

the UHF-charged supercapacitor. Although the voltage is smaller compared to that using two-way talk radio, the driving IC is still successfully turned on. Furthermore, the time duration of the voltage spikes shown in Figure 5.11 is determined by the driving IC. The

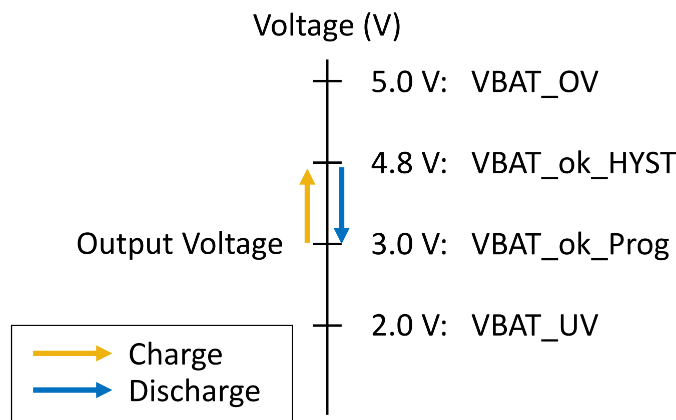


Figure 5.13: The definitions of output voltages form the power management circuit (BQ 25570).

band-stop filter shown in Figure 5.10 is tunable due to the embedded microfluidic channel. The measured $S_{21}$ values are shown in Figure 5.12 and the stopband can be changed by pumping water into the microchannel using the proposed micropump system. It takes less than 1 s to fill the channel with 6 µL water. Besides, the moving speed of the fluid using the proposed micropump system is measured and the result is 37.8 µL/s. Thus, it takes only 0.16 s to finish the transition which is a much shorter time than the autonomous micropump operation time provided by the harvested energy.

## 5.3 Duty Cycling with Power Management Circuits

### 5.3.1 Power Management Circuits

There are a couple of reasons to include the power management circuit. First, the charging and discharging supercapacitor measurement in the previous section is done manually. Thus, the power management circuit is necessary to improve the system and integrate both the near-field high power and far-field low power with automatic duty cycling. Second, since more than 1 V is required to drive the driving IC for the micropump, more than 14 dBm of UHF power is required and thus, the operating range is small. The power management circuit used here is a TI BQ 25570. The input cold-start voltage is 0.33 V and

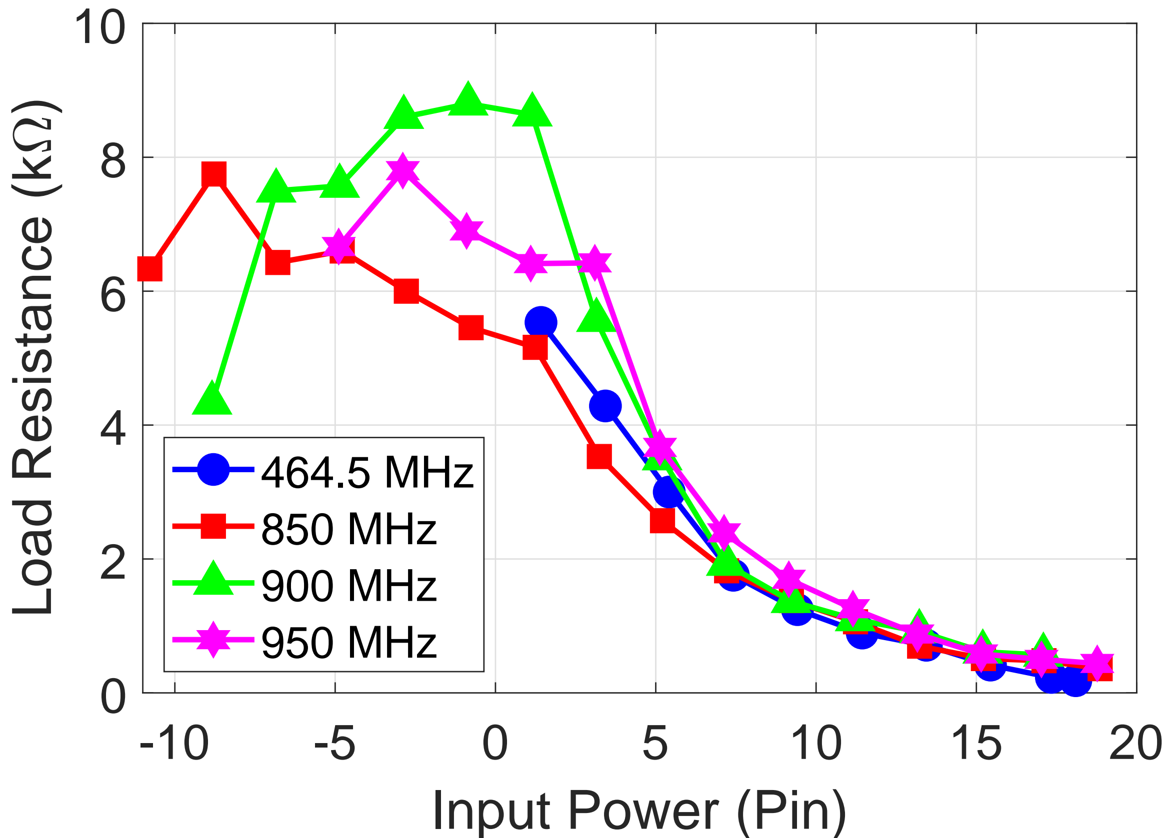


Figure 5.14: The input impedances of the power management circuit (BQ 25570).

the continuous voltage is 0.1 V once turned on. Due to the low turn voltage, only 0 dBm of the input power is necessary to turn on the power management circuit and charging the supercapacitor. Therefore, the operating range is expected to be extended significantly.

The definitions of output voltages from the power management circuit (BQ 25570) is shown in Figure 5.13. The VAT_UV is the under-voltage protection for the power storage unit which are supercapacitors here and the designed value is 2 V. The VBAT_ok_Prog is the voltage where the charging mode will start when the voltage of the supercapacitors dropped to this value and the designed value is 3 V. The VBAT_ok_HYST is the voltage where the discharging mode will start when the voltage of the supercapacitors are charged to this value and the designed value is 4.8 V. The VBAT_OV is the over-voltage protection so that the voltage of the supercapacitors will never go over this value, 5 V, to protect the supercapacitors. The output voltage is a steady 3 V which is large enough to drive the

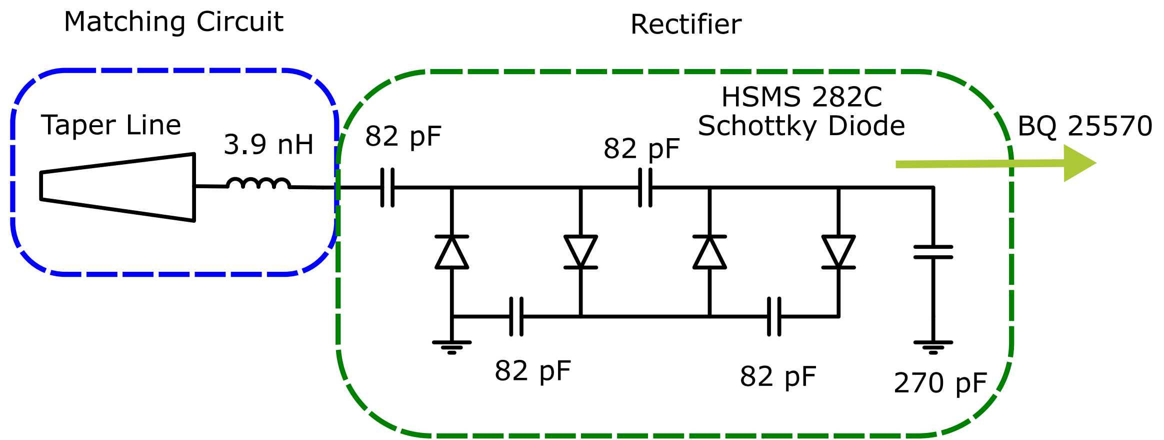


Figure 5.15: The circuit diagram of the proposed rectifier with power management circuit (BQ 25570) load.

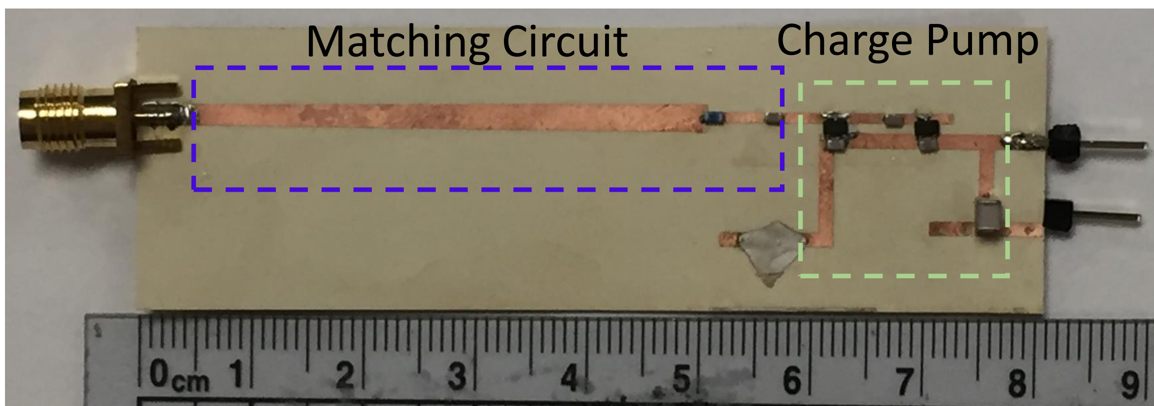


Figure 5.16: The fabricated prototype of the proposed rectifier with power management circuit load.

driven-IC for the micropump.

### 5.3.2 Rectifier Design for Power Management Circuits

The new rectifier which harvests energy from both low-power UHF and high-power two-way talk radio has to be modified due to the change of the load resistance. The load of the rectifier now is the input impedance of the power management circuit and the measured results are shown in Figure 5.14. As shown in Figure 5.14, the load impedance will change at different input power, for high input power at 464.5 MHz, the load impedance is small at around 0.2 kΩ. On the other hand, when the input power is low such as 0 dBm at 850 -

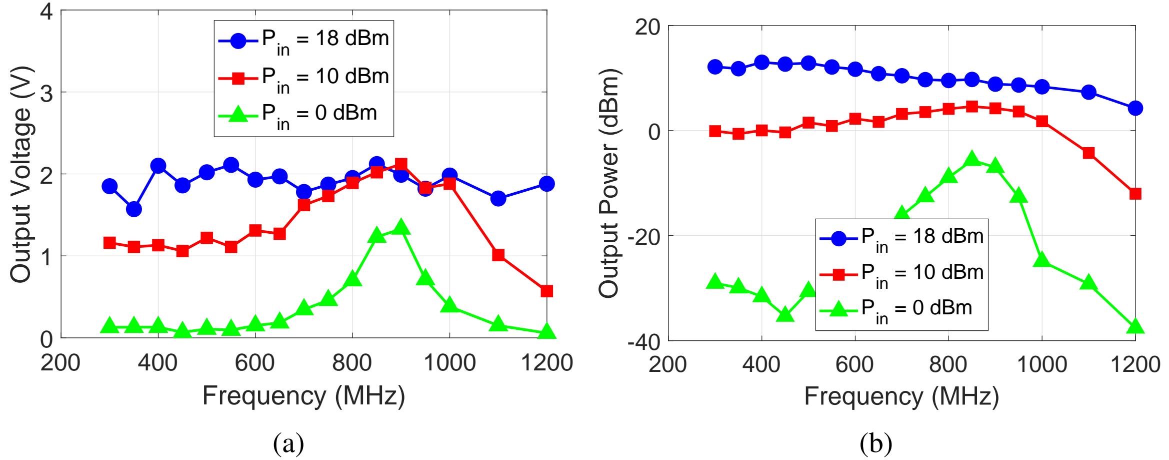


Figure 5.17: (a) The measured (a) output DC voltage and (b) output DC power of the proposed rectifier with BQ 25570 load at different frequencies.

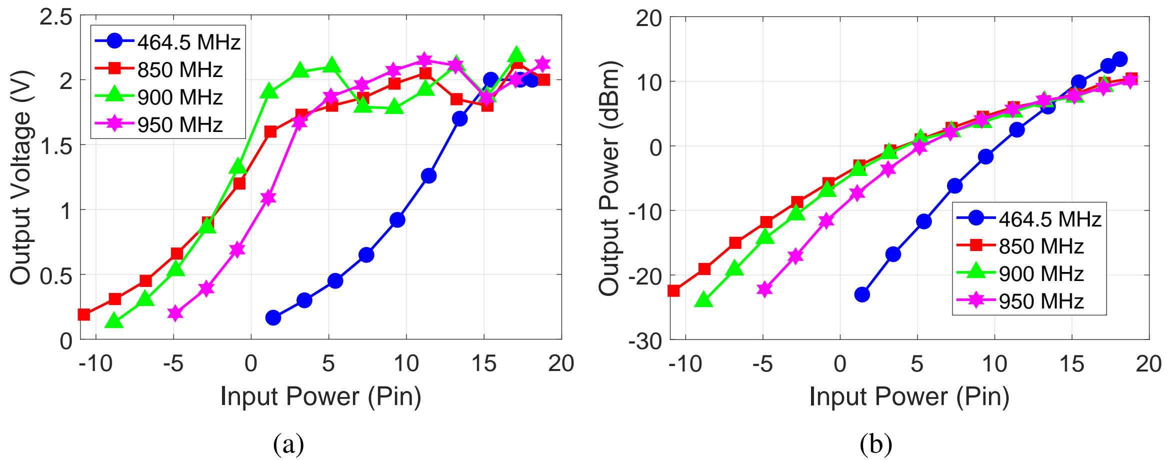


Figure 5.18: (a) The measured (a) output DC voltage and (b) output DC power of the proposed rectifier with BQ 25570 load at different input powers.

950 MHz, the load resistance is about 5-9 kΩ. The large variation of the load resistance at different input power is a large challenge for the rectifier design.

The circuit model of the new rectifier with BQ 25570 as the load is shown in Figure 5.15 and the fabricated prototype is shown in Figure 5.16. A two-stage charge pump topology is adopted and the matching circuit is composed of a tapered line and a lump 3.9 nH inductor. The length of the tapered line is 50 mm with a left-end width of 1.67 mm and a right-end width of 2.4 mm. A 270 pF capacitor is placed at the load to filter the higher-order harmonics.

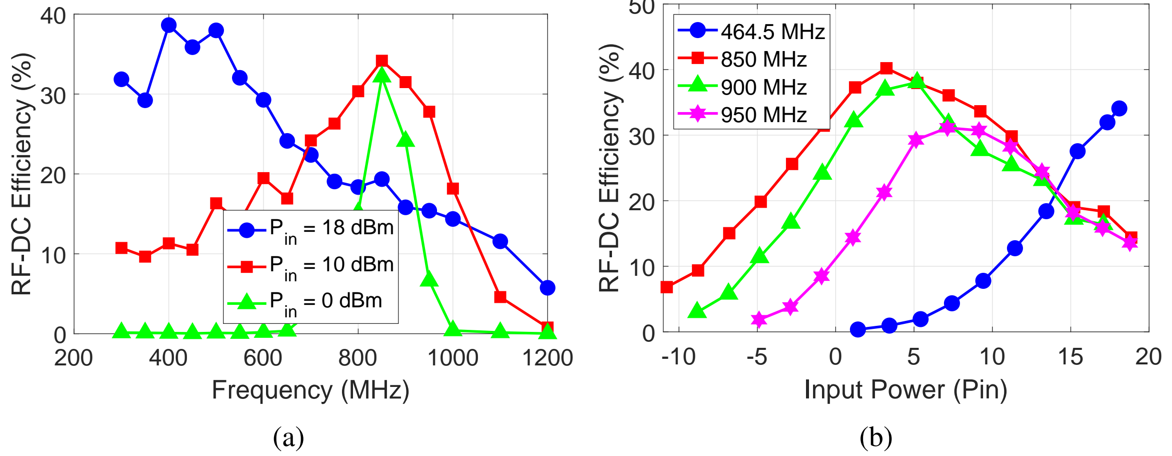


Figure 5.19: (a) The measured RF-DC efficiency of the proposed rectifier with BQ 25570 load (a) at different frequencies and (b) at different input powers.

Table 5.1: The highest efficiency of different frequencies.

| **Frequency (MHz)** | **Efficiency (%)** | **Input Power (dBm)** |
|---|---|---|
| 464.5 | 34.1 | 18.1 |
| 850 | 31.1 | 7.13 |
| 900 | 38.1 | 5.2 |
| 950 | 40.2 | 3.24 |

The measured output voltage and output power from the energy harvest at different frequencies are shown in Figure 5.17. The step of each marker is 50 MHz. As shown in Figure 5.17a, the output voltages at 850-950 MHz while input power is 0 dBm is larger than 0.7 V which is much larger than the cold-start voltage (0.33 V) of the BQ 25570. The measured output voltage and output power from the energy harvest at different input powers are shown in Figure 5.18. As shown in Figure 5.18a, for two-way talk radio at 464.5 MHz, the output voltage is 0.3 V while input power is 3.43 dBm. Thus, the minimum input power to overcome the cold-start voltage (0.33 V) of BQ 25570 while harvesting power from two-way radio is about 4 dBm. On the other hand, the minimum input power to overcome the cold-start voltage while harvesting power from UHF RFID reader is -2.9 dBm.

The measured RF-DC efficiency of the proposed rectifier with BQ 25570 load is shown in Figure 5.19. As shown in Figure 5.19a, the largest efficiency for 18 dBm input power is

38.6 % at 400 MHz which is very close to the two-way radio. The largest efficiencies for 10 dBm and 0 dBm input power are 34.2 % and 32.2 %, respectively and both are at 850 MHz. The highest efficiencies while input energy is at 464.5, 850, 900, and 950 MHz, and the respective input powers are summarized in Table 5.1. The designed energy harvester is perfect for the system since for 464.5 MHz, the highest efficiency is at large power and for 850-950 MHz, the highest efficiency is achieved at middle and low large power. The situation meets the system requirement which harvests high-power near-field energy from two-way radio and low-power far-field energy from UHF RFID.

## 5.4 Microfluidic Sweat Sensor

Additive manufacturing techniques can be used to realize the microfluidic channels with lower cost, faster prototyping, and more complex structure. In this section, additive manufacturing microfluidic sensors are designed, fabricated, and characterized. This sensor can be used to sense the conductivity change of the fluid. Therefore, the proposed sensor can be applied to sweat sensors or environmental sensors which detect acid rain. Taking the sweat sensor for example, this section starts with the conductivity of normal human sweat. The conductivity of human sweat can be modeled as the conductivity of the NaCl under different concentrations. Then two fabrication processes to realize the microfluidic sensor are proposed. The first one utilize 3D printing mold for microchannel fabrication and inkjet printing for electrodes. The second fabrication process is faster and simpler than the first process by directly 3D printed the microchannel. Since the second process is better, it is used in the rest of the analysis. The test samples are fabricated and measured. The stability and repeatability of the process are also characterized for future large-scale fabrication.

### 5.4.1 Sweat Conductivity

The sodium concentration for healthy human sweat ranges from 20 to 100 mmol/L and the concentration of chloride is from 26 to 80 mmol/L [96]. The NaCl concentration inside

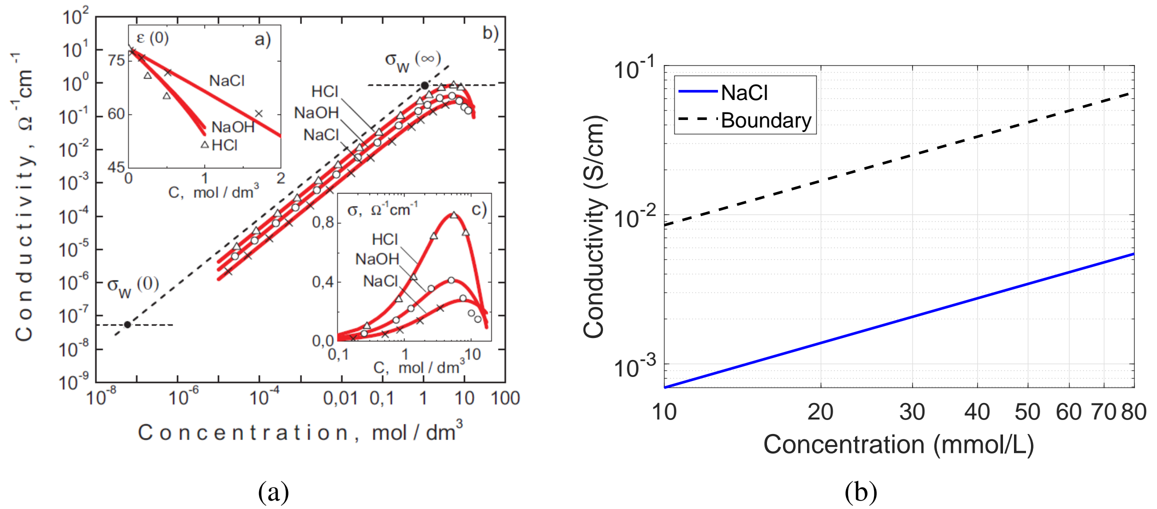


(a) (b)

Figure 5.20: (a) The conductivity of NaCl under different concentrations [95] and (b) the conversion of NaCl concentration to conductivity.

Table 5.2: The conversion of NaCl concentration to conductivity.

| **Concentration (mmol/L)** | **Conductivity (S/cm)** |
|---|---|
| 26 | 0.00179 |
| 50 | 0.00343 |
| 80 | 0.00547 |

healthy human sweat is assumed from 26 to 80 mmol/L. The conversion between conductivity and concentration is built in [95] as shown in Figure 5.20a. The smaller-scale figure focusing only on the interesting range of concentration is shown in Figure 5.20b. The boundary line in Figure 5.20b is the same definition as in Figure 5.20a. A couple of concentrations and the respective conductivities are summarized in Table 5.2. For the lowest concentration (26 mmol/L), the conductivity is 0.00179 S/cm. For the highest concentration (80 mmol/L), the conductivity is 0.00547 S/cm. The conductivity change is more than 3 times which gives a big range of variation for the backscatter sensor.

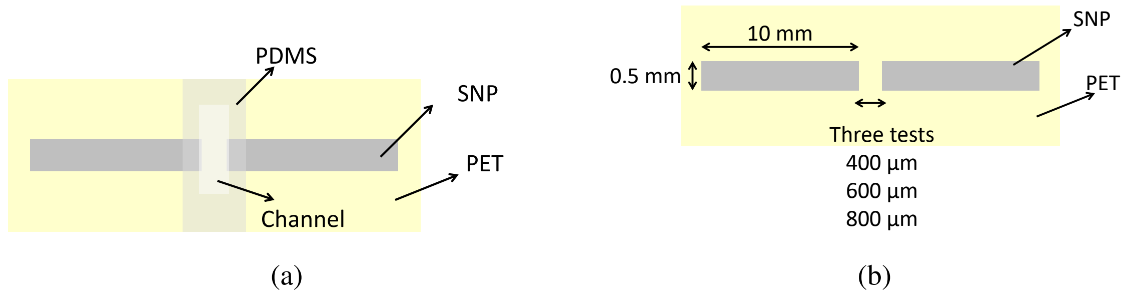


(a) (b)

Figure 5.21: (a) The topology of a microfluidic sensor and (b) its electrodes.

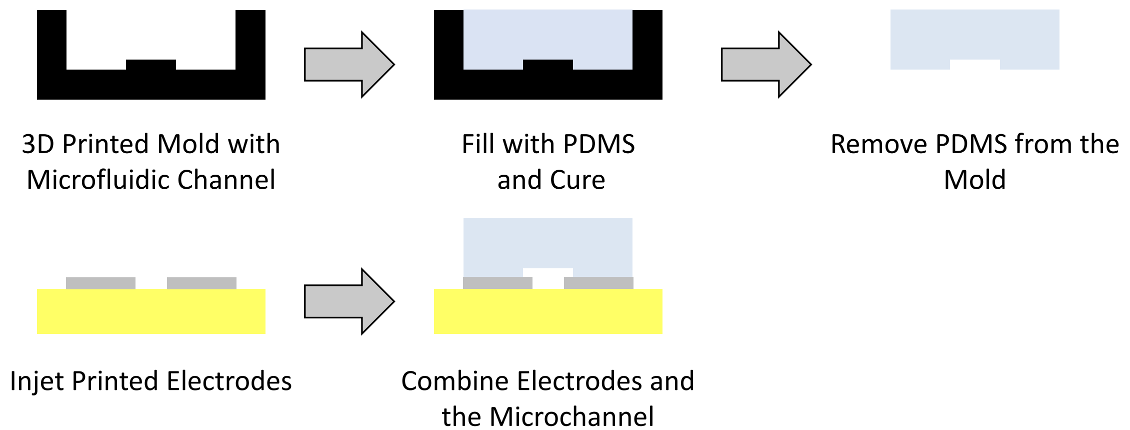


Figure 5.22: The fabrication process of an additive manufacturing mold for microfluidic sensor.

### 5.4.2 Fabrication Process

*Additive Manufacturing Mold for Microfluidic Sensor*

A fully additive manufacturing microfluidic sensor will be introduced in this section. Most of the microfluidic sensors rely on detecting the change of the dielectric constant of the liquid using resonance structures [86]. These resonances can be easily detected while wire connected to VNA. However, it is very difficult to detect the resonance wirelessly under a complex environment with clutters. Thus, microfluidic sensors used here rely on detecting the change of the conductivity of the liquid using topology like subsection 4.4.2. The backscattered topology and this type of microfluidic sensors detecting the change of the conductivity can be used and detected under complex environment and the reading range can be longer than 70 m if designed carefully as introduced in section 4.5.

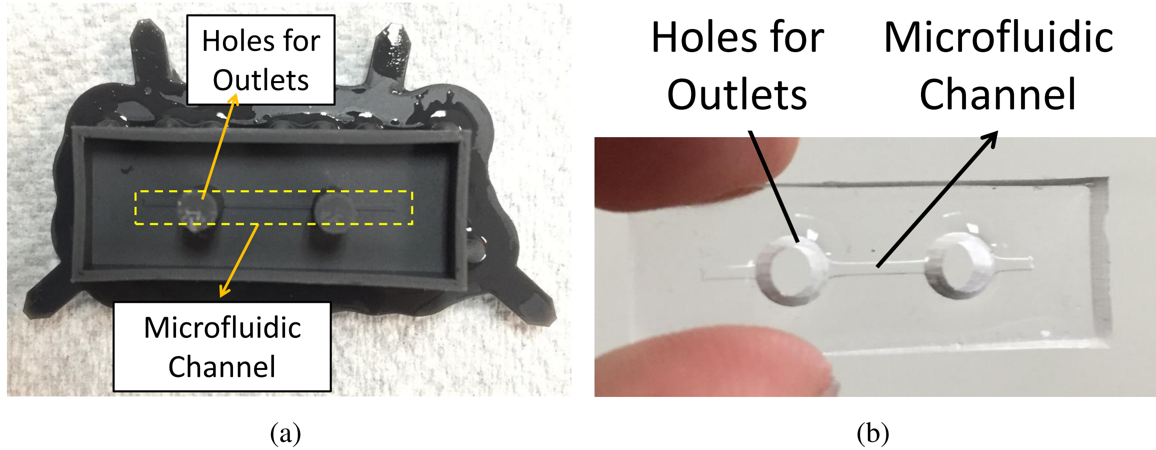


(a) (b)

Figure 5.23: (a) The fabricated prototypes of the mold and (b) microfluidic channel.

The fully additive manufacturing process is extremely helpful to realize microchannel with different sizes and shapes. The design of the microfluidic sensors is shown in Figure 5.21. It is composed of two electrodes printed using SNP on PET and a microfluidic channel realized with PDMS. The dimensions of the electrodes are shown in Figure 5.21b. The microfluidic channel height is 100 µm. The width and length are 800 µm and 20 mm, respectively. The fabrication process is demonstrated in Figure 5.22. For the microfluidic channel, a mold is 3D printed and then filled with PDMS. The PDMS microchannel is then peeled off from the mold. The electrodes are inkjet printed on PET and then combine with the microfluidic channel using PDMS as glue. The fabricated mold and the microfluidic channel are shown in Figure 5.23.

A 44 mmol/L NaCl solution is injected into the fabricated sensors. The measured DC resistance of the sweat sensor with 400 µm gap size between two electrodes is 1 kΩ. The measured DC resistance of the sweat sensor with 600 µm and 800 µm gap size between two electrodes is 1.2 kΩ and 2 kΩ, respectively. Thus, the sweat sensor functions successfully and can be used to real-time monitor the sweat and dehydrate levels of users.

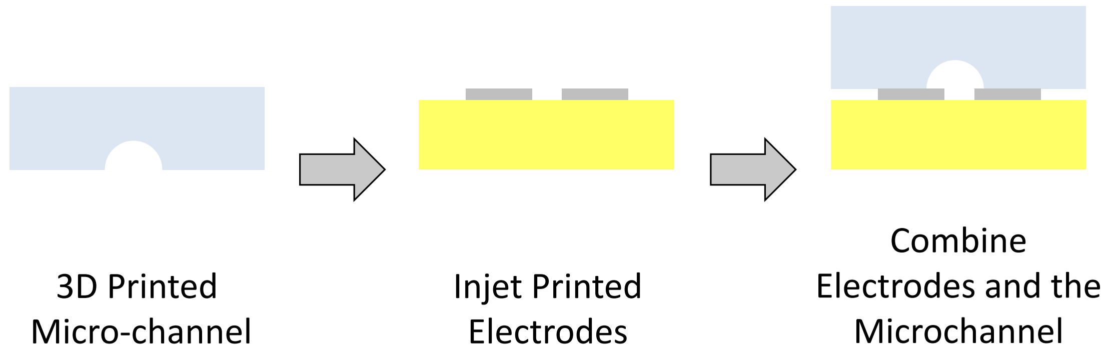


Figure 5.24: The fabrication process of an additive manufacturing microfluidic sensor.

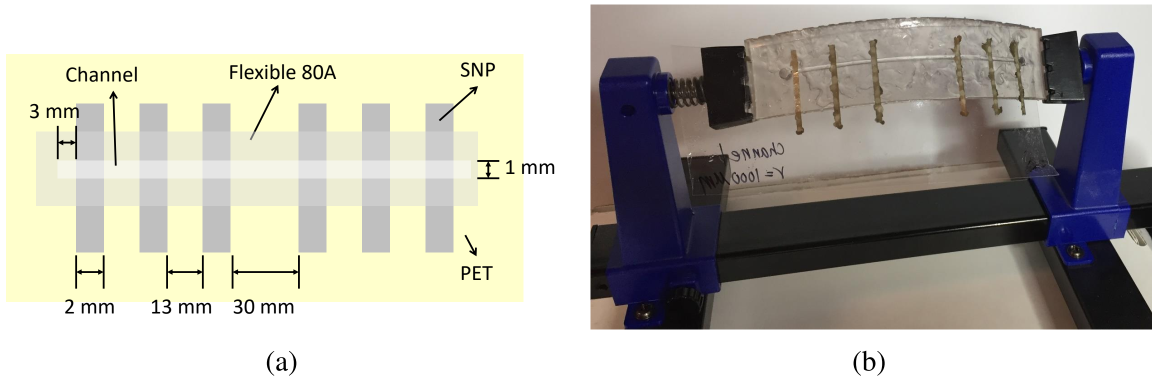


(a) (b)

Figure 5.25: (a) The topology of the microfluidic sensor test vehicle and (b) the flexibility of the proposed microfluidic sweat sensor.

*Additive Manufacturing Microfluidic Sensor*

A further simplified additive manufacturing process for the microfluidic sensor is proposed as shown in Figure 5.24. There are only three steps. The first step is to 3D printing the microchannel. The second step is to inkjet printing the electrodes. The final step is to combine the electrodes and the microchannel. The glue used to combine them is the same material as the microchannel. The glue is applied around the microchannel and then the microchannel is pressed together with the PET. Three minutes of UV curing is applied to make sure the combination and watertight. Since there are fewer steps, this process can be finished within less processing time. Furthermore, there is no need for molds and thus, this process can save materials and be achieved at a lower cost.

A proof-of-concept design of the sweat sensor is shown in Figure 5.25a. The inkjet-

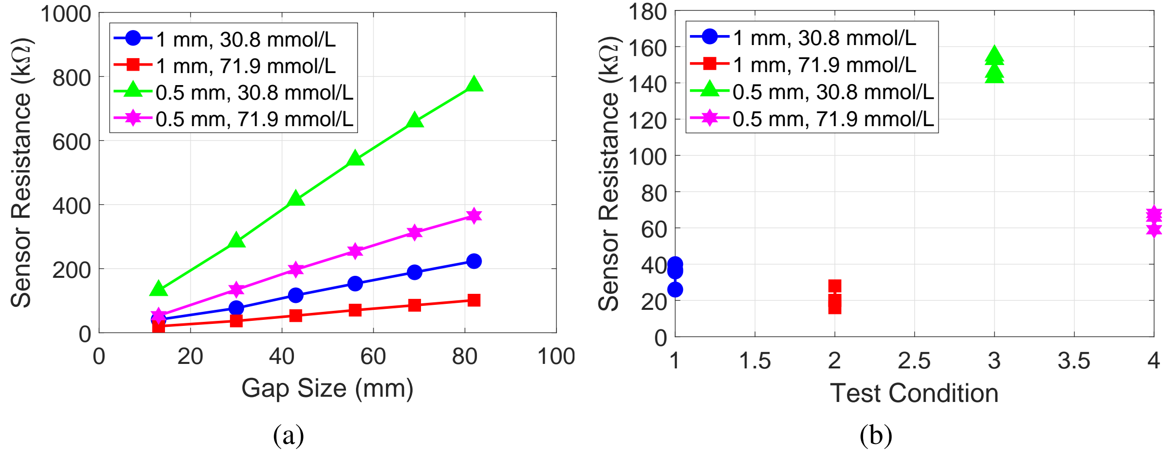


Figure 5.26: (a) The measured resistances of the microfluidic sweat sensor (b) the stability and repeatability test of the microfluidic sweat sensor.

printed SNP electrodes are printed on a flexible PET substrate. Multiple electrodes separated with different distances are printed for the resistance test. A half-circle cylinder channel (as shown in Figure 5.24) with 1 mm diameter is 3D printed with flexible resin named Flexible 80A from Formlabs. The entire sweat sensor is flexible and wearable as shown in Figure 5.25b. To combine the electrodes and the microchannel, a thin layer of Flexible 80A is applied around the microchannel. Then the PET and the 3D printed microchannel is pressed together and cured under UV light for 3 minutes.

### 5.4.3 Microfluidic Sweat Sensor Performance

The fabricated test vehicles with different micro-channel sizes are measured with a multimeter. The DC resistances under different gap sizes between two electrodes are summarized in Figure 5.26a. Two micro-channel diameters, 1 mm and 0.5 mm, are used. Besides, two different concentrations, 30.8 mmol/L and 71.9 mmol/L, of NaCl solutions are injected into the microchannel to mimic the human sweat. As shown in Figure 5.26a, the resistances of the smaller microchannel are larger than larger microchannel cases. Moreover, the solution with a larger concentration has larger conductivity and thus, the resistances are smaller. For the same micro-channel diameter and concentration, the resistance is proportional to the gap size.

To test the stability and repeatability of the process, multiple test samples are fabricated. The gap sizes between two electrodes of all test samples are 13 mm. There are four test conditions as shown in Figure 5.26b. As shown in Figure 5.26b, for the same test condition, multiple samples demonstrate very close measured results. Therefore, the repeatability of this process is very good which means this process can be applied to large-scale fabrication and the differences between each sample are small.

## 5.5 Energy-autonomous Backscatter Microfluidic Sensing System

The energy harvester, power management circuit, and microfluidic sensors are all finished in the previous sections. In this section, all circuits are integrated to form a wearable long-range backscatter microfluidic sensing system.

### 5.5.1 RF Switch Design

The first part of the backscatter microfluidic sensing system is a RF switch which can create two states of loading impedances for the antenna. Two switches including a MOSFET BF 1118 and a pin diode SMP 1340 are tested. The performances are compared and trade-off to select the most suitable topology.

*RF Switch BF 1118*

The RF switch BF 1118 and the testing circuit as shown in Figure 5.27 is fabricated and measured. The two 470 pF capacitors are used as the DC block while a 390 nH inductor is used to feed the oscillator output signal. The measured $S_{21}$ is shown in Figure 5.28. At 0 V (short), the ideal result is 0 dB which means all power is passing to the rectifier. On the other hand, the result at 3 V (open) should be as low as possible to create two distinct states for backscatter. The carrier frequencies for the backscatter is UHF from 860 to 960 MHz. The 3 V $S_{21}$ is lower than -20 dB within 860 to 960 MHz which meets the requirement. However, the 0 V $S_{21}$ is -2.68 dB which is the loss due to the switch. The loss is so high that

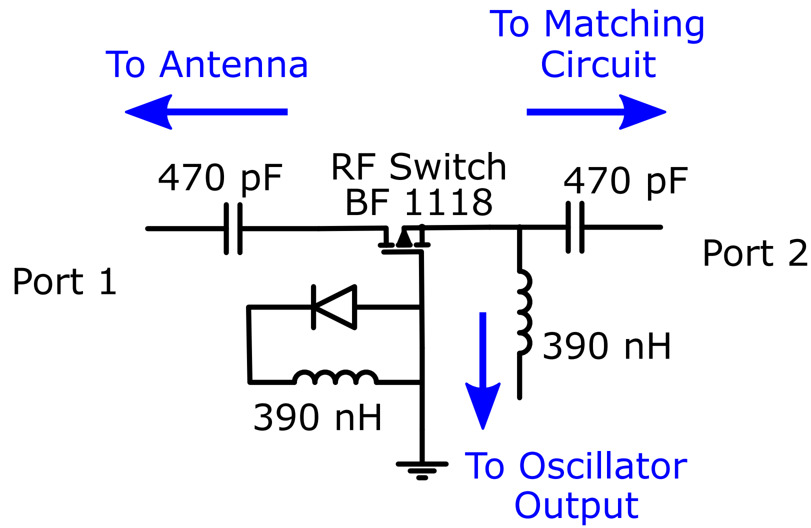


Figure 5.27: The circuit diagram of the RF switch design using MOSFET BF 1118.

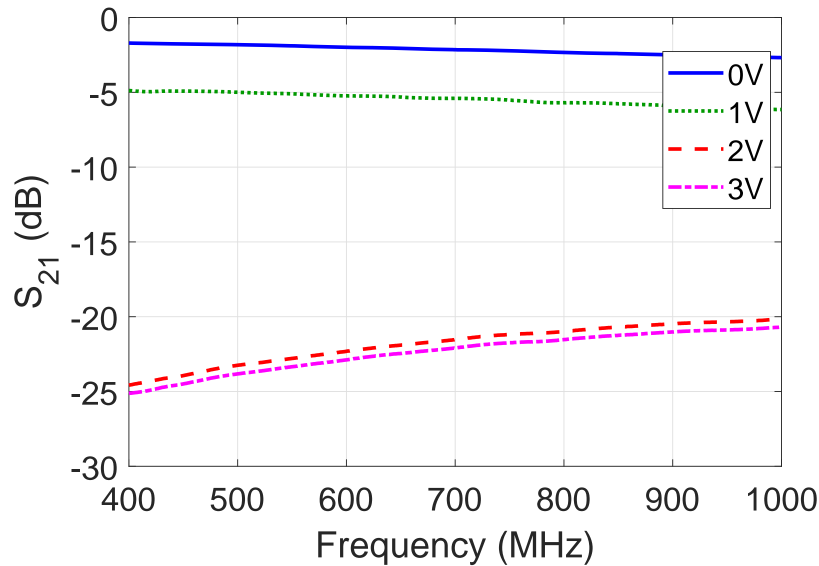


Figure 5.28: The measured $S_{21}$ of the RF switch using MOSFET BF 1118.

the efficiency of the entire energy harvester is dropped. Therefore, another switch topology is adopted.

*Pin Diode SMP 1340*

The pin diode SMP 1340 is used to create RF switch for backscatter. The testing circuit and the fabricated prototype are shown in Figure 5.29. A 490 pF capacitor is used as the DC block and a 39 nH inductor is used to feed the oscillator output signals. The measured

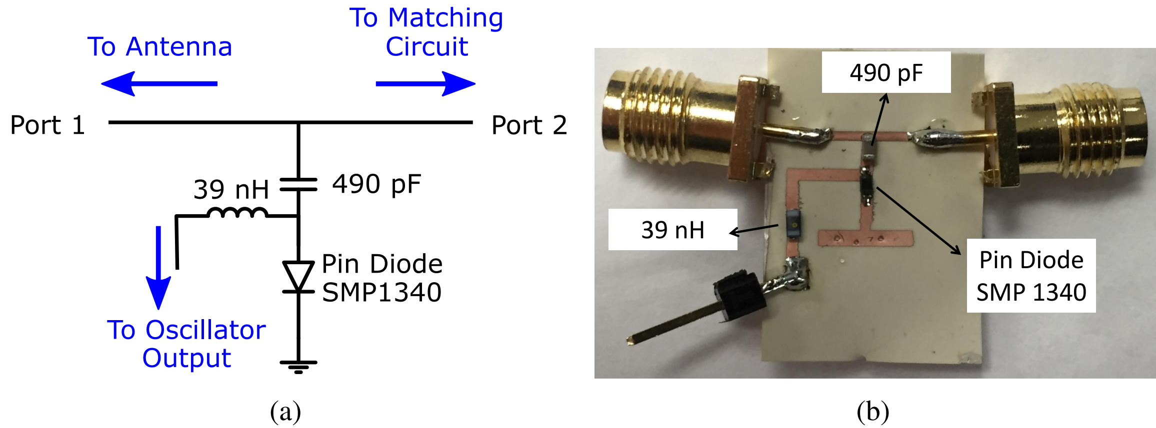


Figure 5.29: (a) The circuit diagram and (b) prototype of the RF switch design using pin diode SMP 1340.

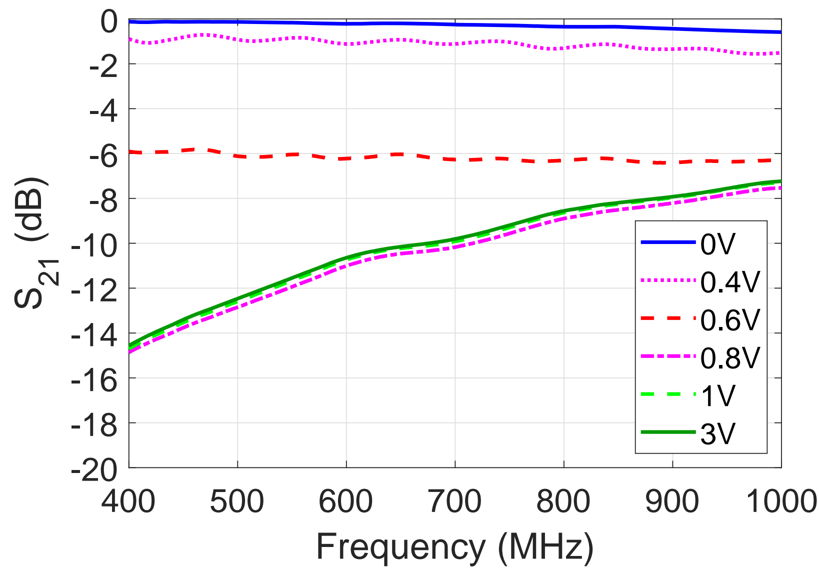


Figure 5.30: The measured $S_{21}$ of the RF switch using pin diode SMP 1340.

$S_{21}$ is shown in Figure 5.30. At 0 V (short), the $S_{21}$ is -0.58 dB which is very close to 0 dB. That means the loss due to the switch is very small. At 3V (open), the $S_{21}$ is -7 dB which is good enough to be distinguished between the matched state. The loss imposed by the pin diode switch (-0.58 dB) is much smaller than the MOSFET (-2.68 dB). Therefore, the pin diode topology is adopted for the backscatter system.

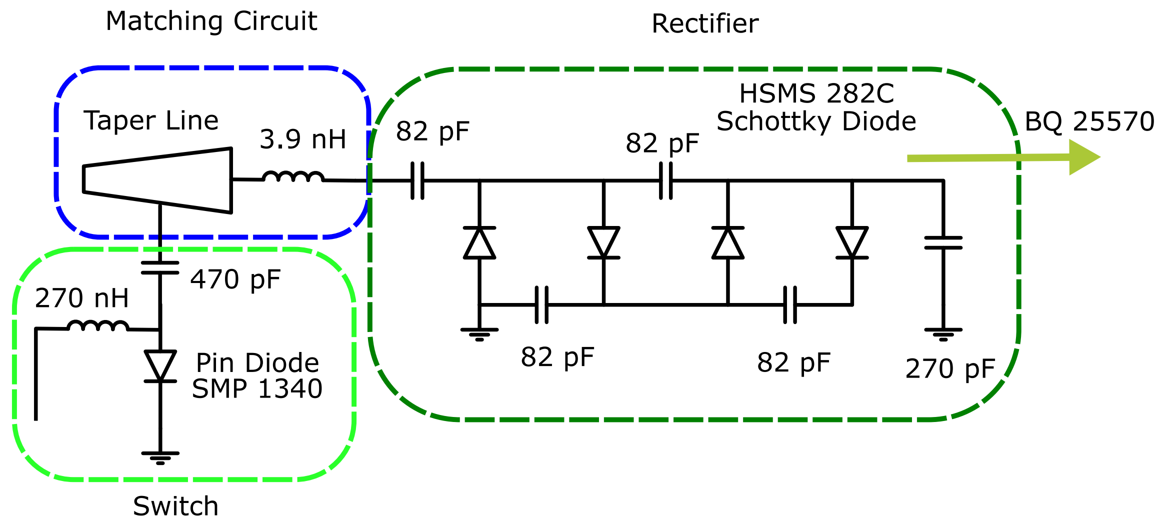


Figure 5.31: The circuit diagram of the proposed rectifier with switch and power management circuit load.

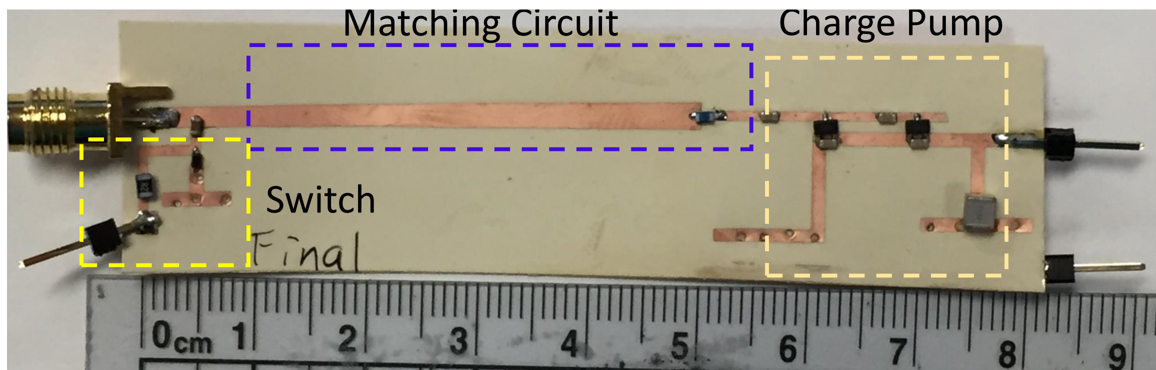


Figure 5.32: The fabricated prototype of the proposed rectifier with switch and power management circuit load.

### 5.5.2 Energy Harvester Design

The energy harvester design including the switch is shown in Figure 5.31 while the fabricated prototype is shown in Figure 5.32. The rectifier is still a two-stage charge pump and the matching circuit is composed of a 3.9 nH capacitor and a tapered line. The length of the tapered line is 50 mm with a left-end width of 1.67 mm and a right-end width of 2.4 mm. A 270 pF capacitor is placed at the load to filter the higher-order harmonics. The pin diode switch is connected to the tapered line at a 4.6 mm distance from the left. The measured output voltage and output power with respect to different frequencies are shown in Fig-

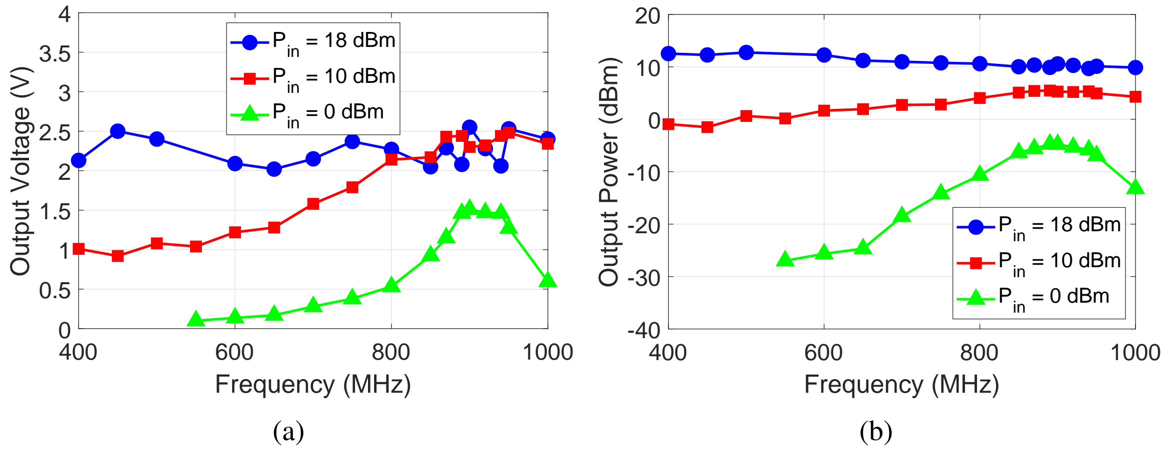


(a) (b)

Figure 5.33: (a) The measured (a) output DC voltage and (b) output DC power of the proposed rectifier with switch and power management circuit load at different frequencies.

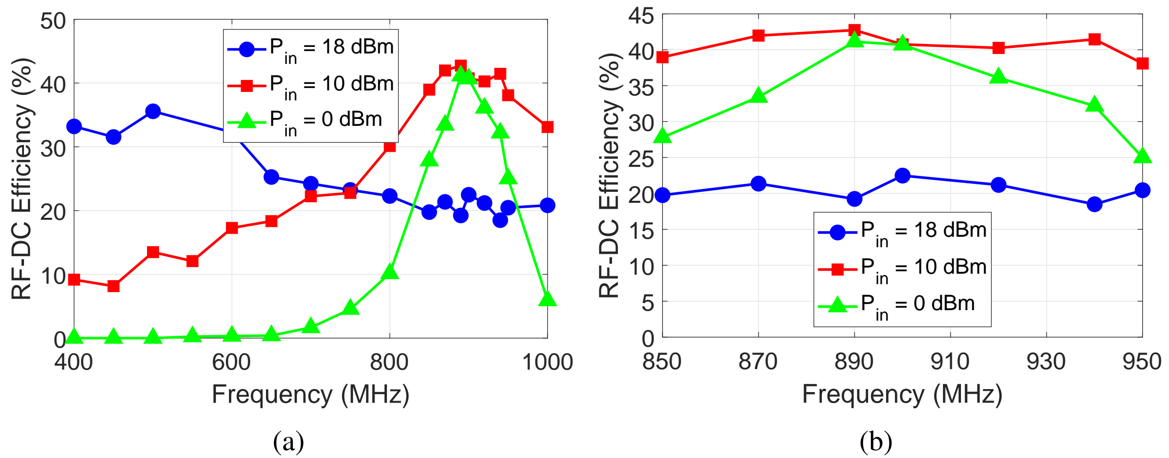


(a) (b)

Figure 5.34: The measured RF-DC efficiency of the proposed rectifier with switch and power management circuit load at different frequencies from (a) 400 MHz to 1000 MHz and (b) from 850 MHz to 950 MHz.

ure 5.33. The step for the marker is 50 MHz. The measured RF-DC efficiency including the pin diode switch loss with respect to different frequencies are shown in Figure 5.34. As shown in Figure 5.34, for large input power (18 dBm), the largest efficiency is at 500 MHz which is very close to the two-way radio operating frequency. For small input power such as 10 dBm and 0 dBm, the highest efficiency is at 890 MHz which is within the UHF RFID band. Furthermore, the RF-DC efficiency within 850-950 MHz is demonstrated in Figure 5.34b. A flat and broadband performance is obtained using the energy harvester design.

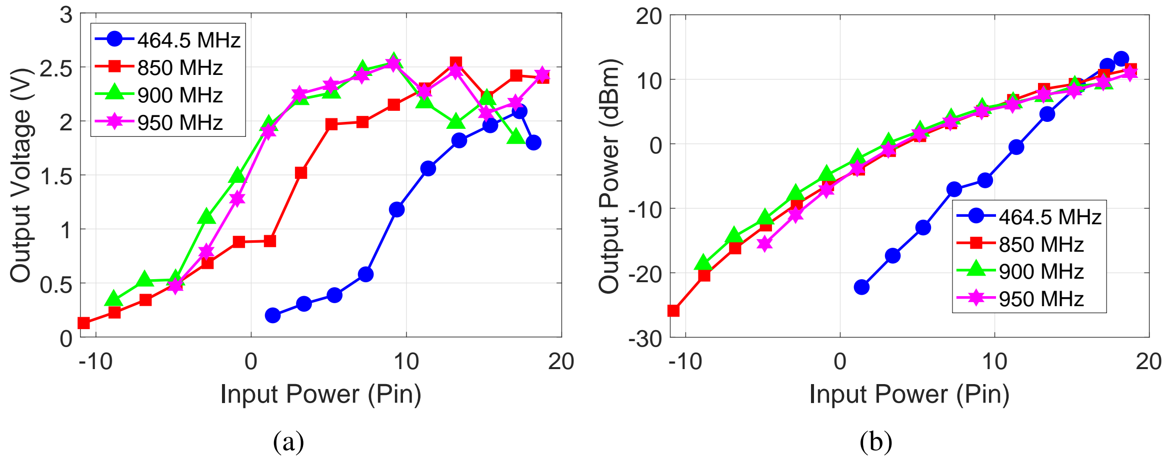


Figure 5.35: (a) The measured (a) output DC voltage and (b) output DC power of the proposed rectifier with switch and power management circuit load at different input powers.

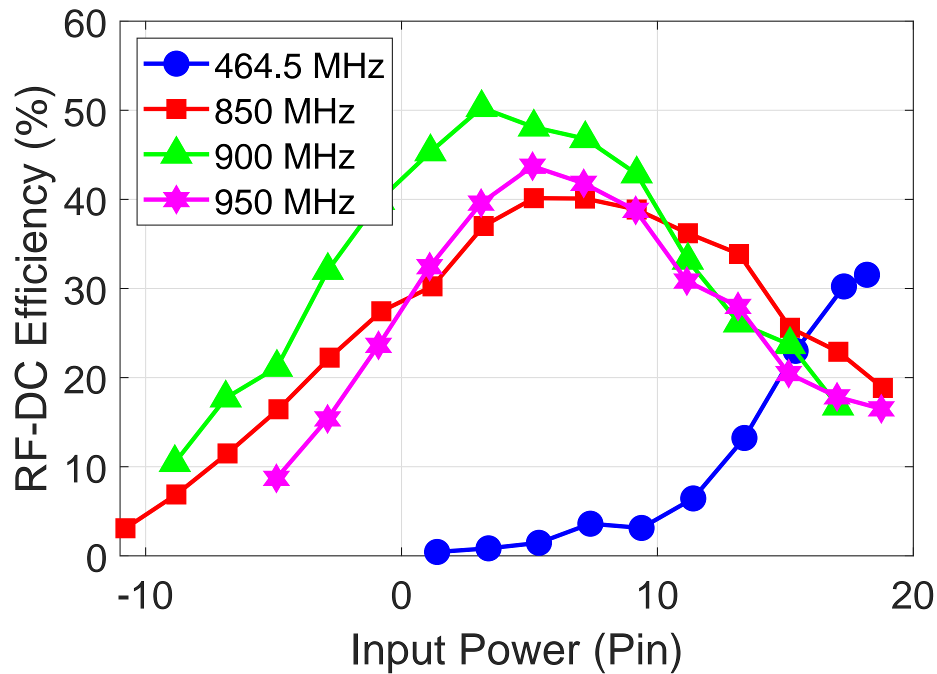


Figure 5.36: The measured RF-DC efficiency of the proposed rectifier with switch and power management circuit load at different input powers.

The measured output voltage and output power from the energy harvest at different input powers are shown in Figure 5.35. As shown in Figure 5.35, for two-way talk radio at 464.5 MHz, the output voltage is 0.31 V while input power is 3.4 dBm. Thus, the minimum input power to overcome the cold-start voltage (0.33 V) of BQ 25570 while harvesting power from two-way radio is about 4 dBm. On the other hand, the minimum input power

Table 5.3: The highest efficiency of different frequencies for the energy harvester with switch.

| **Frequency (MHz)** | **Efficiency (%)** | **Input Power (dBm)** |
|---|---|---|
| 464.5 | 31.54 | 18.19 |
| 850 | 40.14 | 5.17 |
| 900 | 50.29 | 3.13 |
| 950 | 43.72 | 5.12 |

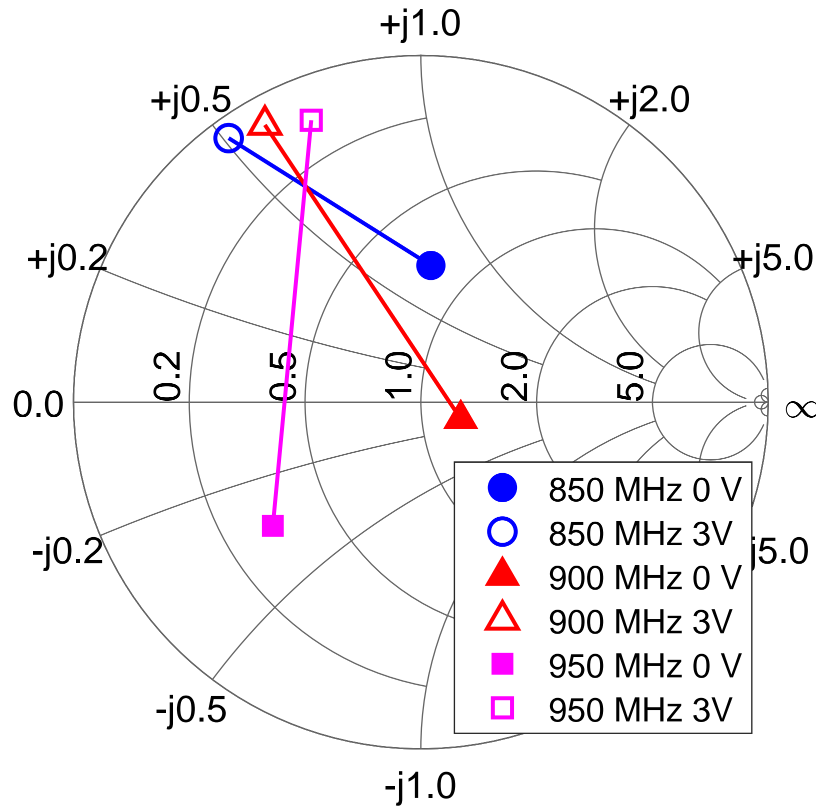


Figure 5.37: The measured input impedances of the rectifier while the switch is on different states.

to overcome the cold-start voltage while harvesting power from UHF RFID reader is -5 dBm. Therefore, for continuous far-field energy harvesting from UHF RFID reader, the minimum input power or sensitivity is -5 dBm which is much better than 14 dBm in the first design introduced in subsection 5.2.3. The measured RF-DC efficiency including the pin diode switch loss with respect to different input power are shown in Figure 5.36 and the largest efficiencies at different frequencies are summarized in Table 5.3. The highest

efficiency for near-field two-way radio is at large input power 18.19 dBm. On the other hand, the highest efficiency for far-field UHF RFID is at low input power around 5 dBm. Therefore, the proposed energy harvester can integrate both near-field and far-field energy sources and achieve the highest efficiencies at respective input power levels. Besides, the change of the loading impedance at different input power as demonstrated in Figure 5.14 is also taken into consideration and good performances are achieved.

The measured input impedance of the rectifier, while the switch is on different states is shown in Figure 5.37. While at 0 V, the antenna is connected to the rectifier with a matching circuit. At 3 V, the antenna load is at a different state. As shown in Figure 5.37, two different states are created successfully for the backscatter sensing purpose and the differences between two states are large enough to be distinguished.

### 5.5.3 Microfluidic Sweat Sensor

The sensor used here is an additive manufacturing microfluidic sweat sensor. The fabrication process has been introduced in section 5.4. The design schematic is shown in Figure 5.38a. Two electrodes are inkjet printed on PET with 30 mm separation distance as shown in Figure 5.38b. The microchannel is 3D printed using Flexible 80A material and the channel diameter is 0.5 mm. The test samples of the microfluidic channel are shown in Figure 5.38c. Then the electrodes and the microchannel are combined as shown in Figure 5.38d.

The DC resistance of the sweat sensor is measured with a multimeter. As demonstrated in Figure 5.39a, the resistance between two electrodes is about 17 MΩ when the microchannel is filled with distilled water. Since the human sweat conductivity is within 26 mmol/L and 80 mmol/L NaCl solution, two NaCl solutions with concentrations 30.8 mmol/L and 71.9 mmol/L are used for testing. The measured resistance is 348 kΩ when the microchannel is filled with 30.8 mmol/L NaCl solution as shown in Figure 5.39b. On the other hand, the measured resistance is 166 kΩ when the microchannel is filled with 71.9 mmol/L NaCl

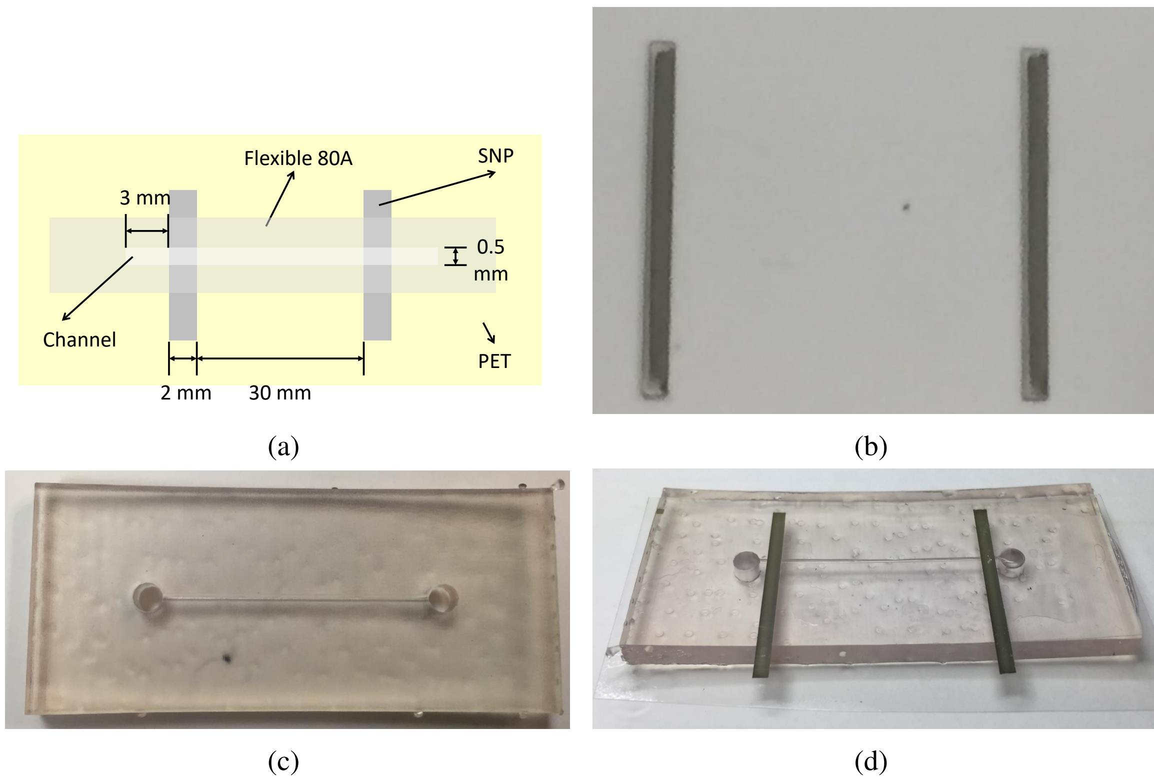


(a) (b) (c) (d)

Figure 5.38: (a) The design schematic of the sweat sensor, (b) the inkjet printed electrodes, (c) the 3D printed flexible microchannel, and (d) the sweat sensor test sample

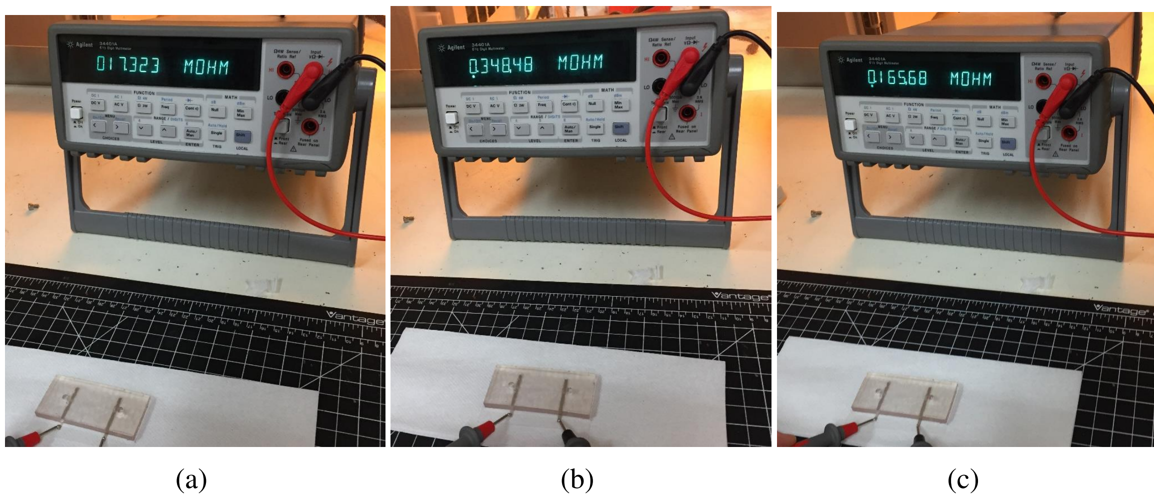

(a) (b) (c)

Figure 5.39: The measured resistance of the microfluidic sweat sensor while the microchannel is filled with (a) distilled water (b) 30.8 mmol/L NaCl, and (c) 71.9 mmol/L NaCl

solution as shown in Figure 5.39c. The resistance of the higher concentration solution is smaller since the conductivity is higher. The resistances are about 2 times of difference which is large enough for the backscatter sensing to distinguish the difference.

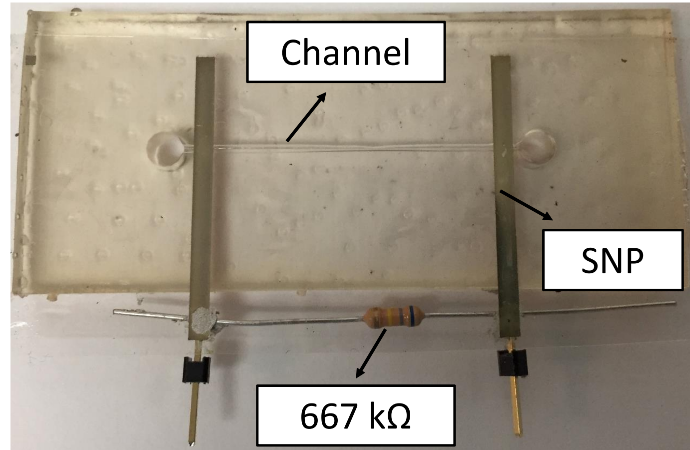


Figure 5.40: The prototypes of the microfluidic sweat sensor with a default resistor.

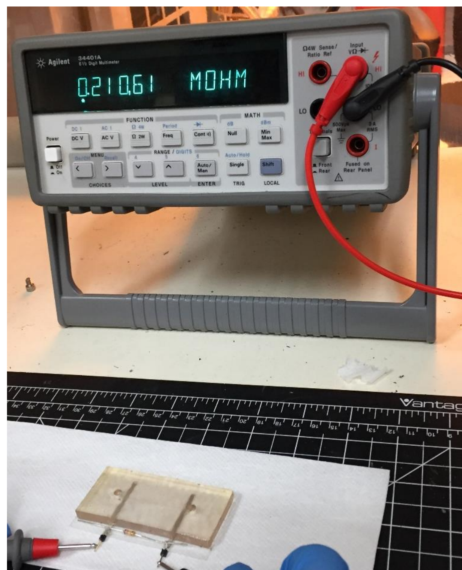


(a)

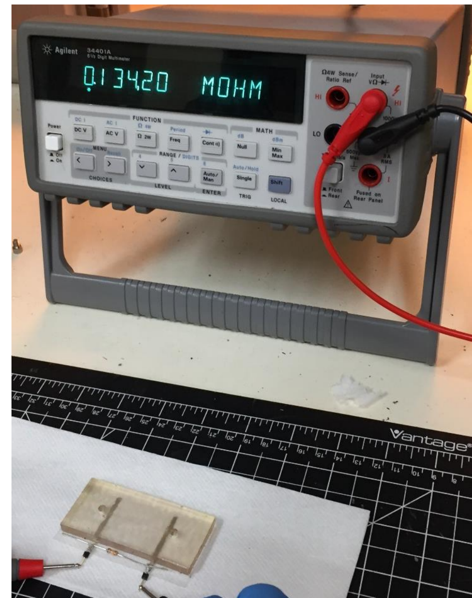


(b)

Figure 5.41: The measured resistance of the microfluidic sweat sensor with default resistor while the microchannel is filled with (a) 30.8 mmol/L NaCl and (b) 71.9 mmol/L NaCl

The sensor is used as the load of the timer to control the oscillating frequency. However, the resistance of the sensor is open when the microchannel is empty and the timer can not handle that. To sense that the channel is empty, a default 667 k$\Omega$ resistor is paralleled with the microfluidic sensor as shown in Figure 5.40. This test vehicle is used as the final sweat sensor for the backscatter sensing system. The sweat sensor with a resistor is also measured using a multimeter and two solutions with concentrations equal to 30.8 and 71.9 mmol/L.

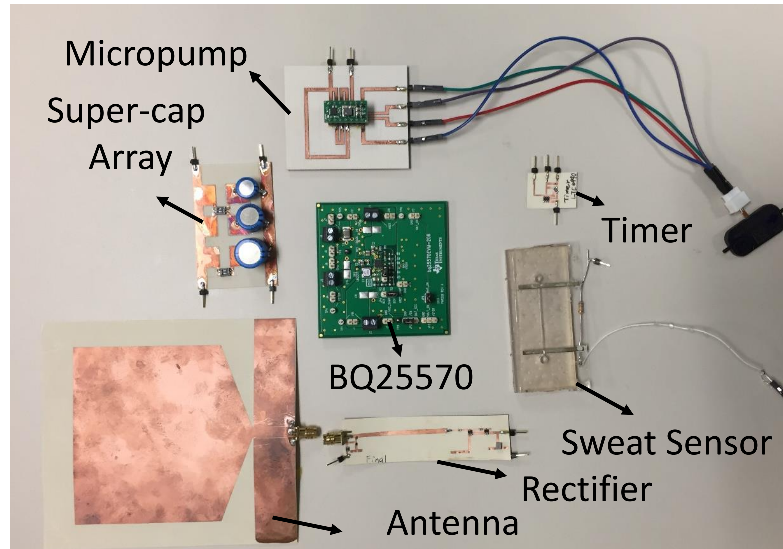


Figure 5.42: The prototypes of all components of the proposed EH powered backscattering sensing system.

As shown in Figure 5.41, the resistances of the sweat sensor when 30.8 and 70.1 mmol/L NaCl solution is filled inside the microchannel are 211 kΩ and 134 kΩ, respectively. The difference between two resistances is still large enough for the system to distinguish them.

### 5.5.4 Backscattering Sensing System Performance Evaluation

All components for the backscatter microfluidic sensing system including the energy harvester, the power management circuit, the power storage supercapacitor array, the micropump, the timer to generate oscillate frequencies, and the microfluidic sweat sensor are shown in Figure 5.42. The BQ 25570 shown here is the evaluation board and the size can be reduced easily. The system topology is shown in Figure 5.3. Two main system performance evaluations are tested in this section. One is from the power perspective. In this test, the main focus is to prove that the timer and micropump can be successfully driven with the power harnessed by the energy harvester. Furthermore, the charging and discharging (operation) times when using two-way radio or UHF RFID as the energy sources are also included. The other test is the wireless backscatter system measurement. The information of the sweat sensor is transmitted to the reader wirelessly. The sensing range and the SNR

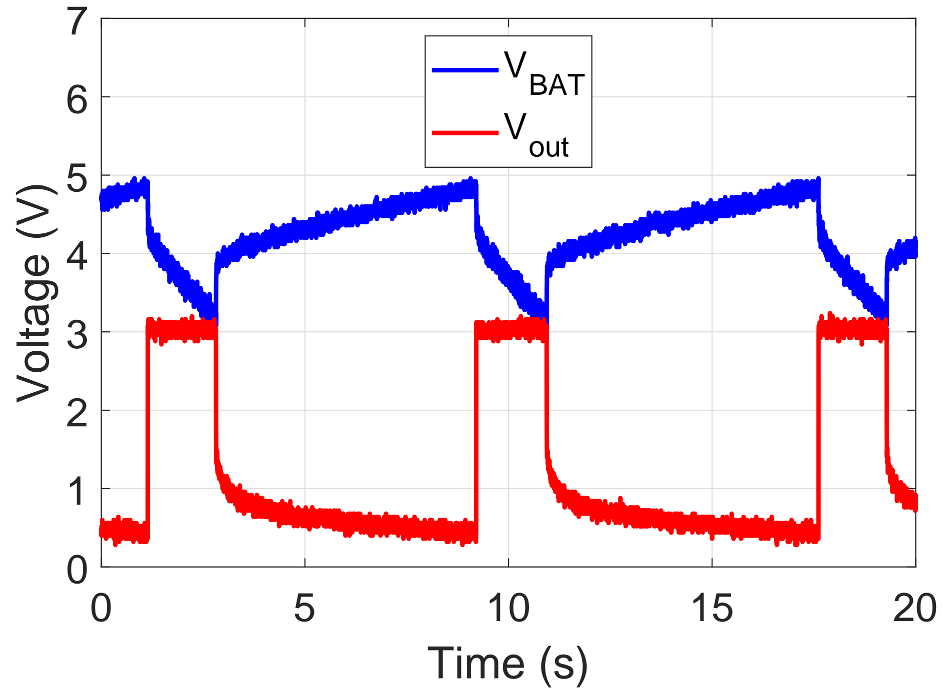


Figure 5.43: The output voltage waveforms of the power management circuit.

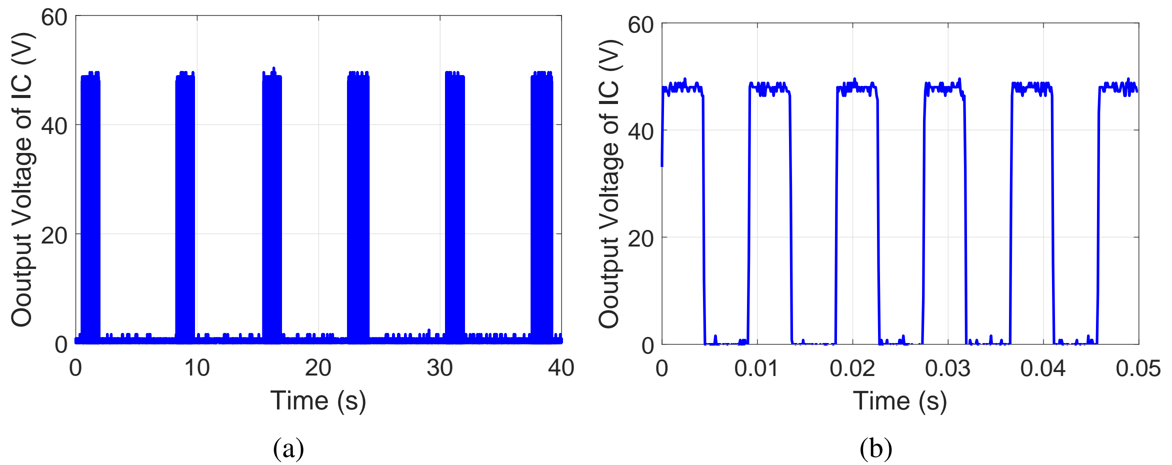


Figure 5.44: The output voltage waveforms of the micropump driving IC in (a) large time scale and (b) small time scale.

of the receiving signal are measured.

*Harvested Power Measurement*

All components are connected to build the backscatter microfluidic sensing system and the measured output voltage waveform from the power management circuit is shown in

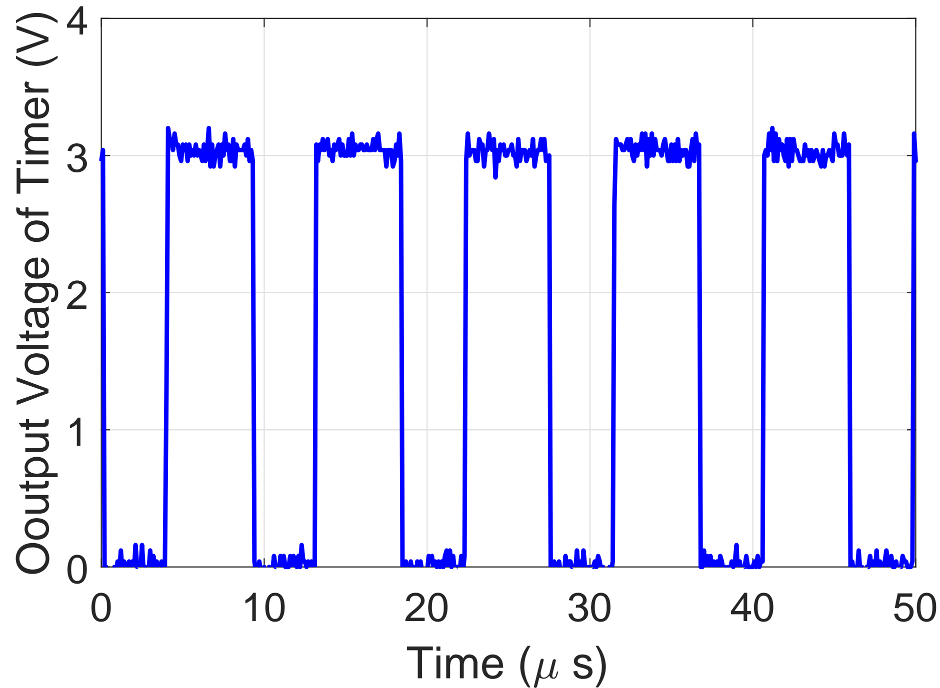


Figure 5.45: The output voltage waveforms of the oscillator.

Figure 5.43. The voltage waveform of the voltage across the supercapacitor ($V_{BAT}$) is also included for comparison. The $V_{BAT}$ is in the charging mode when the voltage drops 3 V and switch to the discharging mode when the voltage reaches 4.8 V as the expected design shown in Figure 5.13. Furthermore, the output voltage is a steady 3 V while in the discharging mode.

The micropump-driving IC is driven by the output 3 V from the BQ 25570 and the respective output voltage waveform is shown in Figure 5.44. The driving IC is successfully driven while the BQ 25570 is in the discharge mode. The oscillating frequency is 109 Hz with a voltage amplitude of 50 V. The micropump which is operated based on a piezoelectric can be driven with this voltage waveform and pump the liquids into the microchannel. In the meantime, the timer (oscillator) is also driven with the output voltage of the BQ 25570 and the waveform is shown in Figure 5.45. The oscillated frequency is 111 kHz while the controlled load resistor for the timer is 470 k$\Omega$. The voltage amplitude is 3V which is large enough to change the states of the switch.

The charging and discharging time using different input power levels at different fre-

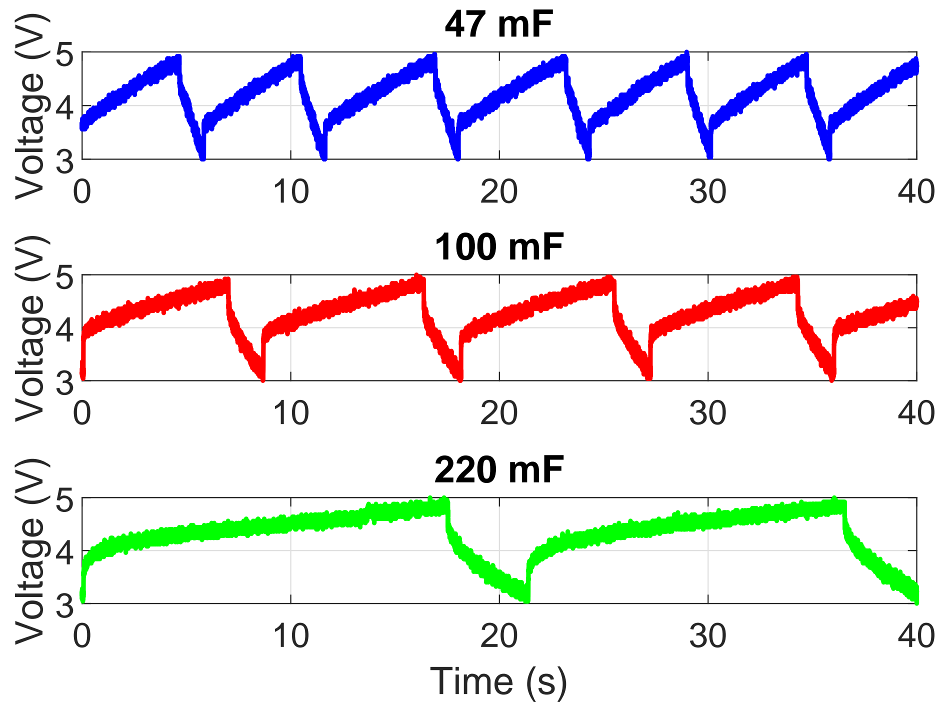


Figure 5.46: The voltages across energy storage devices (super-capacitor) while charging and discharging using a 20 dBm 464.5 MHz input signal.

Table 5.4: The charging and discharging time of the system while using a 20 dBm 464.5 MHz input signal.

| **Super-capacitor (mF)** | **Charging Time (s)** | **Discharging Time (s)** |
|---|---|---|
| 47 | 4.63 | 1.19 |
| 100 | 7.69 | 1.68 |
| 220 | 15.28 | 4.03 |

quencies are measured. The charging and discharging waveforms for different supercapacitors are shown in Figure 5.46. The input power is a 464.5 MHz, 20 dBm signal. The charging and discharging time are summarized in Table 5.4. For a smaller supercapacitor, it takes a shorter time to fully charge to 4.8 V and the discharging time is also shorter. As shown in Table 5.4, it takes only 15.28 seconds to fully charge the 220 mF supercapacitor and the micropump as well as the timer can be used for 4.03 second to pump the liquid into the microchannel and create the modulated backscatter signals.

The charging and discharging waveforms using 0 dBm UHF RFID signals are shown

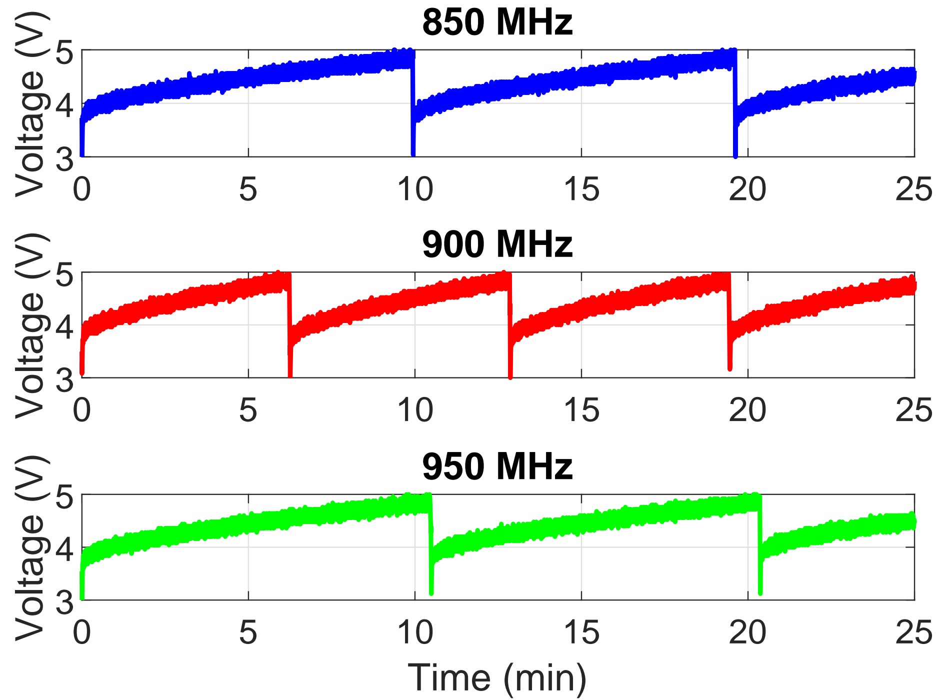


Figure 5.47: The voltages across a 47 mF super-capacitor while charging and discharging using 0 dBm input signals.

Table 5.5: The charging and discharging time of the system while using a 0 dBm input signal and a 47 mF super-capacitor.

| Frequency (MHz) | Charging Time (min) | Discharging Time (s) |
|---|---|---|
| 850 | 9.7 | 1 |
| 900 | 6.6 | 1 |
| 950 | 9.9 | 1 |

in Figure 5.47. The supercapacitor used here is 47 mF. The charging and discharging time are summarized in Table 5.5. As shown in Table 5.5, it takes about 6.6 to 10 minutes to fully charge the 47 mF supercapacitor and the micropump as well as the timer can be used for 1 second to pump the liquid into the microchannel and create the modulated backscatter signals. The moving speed of the micropump is 37.8 µL/s and the channel size can be filled with 3.9 µL of liquid. Thus, it only takes 0.1 seconds to fill the microchannel. Thus, 1 second usage time is long enough to fill the microchannel and detect the backscatter signals.

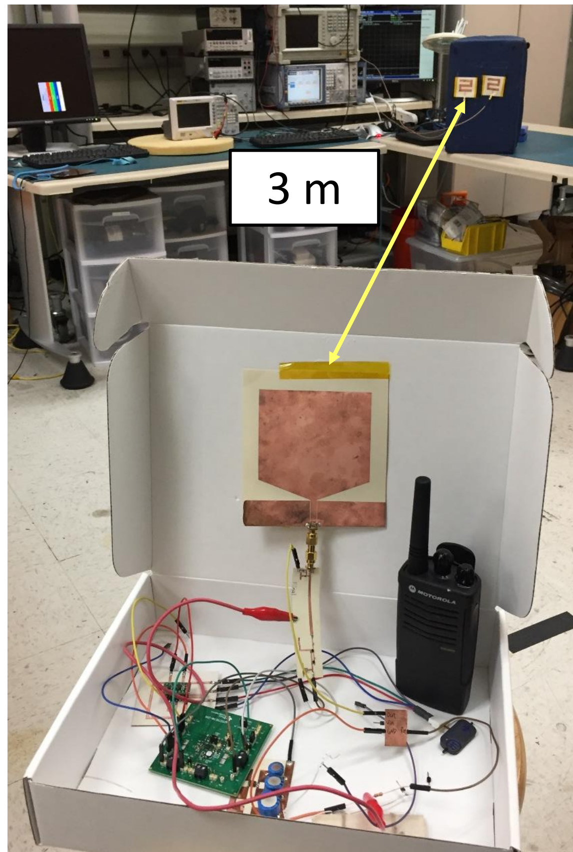


Figure 5.48: The measurement setup of the proposed EH powered backscattering sensing system.

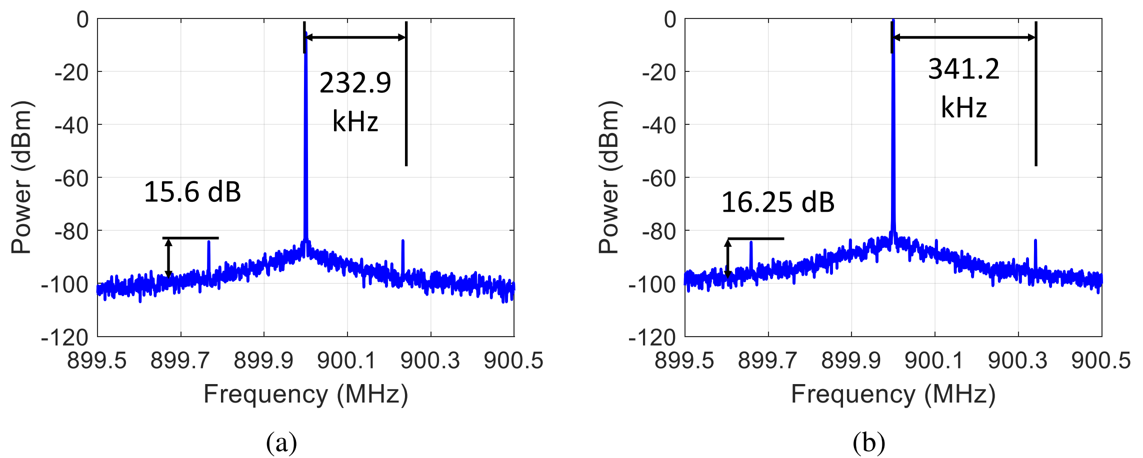


(a) (b)

Figure 5.49: The measured wireless backscattered signals when the sweat sensor is filled with (a) 30.8 mmol/L NaCl and (b) 71.9 mmol/L NaCl

*System Wireless Interrogation Measurement*

The wireless measurement setup for the backscatter sensing system is shown in Figure 5.48. The transmitter is the signal generator broadcasting a 12 dBm carrier signal that operates at 900 MHz and a monopole antenna. Thus, the transmitted EIRP is around 14 dBm. The receiver is a spectrum analyzer with a monopole antenna. The transmitter and the receiver are acted as a RFID reader and can be replaced with a cheap SDR. The distance between the reader and the sensing tag is 3 m. When the microchannel is filled with a 30.8 mmol/L NaCl solution, the measured results are shown in Figure 5.49a. There are three spikes. The center one at 900 MHz is the carrier signal. The other two spikes are the backscatter signals located at 232.9 kHz away from the carrier signal. The SNR is 15.6 dB. When the solution is replaced with a 71.9 mmol/L NaCl solution, the measured results are shown in Figure 5.49b. There are also three spikes. The center one at 900 MHz is still the carrier signal. The other two spikes are the backscatter signals but the distances between the carrier and the backscatter signals are now 341.2 kHz. The SNR is 16.25 dB.

The experiment can be used as proof showing that the system can be fully operated relying on the power collected by the energy harvester. The difference between two concentrations of the solutions is 108.3 kHz which is large enough to be distinguished. Furthermore, normally 3 dB of the SNR is large enough to detect the signal and the allowed EIRP is 36 dBm. Therefore, there is a 34.6 dB link budget spared and the reading range can be extended to 22 m if all link budget is used. The proposed system used backscatter topology. Therefore, the effects of clutters can be minimized.

## 5.6 Summary

A novel fully additive manufacturing energy-autonomous microfluidic backscatter sensing system is proposed. An energy-autonomous micropump system is proposed to provide actuation forces and open new applications for microfluidic such as smart skin and IoT. The

proposed energy harvester is the first design which harvests near-field two-way talk radio at 464.5 MHz and far-field UHF RFID reader from 860 MHz to 960 MHz simultaneously. The near-field two-way radio provides high input power but can only be harvested while it is in-use. The far-field UHF RFID provides continuous but lower power. By integrating both energy sources, the advantages of both kinds of energy sources can be included. The near-field energy harvesting can support high power at a certain time to overcome IC cold start and the far-field energy harvesting can harvest power all the time to maintain the function.

The power management circuit BQ 25570 is utilized. The energy harvester is carefully designed so that it has high RF-DC efficiency at 464.5 MHz with high input power. Furthermore, the same energy harvester can also achieve high RF-DC efficiency at 860-960 MHz with low input power. The proposed energy harvester is suitable to integrate both power and adapt to the impedance change of the BQ 25570 with respect to the input power level change.

A new fully additive manufacturing process to fabricate microchannels for microfluidic applications is also proposed. The new process is lower cost, fast prototyping, and can achieve a more complex structure. The conductivity changes of the fluids are utilized to realize a microfluidic sensor for backscatter sensing topology. Compared with the resonant type microfluidic sensor, the proposed backscatter sensing topology can be detected easily in a complex environment with clutters with a much cheaper SDR. A proof-of-concept microfluidic sweat sensor is fabricated and measured. The design shows good repeatability and the performance meets the expectation.

The energy-autonomous backscatter sensing system is built and measured. A flexible sweat sensor is demonstrated to realize real-time on-body health monitoring. The same type of microfluidic sensor can also be used for environmental sensing such as detecting acid rain. The system can be fully functional relying only on the power collected by the energy harvester. The backscatter signals are also measured to prove that the sensor information

is wirelessly delivered to the reader with long distances. The reading range is 3 m with 14 dBm EIRP and the SNR is larger than 15 dB. The reading range can be extended to 22 m when all 36 dBm EIRP is used and the SNR required is 3 dB. The detecting range is much longer compared with the resonant type microfluidic sensor.

From the energy harvester point of view, the proposed energy harvester is the first one which collects more energy by combining both near-field and far-field energy to have all advantages. It is also the first time the energy harvesting is applied to micropump to achieve a fully autonomous microfluidic application and expand the horizons of microfluidic applications. From the fabrication point of view, a fully additive manufacturing process for the microfluidic sensor is proposed. Thanks to the additive manufacturing technologies, the microfluidic sensor can be realized with lower cost, less waste, and more 3D structural flexibility. Finally, a novel energy-autonomous backscatter sensing system utilizing microfluidic sensing techniques is demonstrated and the reading range is much larger compared with other related works.

# CHAPTER 6
# BROADBAND 5G PACKAGE INTEGRATED ENERGY HARVESTER USING GLASS PACKAGING TECHNOLOGIES

With the incoming 5G wireless communication, there are numerous opportunities and challenges. The high EIRP allowed by FCC makes 5G signals a suitable source for energy harvesters. However, the high path loss and transmission loss remains a great challenge. Since the 5G wireless communication utilizes broad operational band at mm-wave frequencies to achieve high data rate and low latency, the wavelengths and the size of RF components can be reduced significantly. The size of RF components shrink to the same order as the IC package and thus, SiP technologies which integrate ICs with peripheral components such as filters, antennas, couplers, and matching circuits attract more attention.

Broadband AiP designs are important since one set of Multi-input Multi-output (MIMO) antenna array can be used to cover the whole 5G operating band. In addition to the component design, the packaging fabrication process is also a critical concern. Some perspectives which can be used to evaluate the packaging process are the electrical properties, surface roughness, Coefficient of Thermal Expansion (CTE) match to silicon, I/O density, and the precision of patterning. The glass packaging process is a good candidate to offer high precision and good performance.

In this chapter, the objectives and design ideas of using 5G wireless communication will be included in section 6.1. Then the glass SAP packaging fabrication process is introduced in section 6.2. The design, fabrication, and measurement of broadband AiP design which cover two 5G bands is demonstrated in section 6.3. The broadband AiP design is further improved with a smaller size and much broader bandwidth to cover all 3 5G bands in section 6.3. Finally, broadband package-integrated energy harvester designs are introduced in section 6.4.

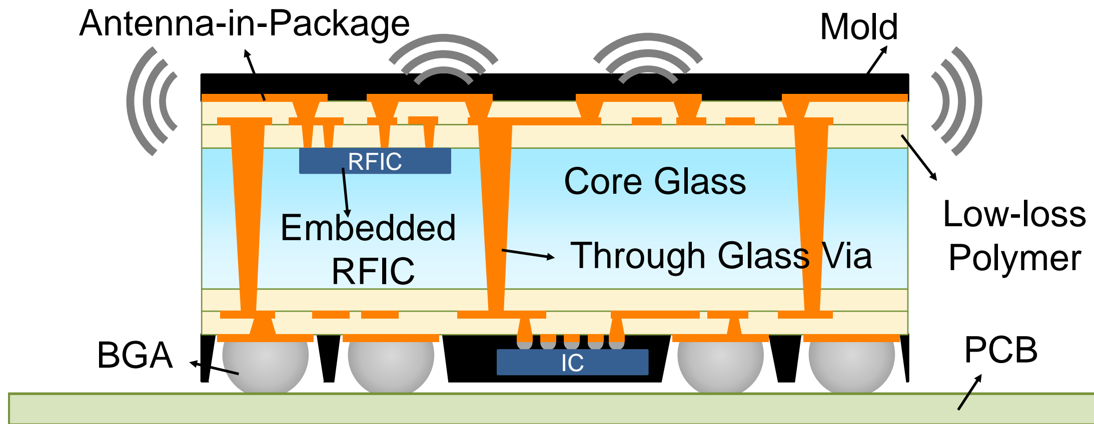


Figure 6.1: The 3D SiP module with AiP designs for 5G applications.

Table 6.1: The frequency bands of the 5G NR wireless communication.

| Band Name | Bang Alias | Frequency Range (GHz) | Bandwidth (GHz) |
|---|---|---|---|
| n257 | 28 GHz | 26.5 - 29.5 | 3 |
| n258 | 26 GHz | 24.25 - 27.5 | 3.25 |
| n260 | 39 GHz | 37 - 40 | 3 |
| n261 | 28 GHz US | 27.5 - 28.35 | 0.85 |

### 6.1 Objectives and Design Ideas

Numerous opportunities and challenges have emerged with the launching of the new 5G wireless communication [97]. The adoption of mm-wave frequencies and a wider spectrum provide the 5G communication a much higher data rate, low end-to-end latency, and the ability to connect more users simultaneously. These advantages are used to advance the development of emerging technologies including automatic driving and IoT. However, the high over-the-air path loss and high transmission loss within the circuit board at mm-wave range remain great challenges.

The mm-wave beamforming technology has been a popular method to solve the high over-the-air path loss problem [98, 99]. In the meantime, AiP technology remains an attractive solution to reduce the high transmission loss at mm-wave range [98, 100, 101]. The schematic of a 3D SiP module with AiP designs for 5G applications is shown in Figure 6.1.

The mm-wave Radio Frequency Integrated Circuit (RFIC) is embedded inside a cavity and placed at the proximity of the AiP designs while other low-frequency ICs can be flip-chip bonded at longer distances. Since the originally on-board antenna arrays are now migrating to AiP designs, the interconnect lengths and the resulting transmission losses between RFIC and antennas are significantly reduced.

Taking both beamforming and AiP into consideration, massive arrays that can enhance the gain values and beamforming capabilities while the overall sizes are small enough to be integrated inside the package are necessary. Current 5G NR standard utilize three different bands: n257 (26.5 - 29.5 GHz), n258 (24.25 - 27.5 GHz), and n260 (37 - 40 GHz) as summarized in Table 6.1. The n261 band is just a sub-band of n257. If three sets of antenna arrays covering each band have to be integrated into a single package, the element number in each array has to be reduced resulting in the decrease of the gain values and beamforming capabilities. Thus, a broadband and miniaturized AiP element design which covers all three bands from 24.25 to 40 GHz is necessary to reduce the set of arrays and achieve better performances. Recently, there have been many reports of AiP element designs and researches using different fabrication processes. In [102], a 3D-printed AiP design is introduced. A multi-layer AiP structure utilizing organic substrates has been described in [98]. However, these designs are not broadband enough to cover the whole 5G band and the sizes can be further improved.

In this chapter, the main objective is to propose a size-reduced UWB planar Yagi-Uda AiP element, array, and energy harvester design which can cover all three 5G bands from 24.25 to 40 GHz. The detailed objectives, comparisons to prior arts, challenges, and solutions are summarized in Figure 6.2. To miniaturize the size, the antenna element structure is modified to simplify the feeding network while removing the requirement for the balun. For the UWB planar Yagi-Uda element design, instead of the dipole-type radiator, the monopole-type radiator is used to further reduce the size. Both a single antenna element and a 2-by-1 array are demonstrated. Broadband characteristics and excellent end-

| Metrics | Objectives | Prior Art | Challenges | Solutions |
|---|---|---|---|---|
| **AiP Element Performance** | • UWB size reduced planar Yagi AiP element design<br>• Gain > 4 dBi<br>• FBW > 49 %<br>• 24.25 - 40 GHz<br>• Size < λ/2 | • FBW < 20%<br>• Size ≈ λ/2 | • Size reduction<br>• Bandwidth enhancement | • Monopole-type Yagi<br>• Eliminated the balun<br>• Simplified the feeding network<br>• Tapered radiator |
| **EH Performance** | • Harvested 5G signals<br>• 24.25 – 29.5 GHz<br>• 37 – 40 GHz | • Narrow band | • Broadband design<br>• Operated in mm-wave range | • Broadband matching network<br>• Adopted mm-wave diodes and a suitable rectifier topology |
| **Glass Packaging Process** | • Applied new low-loss material to glass SAP packaging process<br>• Reduced the warpage<br>• Dk = 2.8 @ 32 GHz<br>• Df = 0.0045 @ 32 GHz | • ABF substrate with larger warpage | • Material compatibility to SAP process<br>• Warpage reduction | • Soft low-loss material from JSR Corp.<br>• Characterized the fabrication process |

Figure 6.2: The summarizing table of the objectives, challenges, and solutions of the proposed 5G UWB AiP and energy harvester design.

fire radiation capability are confirmed with the measured return losses, gain values, and radiation patterns. For the fabrication of the proof-of-concept test vehicles, the low-cost good-scalability glass packaging technology [103–105], which offers great surface roughness, CTE match to silicon dies, and fine-pitch lines, spaces [106], and vias [107] for high-speed high-I/O computation is adopted. New low-loss material from JSR Corp. is also used. Since the new material is softer with a larger elongation factor, the warpage can be reduced. For the 5G UWB energy harvester design, broadband matching networks and rectifiers operated at mm-wave frequencies are also proposed. Two rectifiers covering 24.25-29.5 GHz and 37-40 GHz are proposed. The broadband package-integrated energy harvesters can be realized by combining the proposed UWB planar Yagi-Uda AiP element design, 5G UWB rectifier designs, and a diplexer.

## 6.2 Glass SAP Process for Package Fabrication

### 6.2.1 Glass Packaging Method

*Glass Properties*

The relative dielectric constant and loss tangent of AGC EN-A1 glass are summarized in Figure 6.3. The dielectric constant at 35 GHz is 5.41 and the loss tangent is 0.009. Low-

| Freq (GHz) | Dk | Df |
|---|---|---|
| 2.4 | 5.49 | 0.0041 |
| 5.2 | 5.48 | 0.0048 |
| 10 | 5.49 | 0.0062 |
| 20 | 5.43 | 0.0069 |
| 24 | 5.26 | 0.0079 |
| 35 | 5.41 | 0.009 |
| 55 | 5.46 | 0.0088 |
| 60 | 5.46 | 0.0096 |
| 65 | 5.45 | 0.0104 |

Figure 6.3: The dielectric constant and loss tangent of the AGC EN-A1 glass substrate.

loss polymer layers are laminated on the glass before the conductive copper layer as shown in Figure 6.1. The commonly used polymers are ABF from Taiyo company. The relative dielectric constant for ABF is 3.3 and the loss tangent is 0.0025. The effective dielectric constant of the system can be reduced significantly. A new liquid type polymer developed by JSR corporation is also a good candidate for low loss polymer. The relative dielectric constant is 2.8 and the loss tangent is 0.0045 at 32 GHz. Compared with ABF, the JSR material is softer and has a larger elongation factor. Thus, it can be used to effectively prevent the warpage in multi-layer packaging structures.

*Packaging Methods Comparison*

The comparisons between the glass packaging process and other packaging processes are summarized in Figure 6.4. The PCB based, Low Temperature Co-fired Ceramic (LTCC), organic, and fan-out wafer-level packaging processes are included for comparison. The green color suggests the property is good while the red suggests that the property is bad. From the material property point of view, as shown in Figure 6.4, the glass process can offer the best surface roughness which is especially critical for mm-wave applications. The

| Characteristic | PCB-based | LTCC | Organic laminates | FO-WLP | Glass |
|---|---|---|---|---|---|
| **Material Properties** | | | | | |
| Relative dielectric constant (εr) | 4 – 6 | 5 – 10 | 2.9-3.2 | 3.68 | 2.7 – 6 |
| Loss tangent × $10^4$ (tanδ @ GHz) | 20 @ 10 | 12 @ 10 | 40 @ 60 | 80 @ 58 | 3 – 62 @ 10 |
| Surface roughness (nm) | 300-5800 | 177 | 400-600 | > 1000 on EMC | <1 |
| Coefficient of thermal expansion - CTE (ppm/K) | 17 | 5.5 – 7.2 | 17 | 30 (EMC) | 3-8.5 |
| Dimensional stability - Young's Modulus (GPa) | 21 – 24 | 90-150 | 10-40 | 22 | 50-90 |
| Water absorption | 0.1%-0.25% | 0 | 0.040 % | | 0 |
| **Process Challenges** | | | | | |
| Multi-layer process alignment | | | | | |
| Small-feature patterning | | | | | |
| Thin substrate reliability | Warpage | | Warpage | | Cracking |

Good — FO-WLP: Fan-Out Wafer-Level Packaging

Medium — EMC: Epoxy Mold Compound

Bad

Figure 6.4: The comparisons between the glass packaging and other packaging methods.

CTE of silicon is 2.6 ppm/K which is close to the glass. This offers a great advantage for the packaging process when the silicon die and packaging structures are integrated to realize a SiP design. The glass is also solid with no water absorption which provides solid protection and great support.

From the process challenge point of view, the glass can achieve precise multilayer patterning with good alignment and small resolution. Moreover, the thin substrate is helpful to reduce the width of the transmission line to maintain 50 Ω and realize high-density I/O

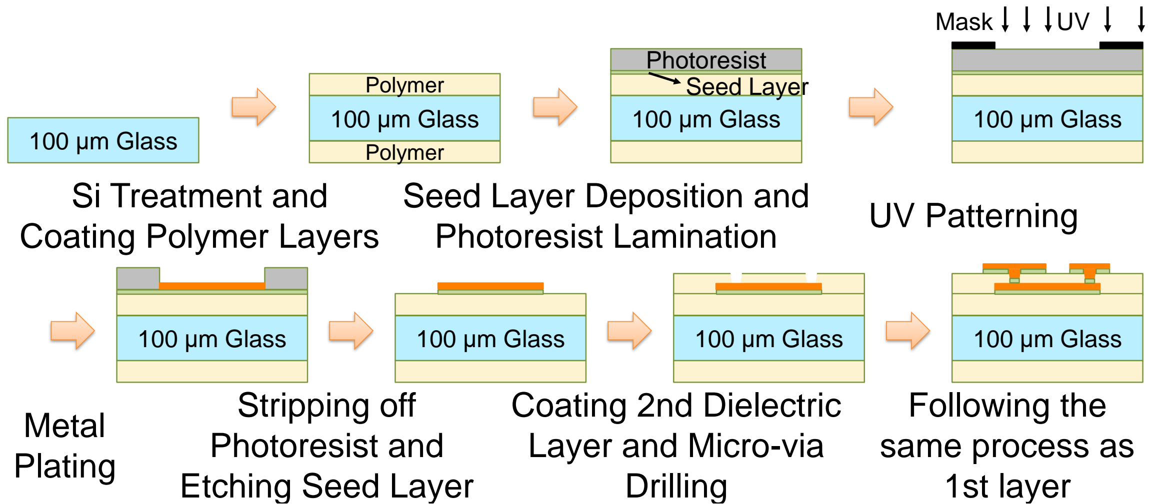

Figure 6.5: Fabrication process of glass SAP packaging technology.

packaging. Thus, the reliability of a thin substrate is also a critical property. Compared with other packaging technologies, the glass offers both good physical properties and electrical properties. Besides, the glass is easier to handle and support good process reliability and resolution.

### 6.2.2 SAP Process

The SAP process was used for the fabrication of designs in this chapter. SAP enables precise patterning and fine features such as sub-5 µm copper traces because of dimensional stability and surface planarity of the glass panel and the capability to accurately control the thickness of the dielectric that is spin-coated onto the glass core. The whole process with side-view images is illustrated in Figure 6.5. The glass panels are treated with silane to promote adhesion between dielectric and them and prevent delamination during the whole fabrication process. The dielectric is spin-coated on both sides of the glass panel and cured. Thin titanium which acted as a barrier to prevent copper from migrating into the substrate and the copper seed layer is deposited with the sputtering process after dry etching which cleans the surface of the dielectric. Although the electroless plating provides an anchor effect with a rough surface and thus high adhesion strength between the seed layer and

| Layer | Thickness | Material |
|---|---|---|
| M1 (Top) | 7 µm | Copper |
| Dielectric-1 | 15 µm | ABF polymer |
| M2 | 7 µm | Copper |
| Dielectric-2 | 15 µm | ABF polymer |
| Core-Glass | 100 µm | AGC EN-A1 |
| Dielectric-3(Bottom) | 30 µm | ABF polymer |

Figure 6.6: The stackup for the proposed broadband AiP design.

dielectric, the combination of the sputtered seed layer and the optimized liquid dielectric also lead to high adhesion strength mitigating surface roughness and conductive loss [108]. Next, the panel is laminated with a dry-film negative photoresist. The panel with photoresist is patterned with optimized UV dose time. Then, the panel is treated with oxygen plasma to remove the photoresist beneath the pattern for copper plating. The metal patterning is performed through the SAP process with a controlled metal thickness of 5 to 8 µm.

Afterward, the second dielectric layer is spin-coated following the same process as the first layer. Micro vias were formed using a UV laser tool. The laser condition such as power density and the number of repetitions is optimized to drill 35 µm vias in the dielectric. After the micro via formation, dry desmear is used to clean the surface and remove residual polymer, followed by seed layer deposition sequentially. Finally, the metal patterning is performed again through the SAP process. The same process can be used to pattern metal on both sides of the glass if needed.

## 6.3 Broadband 5G Antenna-in-Package Design

### 6.3.1 Broadband Yagi Design

*Design and Stackup*

The stackup of the proposed broadband planar Yagi antenna is shown in Figure 6.6. The core substrate is a 100 µm AGC EN-A1 glass. The low-loss polymer used in this design is

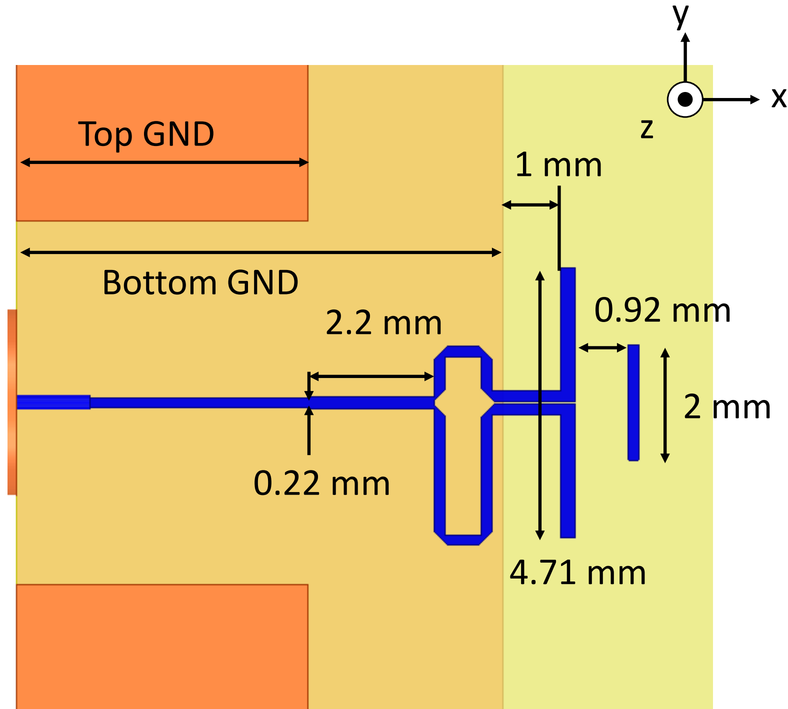


Figure 6.7: The geometry of the proposed broadband AiP element design.

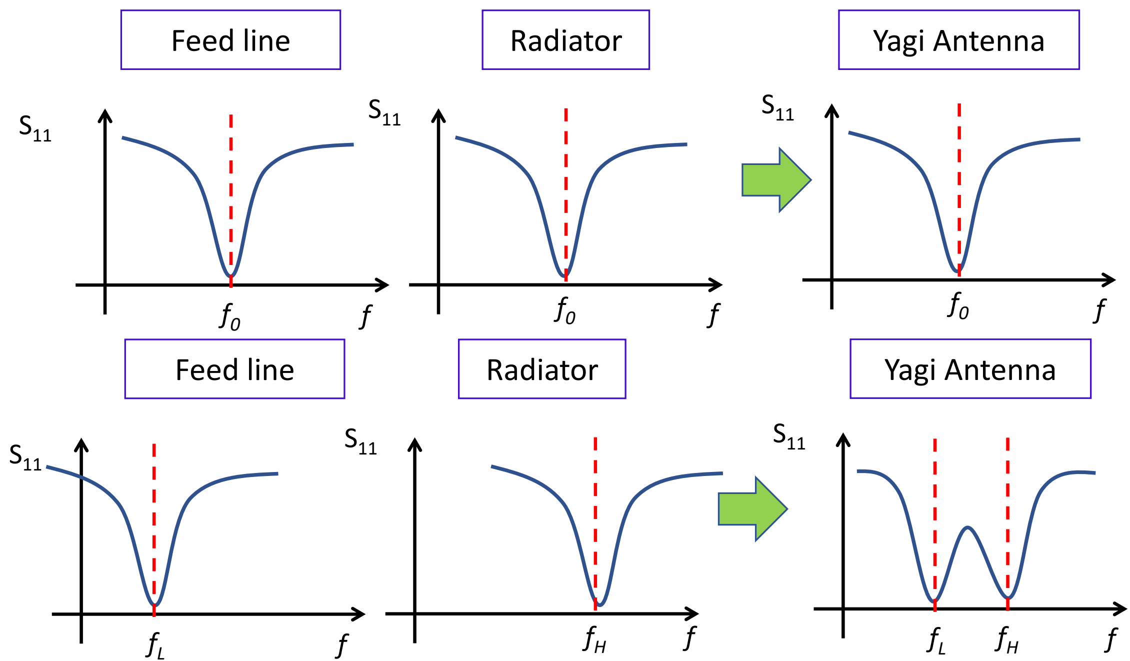


Figure 6.8: The design idea to realize broadband Yagi AiP Design.

ABF and the thickness is 15 µm. Two layers of copper are used to realize the design. The bottom of the glass is coated with 30 µm ABF to balance the weight and prevent warpage.

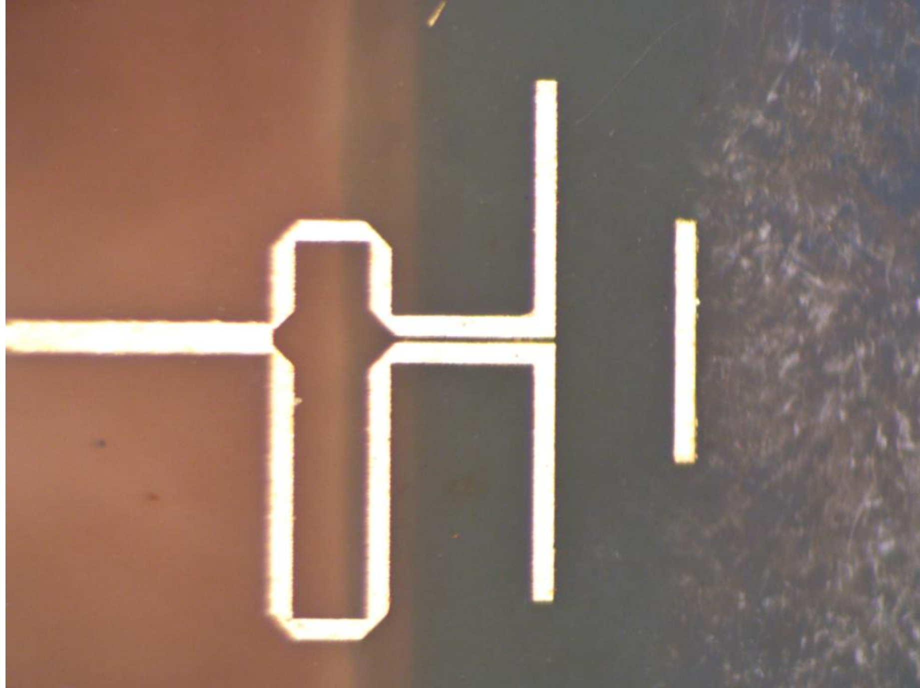

Figure 6.9: The fabricated prototype of the proposed broadband AiP element design.

The geometry of the proposed broadband AiP element design is shown in Figure 6.7. The physical dimensions are also included in the figure. The dipole-type radiator is adopted and a simple 180° phase difference balun is used. Two branches of the balun can be viewed as two 50 Ω parallel together and thus, a quarter-wave transformer with 35.3 Ω characteristic impedance is used to match them back to 50 Ω. The ground plane at M2 (as shown in Figure 6.6) is used as a reflector and micro vias are used to connect them to the top ground pads for the end-launch connector. The full-wave simulation results are obtained using HFSS. The end-launch connector model is also included in HFSS since at mm-wave range, the parasitics of the end-launch connector can not be ignored.

The objective of the proposed design is to cover the 5G band n257 (26.5-29.5 GHz) and n258 (24.25-27.5 GHz) simultaneously. Therefore, a broadband performance covering 24.25-29.5 GHz is required. The design idea to make the proposed Yagi antenna broadband is shown in Figure 6.8. As shown in Figure 6.8, if the feed line and the radiator is designed at the same frequency, there will be only one zero. The feed line and radiator of

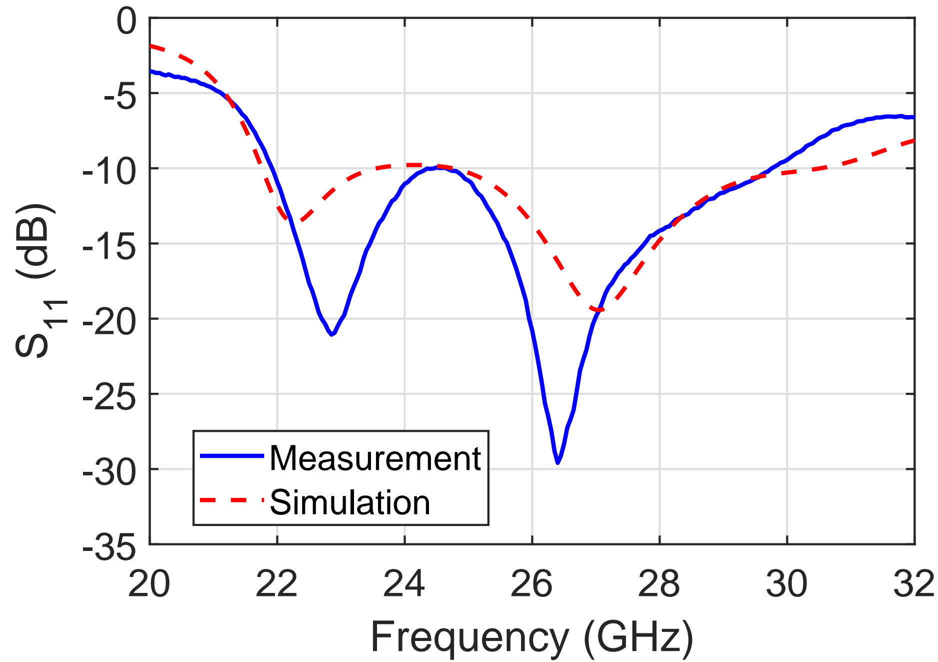


Figure 6.10: The measured and simulated $S_{11}$ of the proposed broadband AiP element.

the proposed Yagi are designed at two close but separate frequencies. Since two zeros are obtained, the proposed Yagi can be realized with broadband performance. The proof-of-concept prototype of the proposed broadband AiP element design using glass packaging SAP process is demonstrated in Figure 6.9.

*Measured Results*

The $S_{11}$ of the proposed broadband AiP element is measured using VNA and the results are shown in Figure 6.10. The simulation results using HFSS are also included and a good agreement can be observed. The measured $S_{11}$ is smaller than -10 dB from 22 GHz to 29.75 GHz. Therefore, both 5G band n257 and n258 can be covered with this broadband AiP design. The realized gain is also measured using the three-antenna gain measurement method. The two standard antennas with known gains are measured to obtain the $S_{21,std}$. Then, one of the standard antennas is replaced with the test antenna to obtain the $S_{21,DUT}$.

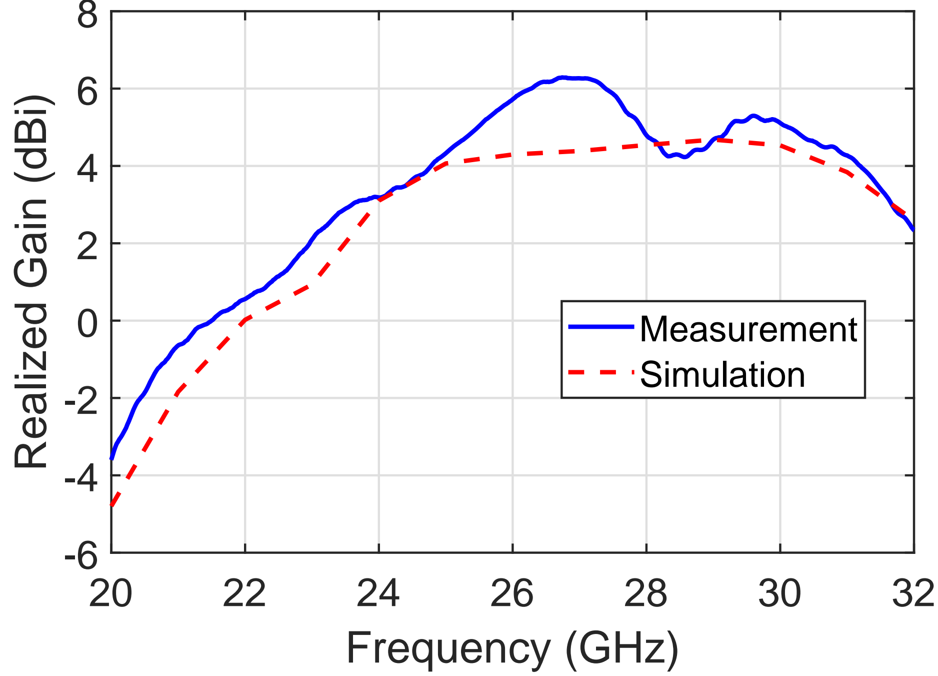


Figure 6.11: The measured and simulated realized gain of the proposed broadband AiP element.

Finally, the realized gain is obtained by

$$G_{\text{DUT}} = S_{21,\text{DUT}} - S_{21,\text{std}} + G_{\text{std}} \quad (6.1)$$

where $G_{\text{std}}$ is the gain for standard antenna. The measured realized gain is shown in Figure 6.11. The simulation result is also included and a good agreement can be observed. The measured realized gain is higher than 3 dBi from 24 GHz to 31.6 GHz. Therefore, both 5G bands from 24.25 GHz to 29.5 GHz are covered by the proposed broadband AiP design.

The measured and simulated normalized E-plane radiation patterns at 24 GHz and 30 GHz are shown in Figure 6.12. The two frequencies are chosen because they are close to the lower and higher bound of the two 5G bands. The 0° direction is the end-fire direction which is also the positive x direction shown in Figure 6.7. The main-beam direction for 24 GHz is at −10° and the main-beam direction for 30 GHz is at 0°. The 3-dB beam width for 24 GHz and 30 GHz are 50° and 70°, respectively. The measured and simulated

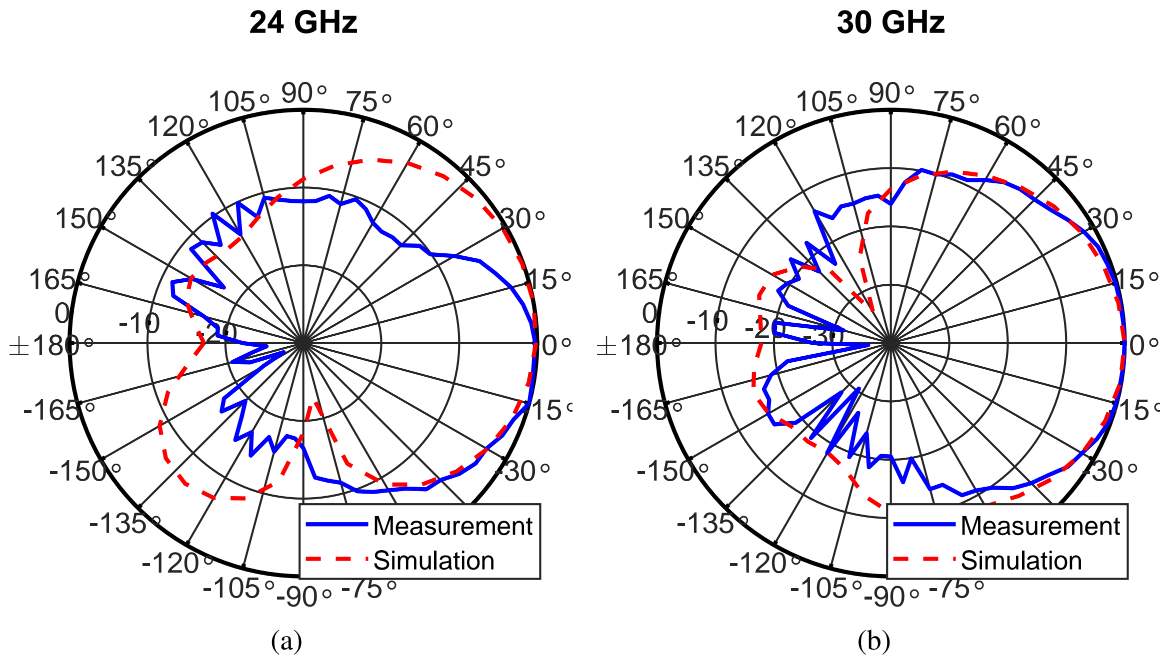


Figure 6.12: The measured and simulated normalized E-plane radiation patterns at (a) 24 GHz and (b) 30 GHz.

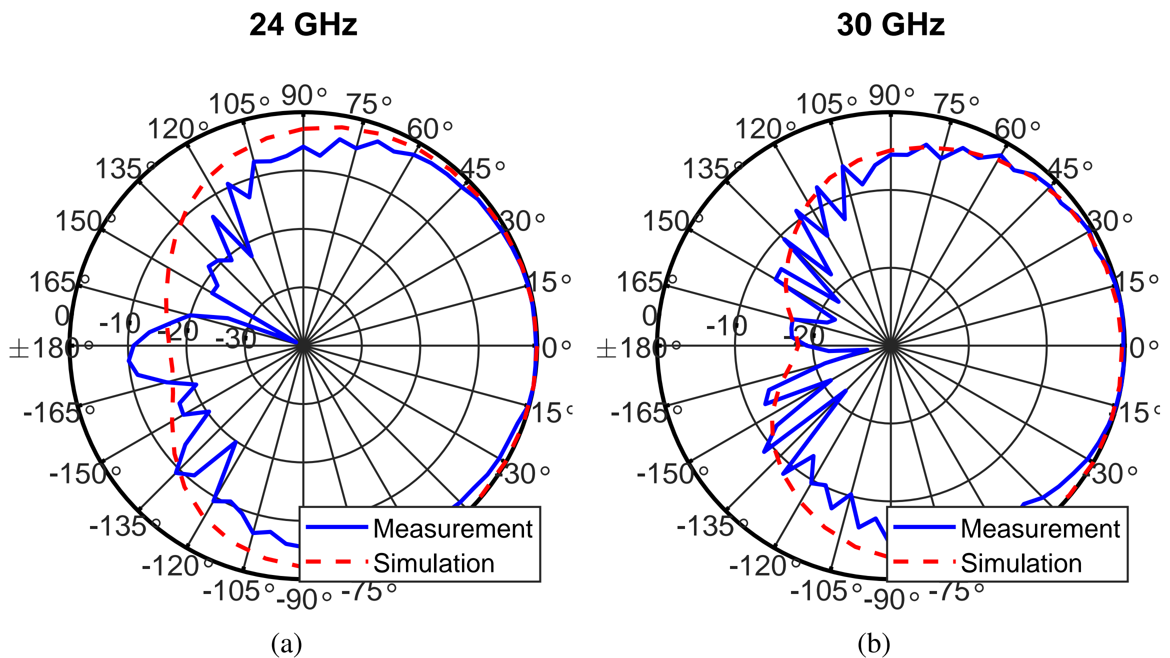


Figure 6.13: The measured and simulated normalized H-plane radiation patterns at (a) 24 GHz and (b) 30 GHz.

normalized H-plane radiation patterns at 24 GHz and 30 GHz are shown in Figure 6.13. The main beams are all at 0°. The 3-dB beam width for 24 GHz and 30 GHz are 130° and

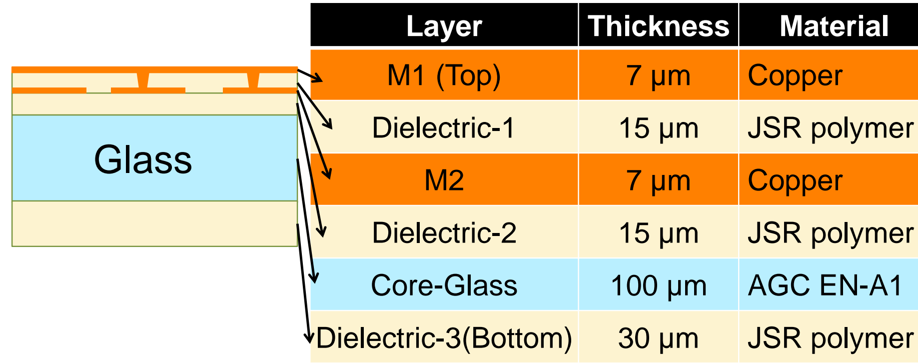


| Layer | Thickness | Material |
|---|---|---|
| M1 (Top) | 7 µm | Copper |
| Dielectric-1 | 15 µm | JSR polymer |
| M2 | 7 µm | Copper |
| Dielectric-2 | 15 µm | JSR polymer |
| Core-Glass | 100 µm | AGC EN-A1 |
| Dielectric-3(Bottom) | 30 µm | JSR polymer |

Figure 6.14: The stackup for the proposed UWB AiP element design.

120°, respectively.

### 6.3.2 UWB Yagi Design

The proposed broadband AiP design shown in the previous section covers two 5G bands. However, there are three main 5G bands as shown in Table 6.1. Therefore, in this section, an improved UWB AiP design which covers 24.25 - 40 GHz with a smaller size is proposed. Besides, the JSR material is first used as the low-loss polymer on the glass packaging process in this design.

*Glass Packaging Stackup*

The stackup for the proposed UWB and miniaturized AiP design is shown in Figure 6.14. The material and the thickness of each layer are also included. The core substrate is a 100 µm EN-A1 glass from Asahi Glass Co. (AGC). The dielectric constant is 5.41 and the loss tangent is 0.006 at 35 GHz. Two 15 µm layers of low-loss polymer developed by JSR corporation are coated on the top of the glass to reduce the overall loss tangent. This new-developed material has a large elongation factor and is softer which can be used to effectively prevent warpage in multi-layer packaging realization and is applied to the glass packaging process for the first time. Measuring at 32 GHz, the dielectric constant and loss tangent for this low-loss polymer are 2.8 and 0.0045 [108], respectively. Two layers of metal denoted by M1 and M2 are realized with copper. Finally, a 30 µm layer of polymer

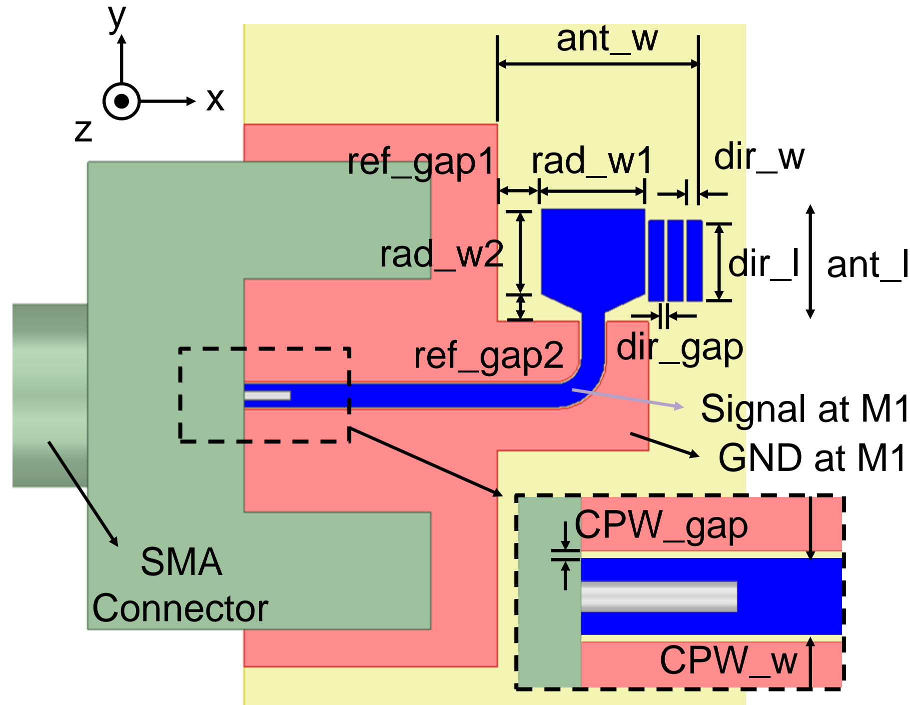


Figure 6.15: The geometry of the proposed UWB AiP element design.

is coated on the bottom of the glass to balance the weight and prevent the warpage.

*UWB AiP Design*

The geometry of the proposed UWB and miniaturized AiP element design is demonstrated in Figure 6.15. The physical dimensions are summarized in Table 6.2. All structures are realized only at metal layer M1 shown in Figure 6.14. The other metal layer M2 is only used in the array design. As shown in Figure 6.15, compared with the conventional quasi-Yagi antenna which utilized dipole as the radiator [109], the proposed antenna element used monopole as the radiator featuring two major advantages. One is the reduction of size by half and the other is the removal of the requirement of the differential feeding or the balun which can further reduce the size and simplify the feeding network design. Thus, a simple CPW can be used as the feeding network and alleviate the difficulties in the UWB feeding network design. A 90° bend on the radiator is introduced so that the ground plane of the CPW can be directly used as the reflector for the Yagi antenna and the layout for the

Table 6.2: Physical dimensions of the proposed UWB AiP element design.

| Parameter | Dimension (mm) | Parameter | Dimension (mm) |
|---|---|---|---|
| CPW_w | 0.62 | ref_gap2 | 0.78 |
| CPW_ gap | 0.06 | dir_l | 2.2 |
| rad_w1 | 2.8 | dir_gap | 0.12 |
| rad_w2 | 2.29 | dir_w | 0.4 |
| ref_gap1 | 1.2 | ant_w | 5.56 |
| ant_l | 3.05 | | |

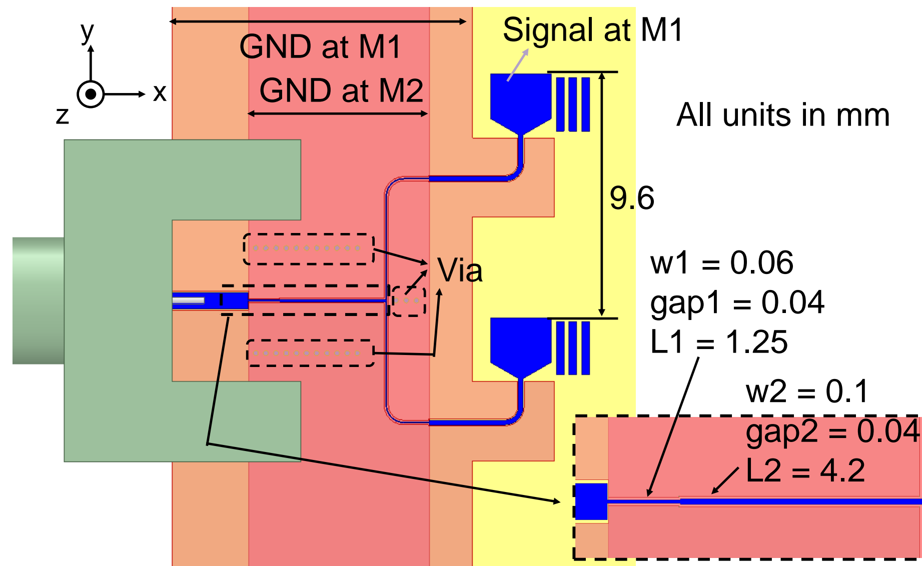


Figure 6.16: The geometry of the proposed UWB AiP array design.

antenna array can be simplified. The square radiator with a tapered shape near the feeding point is used to broaden the operating bandwidth.

The structure of the 2-by-1 array design is shown in Figure 6.16. The inter-element spacing is 9.6 mm. Additional ground planes at the M2 layer and via arrays connecting M1 and M2 with 235 μm pitches and 35 μm diameters are used to ensure that all ground planes are connected together. A two-stage quarter-wave transformer is used for impedance matching at the feeding network and the respective CPW widths, gaps, and lengths are shown in Figure 6.16.

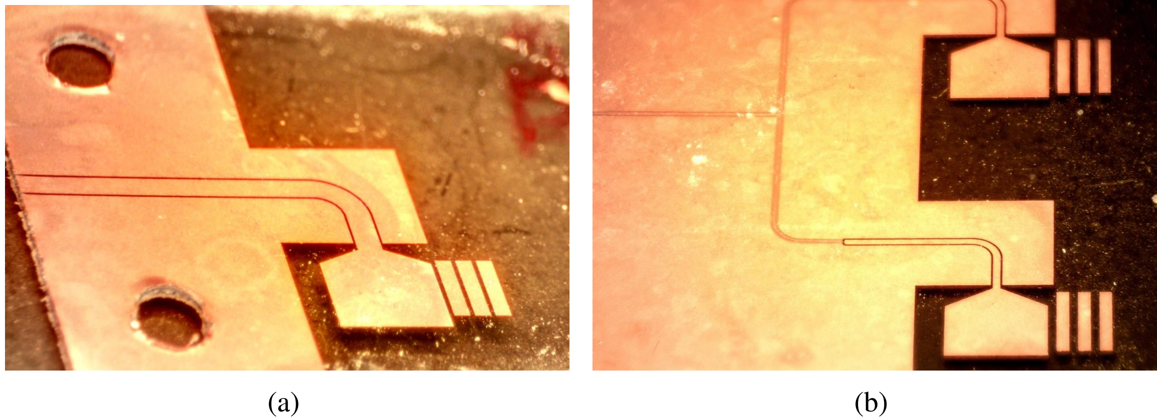

(a) (b)

Figure 6.17: The fabricated prototypes of the UWB AiP (a) element design and (b) array design.

*UWB AiP Fabrication*

The fabricated proof-of-concept prototype of the proposed broadband and miniaturized Yagi AiP element is shown in Figure 6.17a and the 2-by-1 array is shown in Figure 6.17b. The comparisons between the measured dimensions and design dimensions of the element are shown in Figure 6.18a. As shown in Figure 6.18a, precise line widths and gap sizes are achieved through the glass SAP packaging process. The comparisons between the measured dimensions and design dimensions of the 2-by-1 array are shown in Figure 6.18b. Almost all fabricated dimensions are very close to the designed values except one line width at the feeding. The measured dimension is 621.2 µm and the designed value is 420 µm. It is because the metal plating time is too long and can be improved easily. The effects of the fabricated discrepancy on the performance are on the measured $S_{11}$ which will be introduced later. However, the overall performance is still very good despite this discrepancy.

*AiP Element Measured Results*

The measured $S_{11}$ as well as gain of the UWB and miniaturized AiP element are shown in Figure 6.19a and Figure 6.19b, respectively. The full-wave simulated results are obtained

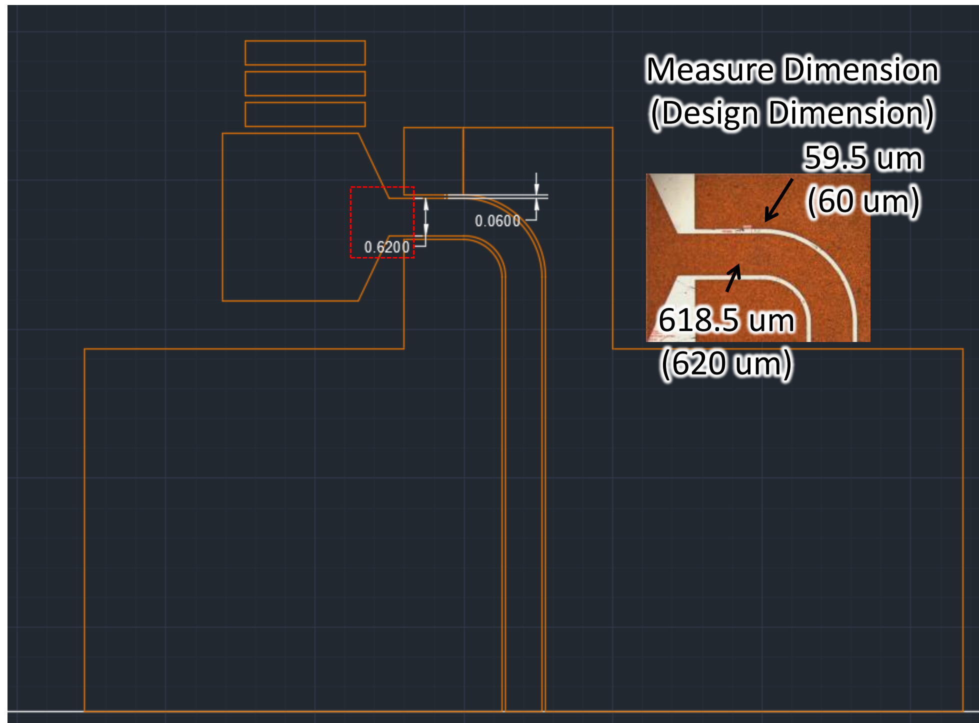


(a)

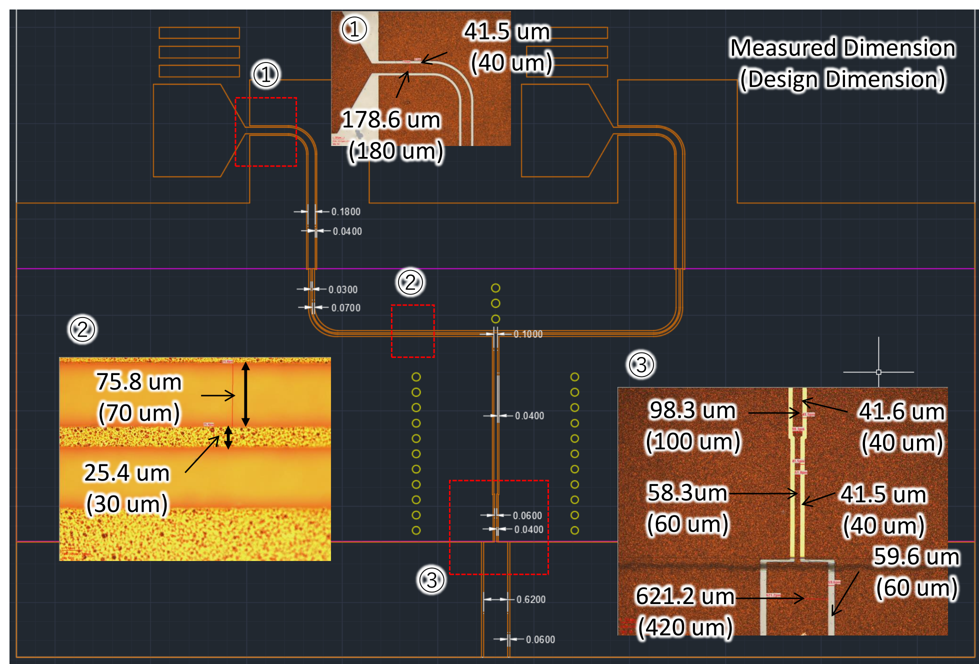


(b)

Figure 6.18: The comparisons of measured and designed dimensions for the UWB AiP (a) element and (b) 2-by-1 array design.

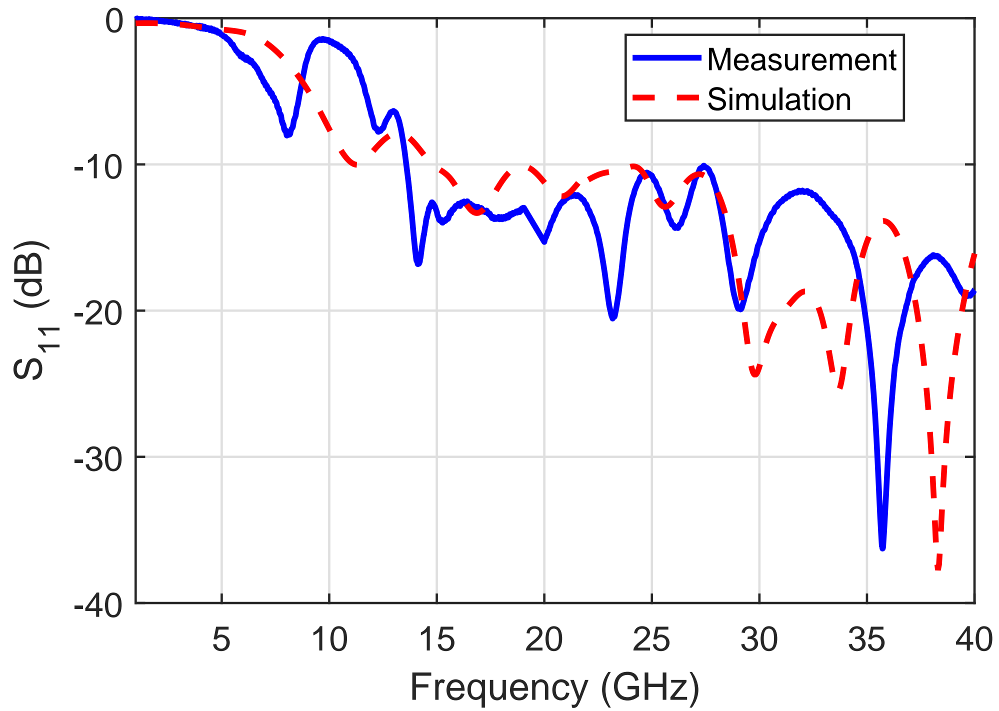


(a)

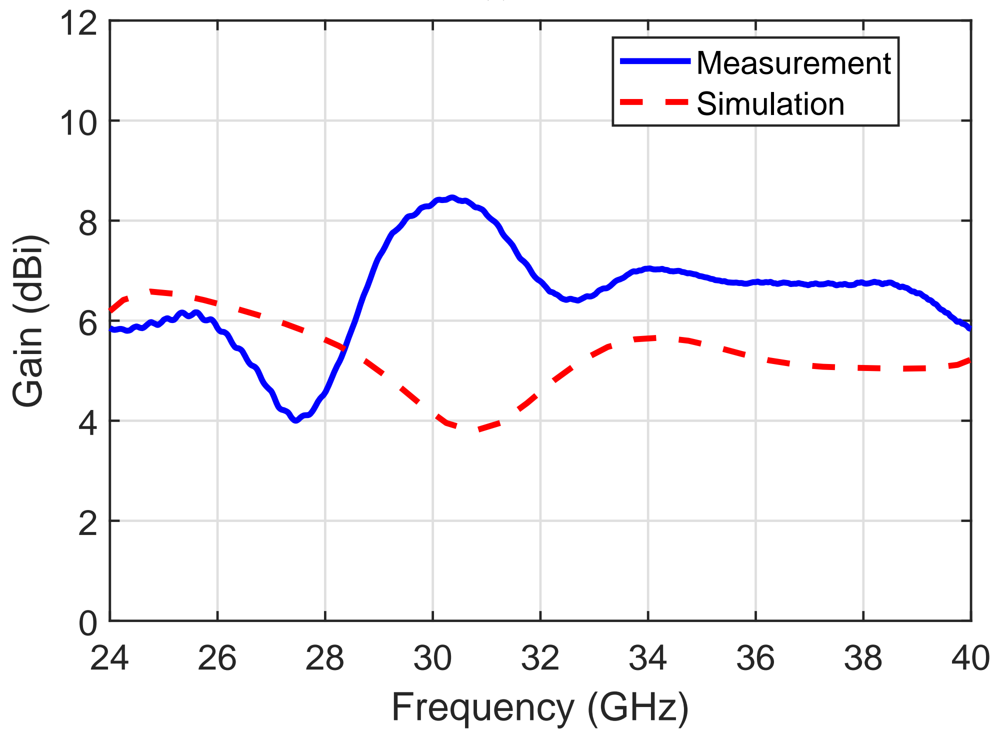


(b)

Figure 6.19: The measured and simulated (a) $S_{11}$ and (b) gain of the proposed UWB and miniaturized AiP element design.

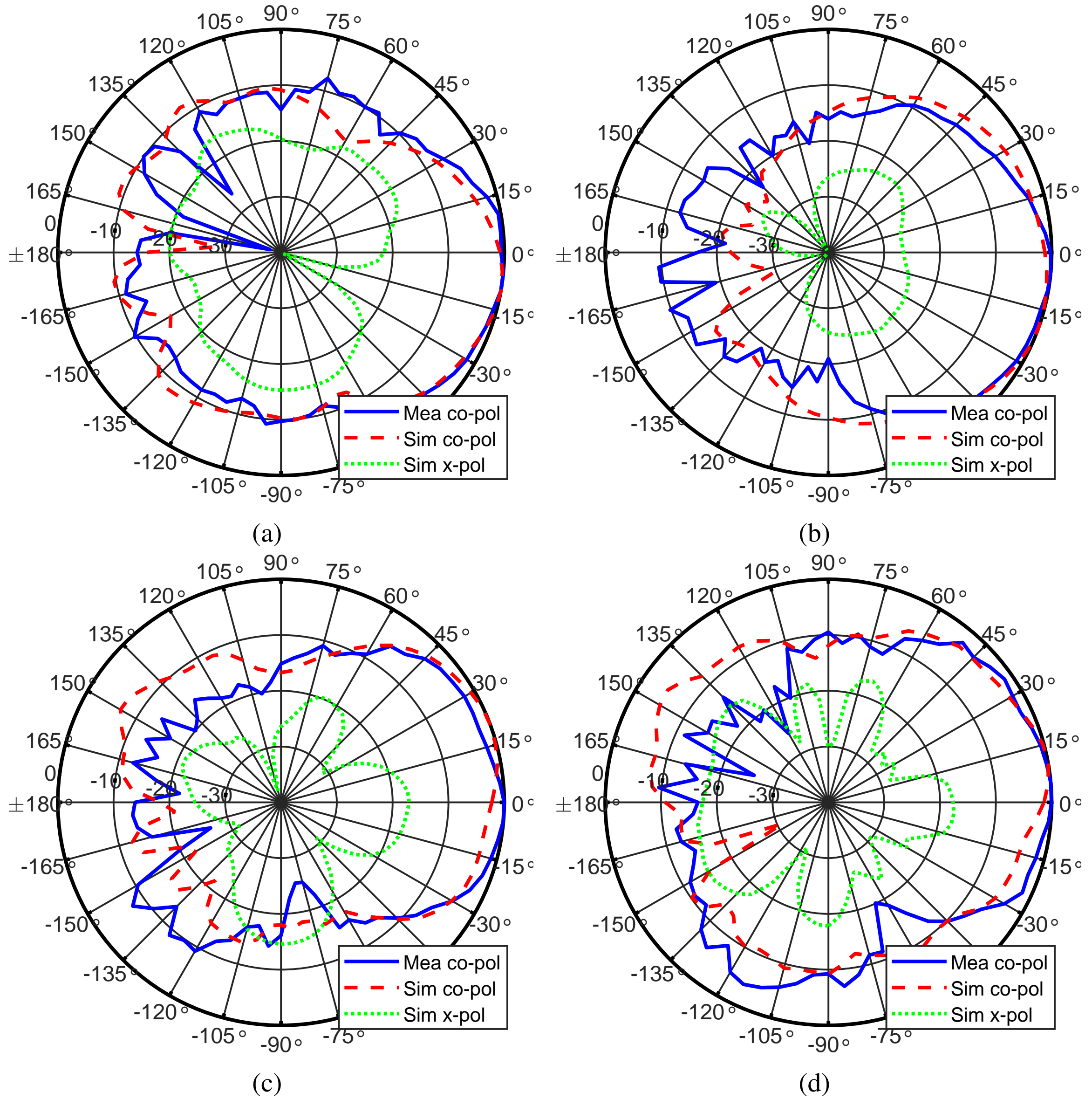


Figure 6.20: Measured and simulated normalized E-plane radiation patterns of the UWB AiP element at (a) 24.25 GHz (b) 29.5 GHz (c) 37 GHz and (d) 40 GHz.

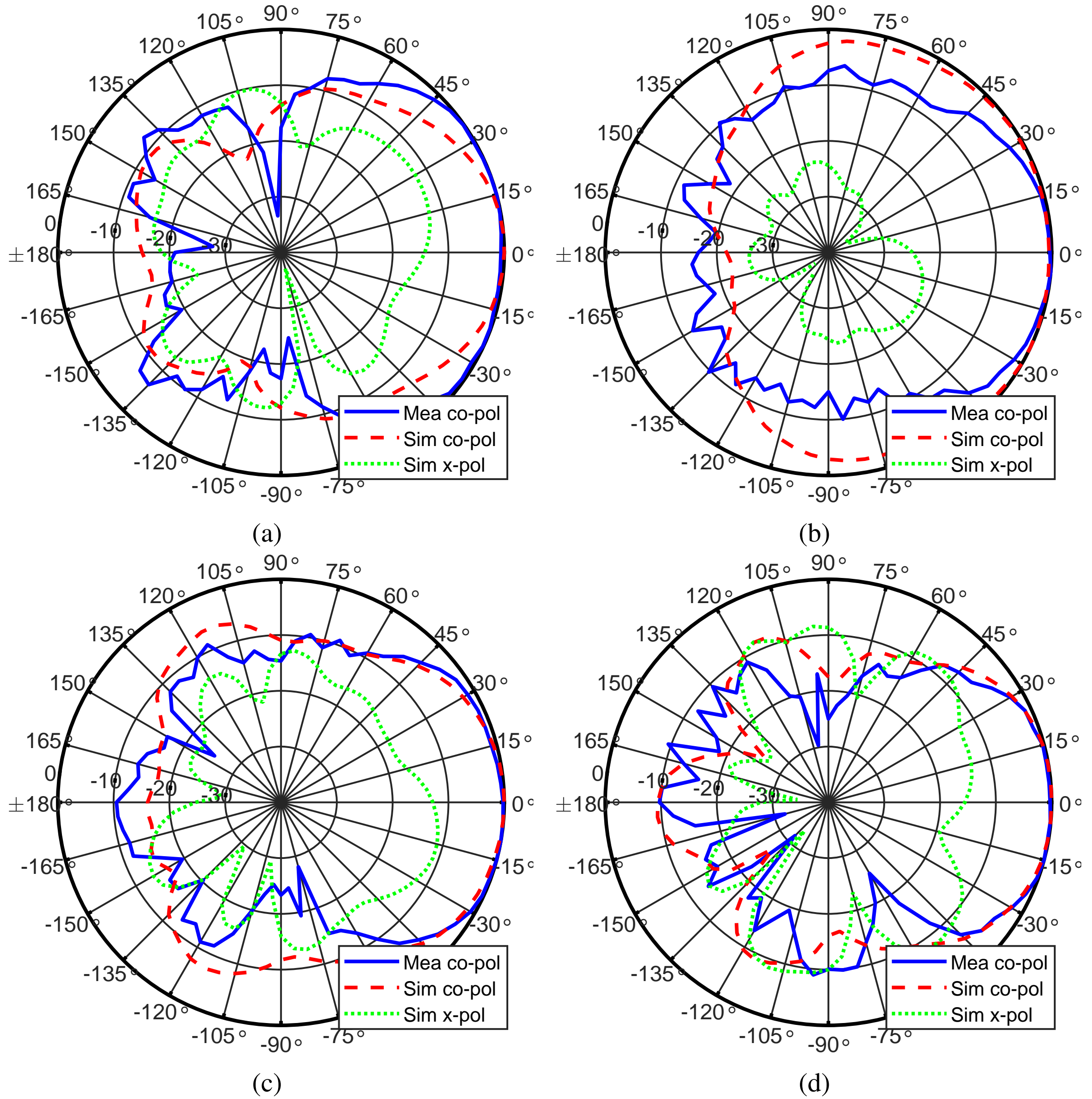


Figure 6.21: Measured and simulated normalized H-plane radiation patterns of the UWB AiP element at (a) 24.25 GHz (b) 29.5 GHz (c) 37 GHz and (d) 40 GHz.

using Ansys HFSS. Since at mm-wave range, the parasitics and effects of the end-launch connector cannot be ignored, the module of the end-launch connector is also included in simulation for co-design as shown in Figure 6.15. As shown in Figure 6.19a, the measured $S_{11}$ is lower than -10 dB from 13.58 GHz to 40 GHz. Thus, the three 5G bands from 24.25 to 40 GHz are fully covered. Moreover, as shown in Figure 6.19b, the measured gain is higher than 4 dBi within the entire 5G bands. The measured gains are slightly higher than the simulated ones since when simulating the designs, the loss tangent values of the core glass and JSR polymer are set to the largest values within the band rather than frequency-dependent to obtain the lower-bound results.

The measured and simulated normalized E-plane radiation patterns at the 24.25, 29.5, 37, and 40 GHz are shown in Figure 6.20. These frequencies are chosen since the 5G bands n257 and n258 together are from 24.25 GHz to 29.5 GHz and the n260 band is from 37 GHz to 40 GHz. Besides, the measured and simulated normalized H-plane radiation patterns at the 24.25, 29.5, 37, and 40 GHz are shown in Figure 6.21. The 0° direction is the end-fire, positive x in Figure 6.15, direction. Although the main-beam directions are not always at 0°, they are very close to it within the entire operating band. The simulated cross-polarization results are also included and are less than -15 dB at main-beam directions.

*2-by-1 Array Measured Results*

The fabricated prototype of the 2-by-1 Yagi array is shown in Figure 6.17b while the measured and simulated $S_{11}$ and gain are demonstrated in Figure 6.22a. The measured $S_{11}$ is lower than -9 dB from 18.87 GHz to 40 GHz. The minor degradation compared to the single element design is due to the discrepancy between the design and fabricated line width at the feeding. However, good performances within the entire 5G bands can be observed. The measured gain is higher than 6.2 dBi within the entire band.

The measured normalized E-field radiation patterns at the 24.25, 29.5, 37, and 40 GHz are shown in Figure 6.23 and the respective H-field patterns are shown in Figure 6.24. The

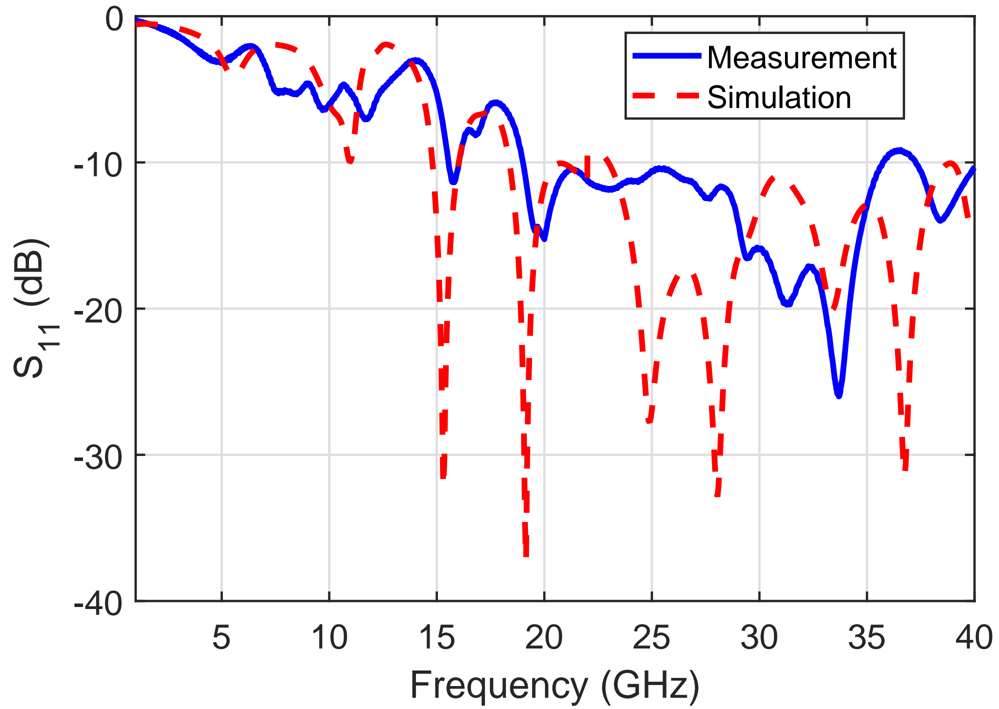


(a)

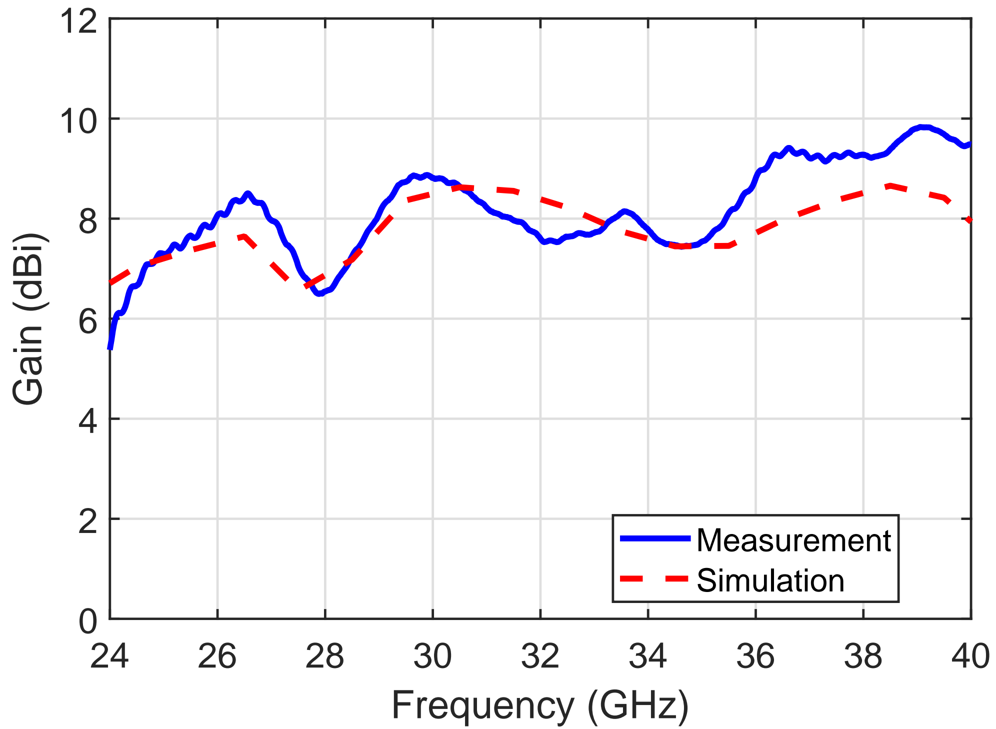


(b)

Figure 6.22: The measured and simulated (a) $S_{11}$ and (b) gain of the proposed UWB and miniaturized AiP 2-by-1 array design.

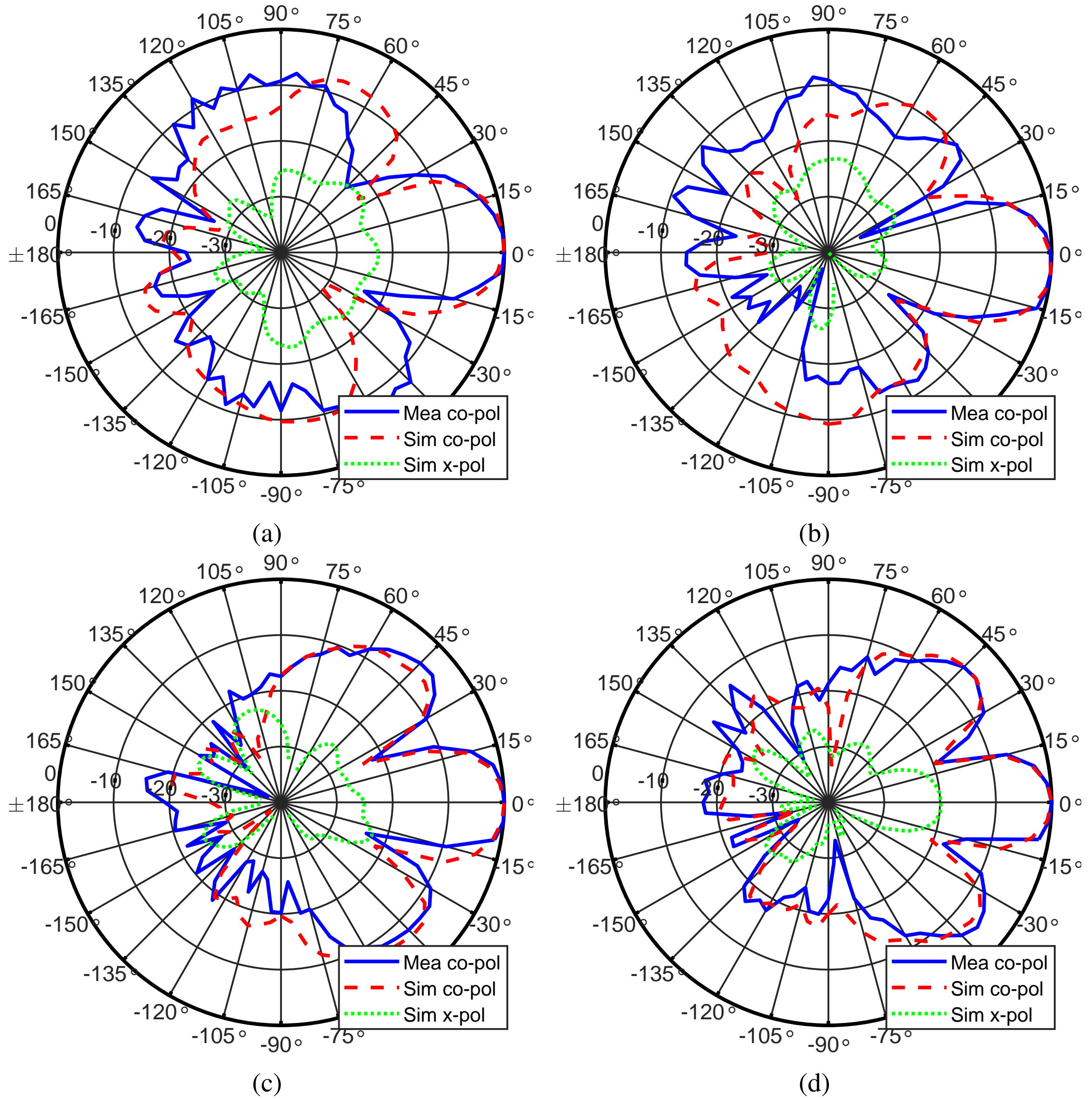


Figure 6.23: Measured and simulated normalized E-plane radiation patterns of the UWB AiP array at (a) 24.25 GHz (b) 29.5 GHz (c) 37 GHz and (d) 40 GHz.

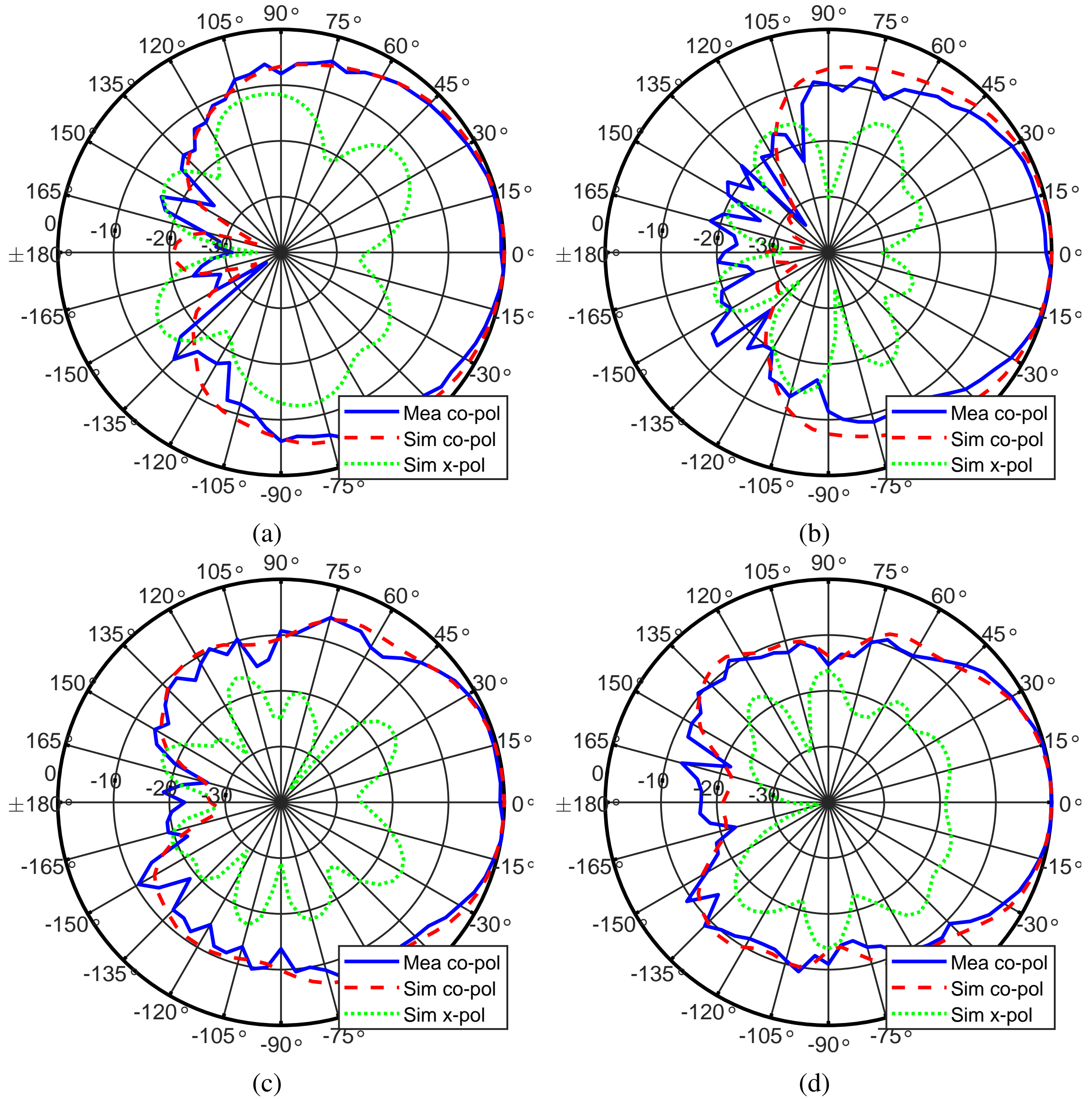


Figure 6.24: Measured and simulated normalized H-plane radiation patterns of the UWB AiP array at (a) 24.25 GHz (b) 29.5 GHz (c) 37 GHz and (d) 40 GHz.

Table 6.3: The Comparisons between the proposed UWB and miniaturized AiP element design and previous related works

| Work | Technique | Operating Frequency (GHz) | FBW (%) | Gain (dBi) | Size ($\lambda_0$) | Pattern | Antenna |
|---|---|---|---|---|---|---|---|
| [110] | PCB | 29.5 – 30.35 | 2.8 | 7.6 | 0.35 × 0.53 | E [1] | Dipole |
| [111] | PCB | 27.1 – 29.75 | 9.3 | 5.7 | 0.45 × 0.45 | E [1] | Yagi |
| [112] | PCB | 24.5 - 31.72 | 25.7 | 7.2 | 0.82 × 1.98 | E [1] | Dipole |
| [113] | PCB | 26.5 - 38.2 | 36.2 | 4.5 | 0.34 × 0.35 | E [1] | Dipole |
| [114] | AiP [a] | 28 - 29.6 | 5.6 | 4.0 | 0.22 × 0.22 | B [2] | Patch |
| [115] | AiP [a] | 26.7 - 30 | 11.6 | 4.0 | 0.6 × 0.6 | B [2] | Patch |
| [116] | AiP [a] | 28 - 32 | 13.3 | 4.5 | 0.48 × 0.57 | B [2] | Patch |
| [98] | AiP [b] | 30 - 30.8 | 2.6 | 4.9 | 0.6 × 0.6 | B [2] | Patch |
| [102] | AiP [c] | 22.4 - 30.1 | 29.3 | 5.0 | 0.28 × 0.64 | E [1] | Yagi |
| **This** | AiP [d] | 24.25 - 40 | 49.0 | 4.0 | 0.25 × 0.45 | E [1] | Yagi |

[a]: AiP from active module, [b]: Organic AiP, [c]: 3D Printing AiP, [d]: Glass packaging AiP
[1]: End-fire, [2]: Broadside

simulated results are also included for comparison and a good agreement can be observed. The grating lobes in Figure 6.23d are because of the relatively long element separation distance at 40 GHz and can be improved by reducing the separation distance. The simulated cross-polarization results are also included and they are all lower than -19 dB in the main-beam direction. The main-beam beamwidths at E-plane are narrower than the respective H-plane results. The reason is that the array is arranged alone y-direction as shown in Figure 6.16.

*Comparisons with Previous Works*

The comparisons between the proposed work and previous work are summarized in Table 6.3. All parameters are based on a single antenna element. Numerous designs operating at 5G frequency bands using either Printed Circuit Board (PCB) or AiP topologies are included for comparison. The $\lambda_0$ in the size is the wavelength at the lowest operating frequency. The simple transmission line parts of the feeding networks are excluded while

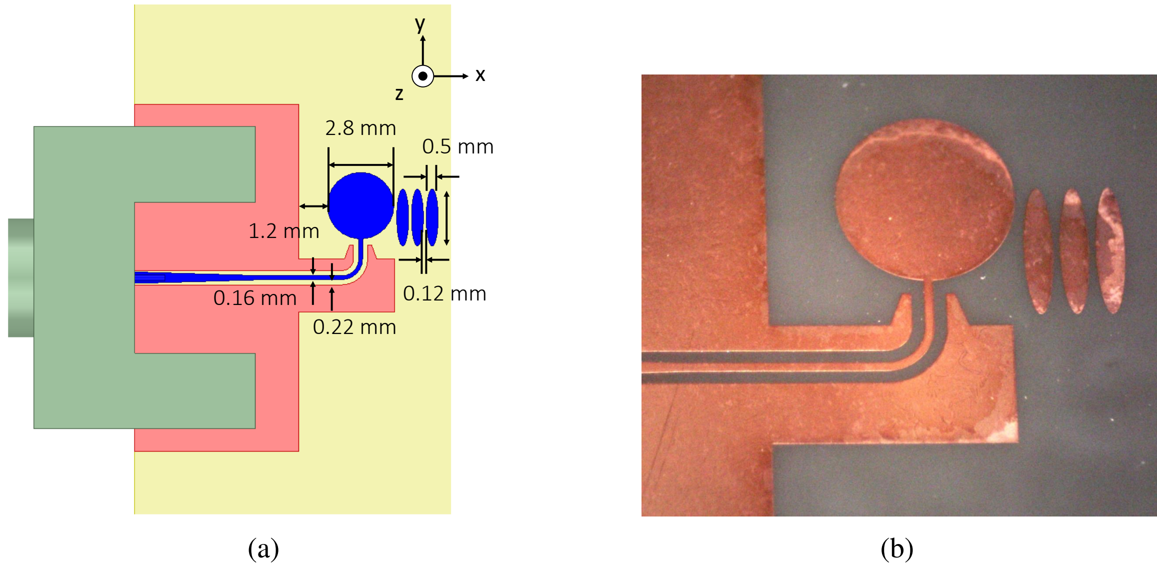


Figure 6.25: (a) The geometry of the modified UWB AiP element design and (b) the fabricated proof-of-concept sample.

calculating the sizes. As shown in Table 6.3, the proposed work achieves the largest Fractional Bandwidth (FBW) and is the only one that can fully cover all three 5G NR operating bands. Moreover, the size of the proposed works is smaller than all other works except the one in [114]. Although the proposed work is about 2.3 times larger than it, the proposed work can offer 8.75 times larger bandwidth compared with it.

## 6.4 Broadband 5G Energy Harvester

### 6.4.1 Modified UWB Yagi Design

The UWB AiP design introduced in the previous section is adopted for the energy harvester design with some modifications. The design of the antenna for the energy harvester is shown in Figure 6.25a and the fabricated proof-of-concept sample is shown in Figure 6.25b. Compared with the design in the previous section, the main improvement is in the matching bandwidth and the variations of the gain within the operating band. The circular radiator and the tapered feeding is used to improve the matching. The measured $S_{11}$ is shown in Figure 6.26a. As shown in Figure 6.26a, the $S_{11}$ is lower than -9 dB from 11.3 to 40 GHz

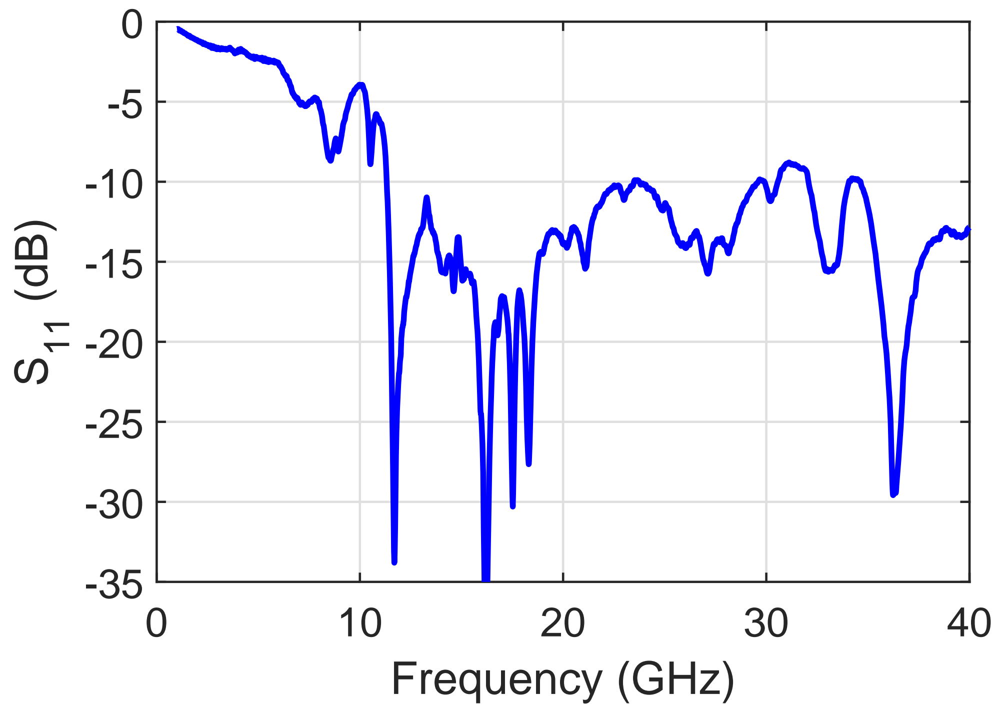


(a)

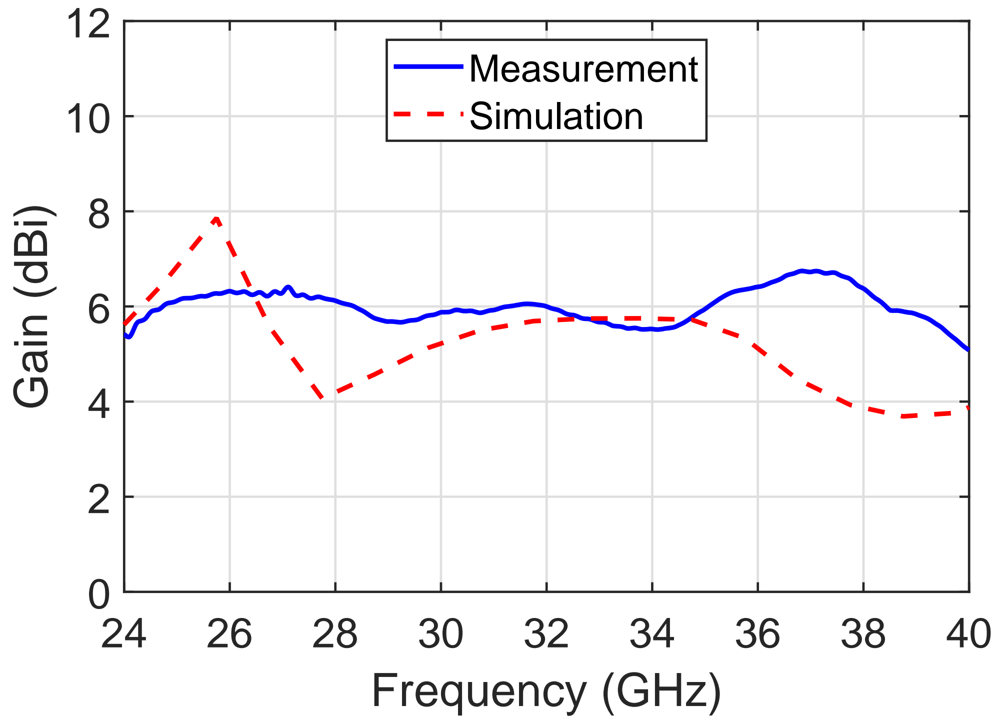


(b)

Figure 6.26: The measured (a) $S_{11}$ and (b) gain of the modified UWB and miniaturized AiP design.

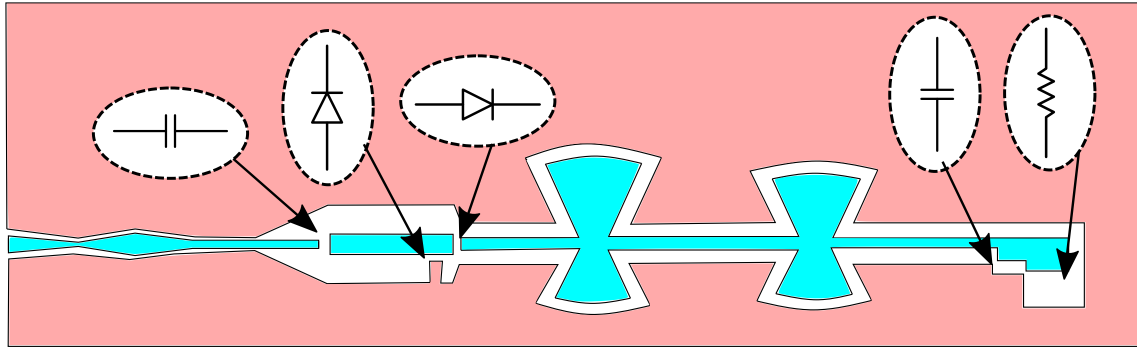

Figure 6.27: The geometry of the proposed broadband rectifier design for 5G lower bands.

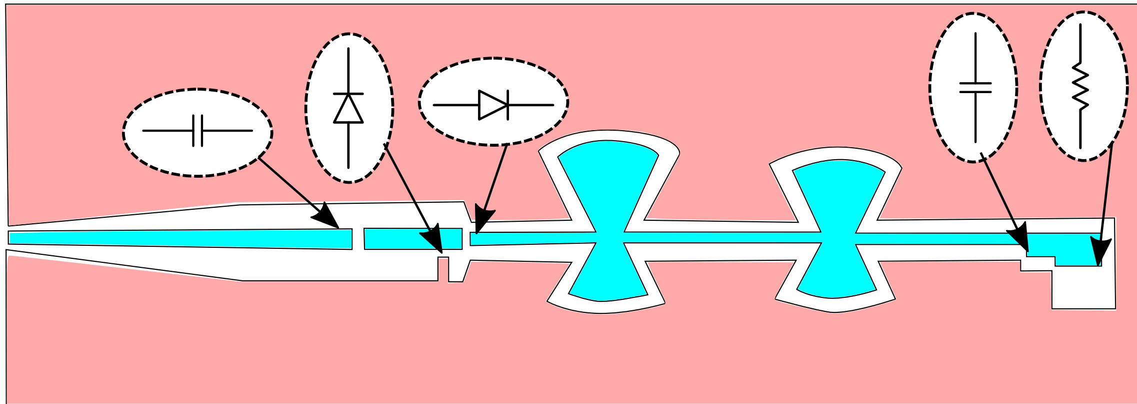

Figure 6.28: The geometry of the proposed broadband rectifier design for 5G upper bands.

which demonstrates a larger bandwidth compared with the previous design. The measured and simulated gain of the new AiP element design is shown in Figure 6.26b and a good agreement can be observed. The measured gain is between 5.1 and 6.7 dBi within the entire 5G bands. The variations of the gain within the operating band are smaller compared with the design in the previous section.

### 6.4.2 Broadband 5G Rectifier Design

The geomertry of the broadband rectifier designs are shown in Figure 6.27 and Figure 6.28. There are two broadband rectifier designs. One of them covers the lower 5G bands from 24.25 to 29.5 GHz and the other cover the higher 5G band from 37 to 40 GHz. For the lower band design shown in Figure 6.27, the non-uniform CPW lines are used for the broadband matching. Four studs with different lengths are placed after the diodes for harmonic fil-

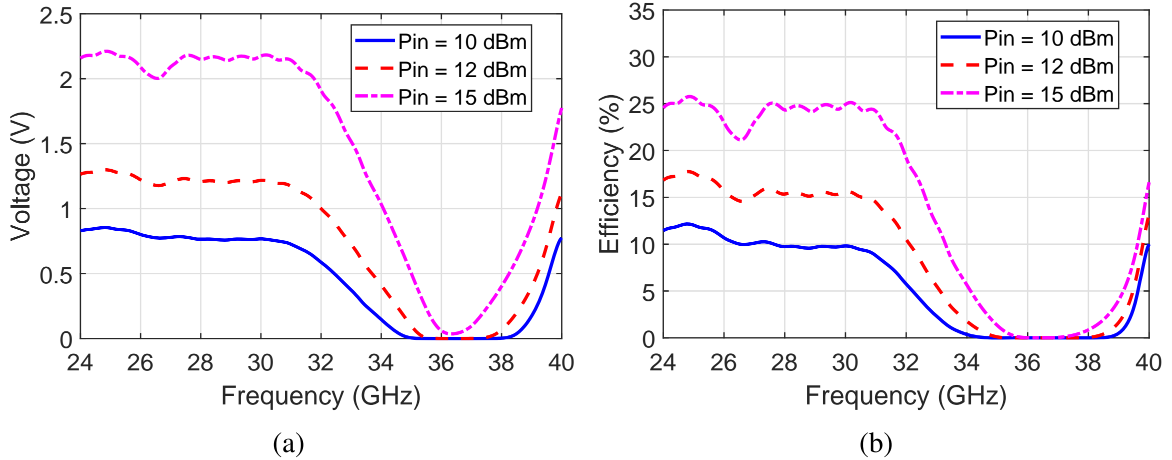


Figure 6.29: The simulated (a) output voltage and (b) RF-DC efficiency of the lower-band rectifier with respect to different frequencies.

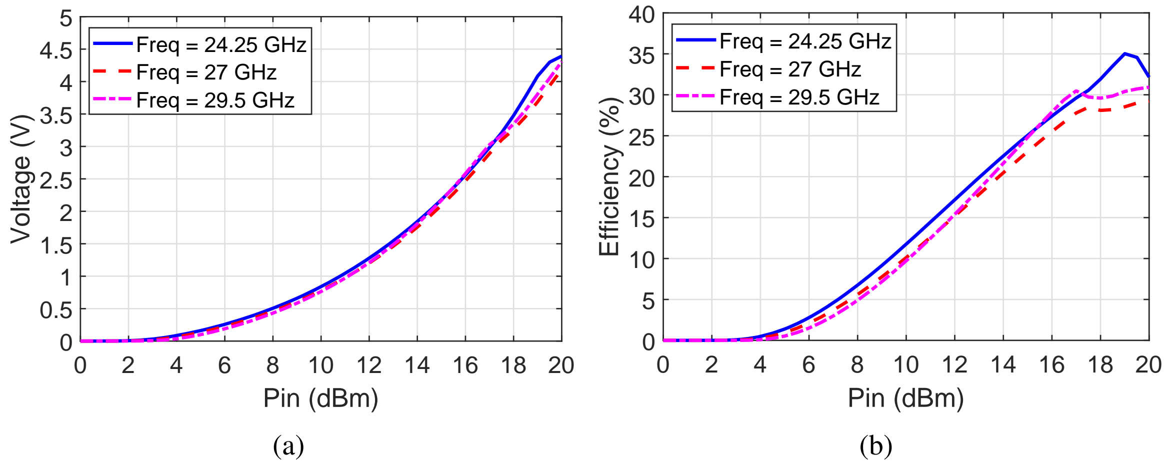


Figure 6.30: The simulated (a) output voltage and (b) RF-DC efficiency of the lower-band rectifier with respect to different input powers.

tering. The 0.1 μF UBSC series high-frequency capacitors which operated up to 60 GHz provided by Murata are used for the rectification and the filtering of the high-order harmonics at the load. The diodes used is MA4E1317 from MACOM company. The diodes can be operated up to 80 GHz according to the datasheet. The load resistor is 600 Ω. For the higher band design, the only difference is the broadband matching is replaced with a tapered line.

The rectifier is simulated using ADS harmonic balance. Besides, the scattering parameters of each CPW transmission lines are simulated using HFSS and import into ADS. The

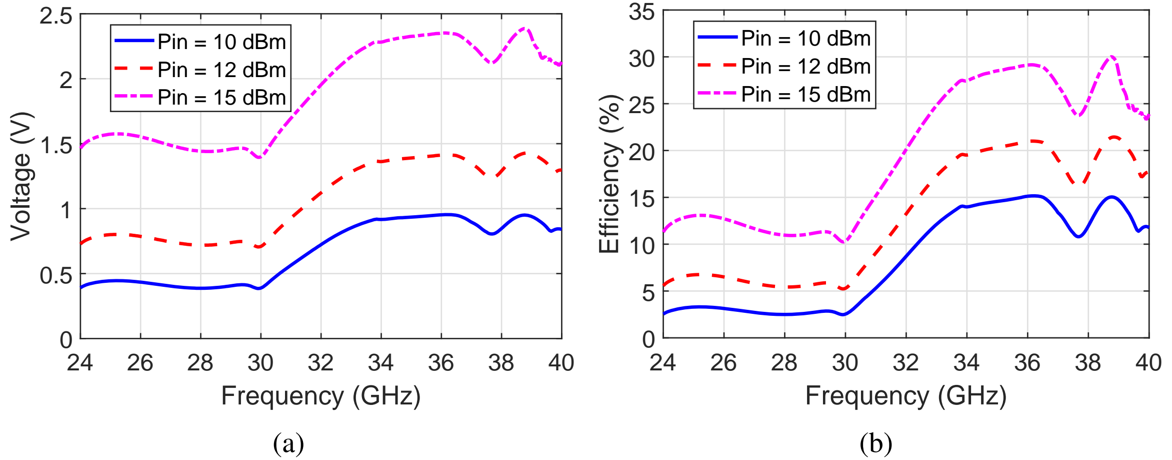


Figure 6.31: The simulated (a) output voltage and (b) RF-DC efficiency of the upper-band rectifier with respect to different frequencies.

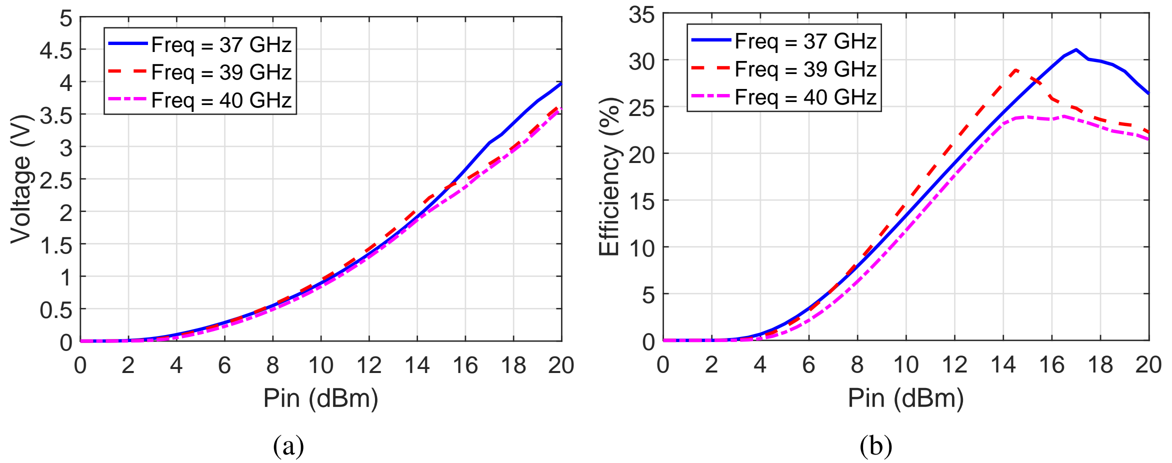


Figure 6.32: The simulated (a) output voltage and (b) RF-DC efficiency of the upper-band rectifier with respect to different input powers.

SPICE model of the MA4E1317 diode is built and the UBSC capacitor model from the datasheet is also included in ADS for simulation. The simulated output voltages and RF-DC efficiencies of the lower-band rectifier with respect to different frequencies are shown in Figure 6.29. The results of three different input power levels, 10, 12, and 15 dBm are included. The broadband and flat response within 24 to 30 GHz can be observed in Figure 6.29. As shown in Figure 6.29a, the output voltage is all larger than 0.77 V within the operating band which is large enough to drive most of the applications. Furthermore, as demonstrated in Figure 6.29b, the RF-DC efficiency is larger than 20 % within the broad

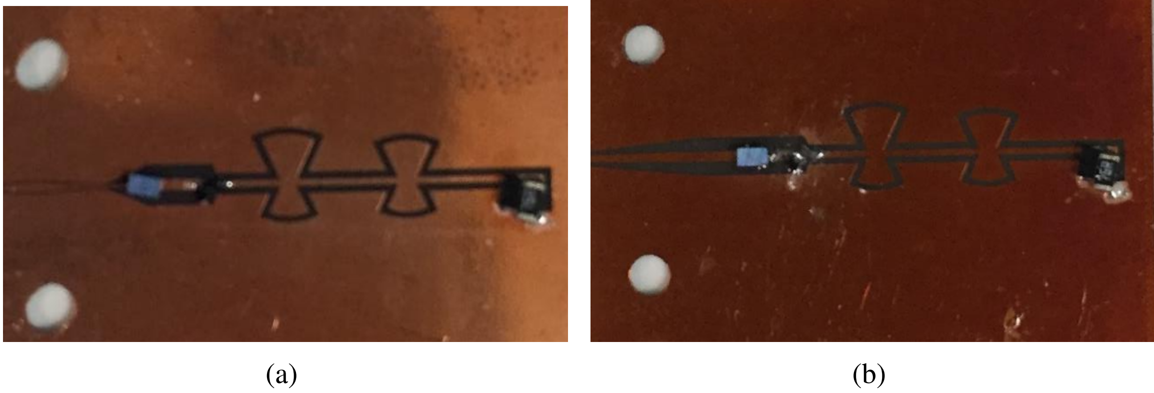

(a) (b)

Figure 6.33: The fabricated rectifiers for the (a) lower-band operation and (b) higher-band operation.

operating band when input power is 15 dBm. The simulated output voltages and RF-DC efficiencies of the lower-band rectifier with respect to different input powers are shown in Figure 6.30. The results at three different frequencies are included. They are the lowest frequency (24.25 GHz), the middle frequency (24 GHz), and the highest frequency (29.5 GHz) of the operating band. Both the voltages and RF-DC efficiencies are higher when larger input powers are used and they are not saturated below 20 dBm input power. The highest RF-DC efficiency is 35 % at 24.25 GHz when input power is 19 dBm.

For the upper-band rectifier, the simulated output voltages and RF-DC efficiencies with respect to different frequencies are shown in Figure 6.31. The broadband and flat responses within 37 to 40 GHz can be observed. As shown in Figure 6.31a, the output voltage is all larger than 0.8 V within the operating band which is large enough to drive most of the applications. The RF-DC efficiency is larger than 23 % within the broad operating band when input power is 15 dBm as demonstrated in Figure 6.31b. The simulated output voltages and RF-DC efficiencies of the upper-band rectifier with respect to different input powers are depicted in Figure 6.32. The highest RF-DC efficiency is 31 % at 37 GHz when input power is 17 dBm.

As shown in Figure 6.33, the proof-of-concept samples is fabricated using glass SAP packaging process. The lump components including the diodes, capacitors, and the resistor

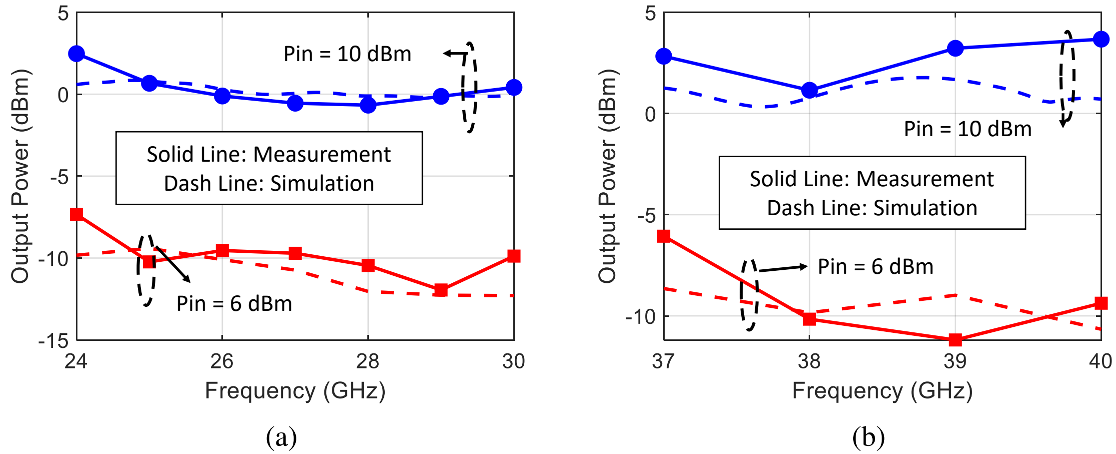


Figure 6.34: The measured and simulated output power levels for the proposed (a) lower-band rectifier design and (b) higher-band rectifier design.

are soldered onto the samples. The respective measured output power levels at different frequencies are shown in Figure 6.34. The simulated results are included for comparison and good agreements can be observed. As shown in Figure 6.34a, the proposed lower-band rectifier can cover from 24 to 30 GHz which covers all the 5G bands lower than 30 GHz (n257 and n258). Furthermore, the RF-DC conversion efficiency is 17.7 % when the input power is 10 dBm and it is higher when the input power level is higher which can also be observed in Figure 6.30b. For the measured results of the proposed broadband higher-band rectifier shown in Figure 6.34b, broadband performance covering 37 to 40 GHz can be observed. Therefore, the 5G n260 band is fully covered. The RF-DC conversion efficiency is 23.3 % when the input power is 10 dBm The efficiency is also higher when the input power level is higher which can also be observed in Figure 6.32b.

### 6.4.3 Broadband 5G Energy Harvester Design

The proposed UWB AiP element design and two rectifiers are combined together to build broadband 5G energy harvesters. The test samples are fabricated with glass SAP packaging process and the results are shown in Figure 6.35. Since the proposed AiP element design can cover from 24.25 to 40 GHz, the same AiP element is used in both energy harvester

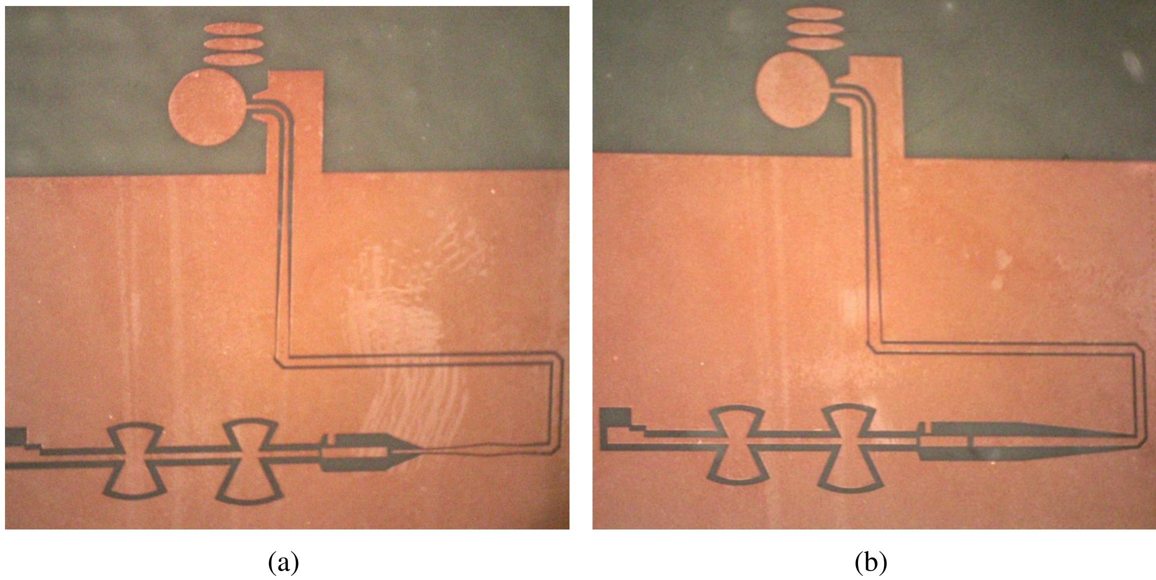
(a) (b)

Figure 6.35: The fabricated broadband 5G energy harvester for the (a) lower-band operation and (b) higher-band operation.

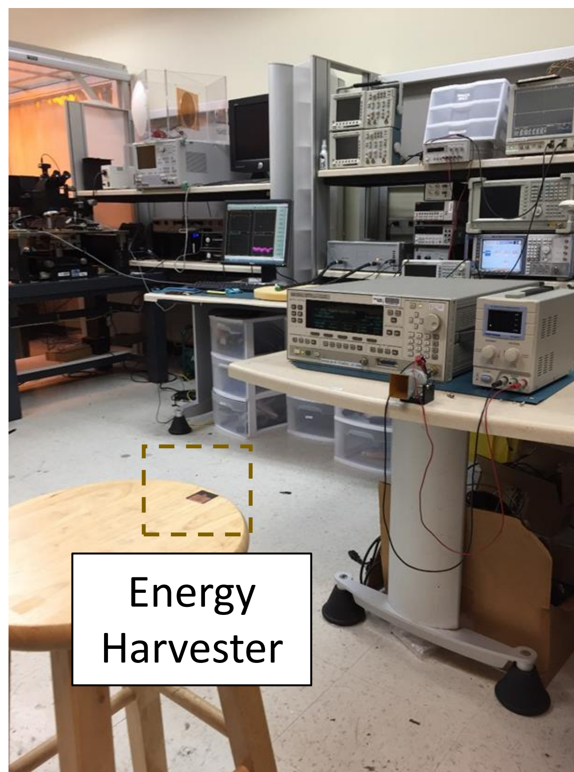


Figure 6.36: The measurement setup for the proposed broadband 5G energy harvester.

designs. The field evaluation of the energy harvester is performed and the measurement setup is shown in Figure 6.36. The signal generator outputs a 12 dBm signals at 26 GHz,

the amplifier gain is 27 dB, and the horn antenna gain is 20 dBi. The total EIRP is 59 dBm. The output voltage is larger than 1 V at 40 cm away. Since the allowed maximum EIRP is 75 dBm, the distance can be increased to more than 2.5 m.

The proposed UWB AiP element design can cover from 24.25 to 40 GHz which cover all three bands of the 5G NR. The two rectifier designs together can also cover all three bands of the 5G NR. Therefore, a diplexer can be used to integrate the antenna and two rectifiers to form a UWB package-integrated energy harvester which can harvest energy from all 5G NR bands.

### 6.5 Summary

This chapter starts with an explanation of the need for an UWB AiP design. Then the first UWB and miniaturized planar Yagi AiP design which can cover all three major 5G NR operating bands from 24.25 GHz to 40 GHz simultaneously while maintaining a small form factor. The FBW is 49% and the size for the antenna element is 3.05 mm $\times$ 5.56 mm which equals 0.25 $\lambda_0$ $\times$ 0.45 $\lambda_0$ where $\lambda_0$ is the wavelength at 24.25 GHz. Both the single element and the 2-by-1 array design are simulated, fabricated, and measured. The glass multi-layered packaging with a new polymer material is used to realize the designs. The element gain is higher than 4 dBi and the array gain is higher than 6.2 dBi within the entire operating band. The normalized radiation patterns at E-plane and H-plane are demonstrated and the main-beam directions are consistent within the entire band. The cross-polarized patterns at the main-beam direction are smaller than -15 dB. The comparison between this work and prior arts are summarized. This work demonstrates the largest bandwidth with a comparable size.

The proposed UWB AiP design is then adopted for the broadband energy harvester design. Two rectifier designs are proposed to cover all three major 5G NR operating bands from 24.25 GHz to 40 GHz simultaneously. For the proposed broadband 5G energy harvester, the output voltage is larger than 1 V at 40 cm away when 59 dBm EIRP is used.

The range can be increased to more than 2.5 m when a maximum 75 dBm EIRP is used. A diplexer can be used to integrate the proposed rectifiers and the proposed UWB and miniaturized AiP design and thus, a broadband energy harvester which can harvest energy from all 5G NR operating bands can be achieved. From the energy harvester point of view, the proposed energy harvester is the first design which can cover all three 5G NR operating bands. The broadband rectification at mm-wave 5G frequencies is demonstrated for the first time. From the fabrication point of view, the new low-loss polymer from JSR company is put to test, used to reduce the warpage, and used to realize mm-wave AiP design for the first time.

# CHAPTER 7

# ENERGY AUTONOMOUS 5G SYSTEM-IN-PACKAGE MODULE USING ADDITIVE MANUFACTURING 3D PACKAGING TECHNOLOGIES

Additive manufacturing technologies have attracted lots of attention in recent years. One of the research directions is to apply additive manufacturing to the packaging process. The better 3D structural flexibility is used to improve the performance and reduce the high-frequency parasitics. Furthermore, less material is required which is helpful for environmental protection and reduction of the cost. Currently, a couple of researches focusing on applying additive manufacturing to packaging structures are proposed. In [55], an inkjet-printed die-to-packaging-substrate connection is proposed. Compared with wire-bonding technologies, the proposed connections have better physical supports and better reliability. In [57], a 3D-printed non-orthogonal inter-layer interconnection is proposed to reduce the parasitics and improve the signal integrity.

Although these researches provide good examples and ideas of applying additive manufacturing to the packaging process, detailed comparison and proof of the superior performance are not included. Furthermore, most of the researches focus only on part of the packaging structure and thus, a complete additive manufacturing packaging process is still not available. The wide variety of material choices is another advantage of additive manufacturing technologies. However, most of the materials are high loss with loss tangent larger than 0.02. Therefore, developing a new low-loss printable material is also an important direction.

In this chapter, a fully energy-autonomous SiP module is proposed. Since the power requirement of the whole SiP module is provided by the package-integrated energy harvester, there is no need to connect to the exterior board or power supply. Therefore, the functional system size can be shrunk from a board-level size to a packaging-level size. The objectives,

| Metrics | Objectives | Prior Art | Challenges | Solutions |
|---|---|---|---|---|
| **Performance** | • Energy autonomous SiP module<br>• Interconnects with lower parasitic L/C<br>• Cavity embedding | • SiP module needs exterior power supply<br>• High parasitic L/C at mm-wave | • Proved that AM packaging process is better<br>• Embedded EH inside package<br>• Reduced parasitic L/C | • Compared off-the-shelf and AM packaging performances<br>• AM cavity and multi-layered packaging process<br>• AM non-orthogonal interconnects |
| **Fabrication** | • AM 3D packaging process<br>• Multi-layered AM packaging<br>• AM low-loss polymer | • Not fully AM<br>• Materials for AM are typically high-loss | • Combined inkjet and 3D printing<br>• Developed low-loss inkjet printable polymer | • Developed fully AM packaging process<br>• Inkjet printable low-loss BCB polymer |

AM: Additive manufacturing

Figure 7.1: The summarizing table of the objectives, challenges, and solutions of the proposed energy-autonomous SiP module.

challenges, and solutions are introduced in section 7.1. The possibilities and potential of a fully additive manufacturing 3D SiP module is addressed in section 7.2. In section 7.3, a comparison between off-the-shelf and additive manufacturing packaging is included to prove that the later one can offer better performance and lower parasitics. Then, a fully additive manufacturing packaging process utilizing both inkjet printing and 3D printing is proposed in section 7.4. The proposed additive manufacturing packaging process is used to realize an energy-autonomous SiP module with multi-layered 3D packaging structures in section 7.5. Finally, a new low-loss inkjet-printable material is proposed and characterized in section 7.6.

## 7.1 Objectives

In this chapter, the main objective is to propose a fully additive manufacturing 3D packaging process and use it to realize an energy-autonomous SiP module. The detailed objectives, comparisons to prior arts, challenges, and solutions are summarized in Figure 7.1. To demonstrate the superior performances of using additive manufacturing process, tunnel diodes with off-the-shelf packaging and inkjet-printed packaging are characterized in section 7.3. The parasitics of both packaging structures are extracted, compared, and used to prove the advantages of the additive manufacturing packaging process. Then the additive

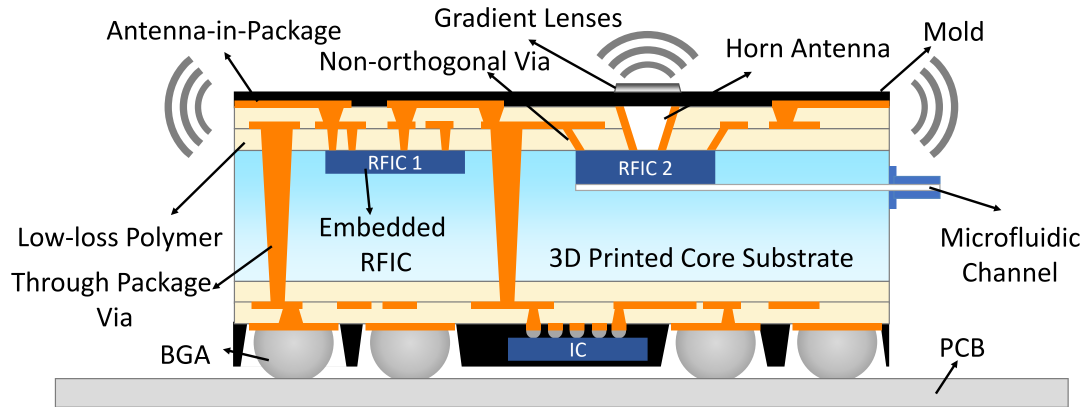


Figure 7.2: The additive manufacturing 3D SiP module for mm-wave applications.

manufacturing packaging process using both inkjet printing and 3D printing is characterized and introduce in section 7.4. The electrical properties such as relative dielectric constant and loss tangent of 3D printing materials are characterized. Moreover, the physical printing capability such as surface roughness and resolutions are also characterized. An AiP design is realized utilized the proposed additive manufacturing packaging process.

The proposed additive manufacturing packaging process is then used to fabricate a package-integrated 5G energy harvester in section 7.5. The non-orthogonal ramp interlayered connections are used to reduce the high parasitics at the mm-wave range. The embedded energy harvester can be viewed as the last puzzle to achieve a fully energy-autonomous SiP module. Finally, to further improve the additive manufacturing packaging process, the first inkjet-printed low-loss BCB material is proposed and characterized in section 7.6. The material provides super low loss tangent up to mm-wave range and thus, expanding the applications of the proposed additive manufacturing packaging process to high-performance mm-wave areas.

## 7.2 Additive Manufacturing 3D System-in-Package Module

A fully additive manufacturing 3D SiP module for mm-wave applications is shown in Figure 7.2. The core substrate is printed using 3D printing technique. The complex 3D structures such as cavities for IC dies, through via holes, and microfluidic channel can be re-

alized with 3D printing. The low-loss polymer can be coated on the 3D printing material to reduce the system loss and improve the surface roughness. The conductors are printed using inkjet printing SNP inks. Multilayer structures can be realized easily by repeating coating low-loss polymer layers and conductor layers. Furthermore, ramp structure interlayer connections and die-to-package connections can be realized with lower parasitics and can be realized much easier with additive manufacturing technologies. Compared with the SiP module realized using glass packaging process shown in Figure 6.1, the additive manufacturing process can realize not only commonly used structures such as micro vias, through vias, and cavities but also complex 3D structures such as microfluidic channels, non-orthogonal vias, gradient lenses, and vertical horn antennas.

To realize SiP module like Figure 7.2, a well-characterized fabrication process is needed. In this chapter, the superior of the additive manufacturing process on mm-wave parasitics is first proven. Then the fabrication process is developed and characterized. The process is then used to realize a AiP design and good performance at mm-wave range will be demonstrated. Then the same process is adopted to realize a SiP module with more complex 3D structures such as the cavity, ramp interconnect, and via. Finally, the process is improved with the adoption of the new low-loss printing polymer.

## 7.3 Parasitic Characterization Using Tunnel Diode

### 7.3.1 Motivation and Design Idea

The 5G communication protocol has been proposed to accommodate the continuously increasing desire for faster data transmission. One of the key reasons to realize a faster data link for 5G communication is the use of high mm-wave frequency bands which open new possibilities as well as new challenges. For starters, the small wavelength due to high frequencies is helpful to reduce the overall size for RF components making it possible to integrate RF components with active components inside a single package to achieve SiP designs [102, 103, 117]. To integrate the dies with peripheral RF components, intercon-

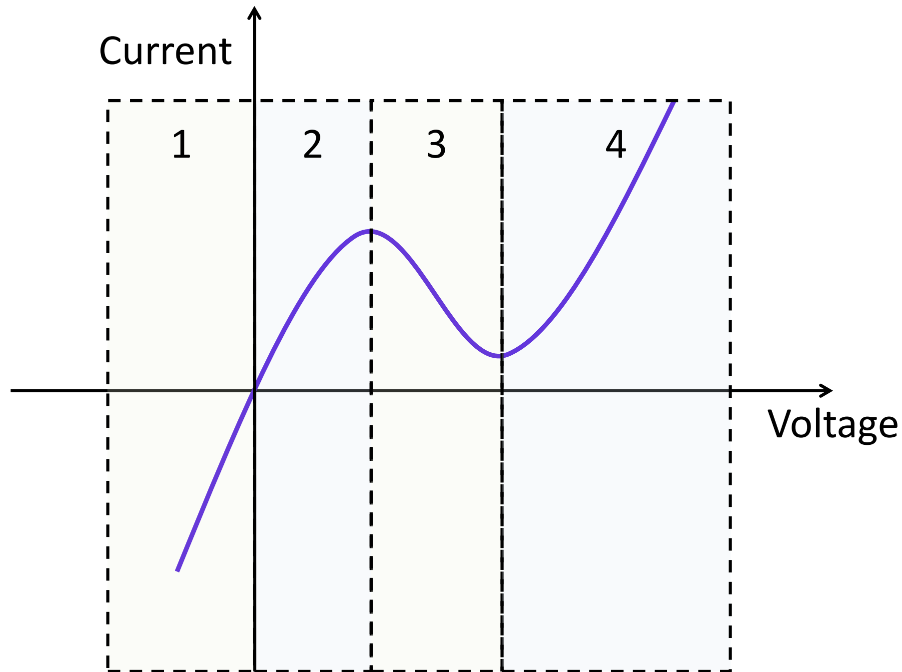


Figure 7.3: The general I-V curve of a tunnel diode.

nections are used to connect the pins of a die to the package body where RF components are located. Normally, wire-bonding interconnections are applied. However, the parasitics due to wire bonds are large and will significantly degrade the performances especially in the high frequencies like 5G and mm-wave.

To alleviate the parasitics due to the interconnections, the inkjet-printed ramp structure is proposed [55]. To overcome the height difference between the die and the package, ramp structures are printed around the die and then the silver traces are printed on the ramp to serve as the interconnections between the die and the package. However, performance comparisons between commonly used packaging structure and the ramp interconnections are not included. Thus, to establish the comparison between the commonly used packaging interconnections and the additively manufactured ones, the same functional die has to be packaged using both ways.

Tunnel diodes are chosen for packaging since efforts have indicated the high potential of tunnel diodes for 5G and mm-wave applications [21, 118]. A tunnel diode can find different applications depending on its biasing condition. A general I-V curve of a tunnel

diode is shown in Figure 7.3 and it can be separated into four different zones. In reverse biasing, zone 1, a heterostructure backward tunnel diode that can be turned on with ultra-low voltages is used for energy harvesting applications. The ultra-low turn-on voltages can be useful to improve the existing energy harvesting techniques and applications [93, 94, 119]. In zone 2, it behaves like a Schottky diode and can be used in mixer applications. Finally, in zone 3, a decreasing current is observed with the increasing voltage which gives to the tunnel diode a natural negative differential resistance. In that negative slope region of its I-V curve, the tunnel diode can be used as a reflection amplifier and an oscillator. The energy harvester, oscillator, and reflection amplifier are all key elements for backscattering sensing techniques. The energy harvester built using the tunnel diodes can operate with high efficiency at low power conditions [21]. The oscillator and the reflection amplifier which can be operated with low biasing power can be also great advantages for backscatter systems whose power budget is typically very low [118].

In this section, the performance comparisons between the commonly used packaging techniques and additive manufacturing packages are done for the first time. The tunnel diode die is packaged using the inkjet-printed technique. The same die is also packaged utilizing commercially available methods. The complete circuit models are built for both test samples. The through, reflect, and line (TRL) calibration method is used to calibrate out the effects of feeding lines and bias-tees. The parasitic inductors and capacitors due to packaging are extracted and used to prove that the additive manufacturing packaging process outperforms the commonly used packaging techniques.

### 7.3.2 Fabrication Process

A bare-die tunnel diode from Aeroflex / Metelics (model no. MBD2057-C18) is interconnected with a laminate substrate using a multi-material inkjet printing fabrication process as a comparison to a traditional diode package (model no. MBD2057-E28X). Inkjet printing is performed using a Dimatix DMP-2831 materials printer with 10 pL drop-volume

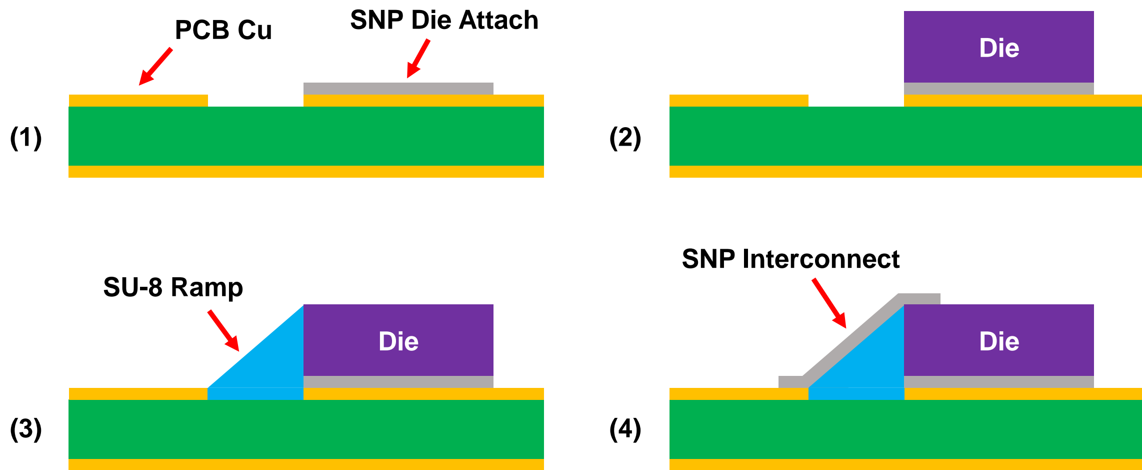


Figure 7.4: Side-view schematic of inkjet-printed interconnect fabrication process: (1) inkjet print SNP die attach, (2) attach diode die, (3) inkjet print SU-8 dielectric ramp, (4) inkjet print SNP interconnect.

cartridges. The host substrate chosen for this evaluation is 32 mil Rogers RO4003C with 1 oz metalization. Printed metallic features, such as the conductive die attach and interconnect, are patterned with Sun Chemical EMD-5730 SNP ink, capable of achieving resistivity of 5 μΩ cm to 30 μΩ cm after thermal sintering. The dielectric ramp is patterned using a MicroChem SU-8 polymer-based ink formulated to achieve a printable viscosity for the Dimatix system [120]. A test board with a microstrip topology is fabricated using an inkjet-printed mask and lithography technique on the Rogers RO4003C laminate. First, the microstrip pattern is printed using 3 layers of the SU-8 polymer ink. The printed SU-8 mask is then crosslinked with a 600 mJ/cm$^2$ exposure of 365 nm UV light. Etching of the board is then performed using $FeCl_3$ at a temperature of 55 °C. Finally, acetone is used to strip the printed SU-8 mask from the board.

A general outline of the fabrication process for the inkjet-printed bare-die interconnects is shown in Figure 7.4. First, a die attach is printed using SNP ink (2 layers, 20 μm drop spacing) onto the copper microstrip trace. The 375×375×125 μm diode die is then manually placed onto the wet SNP and then dried and sintered at 150 °C for 2 h. Next, SU-8 is printed (6 layers, 10 μm drop spacing) to pattern the 3D dielectric ramp from the PCB

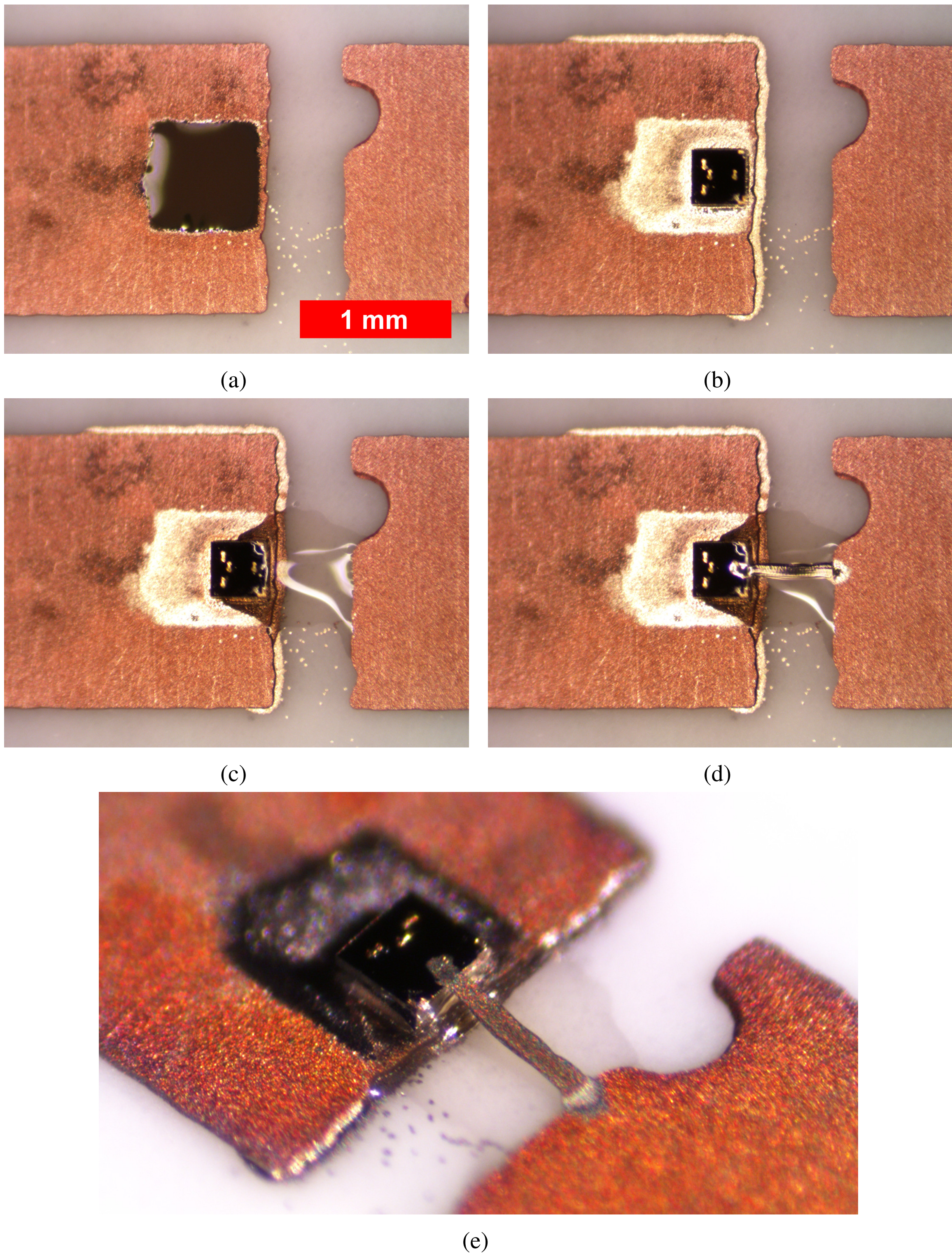


(a) (b) (c) (d) (e)

Figure 7.5: Inkjet-printed interconnect fabrication process with tunnel diode die: (a) SNP die attach patterning, (b) die placement, (c) SU-8 ramp patterning, (d) final SNP interconnect patterning, and (e) perspective micrograph.

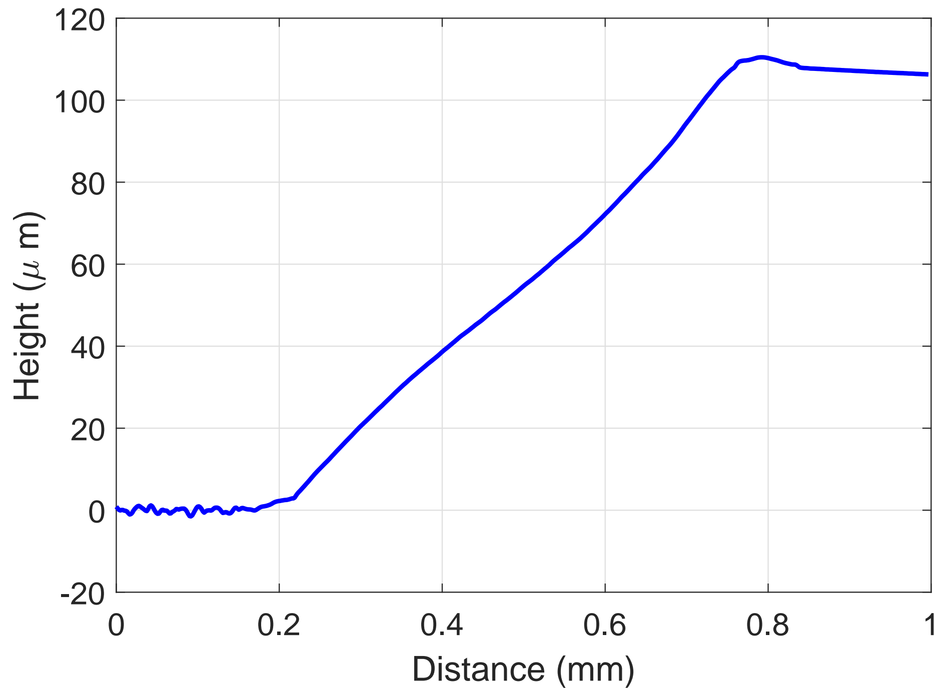

Figure 7.6: Profilometer scan of inkjet-printed ramp interconnect to diode die.

microstrip trace to the top of the diode die. The three-step curing profile for the SU-8 ink is as follows: thermal soft bake ramping from 60 °C to 95 °C over 10 min on a hotplate, 300 mJ/cm$^2$ UV crosslinking exposure, and finally a thermal hard bake at 95 °C for 7 min on a hotplate. After the SU-8 ink is cured, a 2.5 min exposure to UV $O_3$ is performed to facilitate proper ink wetting for the subsequent SNP printing. Finally, SNP is printed (5 layers, 20 μm drop spacing) to pattern the interconnect to the anode pad of the diode die, followed by final sintering at 150 °C for 2 h. Micrographs of the fabrication process with a tunnel diode sample are presented in Figure 7.5.

The printed transition between the copper microstrip topology of the PCB and the top surface of the diode die is measured using an Alpha-Step D-500 surface profilometer from KLA Tencor. Figure 7.6 shows the measured profile of the ramp interconnect, exhibiting a slope of approximately 10°. As seen in the measured profile, the printed transition is smooth and lacks abrupt discontinuities at the interfaces between the PCB, ramp, and die.

From the mechanical viewpoint, the proposed additive manufacturing interconnections are more reliable. Since the wire bonds are floating in the air, they are vulnerable to shocks

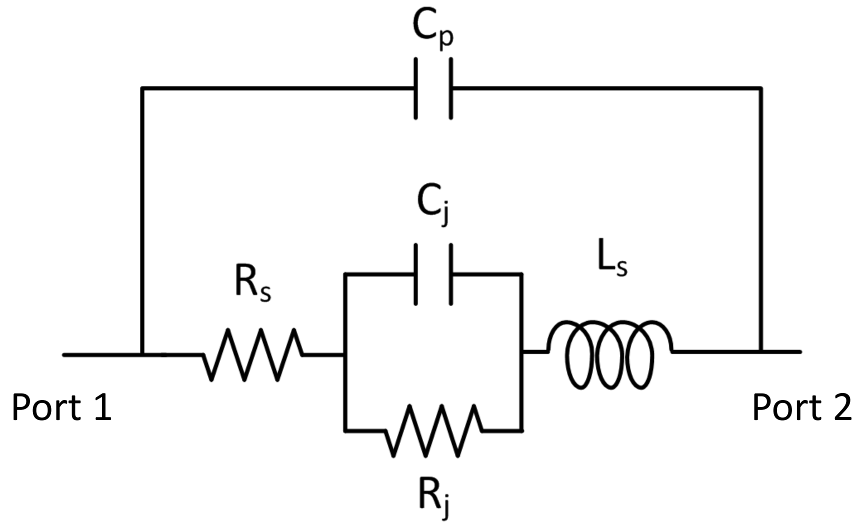


Figure 7.7: The equivalent circuit model of the tunnel diode with packaging.

or vibrations and it is easier to cause breaking wires or delamination. On the contrary, the printed silver traces are placed on the SU-8 substrate instead of floating, and thus can resist shocks and vibrations. The property makes the additive manufacturing packaging process suitable for wearable applications which often embrace shocks and vibrations due to constant human movements. From the electrical standpoint, the additive manufacturing interconnections are shorter compared with the wire bonds. Therefore, the parasitics due to the interconnections are also expected to be smaller. This is critical for high-frequency applications such as 5G and mm-wave where the effects of parasitics become more significant.

### 7.3.3 Tunnel Diode Characterization

*Tunnel Diode Model*

The equivalent circuit model of the tunnel diode with packaging is shown in Figure 7.7. The circuit model is composed of 5 components. The $C_j$ is used to model the junction capacitance of the tunnel diode. The $R_j$ is used to model the non-linear I-V relation of the tunnel diode. The $R_s$ is for the exterior series resistance. Finally, the $L_s$ and $C_p$ are used to

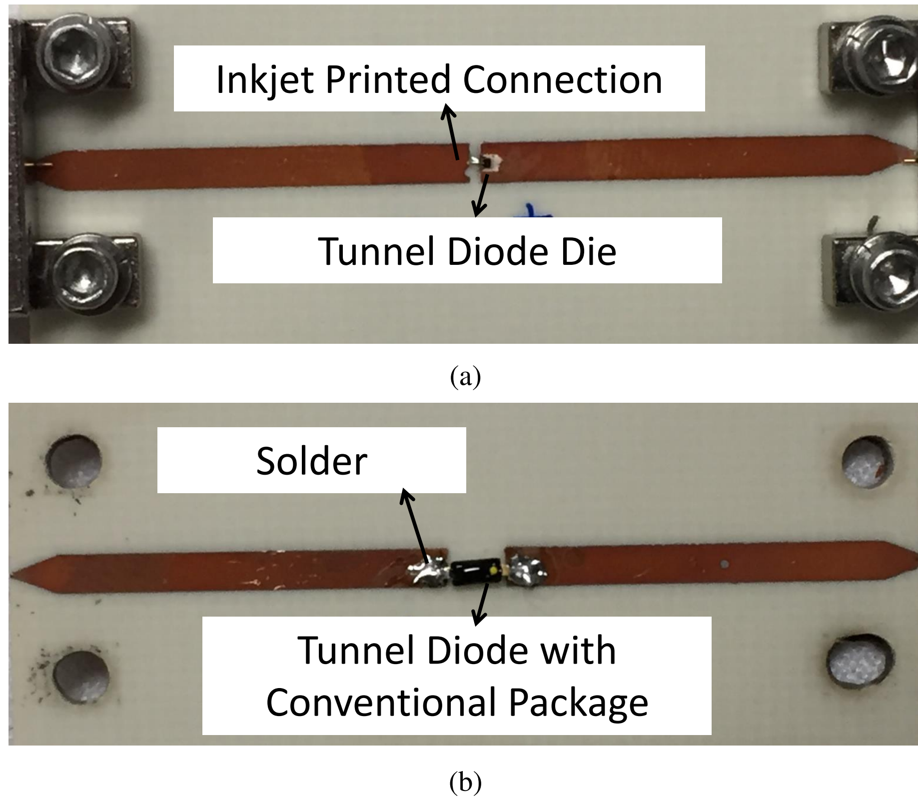


Figure 7.8: The photo of the (a) die with inkjet printed package and (b) die with traditional package.

model the capacitance and inductance induced by packaging structures.

The junction capacitance, $C_j$, is 0.3 pF from the datasheet. The $R_s$ and $R_j$ can be extracted from the measured I-V curve of the tunnel diode. The $L_s$ and $C_p$ are extracted by the measured 2-port scattering parameters of the tunnel diode. Since the 2-port scattering parameters are used, the TRL calibration method is used to de-embedded the tunnel diode to get higher accuracy of the extracted values for the equivalent models.

*TRL Calibration*

The fabricated samples of the tunnel diode with an inkjet-printed package and with the traditional package are shown in Figure 7.8. As shown in the figure, there are two 20 mm long feeding line with tapering structures at the end. This feeding line will induce additional loss and mismatch to the entire system. Thus, in order to obtain equivalent models with

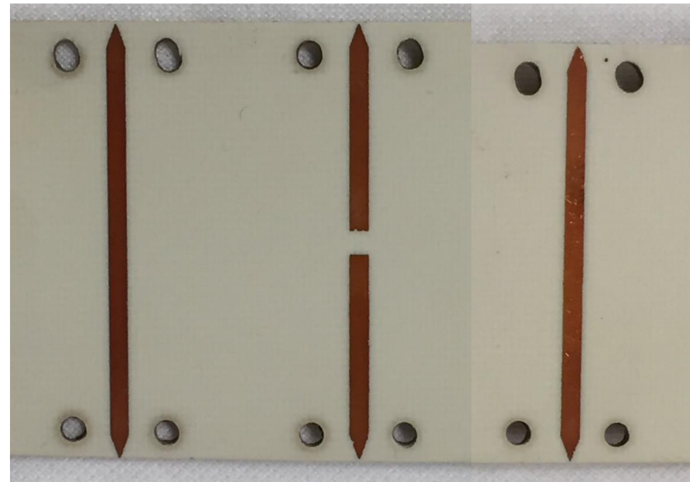


Figure 7.9: The TRL calibration circuits.

higher accuracy, the TRL calibration method is adopted. The TRL calibration circuits are shown in Figure 7.9. The through circuit is composed of two feeding lines connecting together without the tunnel diode. The reflect circuit is the two feeding lines with open circuits. The line circuit is the two feeding lines with one additional length inserted between them. The inserted line length has to be $\lambda/4$ at the geometric mean of the highest and lowest frequencies. Furthermore, the ratio between the lowest and highest frequencies has to be smaller than 1:8. For example, the lowest frequency here is 10 GHz while the highest frequency is 35 GHz. Thus, the inserted $\lambda/4$ line is calculated at 18.7 GHz. Besides, the ratio between the lowest and highest frequencies is 1:3.5 which is smaller than the maximum of 1:8.

The measured $S_{21}$ of the TRL circuits are shown in Figure 7.10. As depicted in the figure, there are ripples and losses due to the taper structure and the microstrip feeding lines. These effects will exist when measuring the 2-port scattering parameter of the tunnel diode test samples and thus has to be calibrated out using TRL before extracting the parameters for the equivalent model. The measured $S_{21}$ of the tunnel diode with the inkjet-printed package and the tunnel diode with the traditional package are shown in Figure 7.11a

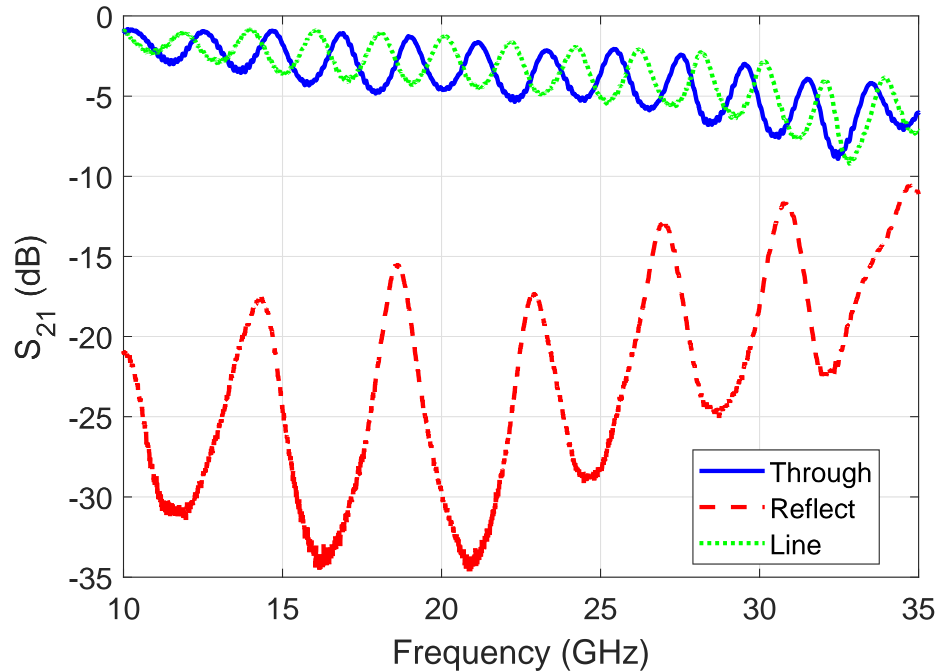


Figure 7.10: The measured $S_{21}$ of the TRL calibration.

and Figure 7.11b, respectively. The de-embedded results calculated using TRL calibration are also included for comparisons. As shown in the figures, The ripples can be alleviated significantly and the de-embedded $S_{21}$ is higher because the loss of the feeding lines is calibrated out. The measured $S_{21}$ after TRL calibration will be used to extract the equivalent models of the test samples.

*Model Parameters Extraction*

As shown in Figure 7.7, in addition to the junction capacitance ($C_j$) which is already provided in the datasheet, there are four remaining parameters including junction resistance ($R_j$), series resistance ($R_s$), and packaging parasitics ($L_s$ and $C_p$) which have to be extracted by the measured results.

**Junction Resistance**

The non-linear effects of the tunnel diode are modeled using the junction resistance. The measured DC I-V curve is shown in Figure 7.12. The measured DC I-V curve has a similar shape as the general tunnel diode as shown in Figure 7.3. The region 2 is ranging from

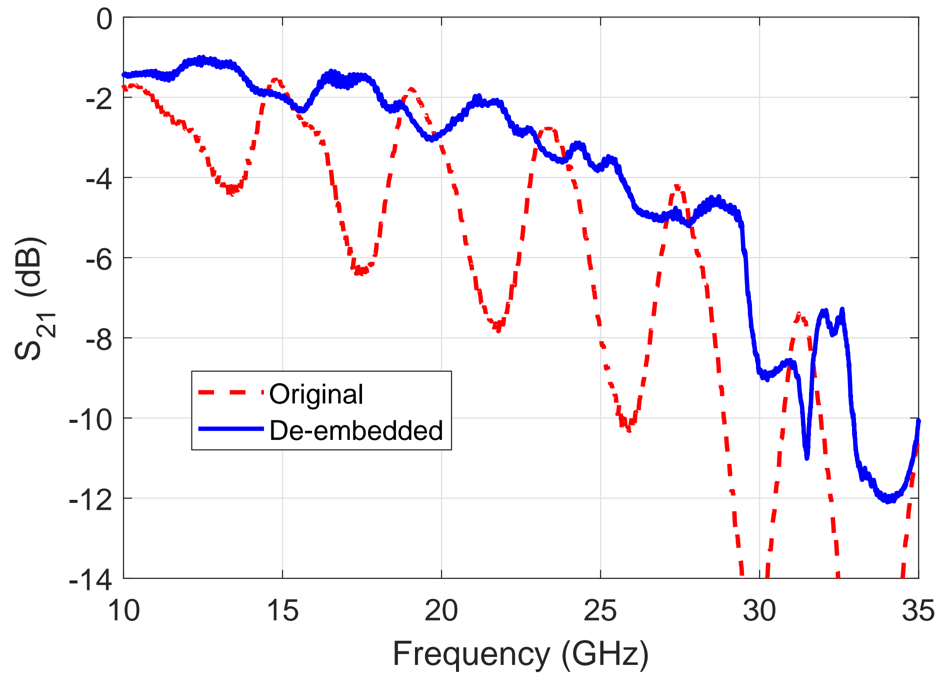


(a)

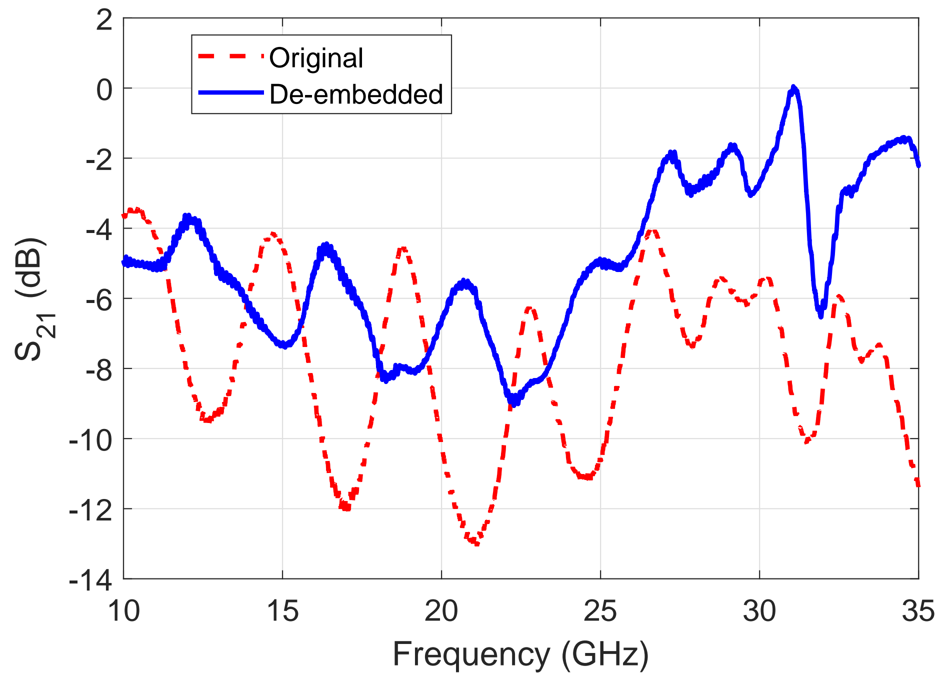


(b)

Figure 7.11: The measured $S_{21}$ of the original and TRL de-embedded tunnel diode with (a) inkjet printing package and (b) traditional package.

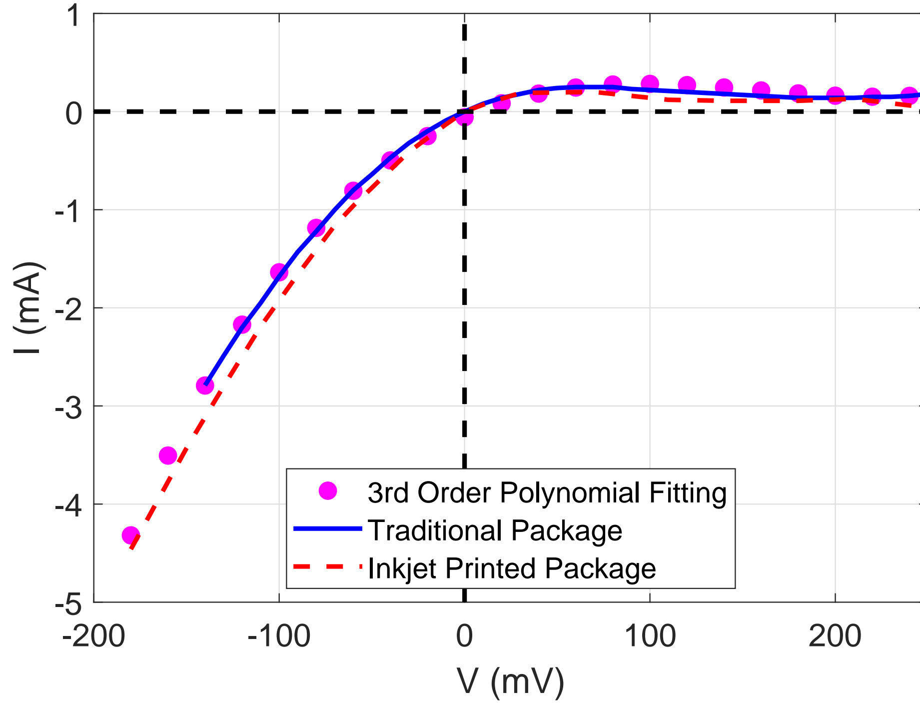


Figure 7.12: The measured DC I-V Curves of the tunnel diodes.

0 mV to 60 mV and the region 3 is between 60 mV and 210 mV. Since it is measured in DC, it is only affected by the junction and series resistance. The overall resistance can be approximated with 3rd order polynomial fitting as the following

$$I(V) = 1.3 * 10^{-7} V^3 - 6.2 * 10^{-5} V^2 + 8.3 * 10^{-3} V - 0.058 \tag{7.1}$$

The resulting curve is also included in Figure 7.12 for comparisons and a good agreement can be observed. The junction resistance is the overall resistance minus the series resistance.

**Series Resistance**

The current through the diode can be expressed as [121]

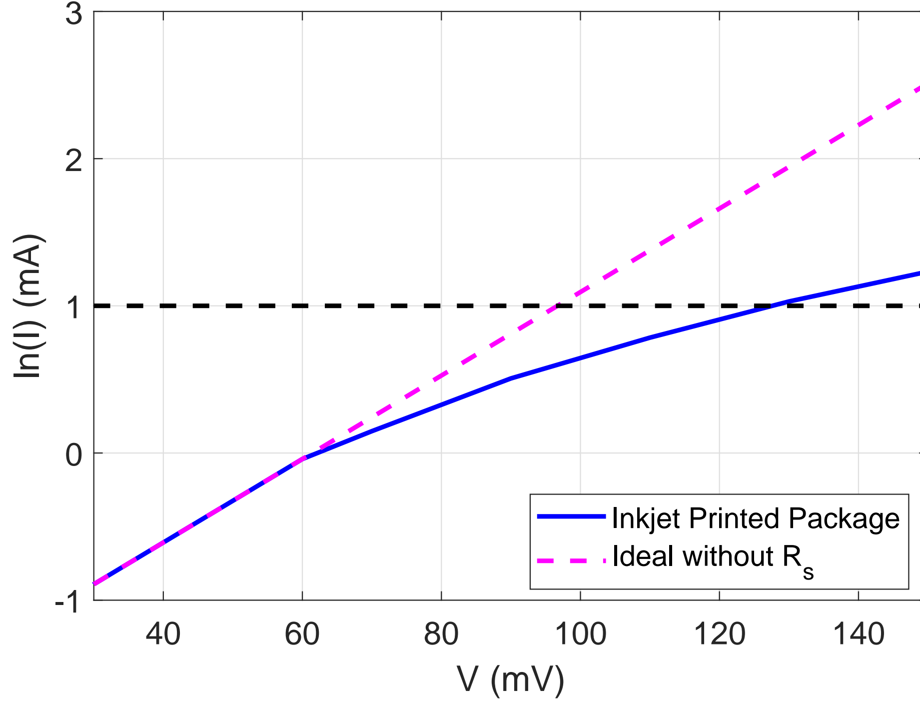

Figure 7.13: The extraction of $R_s$ for the tunnel diode with the inkjet-printed package.

$$I \approx I_s \exp(\frac{V - IR_s}{V_T}) \tag{7.2}$$

$$V_T = \frac{nkT}{q} \tag{7.3}$$

where $I_s$ is the saturation current. Thus, by (Equation 7.2), we can know

$$ln(I) \approx ln(I_s) + \frac{V - IR_s}{V_T} \tag{7.4}$$

Therefore, if the series resistance is zero, the relationship between the natural log of current and the voltage is linear. Hence, we know that

$$ln(I) \approx ln(I_s) + \frac{V_1 - IR_s}{V_T} \tag{7.5}$$

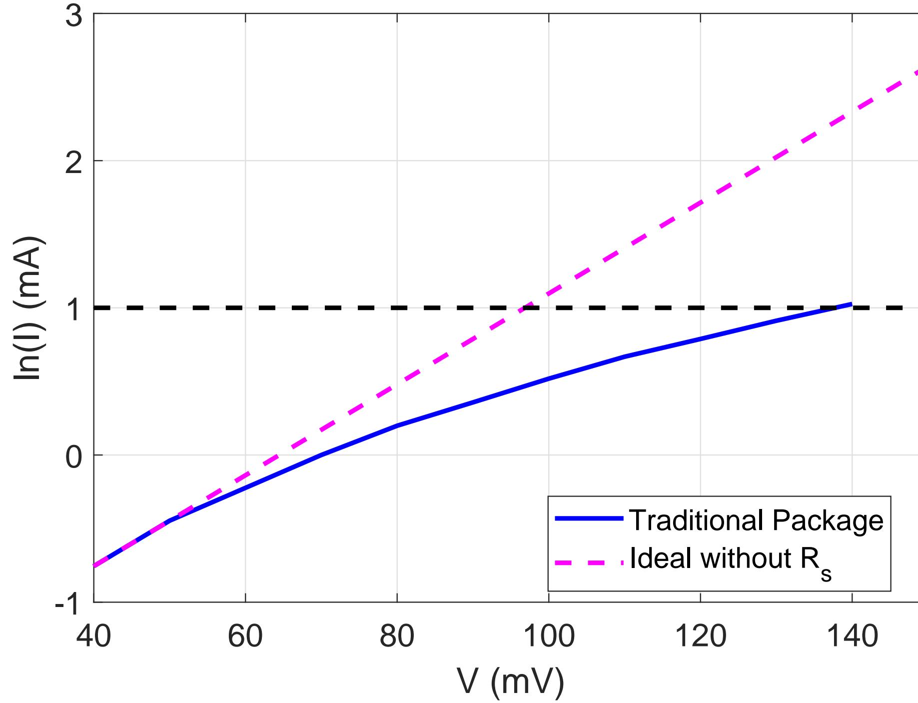


Figure 7.14: The extraction of $R_s$ for the tunnel diode with the traditional package.

$$ln(I) \approx ln(I_s) + \frac{V_2}{V_T} \tag{7.6}$$

where (Equation 7.5) is for the measured curve and (Equation 7.6) is the ideal curve without series resistance. Thus, for the same value of current and by (Equation 7.5) and (Equation 7.6), we can obtain

$$\frac{V_1 - IR_s}{V_T} = \frac{V_2}{V_T} \tag{7.7}$$

$$R_s = \frac{V_1 - V_2}{I} \tag{7.8}$$

The resulting figures for both the tunnel diode with the inkjet-printed package and the traditional package are shown in Figure 7.13 and Figure 7.14, respectively. The ideal linear tangential curve is created to calculate the series resistance. For the tunnel diode with the inkjet-printed package (Figure 7.13), the $V_1$ and $V_2$ are 127.6 mV and 96.83 mV, re-

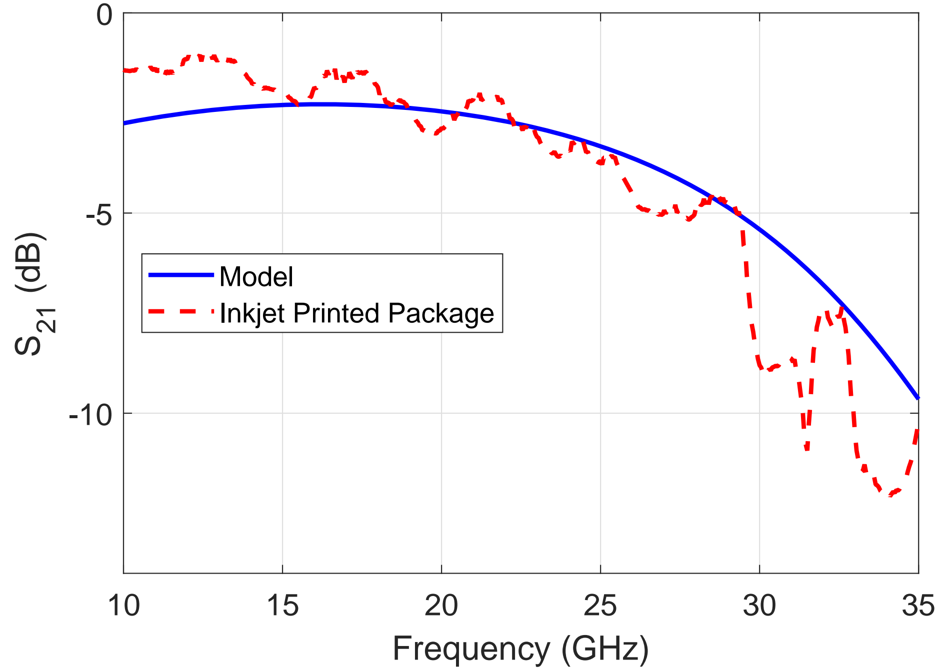


Figure 7.15: The comparisons between the equivalent model and the measured $S_{21}$ of the tunnel diode with the inkjet-printed package.

spectively where the current is e(2.71828) mA. Therefore, by (Equation 7.8), the series resistance for the tunnel diode with the inkjet-printed package is 11.3 Ω. Similarly, for the tunnel diode with the traditional package (Figure 7.14), the $V_1$ and $V_2$ are 138 mV and 97 mV, respectively where the current is e(2.71828) mA. Thus, the series resistance for the tunnel diode with the traditional package is 15 Ω. The series resistance for the inkjet-printed package is smaller than the traditional package, and thus the loss induced by the package is smaller.

**Package Parasitics**

The final step toward the extraction of the equivalent model is the package parasitics ($C_p$ and $L_s$). These parameters are extracted by placing the equivalent model in Figure 7.7 with the values of $R_s$ and $R_j$ calculated previously in the simulation software, ADS, and performs the curve fitting to fit the measured $S_{21}$ which is calibrated using TRL calibration.

The resulting $S_{21}$ for the model and the tunnel diode with the inkjet-printed package is shown in Figure 7.15. The good agreement between the equivalent model and the measured

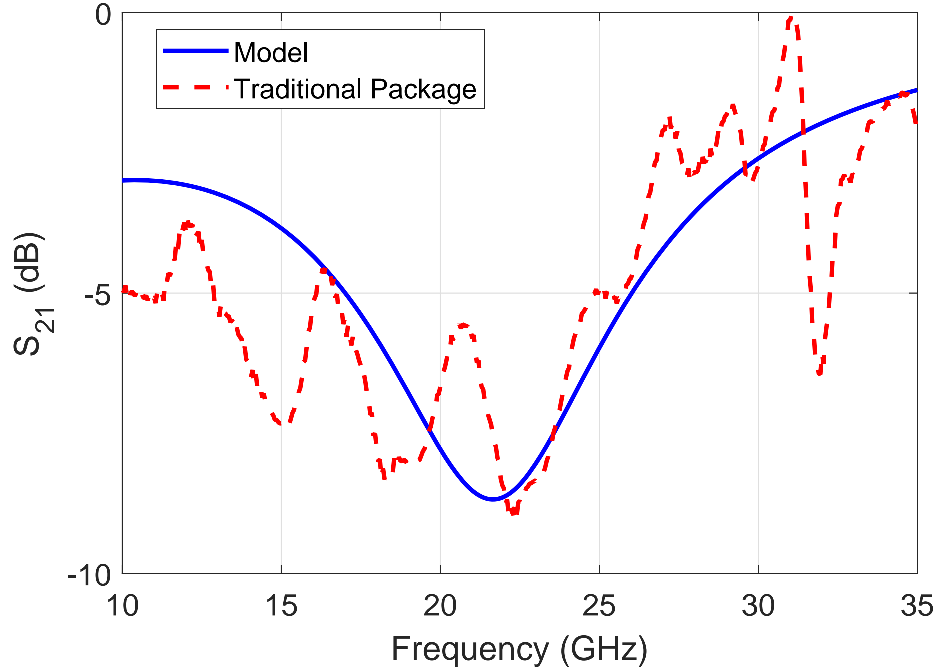


Figure 7.16: The comparisons between the equivalent model and the measured $S_{21}$ of the tunnel diode with the traditional package.

Table 7.1: Parameter comparison between the inkjet-printed package and the traditional package.

| Parameter | Inkjet-printed Package | Traditional Package |
|---|---|---|
| $C_j$ (pF) | 0.3 | 0.3 |
| $R_s$ ($\Omega$) | 11.3 | 15.0 |
| $C_p$ (pF) | 0.056 | 0.120 |
| $L_s$ (nH) | 0.351 | 0.610 |

results can be observed and validate the correctness of the equivalent model. The same process is applied for the tunnel diode with the traditional package and the results are shown in Figure 7.16. The good agreement can also be seen in the figure.

#### 7.3.4 Parasitic Comparisons

The extracted parameters for the equivalent models for both the inkjet-printed package and traditional package are summarized in Table 7.1. The inkjet-printed package can support lower series resistance. Furthermore, the capacitance due to the traditional package is

0.12 pF which is 2.14 times of the inkjet-printed package one, 0.056 pF. The inductance due to the traditional package is 0.61 nH which is 1.74 times of the inkjet-printed package one, 0.351 nH. In summary, by extracting the parameters of the equivalent models for the tunnel diode with different packaging method, the inkjet-printed packaging method outperforms the traditional method since both the resistance and the parasitics are lower. Thus, the inkjet-printed package is more suitable for high-frequency applications such as 5G and mm-wave.

## 7.4 Fully Additive Manufacturing Fabrication Process Characterization

### 7.4.1 Motivation and Design Idea

The next-generation 5G wireless communication standard has been proposed to alleviate the constant desire for dramatically faster data transmission [122]. One of the reasons that 5G wireless communications can provide higher data rate is the use of significantly larger bandwidths at mm-wave frequencies which result in high interest and numerous researches within this frequency band [103, 123, 124]. To further reduce sizes of the 5G wireless communication system, SiP topologies which integrated the ICs with peripheral components such as filters, couplers, and antennas have been proposed and attracted lots of attention. One of the major challenges to realize 5G SiP designs is to reduce the large parasitics in packaged module configurations at mm-wave frequencies. Thus, the design of cost-/performance-efficient packaging solutions for 5G modules while minimizing parasitics has become one of the major research areas. In the meantime, deploying circuits at different locations is required for the age of IoT necessitating the design and implementation of flexible packages which have better resistant to the shocks and vibrations and can be fitted into different locations easily.

Additive manufacturing techniques such as inkjet and 3D printing have been proven to be an effective solution to fabricate circuits with lower cost, less waste of materials, and higher on-demand customization. In [55], inkjet printing has been used to fabricate in-

terconnects between IC die and packaging up to mm-wave range, featuring much smaller parasitics than using wire bonding which is proven in the section 7.3. In [57], inkjet-printed transmission lines on 3D printed dielectric ramps have been used to serve as a substitution to conventional vias. Nevertheless, most previously reported efforts have demonstrated only characterization results of individual additively manufactured interconnects. Moreover, the interconnections in previous works are not flexible.

In this section, a flexible 3D-printed material, FLGR02, is first used on the design of 5G and mm-wave packaging structure. The characterization of this material such as the proper deal with light exposure time, surface treatment, ink adhesion, and thermal expansion are included. A broadband AiP design operated at mm-wave range is proposed and fabricated using inkjet-printed silver trace and 3D-printed flexible substrate with this material. The proposed broadband package-integrated antenna are integrated with the 3D-printed ramp structure, CPW lines, and a sample IC to demonstrate the possibility of SiP design using additive manufacturing procedures.

### 7.4.2 3D Printing Flexible Material Characterization

The material has to be fully characterized before applying it to the packaging process. The 3D printing material used is flexible resin FLGR02 from FormLabs. The relative dielectric constant and loss tangent is characterized by the waveguide method as introduced in section 3.5. The measured dielectric constant and loss tangent up to 40 GHz are shown in Figure 7.17 and Figure 7.18, respectively. Three sets of standard waveguides including WR-62 (Ku band: 12.4-18 GHz), WR-42 (K band: 18-26.5 GHz), and WR-28 (Ka band: 26.5-40 GHz) are used to perform the characterization at respective bands. As shown in Figure 7.17, the relative dielectric constant for Flexible FLGR02 is from 2.79-2.89. The loss tangent is between 0.028 to 0.031 as shown in Figure 7.18. The loss tangent of general 3D printing resins is high. However, low-loss polymers can be coated on the 3D printing materials to bring down the overall effective loss tangent which is a similar procedure as

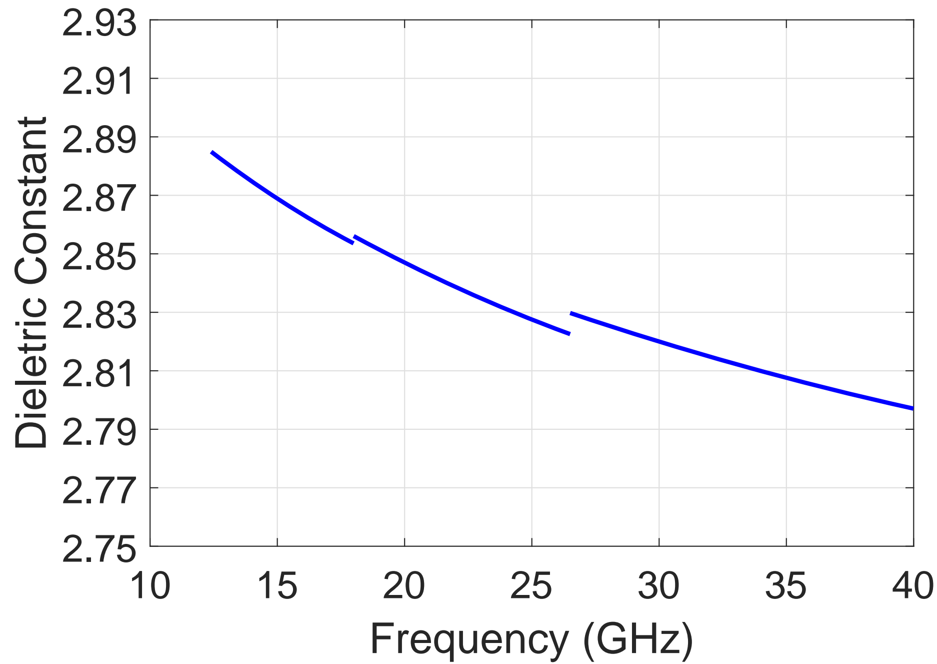


Figure 7.17: The measured dielectric constant of the 3D printing material, Flexible FLGR02.

discussed in section 6.2.

#### 7.4.3 3D Printing Core Substrate

The substrate is fabricated using a DLP SLA 3D printer with flexible resin FLGR02 from FormLabs. Since the material is cured around 405 nm, a white light projector is used to project the images of designs and cure the material layer by layer. The thickness resolution is set to be 50 µm. The light exposure time each layer has significant effects on the design. As shown in Figure 7.19, not enough light exposure will result in serious defects on the samples. For example, the hole is not complete and the thickness is not enough for the first couple of samples. On the other hand, too much light exposure will close the holes and deviate the design parameters. The light exposure time for each layer is set to 13 s after testing with different setups. Another thing that needs to be considered while using this material is that the adhesion for this material is weaker. Thus, the build plate has to be rough enough for the material to adhere to the build plate.

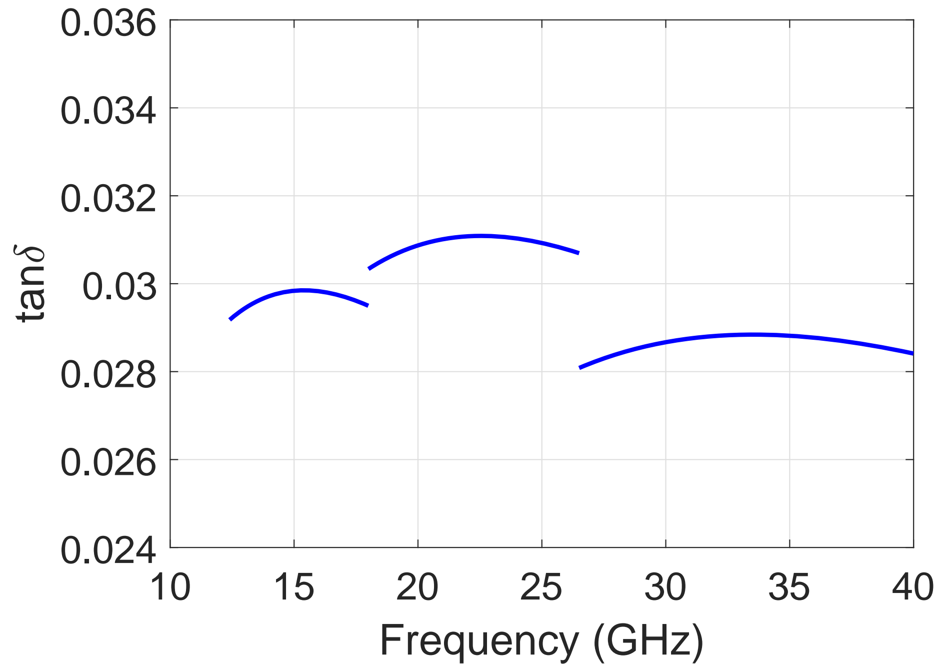


Figure 7.18: The measured loss tangent of the 3D printing material, Flexible FLGR02.

One of the key advantages of this technique is the large-scale manufacture. Since the images of multiple samples can be projected and cured simultaneously, the fabrication time is similar for one sample and multiple samples. For example, as demonstrated in Figure 7.20, two samples are fabricated simultaneously with the same lead time as one sample. This is a significant advantage for large-scale fabrication. Furthermore, a piece of glass is attached to the build plate and the samples are fabricated on the glass. Thus, the whole glass can be taken off and move to the inkjet printer while maintaining the relative positions of all samples so that metal traces for both samples can be fabricated using the inkjet printer simultaneously, too. As shown in Figure 7.21, the resulting samples with thickness equals to 1.7 mm is folded on a 14.3 mm diameter torque wrench to demonstrate the flexibility of the samples.

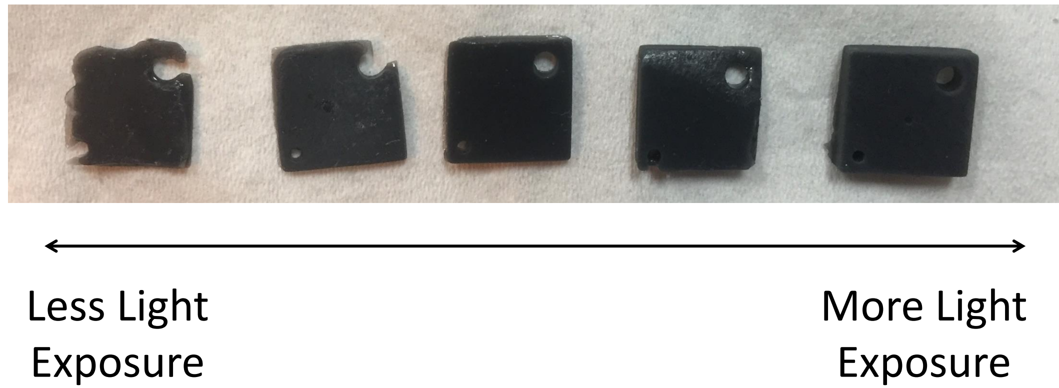


Figure 7.19: The effects of exposure time on the 3D-printed substrates.

Figure 7.20: Demonstration of large-scale fabrication.

### 7.4.4 Inkjet Printing Polymer and Conductor

*Ink Adhesion Improvement*

Once the substrate is fabricated with 3D printer, it is switch to the inkjet printer to print the metal trace with SNP ink. As shown in Figure 7.22a, the ink adhesion is terrible without surface treatment. Thus, the surface treatment is necessary before printing other inks on

Figure 7.21: Flexibility of the 3D-printed substrate.

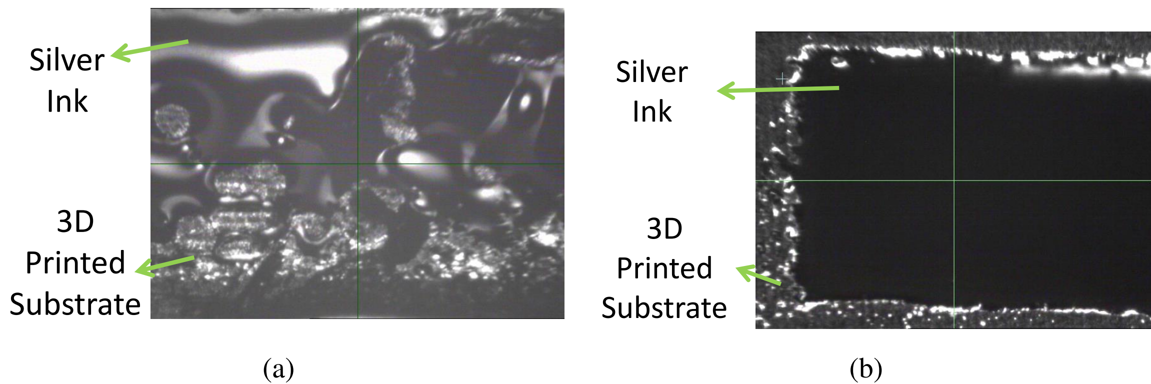


(a) (b)

Figure 7.22: Ink adhesion while (a) no surface treatment is applied and (b) exposure to UV ozone before inkjet printing.

the flexible substrate. After testing different types of surface treatments, 30 seconds of UV ozone is adopted before printing the silver trace and the significant improvement can be observed in Figure 7.22b. As a result of the surface treatment, the ink spreads uniformly compared with the results without surface treatment and the conductivity can be improved significantly.

*Surface Roughness and Quality Enhancement*

The other problem has to be solved is the CTE differences between the substrate and the SNP ink. Since the SNP ink has to be sintered at 150 °C, the substrate will expand while sintering, and cracks would appear due to the imbalance of CTE between the substrate and

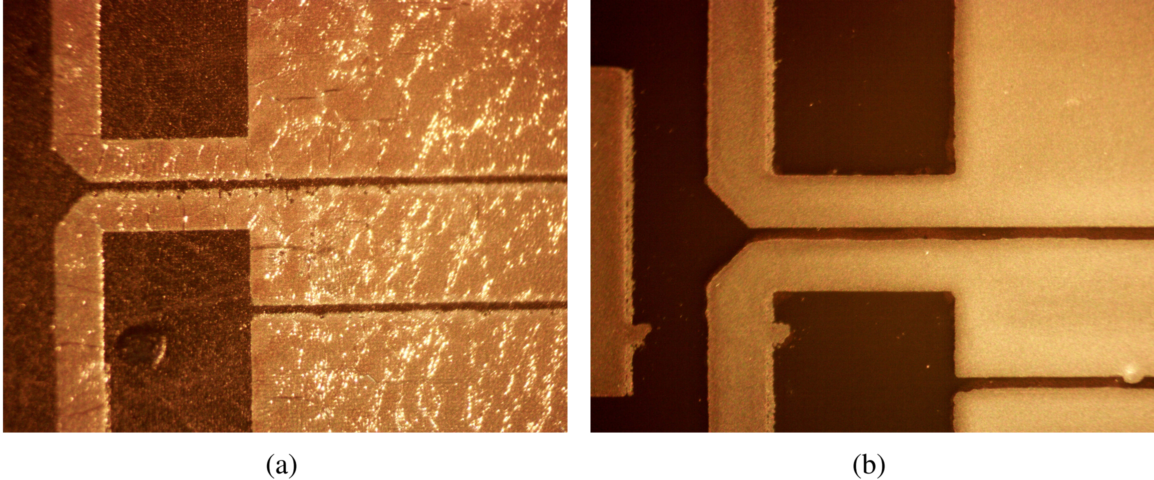

(a) (b)

Figure 7.23: Inkjet printing results (a) without SU-8 coating and (b) with SU-8 coating.

the SNP ink as shown in Figure 7.23a. The way to alleviate the situation is to print a thin layer of SU-8 between the substrate and the silver to act as a buffer to smooth the difference of CTE. As shown in Figure 7.23b, a thin layer of SU-8 is printed on the substrate before printing the silver trace. Compared with the Figure 7.23a, significant improvement can be observed. There are no cracks after sintering at 150 °C. Another advantage of printed a layer of SU-8 is to smooth the surface roughness of the 3D printed flexible substrate. As demonstrated in Figure 7.23b, the edge of the silver trace is sharper and straighter with less ink spread. Therefore, higher conductivity and more precise circuits can be achieved.

### 7.4.5 Fabrication Process

The procedure of fabricating precise samples with 3D and inkjet printing is summarized in Figure 7.24. The core packaging substrate is printed using a custom made DLP SLA 3D printer and the material used is flexible FLGR02 resin from FormLabs. Then, the surface finishing is done by exposing the samples under UV ozone for 30 seconds to improve the ink adhesion. Three layers of MicroChem SU-8 (20 µm drop spacing) is then inkjet printed on the substrate using Dimatix DMP-2831 to smooth the surface and buffer the CTE difference. The SU-8 is soft baked at 95 °C for 10 minutes, cross linked under UV for 2 minutes, and hot baked at 95 °C for another 10 minutes. The Sun Chemical EMD-5730

Figure 7.24: Fully additive manufacturing SiP process with surface treatment.

Figure 7.25: The geometry of the proposed broadband AiP design.

SNP ink is used to inkjet printed the silver traces and three layers of SNP (20 µm drop spacing) is printed on the SU-8. The sample is then sintering at 150 °C for 2 hours.

Table 7.2: Physical dimensions of the proposed broadband AiP design.

| Parameter | Dimension (mm) | Parameter | Dimension (mm) |
|---|---|---|---|
| dir_l | 3 | dir_w | 0.6 |
| dir_s | 0.8 | dri_w | 0.6 |
| dri_l | 8.57 | dri_s | 1.8 |
| ref_w | 8 | ref_l | 8 |
| CPW_w | 1.3 | CPW_gap | 0.17 |

Figure 7.26: The fabricated prototype of the proposed broadband AiP design.

### 7.4.6 Broadband 5G Antenna-in-Package Design

After all the printing procedures are well-characterized, they are applied to fabricated test samples of the proposed broadband package-integrated Yagi antenna. To reduce the size of the 5G wireless communication system, the antenna has to be broadband enough to cover the whole 5G bandwidth so that only one set of the antenna is required. The proposed 5G broadband package-integrated antenna is shown in Figure 7.25. Since the antenna is operated at mm-wave frequencies, the size of end-launch connector would induce significant effects and has to be taken into consideration. Thus, the end-launch connector structure is included while performing the full-wave simulation and design. A positioning marker is included in both the substrate and metal trace to align the 3D printed substrate and inkjet printing silver. The physical dimensions of the proposed broadband package-integrated antenna are shown in Table 7.2. The minimal gap for CPW lines is 170 µm which is much larger than the minimal resolution (20 µm) of the inkjet printer. The thickness of the sub-

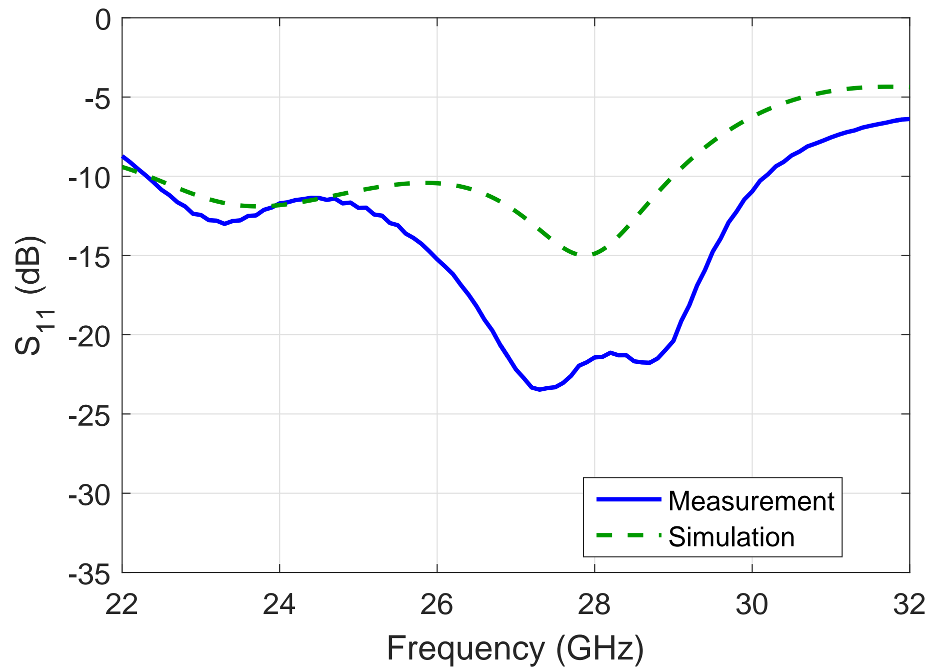


(a)

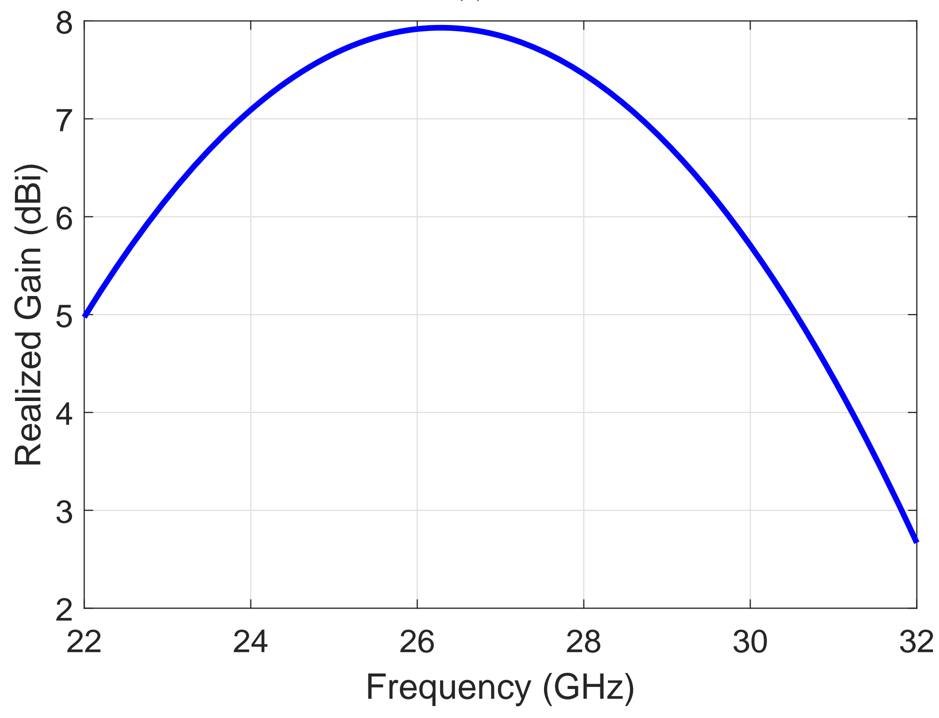


(b)

Figure 7.27: Measured and simulated (a) $S_{11}$ and (b) gain of the proposed broadband AiP design.

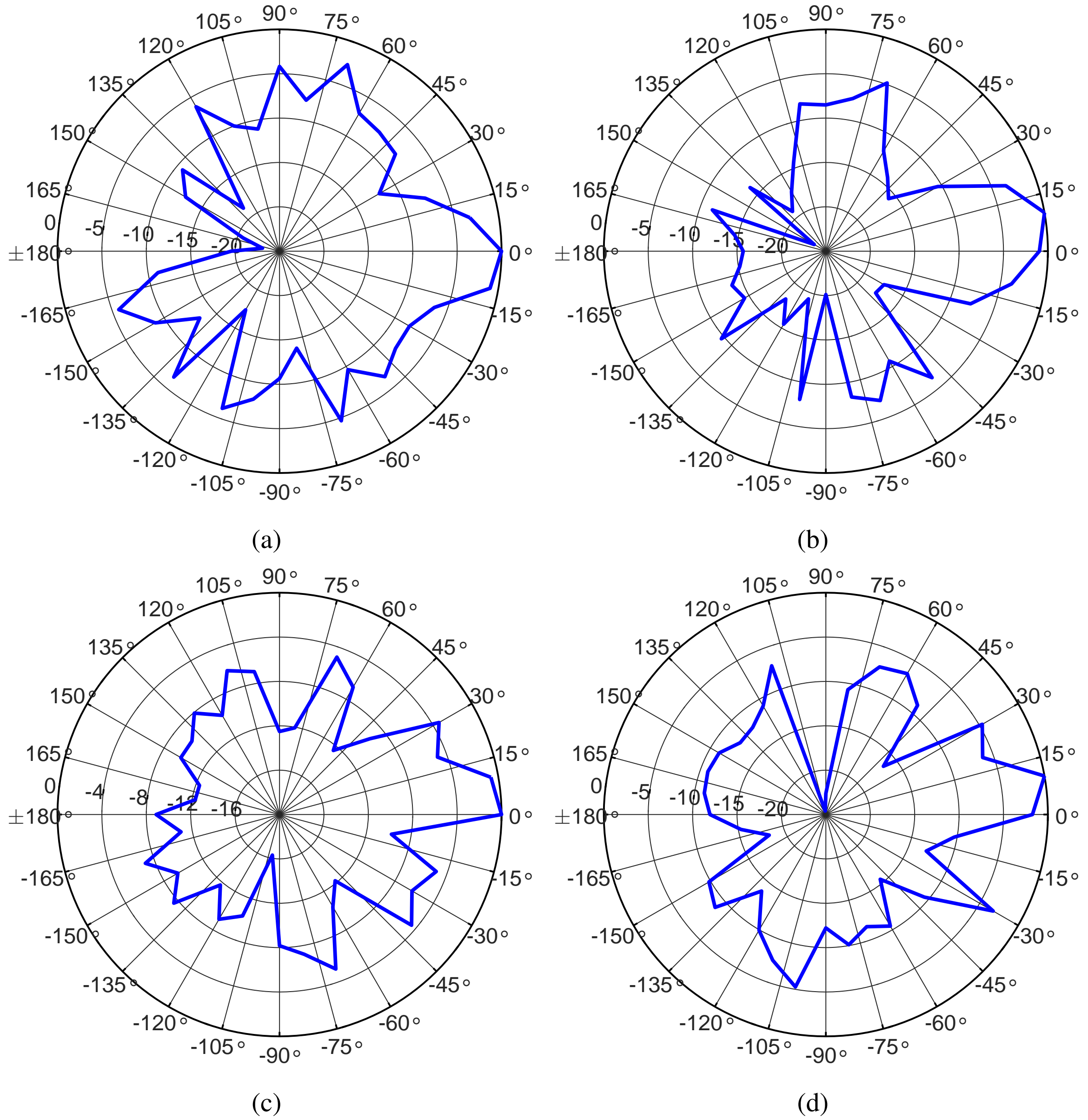


Figure 7.28: Measured normalized radiation patterns of the proposed broadband AiP design at (a) 22 GHz (b) 24 GHz (c) 28 GHz and (d) 30 GHz.

strate is 1.7 mm. The total size excluding the positioning marker is 11.8 mm×17.8 mm. It can be further reduced to 5 mm×9 mm which is $0.44\lambda_0 \times 0.79\lambda_0$ after excluding the structure for end-launch connector.

The fabricated sample is shown in Figure 7.26. A transparent layer of SU-8 and silver traces can be observed in the figure. The $S_{11}$ of the proposed broadband package-integrated antenna is measured and shown in Figure 7.27a. The full-wave simulated results using Ansys HFSS are also included for comparison and a good agreement can be observed. The differences between the measured and simulated results are due to the higher conductive loss in fabrication and minor thickness inconsistency for the substrate. Despite the differences, the general trend and the location of zeros are the same for the simulated and measured results. The measured $S_{11}$ is smaller than -10 dB from 22.4 GHz to 30.1 GHz. The FBW is 29.3 %. The antenna is broadband enough to cover the 5G band n257 (28 GHz) and n258 (26 GHz).

The realized gain of the proposed broadband package-integrated antenna is measured using the three-antenna measurement (receive, standard, and test antennas). The measured results are shown in Figure 7.27b. The measured realized gains are larger than 5 dBi from 22 GHz to 30.5 GHz. Moreover, the differences in the realized gain within this operating band are smaller than 3 dB. The normalized radiation patterns of the proposed antenna are also measured and shown in Figure 7.28. Since the proposed antenna is a broadband antenna, the radiation patterns at 22 GHz, 24 GHz, 28 GHz, and 30 GHz are all included. The 0° is the end-fire direction and the patterns rotate in the x-y plane as shown in Figure Figure 7.25. As shown in Figure 7.28, the main beam direction is at the end-fire direction which is as expected. The fabricated antenna can be served as a successful proof of applying this flexible 3D-printed material and the process developed in this paper to mm-wave applications.

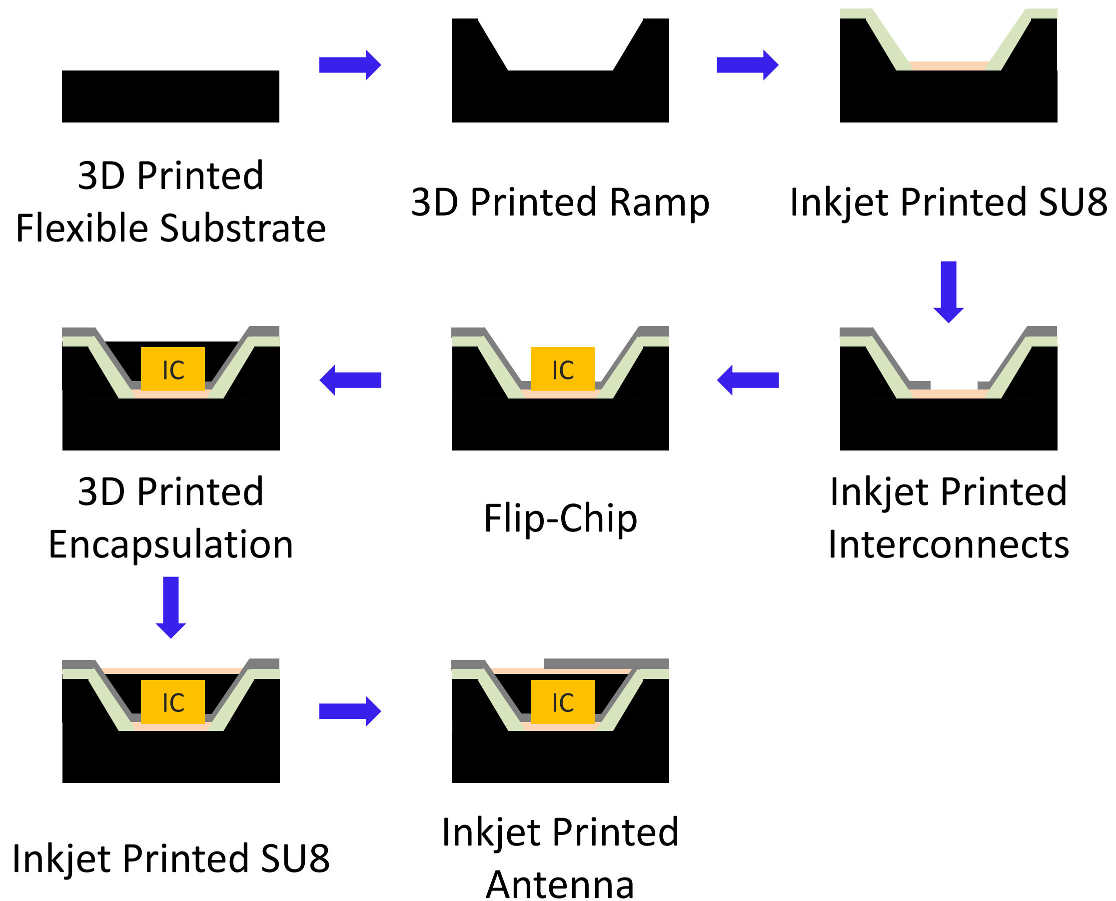


Figure 7.29: Fully additive manufacturing SiP Process with an embedded IC.

### 7.4.7 System-in-Package Design

The antenna, ramp interlayer connections, and IC are integrated together to demonstrate a SiP design. The process steps are summarized as in Figure 7.29. The fabrication starts with 3D-printed flexible substrate and ramps. The layer thickness resolution is reduced to 10 µm to achieve a smoother ramp structure. Then the SU-8 is printed to further smooth the surface roughness and act as CTE buffer. The metal connections are then inkjet-printed on the ramp and the bottom of the cavity. The IC is attached to the bottom of the cavity using conductive epoxy. Then, the flexible material is used to seal the cavity. The SU-8 is printed again for the same reason. The final step is to print passive components such as an antenna on the top of the seal.

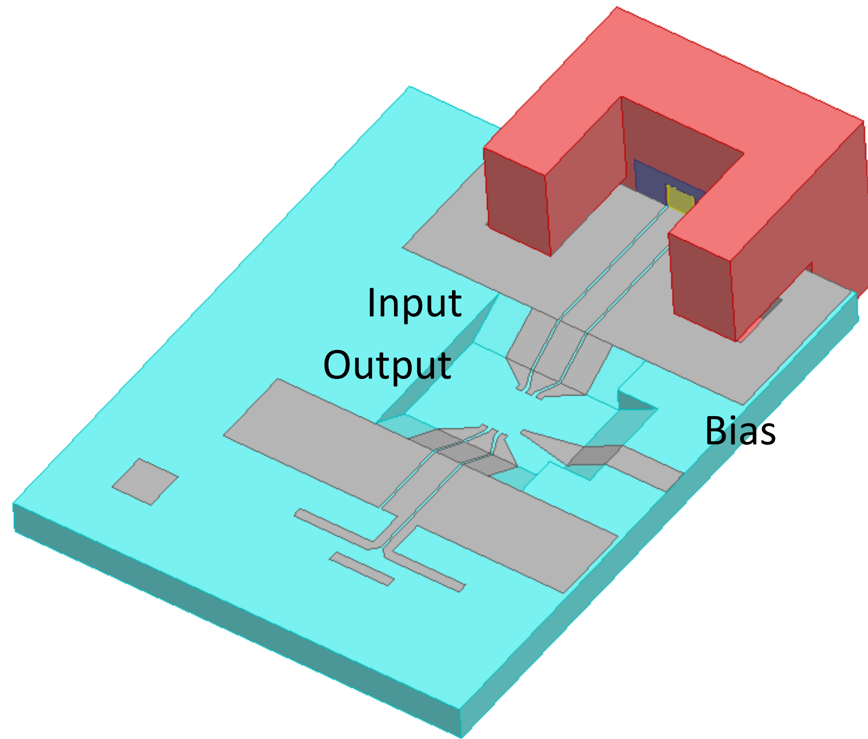


Figure 7.30: 3D- and inkjet-printed SiP design with an embedded IC.

The SiP structure is shown in Figure 7.30. There are three sets of ramps. One is CPW lines for the IC input. Another is CPW lines for the IC output. The final one is for the DC bias. The ramp height is 1.2 mm with the slope angle equals to 30°. The end-launch connector and the positioning marker are also included in the figure. The fabricated sample is shown in Figure 7.31. Three layers of SU-8 are printed on the substrate and can be observed in the figure. Since the thickness resolution is 10 µm, the ramp would be a staggered structure with height equals to 10 µm. This would cause conductivity issues for the silver trace. However, the staggered structure can be smoothed out with three layers of printed SU-8. The IC is attached on the silver trace using silver conductive epoxy as shown in Figure 7.32a. Furthermore, the structure after sealing with flexible material is shown in Figure 7.32b. The structure size can be reduced significantly by removing the end-launch connector and placed the antenna on the top of the IC as shown in Figure 7.33.

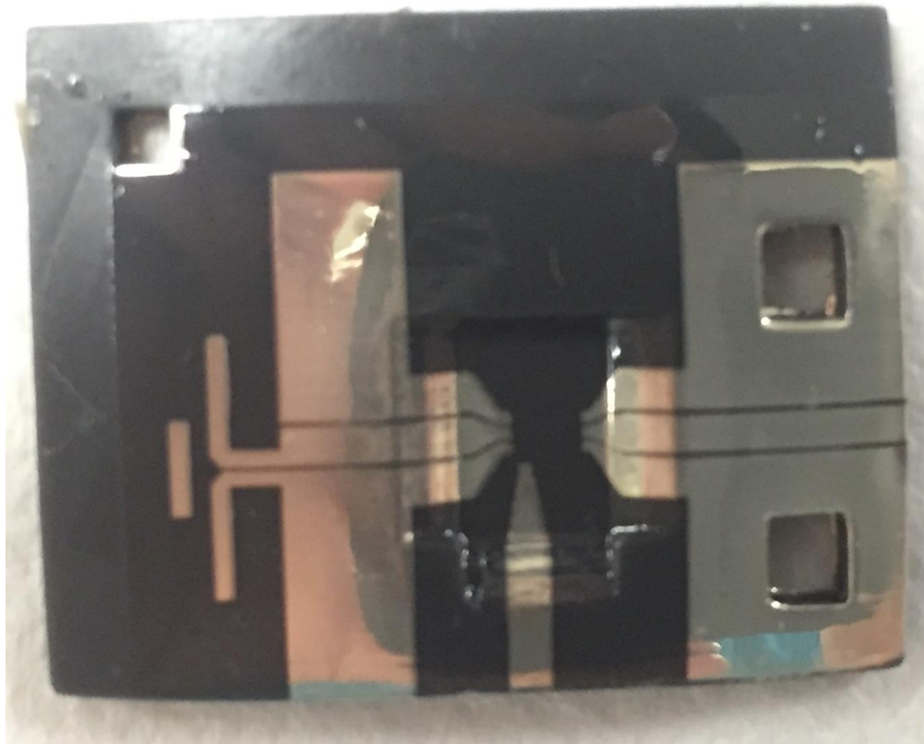

Figure 7.31: Fabricated prototypes of 3D- and inkjet-printed SiP design with an embedded IC.

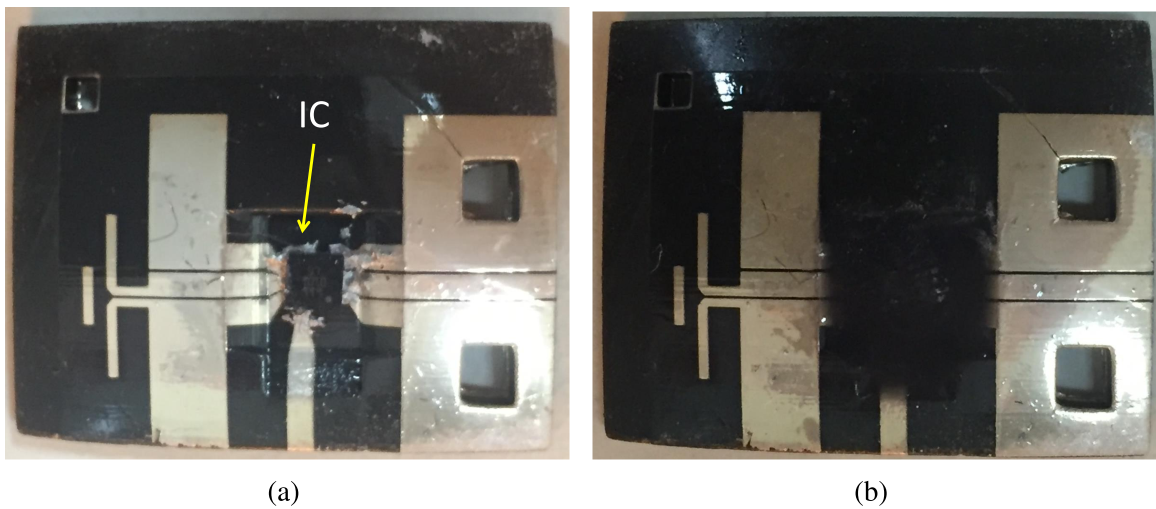


(a) (b)

Figure 7.32: SiP design (a) with an embedded IC attached and (b) sealed with flexible material.

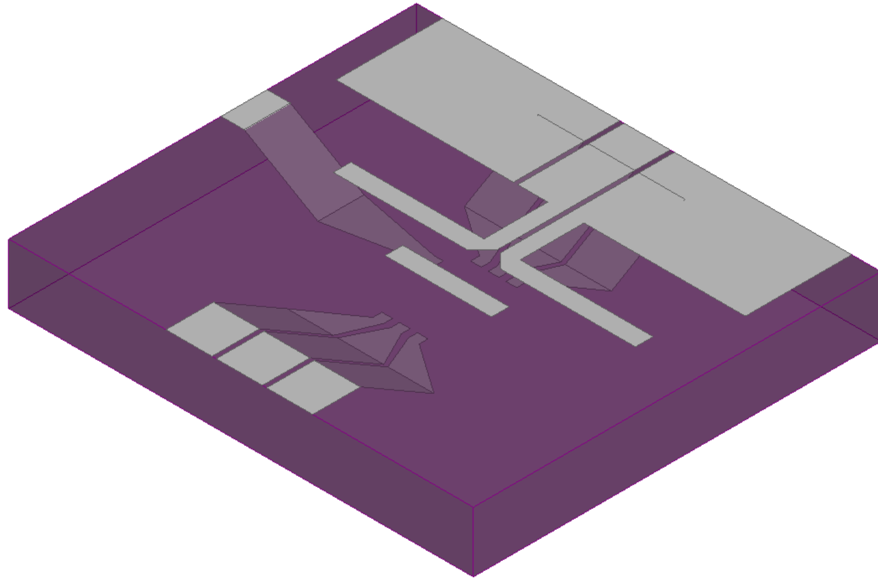

Figure 7.33: Miniaturized 3D- and inkjet-printed SiP design with an embedded IC.

## 7.5 Energy-autonomous 5G System-in-Package Design

### 7.5.1 Motivation and Design Idea

At the end stage of Moore's law, the idea of SiP which integrates multiple ICs with peripheral passive components such as antenna arrays, filters, and couplers using 3D stacking has been proposed to open a new era. Recently, SiP topology has attracted enormous attention because of the new 5G communication protocol. Since mm-wave frequencies are adopted for 5G communication to reach faster data transmission rates, the size of RF components can be reduced significantly and compatible with the size of packages [103]. However, conventional SiP designs are not fully autonomous because there are no energy sources within the package. Without an internal energy source, conventional SiP designs have to be connected to external boards or power supply elements to drive ICs inside the package and sustain the functionality.

To achieve a fully autonomous SiP design and shrink the functional system size from the board level to the package level, an energy source has to be embedded inside the package. While considering appropriate package-integrated energy sources, the conventional

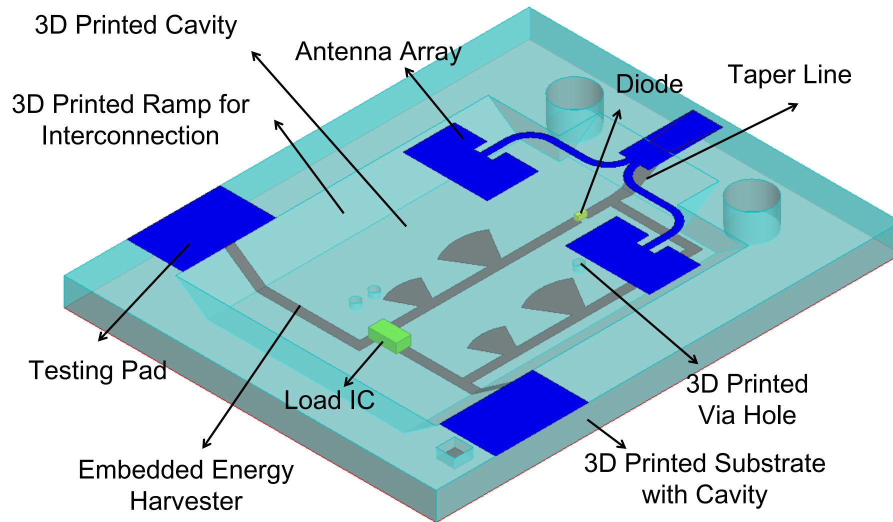


Figure 7.34: The embedded-in-package energy harvester within 3D-printed multilayer packaging structure.

batteries are ruled out first because the lifetime is limited and it is impossible to replace them inside the package [125]. The ambient energy which can be accessed all day without the limitation of a lifetime makes it a suitable solution to be used within the package. Among all ambient sources, RF energy is especially suitable for SiP design because the solar cells are typically too large to be integrated into the package while heat and vibrations are typically suppressed by the package [93, 102]. Furthermore, for most of the SiP designs, the antenna is already integrated in the package and can be reused by RF energy harvesting. The low power density for the RF energy [8] is no longer a problem since the EIRP allowed for the 5G communication is 75 dBm [49] which is much larger than other spectrums.

There are also new challenges while operating at mm-wave frequencies. For example, the large parasitics for conventional packaging structures such as via would affect the system performance significantly. 3D printing techniques can be a good solution to solve the problem as well as achieving more compact integration [57, 102]. The material flexibility including flexible, durable, and high-temperature materials can offer more choices based on different applications. Furthermore, the better structural flexibility makes numerous 3D

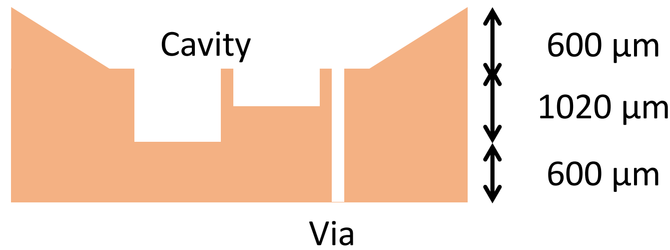


Figure 7.35: The stackup of the test samples for 3D printing material, Flexible FLGR02.

complex designs possible.

In this section, a package-integrated energy harvester operated at 26 GHz within 3D-printed multilayer flexible packaging structures is proposed for the first time. The whole system is fabricated with low cost and fast prototyping additive manufacturing techniques including inkjet printing and 3D printing. The flexible substrate is adopted to resist to shocks and vibrations. The system structure is demonstrated in Figure 7.34. The energy harvester is embedded inside a cavity. The 3D-printed ramp and the inkjet-printed tapered line on the top of the ramp are used as inter-layer connections between the energy harvester and the antenna on the top layer to reduce parasitics. The antenna is printed right on the top of the energy harvester to reduce the overall size. The harvested energy is measured and the power level is large enough to drive a TS3001 low-power timer which can be used as the modulation control to build a fully autonomous backscattering RFID SiP module. The proposed package-integrated energy harvester and the multilayer 3D printing process can be used to realize a fully autonomous SiP module and bring the fully functional system size from the board level down to the package level.

### 7.5.2 3D Printer Characterization

The same material as used in section 7.4, flexible resin FLGR02 from FormLabs, is used to characterize the 3D printer. The model of the 3D printer used is FormLabs Form 2. The laser spot size of Form 2 is 140 µm and the X/Y resolution is about 50 µm. The Z resolution is about 50 µm. The newer version of the 3D printer, FormLabs Form 3, can offer better

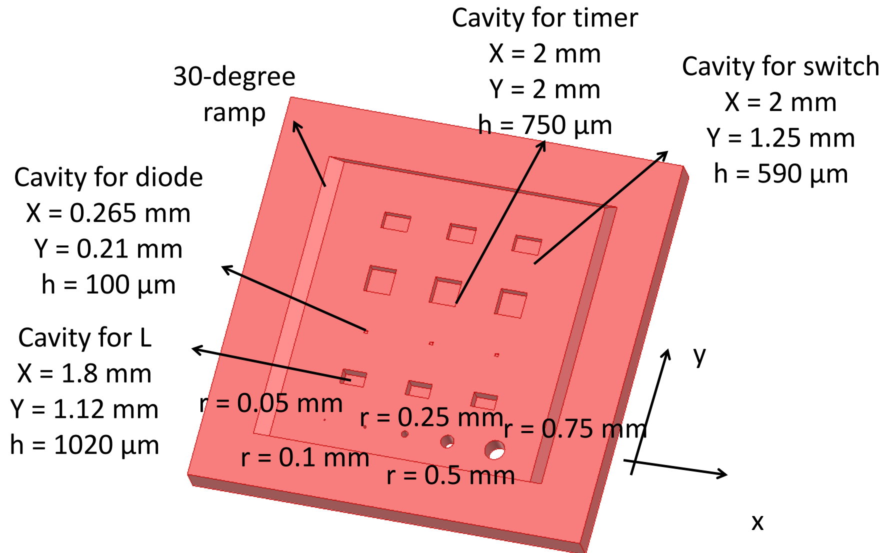


Figure 7.36: The geometry of the test samples for 3D printing material, Flexible FLGR02.

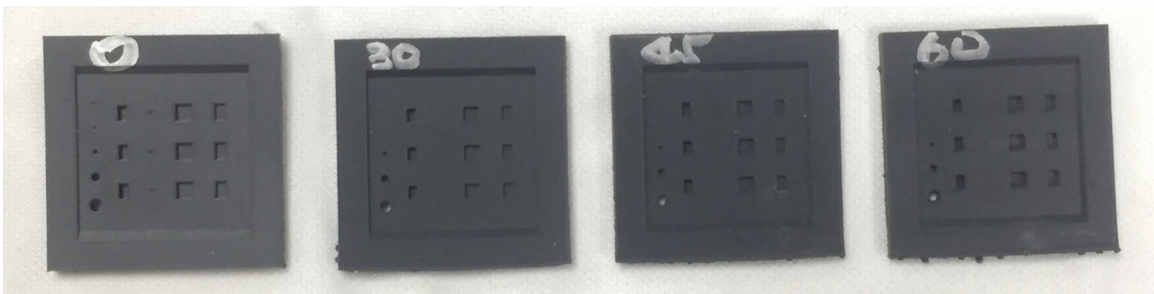


Figure 7.37: The fabricated prototypes of the test sampless for 3D printing material, Flexible FLGR02 under different printing tilt angles.

X/Y resolution at 25 µm using 85 µm laser spot size.

In addition to the electrical properties characterized in section 7.4, the physical resolutions are tested by printing different geometries. The stack up is shown in Figure 7.35. The cavities, ramp structures, and through vias are all included for the test of the physical resolution. The geometry of the test samples for 3D printing Flexible FLGR02 are shown in Figure 7.36. The physical dimensions of the ramp, cavities, and through via are also included in Figure 7.36. The fabricated prototypes are 3D-printed under different tilt angles to increase the Z resolution. The tilt angle is defined as the angle between the build plate and the sample as demonstrated in Figure 7.38. As shown in Figure 7.38, the Z resolution limit for 3D printer, FormLab Form 2, is 50 µm. However, the respective Z-direction reso-

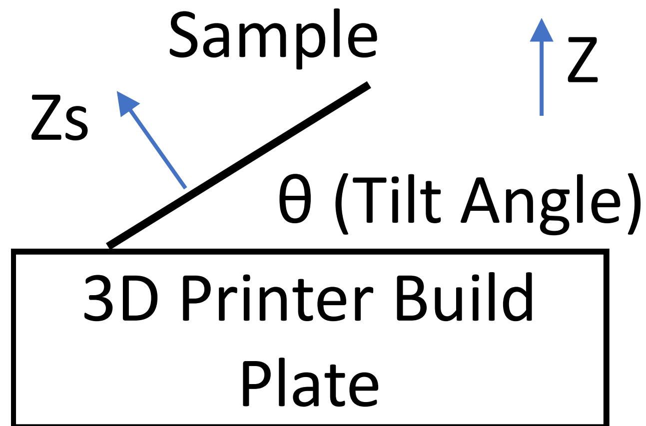


Figure 7.38: The definition of the tilt angle.

Table 7.3: Measured surface roughness.

| **Tilt angle (degree)** | **Ramp 1** (µm) | **Ramp 2** (µm) | **Flat Region** (µm) |
|---|---|---|---|
| 0 | 7.44 | 6.30 | 1.26 |
| 30 | 4.62 | 5.10 | 5.48 |
| 45 | 2.87 | 9.12 | 3.03 |
| 60 | 3.67 | 5.72 | 6.28 |

lution for the sample, which is Zs direction in Figure 7.38, is depending on the tilt angle. The respective Z-direction resolution can be calculated as

$$Zs = Zcos\theta \tag{7.9}$$

where Z is the Z-direction resolution (50 µm), Zs is the respective Z-direction resolution for the sample, and $\theta$ is the tilt angle. As shown in Equation 7.9, the resolution is better under larger tilt angles. Since a larger tilt angle might cause other issues, prototypes with 0°, 30°, 45°, and 60° tilt angles are printed, measured, and compared to find the most suitable tilt angle.

The surface roughness of the prototypes with different tilt angles is summarized in Table 7.3. Both the surface roughnesses on the non-planar ramp and flat region are measured.

Table 7.4: Measured thickness for cavities.

| Tilt Angle | S4 | S5 | S6 | S7 | S8 | S9 | S10 | S11 | S12 | Average Error (%) |
|---|---|---|---|---|---|---|---|---|---|---|
| 0 | x | 95 | 103 | 714 | 753 | 690 | 552 | 574 | 589 | 3.82 |
| 30 | x | x | x | 670 | 655 | 644 | 543 | 530 | 543 | 10.59 |
| 45 | 83 | x | x | 690 | 670 | 660 | 594 | 529 | 512 | 10.27 |
| 60 | 53 | x | x | 656 | 650 | 670 | 521 | 538 | 519 | 11.51 |
| Design Value | 100 | 100 | 100 | 750 | 750 | 750 | 590 | 590 | 590 | |

x: means print fail
Unit is µm unless specify

As shown in Table 7.3, the surface roughness at the flat region is smaller while tilt angle is 0°. However, the surface roughness at the ramp is generally smaller while the tilt angle is larger. The reason is that the respective Z resolution is better while the tilt angle is larger.

The thicknesses for the cavities are measured and summarized in Table 7.4. The design values are included for comparison. As shown in Table 7.4, the cavities with 100 µm thickness can only be realized with a 0° tilt angle. Furthermore, the average error (discrepancies between the designed and measured dimensions) is smaller for 0° printing, and the overall errors for cavity thicknesses are about 10 %. The through via measurement is summarized in Table 7.5. For 0° printing, the minimum radius for the through via is 500 µm. The minimum radius for other tilt angle printing is 250 µm which is much smaller compared with the 0° printing.

The substrate thickness measurement is summarized in Table 7.6 and the position definition is shown in Figure 7.39. The design values are also included for comparison. The minimum average error is using 30° tilt printing and the overall errors are all smaller than

Table 7.5: Measured via holes.

| Tilt | r = 50 µm | r = 100 µm | r = 250 µm | r = 500 µm | r = 750 µm |
|---|---|---|---|---|---|
| 0 | x | x | x | o | o |
| 30 | x | x | o | o | o |
| 45 | x | x | o | o | o |
| 60 | x | x | o | o | o |

o: Success
x: Fail

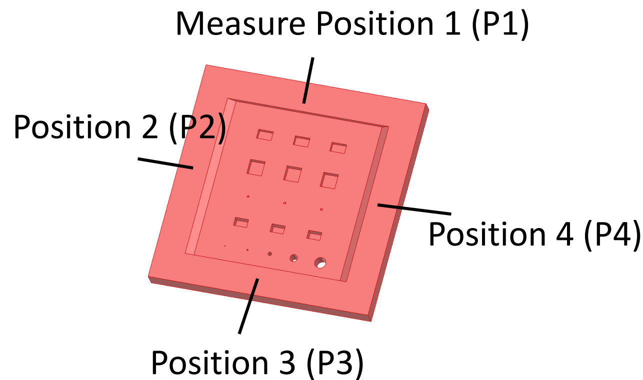


Figure 7.39: The measured positions of the test samples for 3D printing material, Flexible FLGR02.

8 %. For the 30° tilt printing, samples with smaller thickness are printed and the measured results are summarized in Table 7.7. The measured thickness is very stable and accurate. The average error is smaller than 2 % even for thin 400 µm substrate printing.

The pros and cons of different tilt angle printing are summarized in Table 7.8. The surface roughness at the flat region is better while printing with a 0° tilt angle. On the other hand, the surface roughness on the ramp is better while printing with a 30° tilt angle. However, the surface roughness of the 3D printed material does not matter since the polymer is coated on the top of it and significantly improve the surface roughness. Furthermore, since the polymer is printed using inkjet printing and there is no tilt angle, the results are similar for different tilt 3D printing angles. The 0° tilt printing is also good for better

Table 7.6: Measured substrate thickness at the edge.

| Tilt | P1 (mm) | P2 (mm) | P3 (mm) | P4 (mm) | Average Error (%) |
|---|---|---|---|---|---|
| 0 | 2.43 | 2.30 | 2.55 | 2.32 | 8.11 |
| 30 | 2.20 | 2.22 | 2.13 | 2.20 | 1.46 |
| 45 | 2.15 | 2.08 | 2.11 | 2.13 | 4.62 |
| 60 | 2.09 | 2.07 | 2.03 | 2.04 | 7.32 |
| Design | 2.22 | 2.22 | 2.22 | 2.22 | |

Table 7.7: Measured substrate thickness when printing with a 30° tilt angle.

| | **h1** | **h2** |
|---|---|---|
| Design Value (μm) | 1500 | 400 |
| Sample 1 (μm) | 1555 | 422 |
| Sample 2 (μm) | 1507 | 388 |
| Sample 3 (μm) | 1525 | 373 |
| Average (μm) | 1529 | 394 |
| Average Error (%) | 1.9 | 1.5 |

cavity thickness accuracy and shorter print time. The 30° tilt printing is the better for the substrate thickness accuracy, minimum via dimension and the backside roughness. Thus, after comparing and trading off between different aspects, the 30° tilt printing is adopted.

### 7.5.3 Fabrication Process

The multilayer fabrication process of the system is demonstrated in Figure 7.40. The first step is to 3D print the flexible core substrate with ramps, vias, and cavity, and the result is shown in Figure 7.41a. The 3D printer used is FormLabs Form 2 SLA 3D printer. The flexible substrate used is FLGR02. The material is characterized using waveguides as in section 7.4. The dielectric constant is 2.83 and the loss tangent is 0.03 at 26 GHz. The total thickness is 1500 μm with cavity thickness equals to 1100 μm. Thus, the substrate thickness

Table 7.8: Summary of different characteristics.

| Tilt Angle | Surface roughness flat region | Surface roughness on the ramp | Substrate thickness | Cavity | Via | Print time | Backside roughness |
|---|---|---|---|---|---|---|---|
| 0 | O | | | O | | O | |
| 30 | | O | O | | O | | O |
| 45 | | | | | O | | O |
| 60 | | | | | O | | O |

o: The best among all tilt angles

beneath the cavity is 400 µm. The z-direction resolution for this printer is 50 µm. In order to print the samples with more accurate thickness and higher z-directional resolution, the samples are printed with a 30° tilt angle. Therefore, the respective z-direction resolution is about 43 µm by Equation 7.9. The thicknesses of three printed test samples are measured. The average total thickness is 1529 µm which is very close to the design value, 1500 µm. The average thickness beneath the substrate is 392 µm and again very close to the design value, 400 µm.

The second step is to inkjet print three layers of MicroChem SU-8 (20 µm drop spacing) using Dimatix DMP-2831 inkjet printer. The purpose of this layer is to smooth the surface roughness of the 3D-printed substrate. As depicted in Figure 7.41b, there are stripes on the surface of the 3D-printed substrate due to the 30° tilting angle which increases the surface roughness. However, with three layers of SU-8 coating, the surface roughness can be improved significantly. Furthermore, the SU-8 layer also serves as a buffer to balance the different CTE between the substrate and the SNP ink.

The silver traces are inkjet-printed with three layers of Sun Chemical EMD-5730 SNP ink (20 µm drop spacing) on the SU-8 coated substrate and the result is shown in Figure 7.42a. The silver is first cured at 60 °C and then sintered at 150 °C. The printing results show clear gaps and sharp edges. Furthermore, as shown in Figure 7.43, the silver traces on the ramp demonstrate good continuity and connectivity. The other side of the 3D printed substrate is coated with a conductive epoxy to create a ground plane. In the meantime, the vias are filled with conductive epoxy, too. Then the sample is put on the hot plate at 120 °C

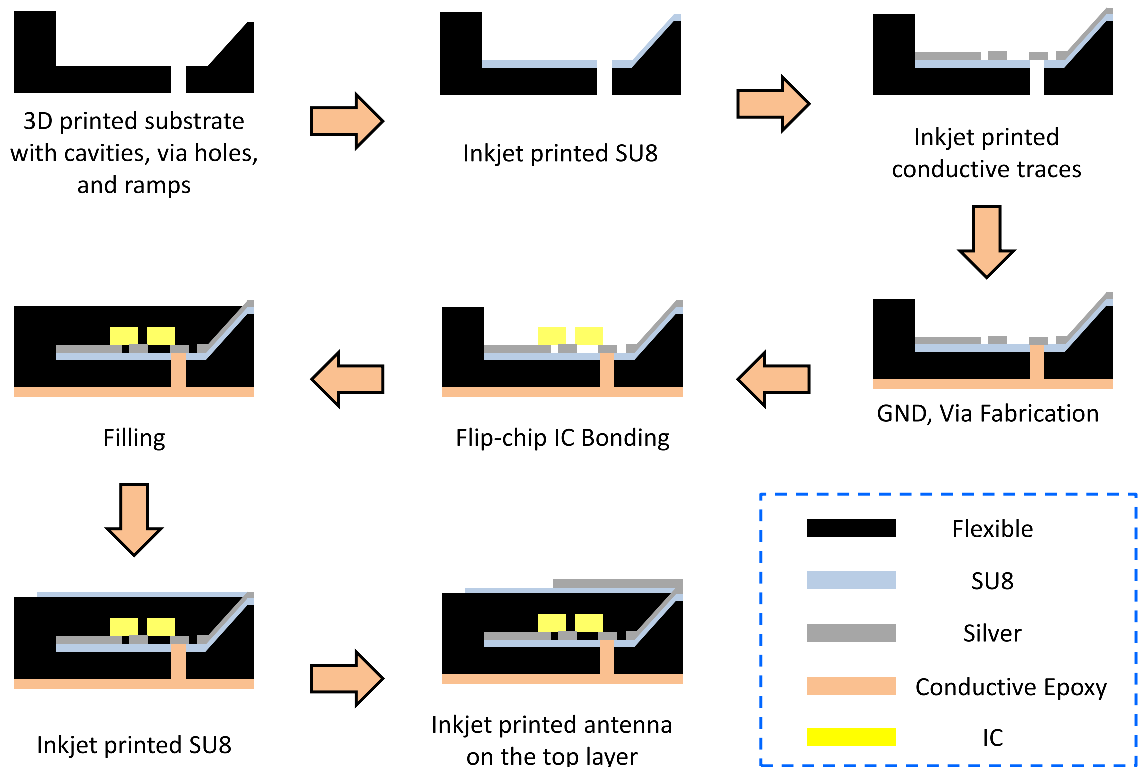


Figure 7.40: Fabrication process for additive manufacturing multilayer packaging structures.

for 15 minutes for the conductive epoxy. The ICs are flip-chip bonded on the inkjet-printed silver traces with conductive epoxy as shown in Figure 7.42b. The cavity is then filled with flexible material to create a new layer. As shown in Figure 7.42c, the filling is flat and the inter-layer connection is ready for the antenna array on the top layer. To print the antenna on the top layer, three layers of SU-8 is applied first and then inkjet print the silver trace on top of that as shown in Figure 7.42d.

The overall size of the entire circuit is 25 mm x 20 mm. However, the size can be reduced to 12 mm x 15 mm if the testing features such as the end-launch connector and testing pads are eliminated. The fabrication process can be extended to more layers of printing by repeating the filling 3D printed materials and inkjet printing silver traces. The use of additive manufacturing technologies offer better performances, more material choices, and better structural flexibilities. For example, the 3D-printed ramps which can only be printed

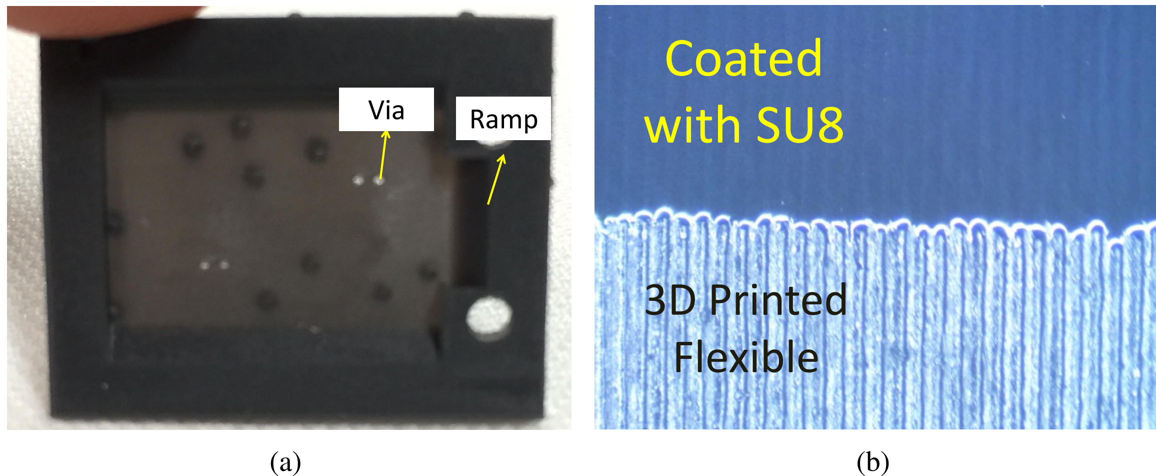


(a) (b)

Figure 7.41: (a) 3D printed substrate with cavity, ramps, and vias. (b) Substrate coated with SU-8.

using 3D printing techniques and inkjet print silver traces on the top of the ramps to serve as inter-layer connections induce lower parasitics compared with conventional via connections. The effects are more significant when operating at mm-wave frequencies. Thus, this multilayer printing process is suitable for mm-wave SiP design.

### 7.5.4 Antenna-in-Package Design And Measurement

The antenna array printed on the filled cavity is composed of two patch antennas and the geometry is shown in Figure 7.44. The patch size is 3.87 mm x 2.21 mm. The distance between the two elements is 3.56 mm. The fabricated prototype is shown in Figure 7.45. The parameters are measured with VNA and the results are shown in Figure 7.46a. The $S_{11}$ at 26 GHz is smaller than -10 dB. The broad bandwidth of this antenna is due to the thick substrate of the patch antenna. The radiation pattern is also measured and shown in Figure 7.46b. The 0° direction is the direction of broadside radiation. The main beam is tilted to 30° toward the substrate. It is also because of the thick substrate and the long distance from the edge of the patch antenna to the edge of the substrate.

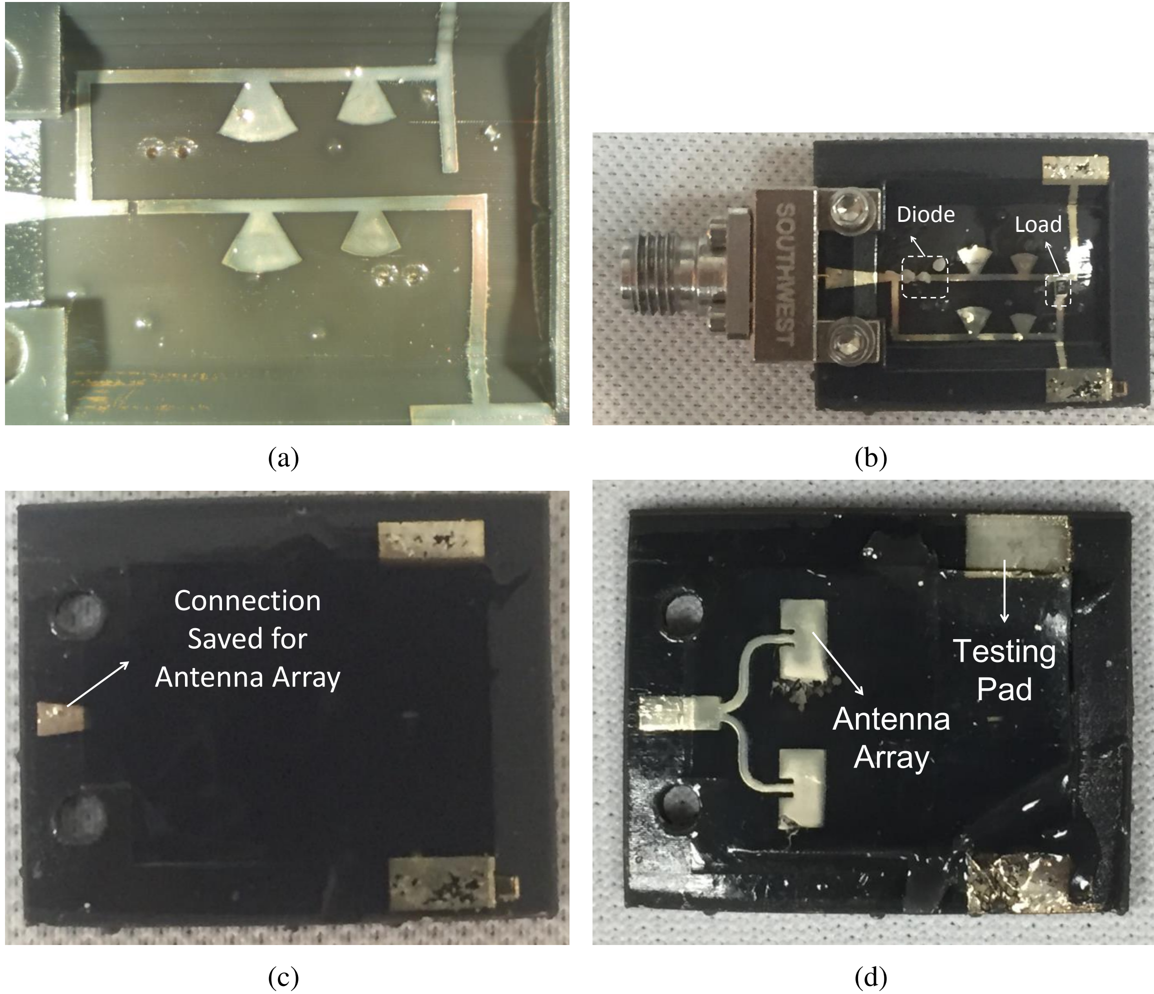


(a) (b) (c) (d)

Figure 7.42: (a) Inkjet printed silver on the top of the 3D-printed substrate (b) The package-integrated energy harvester (c) Filling the cavity with flexible material and (d) Inkjet-printed antenna array on the top layer.

### 7.5.5 Embedded 5G Energy Harvester Design and Measurement

The fabricated embedded 5G energy harvester is shown in Figure 7.42b. The energy harvester starts with a tapered line from the top layer to the cavity. The tapered line is used to take the thickness change between the line and the ground into consideration. The MA4E2038 diode is used for rectification. Only one-diode topology is used because the effect of loss is more significant than the efficiency increase while adding more diodes at 26 GHz. After the rectification, both DC and harmonics are generated. Thus, the sector-shape open stubs are used as the termination for the harmonics at 26 GHz and 52 GHz. Moreover,

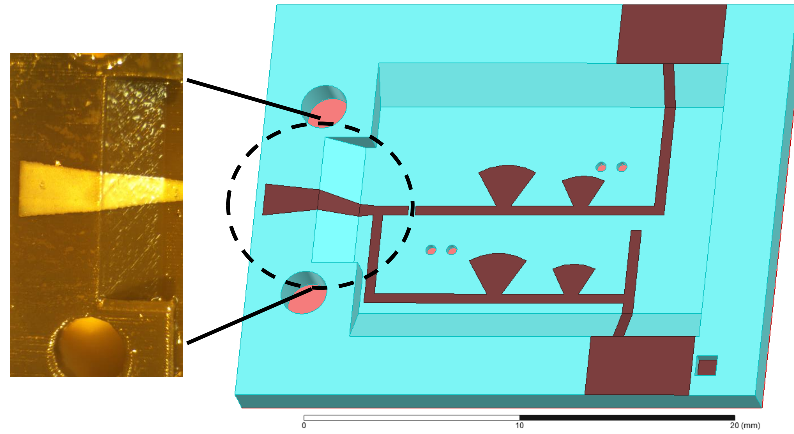

Figure 7.43: The prototypes of ramp interconnections.

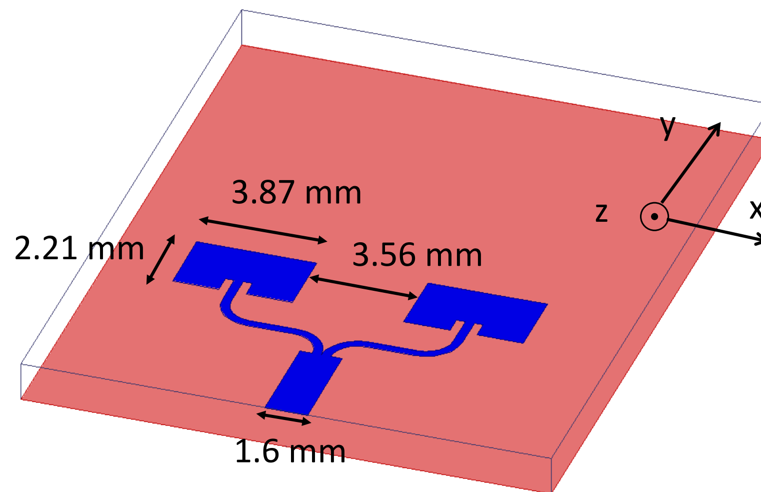

Figure 7.44: The geometry of the package-integrated antenna array design.

the DC reference plane is connected to the diode anode to avoid the via and high parasitics. A 750 kΩ resistor is placed at the load position to mimic the timer TS3001 from Silicon Labs. Two testing pads are branching out and connect to the top plane through 3D printed ramps for testing after filling the cavity.

The cavity-embedded energy harvester is connected to a signal generator through a Southwest end-launch connector. The output voltage probing is performed by two testing pads for different input power levels at 26 GHz and measured results are shown in Figure 7.47a. The simulated results of the energy harvester before the filling of the cavity from ADS harmonic balance simulation is also included for comparison. The microstrip

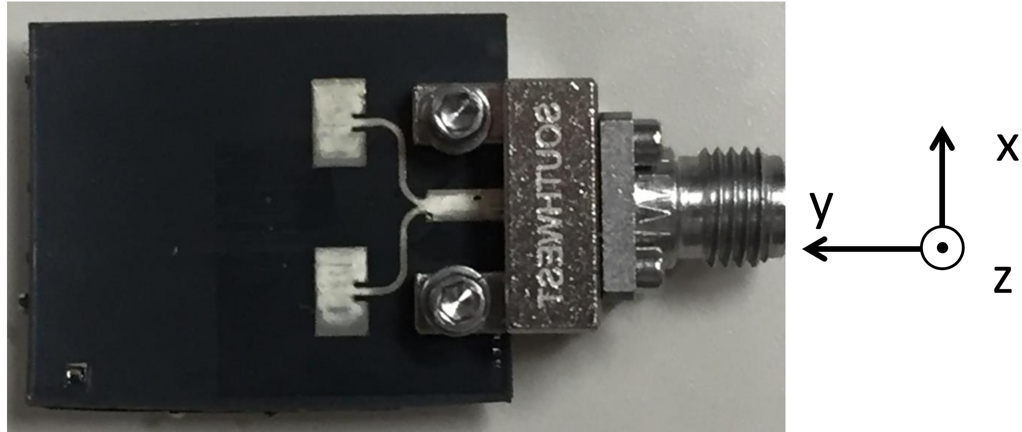


Figure 7.45: The prototype of the package-integrated antenna array design.

line model is used for simulating the results before filling. As shown in Figure 7.47a, the simulation and measured results are very close to each other. The measured output voltage after filling the cavity is higher than before filling. The reason is that the frequency shift due to filling is taken into consideration. Thus, the optimal operating point for the design before the filling is not at 26 GHz but the optimal operating point after filling is at 26 GHz. The input scattering parameter of the energy harvester after filling the cavity is measured and shown in Figure 7.47b. The $S_{11}$ at 26 GHz is around -15 dB indicating good matching is achieved.

### 7.5.6 Energy Harvester Operation Test

The entire system is measured wirelessly to evaluate the harvested energy. The measurement setup is shown in Figure 7.48. The signal generator's output is 12 dBm. The amplifier is 27 dB and the gain of the horn antenna is 20 dBi. The distance between the sample and the horn antenna is 20 cm. The output voltage at the load of the energy harvester is 0.9 V which is large enough to turn on and supply the TS3001 timer from Silicon Labs. Since the EIRP limit for 5G communication is around 75 dBm [49], the range can be extended to more than 1 m if 75 dBm EIRP is used.

The proposed embedded energy harvester can be used to realize a fully autonomous backscattering SiP sensing module. The system topology is shown in Figure 7.49 while the

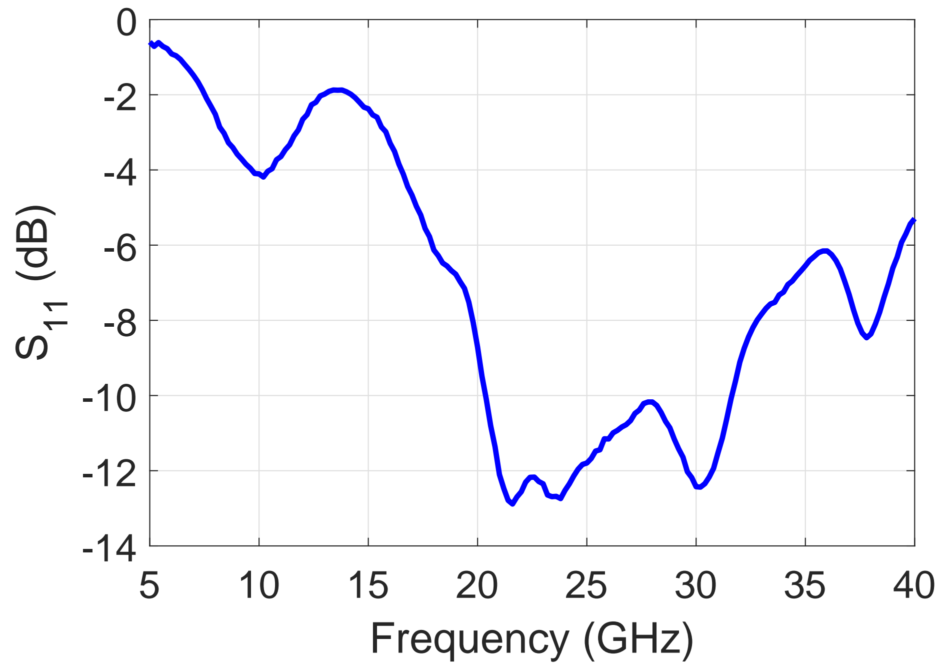


(a)

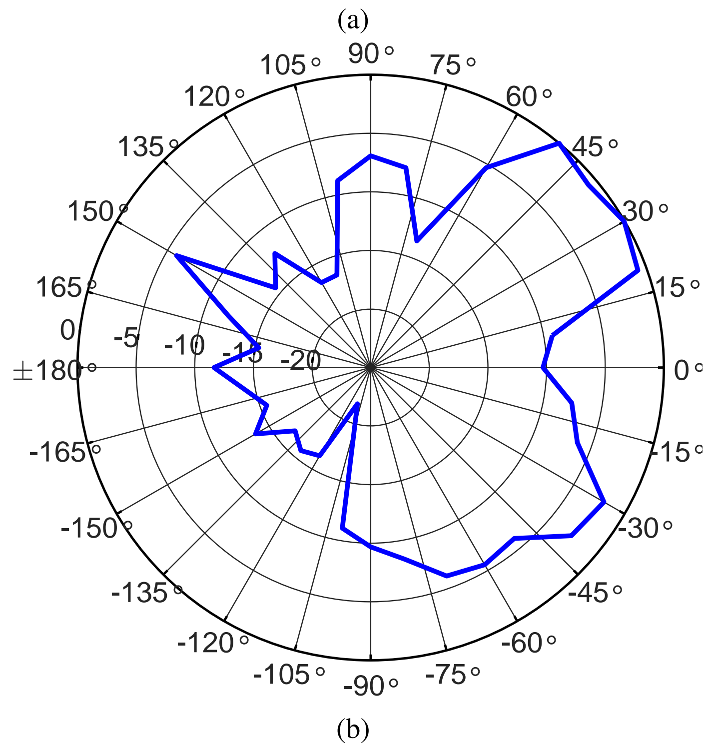


(b)

Figure 7.46: The measured (a) $S_{11}$ and (b) normalized radiation pattern at 26 GHz of the package-integrated antenna array design.

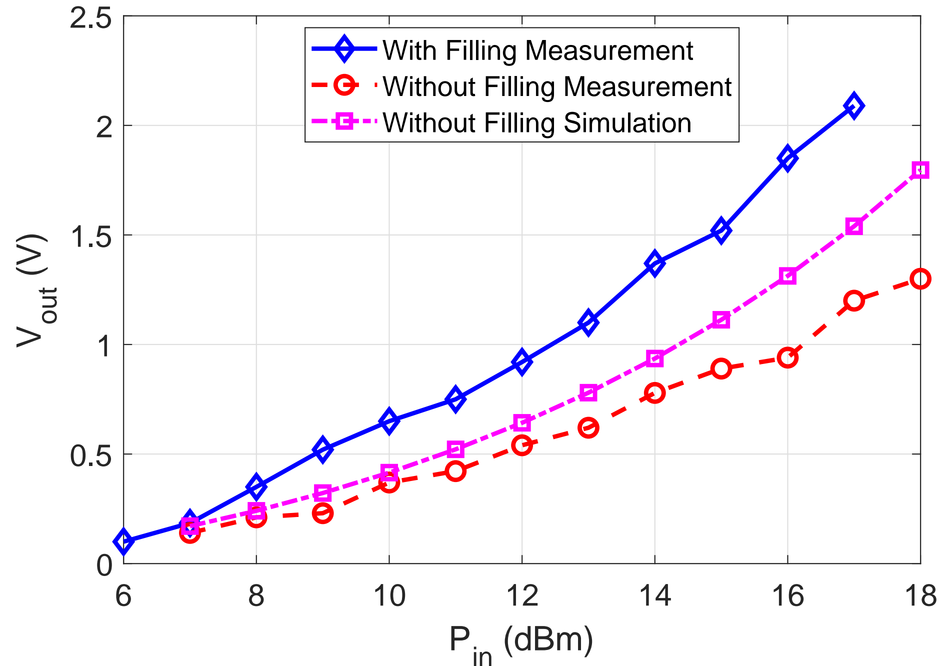


(a)

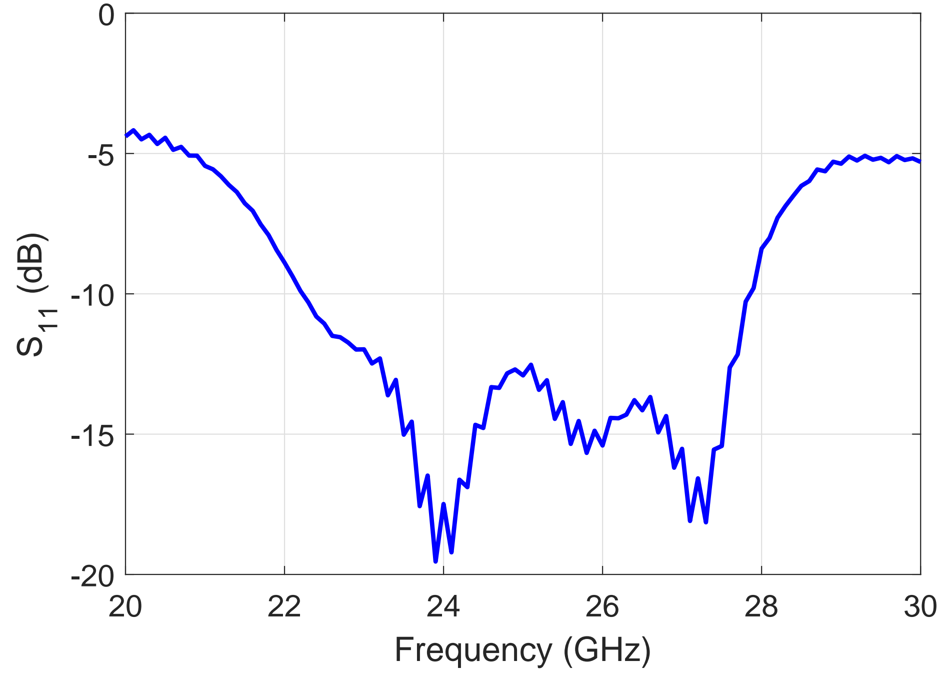


(b)

Figure 7.47: Measured and simulated (a) output voltage of the embedded energy harvester with respect to different input powers at 26 GHz and (b) $S_{11}$ of the embedded energy harvester after filling.

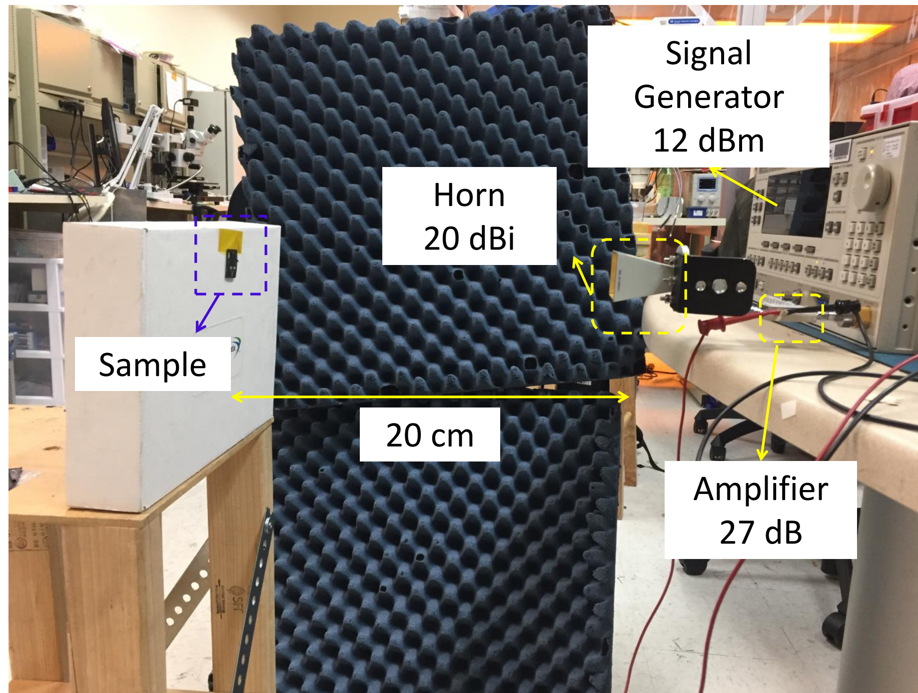


Figure 7.48: The wireless performance evaluation setup for the 5G package-integrated energy harvester.

fabricated circuit prototype is shown in Figure 7.50. The energy harvester is used to harvest energy to power a TS3001 timer. The timer would alter the oscillation frequency based on the resistance value of the sensor. The oscillated signal is used to control a CE3521M4 switch to create modulated signals and backscatter the information back to the reader.

## 7.6 Inkjet-printed Low-loss Polymer for Millimeter-wave Applications

### 7.6.1 Motivation and Design Idea

The main drawback of the additive manufacturing process compared with glass SAP process is the material loss. The general loss tangents of 3D printing materials fall into the range between 0.03 to 0.05. The loss tangent of inkjet printed MicroChem SU-8 is around 0.04 at 5G mm-wave frequency range [59]. Therefore, the overall loss tangent of the system is larger than 0.03 which is large at mm-wave frequency range. One way to solve the problem is to develop a inkjet-printable low-loss polymer and coated it on the 3D-printed

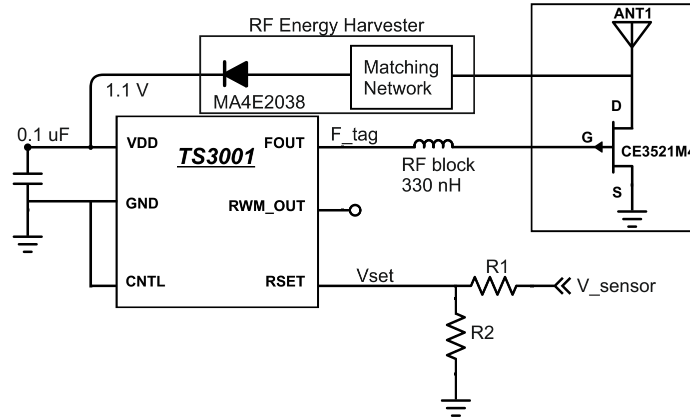


Figure 7.49: Fully autonomous SiP backscattering sensor topology.

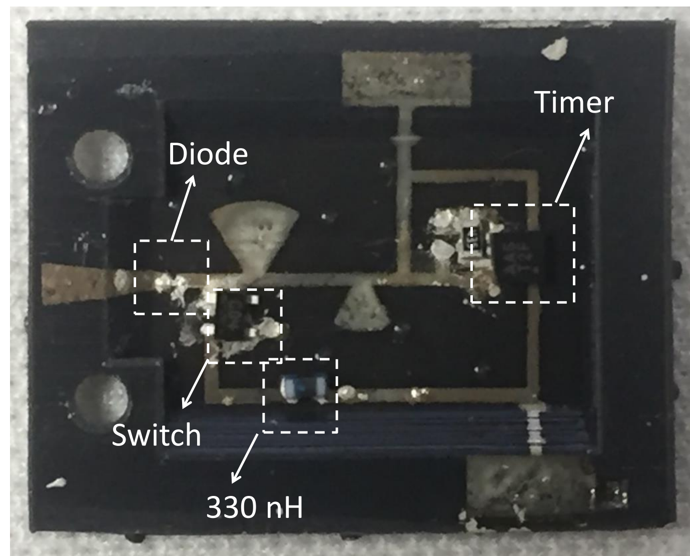


Figure 7.50: Prototype for fully autonomous SiP backscattering sensor.

core substrate. It is easy to design circuits with RF components entirely on one side of the core substrate and are not affected by the high substrate loss of the core substrate. For example, a layer stackup from the top to the bottom can be arranged like metal M1, low-loss polymer, metal M2, low-loss polymer, and 3D printed material. The metal M2 can be used as the ground plane and the metal M1 can be used as the microstrip line components. Therefore, the effects of the substrate loss due to 3D printing core substrate can be minimized.

The low-loss polymer developed in this section is BCB. The relative dielectric constant is 2.65 and the loss tangent is 0.002 at 10 GHz [60]. Compared with SU-8, the loss tangent

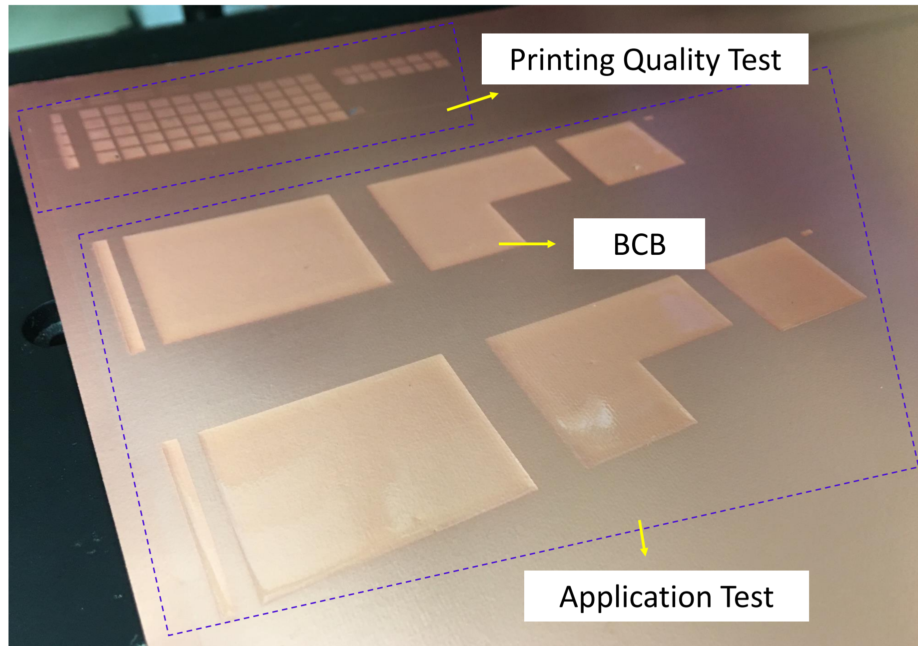


Figure 7.51: The inkjet-printed BCB patterns.

of the BCB is much smaller. Thus, inkjet-printed BCB can be used to replace the SU-8 and realize a high-performance fully additive manufacturing packaging process for mm-wave applications.

### 7.6.2 Layer Thickness Characterization

The inkjet-printable BCB ink is developed and used to print test samples as shown in Figure 7.51. The top little squares are 4 mm by 4 mm and are used to characterize the layer height as shown in Figure 7.52. The substrate used is a Rogers RT 5870 with 1 oz copper cladding. The BCB ink is inkjet printed with 20 µm drop spacing on the copper. The printed samples are dried on the hot plate at 140 °C for 10 minutes. Then, the samples are sintered in a vacuum oven filled with Nitrogen. The sintering temperature is 248 °C and the sintering time is 1.5 hours. As shown in Figure 7.52, sharp edges with good wetting and adhesion on the copper can be observed. Furthermore, there are no discontinuity or empty holes in the middle of printing. Thus, good quality printing can be proven using the developed BCB ink.

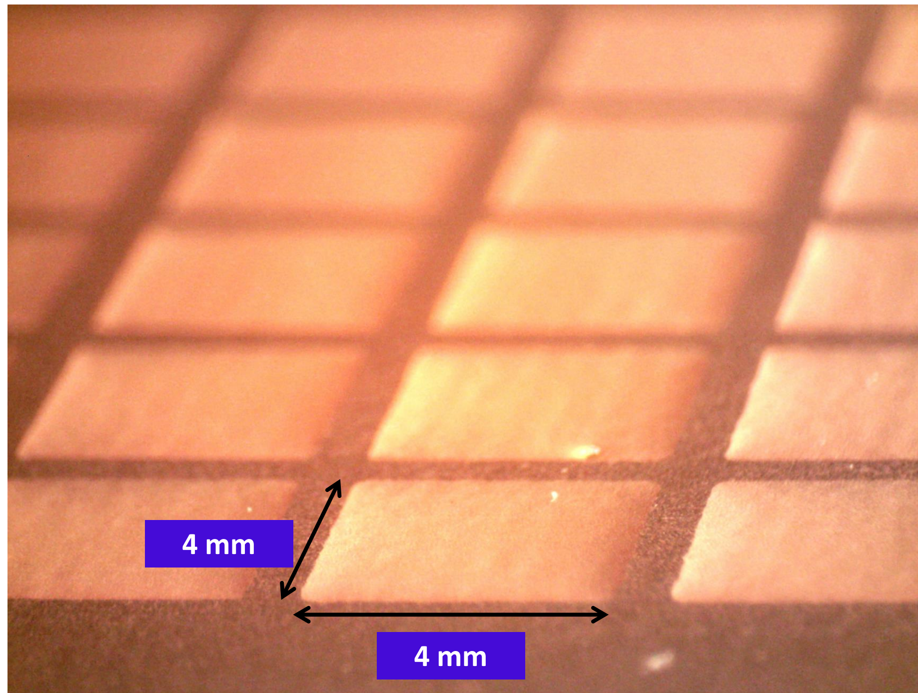


Figure 7.52: The inkjet printing BCB squares for layer thickness characterization.

The profilometer measurement of the inkjet-printed BCB with 1-layer, 3-layer, 5-layer, 7-layer, and 9-layer printing is demonstrated in Figure 7.53. Multiple samples are fabricated and measured. As shown in Figure 7.53, the consistency between different samples is very good. The comparison between different numbers of printing layers is shown in Figure 7.54. The 1-layer printing is not enough and the variance within the center flat region is large. However, the variance becomes smaller when more layers are printed. The coffee ring can be observed at 3-layer and 5-layer printing. While at 7 and 9 layers of printing, since the pad size is small, too many materials accumulated at the middle and protrusion can be seen. As shown in Figure 7.55, a larger 8 mm by 8 mm pad is printed using 12 layers of BCB inks. Ever with 3 more layers of printing, the flat region without protrusion can be observed. Therefore, each layer of BCB is about 5 µm.

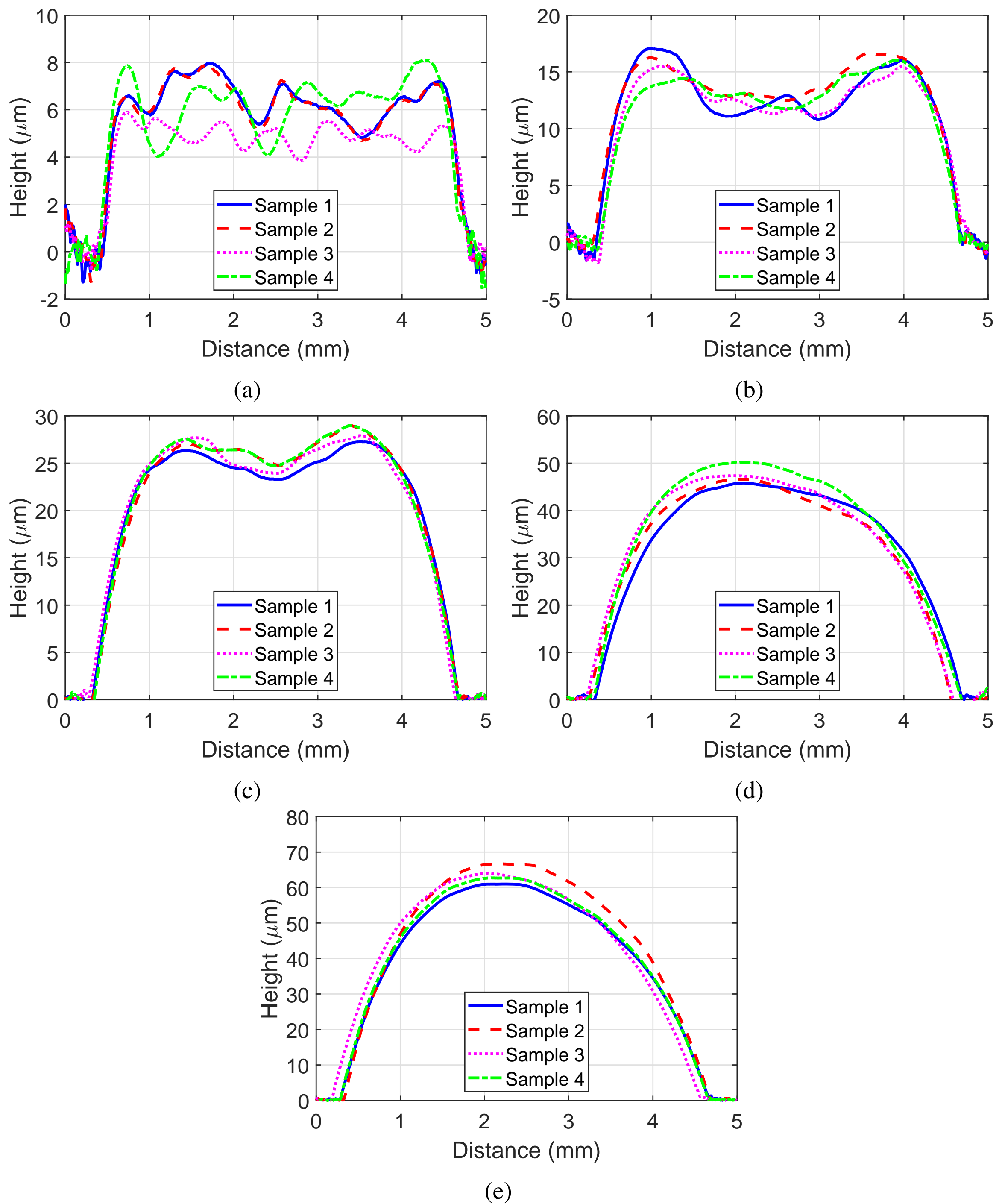


Figure 7.53: The profilometer measurement of the inkjet-printed BCB with (a) 1-layer, (b) 3-layer, (c) 5-layer, (d) 7-layer, and (e) 9-layer printing.

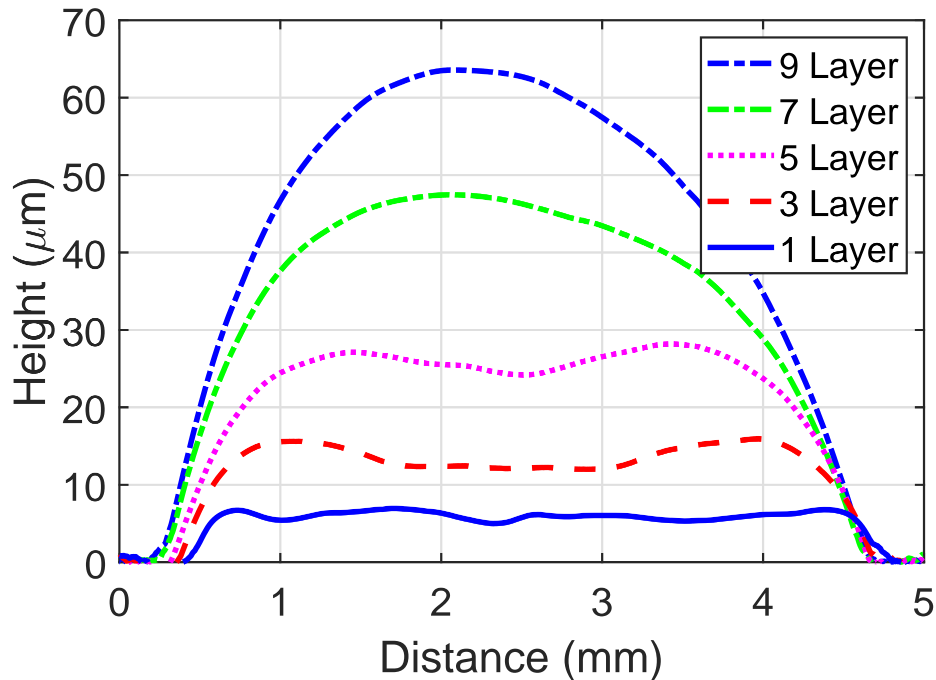


Figure 7.54: The thickness comparisons between different numbers of layer.

### 7.6.3 Via Holes Characterization

The inkjet-printed via holes with different diameters are shown in Figure 7.56. 12 layers of BCB is printed with a thickness about 60 μm. The designed diameter sizes of the via hole are also included in the figure. As shown in Figure 7.56, the minimum diameter which is printed successfully is 400 μm. The printed via holes can be used to realize both micro vias and through vias. The measured dimensions under the microscope are shown in Figure 7.57. As shown in the figure, the printed via holes are all smaller than the designed values. Furthermore, the vertical size is smaller than the horizontal size. The reason is that the inkjet printer prints the horizontal strips and thus, horizontal features will be more accurate.

## 7.7 Summary

The objective of this chapter is to develop a fully additive manufacturing packaging process and applied the process to realize an energy-autonomous SiP design. Four pieces of

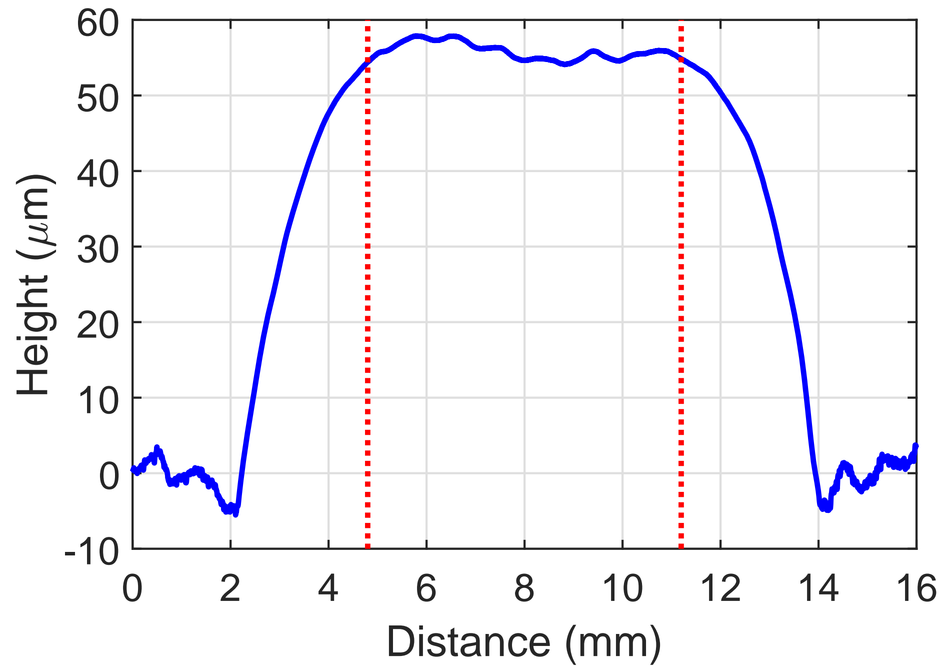

Figure 7.55: The profilometer measurement of the inkjet-printed BCB with 12-layer printing and the pattern is a larger 8 mm square.

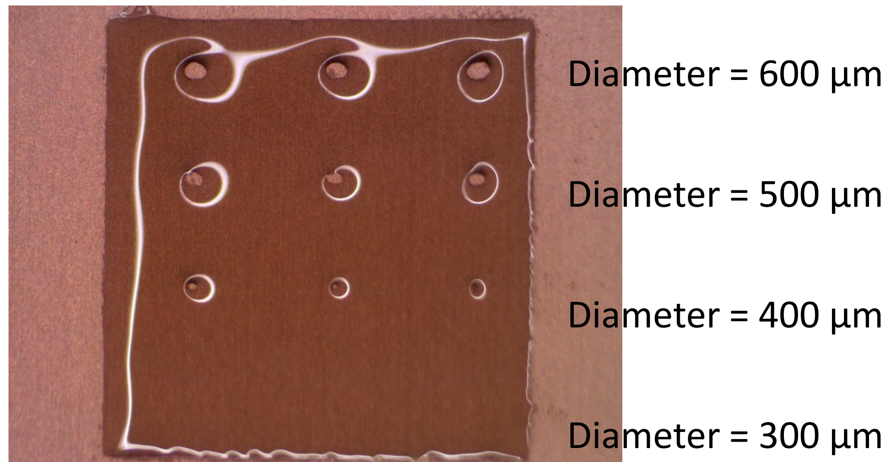

Figure 7.56: The inkjet-printed via holes with different dimensions using BCB ink.

research are introduced in this chapter to achieve the goal. Additive packaging has garnered an increasing amount of interest due to its promising industrial scalability, enormous material choices, and topological patterning versatility. The effort described in the first research benchmarks the performance of the additive manufacturing packaging approach relative to its commercial counterpart for the integration of devices operating in the 5G

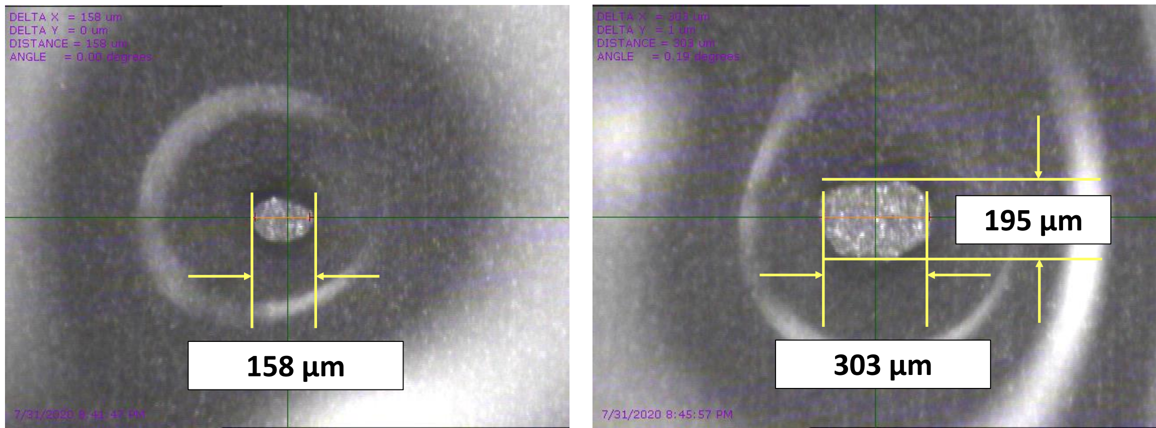


(a) (b)

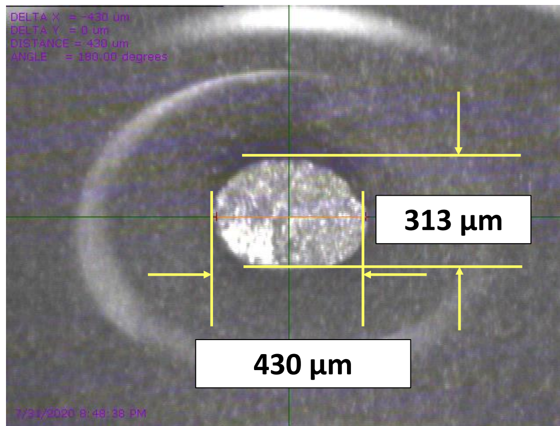


(c)

Figure 7.57: The measured sizes of 12-layer via holes under microscope with diameter equals (a) 400 µm, (b) 500 µm, and (c) 600 µm.

mm-wave bands. The approach first demonstrates the fully inkjet-printed integration of a tunnel diode, a component empowering a plethora of emerging applications in these frequency bands, before comparing it to its pre-packaged counterpart. To enable an accurate and quantifiable comparison, the measured properties of the two integrated diodes were de-embedded using a TRL extraction method before their lumped element models were determined and compared. The comparison demonstrates a general and often significant reduction in all the packaging parasitics, up to 53%, using the additive approach. This result adds upon the growing evidence supporting the superior electrical performance of additive packaging for the integration of mm-wave dies and strengthens the appeal for the development of ultra-compact and ultra-high-performance fully additive manufacturing mm-wave SiP.

After showing evidence of the superiority of the additive manufacturing process for packaging structures, a fully additively manufacturing process using 3D and inkjet printing is proposed in the second research. The process is then used to fabricate antenna and packaging structure at mm-wave range for 5G applications. The 3D printed flexible material, FLGR02, is applied to the flexible mm-wave packaging application. The fabrication process and material characterizations including solutions to surface treatment for ink adhesion, smoothing of the surface roughness, and balancing the CTE mismatch between the flexible material and the SNP ink are proposed. Then, the proposed process is used to fabricate a broadband 5G package-integrated antenna. The measured $S_{11}$ of the proposed package-integrated antenna is smaller than -10 dB from 22.4 GHz to 30.1 GHz. Besides, the measured realized gain is larger than 5 dBi from 22 GHz to 30.5 GHz. The differences in the realized gain within the operating bandwidth are smaller than 3 dB. The FBW is 29.3 %. The proposed antenna is broadband enough to cover the whole 5G band from 24.5 GHz to 29.5 GHz. The size of the antenna is $5\,\text{mm}\times 9\,\text{mm}$ which is $0.44\lambda_0 \times 0.79\lambda_0$. Radiation patterns within the operating band are also measured. Finally, a proof-of-concept demonstration of SiP design is fabricated.

Since the fully additive manufacturing packaging process is proposed and characterized in the second research, the third research focuses on integrating energy harvester inside the packaging to realize a fully autonomous SiP design. The 3D-printed ramp structures and inkjet-printed transmission lines on the top of them are suitable for mm-wave inter-layer connections because lower parasitics are induced to the system. Moreover, a SiP design for backscattering sensor is proposed. It has to be stressed that an RF energy harvester operated at 26 GHz which is embedded inside the packaging using additively manufacturing techniques is proposed for the first time. The output voltage of the harvested energy at a distance of 20 cm away from the source is 0.9 V with transmitted EIRP equals to 59 dBm. The harvested energy is large enough to power the TS3001 timer for backscattering and can support all energy requirements of the entire SiP module so that the SiP design is fully energy-autonomous and no external board or components are required. The system size can be shrunk to the package level and thus paving the way for a multitude of novel miniaturized energy-autonomous modules for wearable, IoT, and 5G applications.

Finally, the fourth research develops a new low-loss inkjet-printable BCB ink. The BCB ink provides 10 times smaller loss tangent compared with SU-8. The BCB ink is put to test and the layer thickness as well as the via holes are characterized. The BCB ink demonstrates good jetting, adhesion, and printing quality.

From the fabrication point of view, a new fully additive manufacturing packaging process is proposed, characterized, and put to test. The complex 3D structures which help improve the performances are fabricated and measured. Furthermore, a new low-loss inkjet-printable polymer is developed and tested. The new material brings the additive manufacturing to high-frequency applications. From the energy harvester point of view, the first SiP design with embedded energy harvester is demonstrated. Since the SiP module is energy-autonomous and fully functional, no exterior components or boards are required. Thus, the functional system size is shrunk from the board size to the packaging size. This serves as a new application for the energy harvester.

# CHAPTER 8
# CONCLUSION AND CONTRIBUTION

## 8.1 Conclusion

The objectives of the works presented in this dissertation are proposing innovative energy harvester designs realizing with a new additive manufacturing fabrication process. The proposed energy harvesters can be used to eliminate the requirement of charging or replacement of batteries and thus, realizing energy-autonomous wearable WSNs, real-time health monitoring systems, IoT, and smart cities. The proposed additive manufacturing process can be utilized to realize high-performance RF and mm-wave systems, packaging structures, and SiP modules.

In this dissertation, a novel on-body wireless sensor network system is proposed. The system is fully energy-autonomous and the reading ranges of the sensor tags are drastically enhanced utilizing a wearable and flexible energy harvester harvesting energy from a two-way talk radio. For the first time reported, the proposed energy harvester utilizes not only the DC power to drive an RF power amplifier but also the second harmonic to build a mobile carrier emitter to significantly enhance reading ranges of on-body sensing RFID tags. The output DC and 929 MHz powers are 16.5 and 13 dBm, respectively, while the transmitting power from two-way talk radio is 34.3 dBm and the distance is 9 cm. The 929 MHz antenna is designed along with an AMC structure to reduce the interference from the human body. Moreover, the custom 3D-printed flexible substrate is applied to the AMC design to eliminate the limitation of the substrate thickness of off-the-shelf materials. The inkjet printing masking technique is also applied to the fabrication of the energy harvester on nearly every flexible substrate to reduce the cost. A custom backscattering tag which operates with −5 dBm of input power was realized and an ammonia sensor was integrated

into the backscattering tag to demonstrate the inherent advantage of the proposed system to IoT applications requiring multiple wireless sensors and tags. The reading range was extended to more than 270 m by integrating the RF amplifier which is powered by harvester energy. Moreover, multiple experiments are performed to demonstrate multiple-tag interrogation and gas detection capabilities. The effects of the human body on the performance is also investigated. A design process is proposed to consider the human body effects and accurately predict the near-field coupling power level.

A long-range microfluidic backscatter sensing system is proposed. The actuation forces to move the fluids inside the microchannel are provided by an energy-autonomous micropump system. Since the actuation forces are provided autonomously, the conventional in-lab microfluidic applications can now be applied ubiquitously. The proposed energy harvester harvesting from both a near-field 464.5 MHz two-way radio and a far-field UHF RFID reader (850-950 MHz) simultaneously. The near-field energy provides a high power level while the far-field energy is continuous. Both advantages can be integrated with a power management circuit. Furthermore, a new additive manufacturing process is proposed to realize microchannels, and a proof-of-concept sweat sensor is realized using this process. The proposed fabrication method can realize microchannels with lower cost, shorter prototyping time, and more complex 3D structures. The backscatter topology is used to detect the variation of the conductivity in the fluid and extend the reading range to more than 22 m. Furthermore, the effects of clutters in a complex environment are minimized due to the use of backscatter topology.

The first broadband and miniaturized planar Yagi AiP design which can cover all three major 5G NR operating bands from 24.25 GHz to 40 GHz while maintaining a small form factor is also demonstrated. The FBW is 49% and the size for the antenna element is 3.05 mm $\times$ 5.56 mm which equals 0.25 $\lambda_0 \times$ 0.45 $\lambda_0$ where $\lambda_0$ is the wavelength at 24.25 GHz. Both the single element and the 2-by-1 array design are simulated, fabricated, and measured. The glass multi-layered packaging process with a new low-loss polymer material

is used to realize the designs. The element gain is higher than 4 dBi and the array gain is higher than 6.2 dBi within the entire operating band. The normalized radiation patterns at E-plane and H-plane are demonstrated and the main-beam directions are consistent within the entire band. The cross-polarized patterns at the main-beam direction are smaller than -15 dB. The AiP design is then integrated with broadband rectifiers to form a broadband energy harvester which covers all three major 5G NR operating bands.

The first fully additive manufacturing multi-layer process including inkjet and 3D printing is proposed for mm-wave packaging structures and modules. The low-loss polymer BCB is characterized to further improve the performance of the fabrication process. The structural flexibility offered by 3D-printed substrates can help reduce the parasitics which are important at mm-wave frequencies. Furthermore, the first package-integrated mm-wave energy harvester is reported. The energy harvester is embedded inside a 3D-printed cavity and the antenna is printed right on the top of it to reduce the size. The harvested energy at 26 GHz is large enough to power up a TS3001 timer for backscattering. 0.9 V output power is measured at 20 cm range with 59 dBm EIRP, while more than 1 m range is expected while the full 75 dBm EIRP for 5G communication is used. The package-integrated energy harvester can support the energy requirements for the entire SiP module and thus enabling the drastic shrinkage of the size of the fully energy-autonomous system from the board level to the packaging level.

## 8.2 Contribution

The contributions of each work are evaluated with four perspectives:

1. Innovative energy harvester topologies to improve performance

2. Designs to increase the harvested power level of the energy harvester

3. Novel energy harvester applications

4. Advancement in the additive manufacturing process

As shown in Table 1.1, these are the same criteria as used from the very beginning.

### 8.2.1 Innovative Energy Harvester Topologies

1. On-body long-range sensing network

   (a) The first energy harvester to utilize both the rectified DC power and the harmonics generated during rectification to achieve two different functions.

   (b) The DC power can be used to power micro-controller unit or ICs.

   (c) The second harmonics at 929 MHz is used to create a carrier emitter to significantly increase the reading range of backscattering RFID system to more than 270 m.

### 8.2.2 Increase Harvested Power Level

1. On-body long-range sensing network

   (a) Harvesting energy from a near-field 464.5 MHz two-way radio with large RF power density.

   (b) The DC output at the load is 17.5 dBm.

2. Microfluidic health monitoring system

   (a) Harvesting energy from both a near-field 464.5 MHz two-way radio and a far-field UHF RFID reader (860-960 MHz).

   (b) The near-field two-way radio supports high power density while the far-field UHF RFID reader provides continuous RF power.

   (c) A power management circuit is utilized to integrate both the near-field and far-field energy so that the system can have advantages of both kinds of sources.

(d) The energy harvester is carefully designed so that the highest efficiency for 860-960 MHz is at low power level (3 dBm) while the highest efficiency for 464.5 MHz is at high power level (18 dBm). This meets the real using situation.

(e) Duty cycling is achieved by the power management circuit to reduce the minimum required input power.

3. Glass packaging AiP and SiP designs

    (a) The first UWB energy harvester which covers all three 5G NR operating bands.

    (b) The first UWB and miniaturized AiP design is proposed to cover all three 5G NR operating bands crom 24.25 to 40 GHz.

    (c) Two rectifiers are proposed. One covers from 24.25 GHz to 29.5 GHz with 25% RF-DC efficiency at 15 dBm input power. The other covers from 37 GHz to 40 GHz with 25% RF-DC efficiency at 15 dBm input power.

    (d) The UWB energy harvester is realized by combining the proposed UWB and miniaturized AiP, two rectifiers, and a diplexer.

#### 8.2.3 Novel Energy Harvester Applications

1. On-body long-range sensing network

    (a) The sensors are all powered by an energy harvester and thus, no batteries are required.

    (b) The on-body carrier emitter is realized using an energy harvester and is used to extend the reading range. The reading range is more than 70 m with SNR 14.7 dB. The reading range can be extended to more than 270 m with 3 dB SNR

    (c) A design process is proposed to predict the received power from the near-field coupling and consider the human body effects.

2. Microfluidic health monitoring system

(a) The first energy-autonomous micropump system is realized using energy harvester technologies.

(b) The energy-autonomous micropump system can be used to drive any microfluidic applications. Thus, the proposed micropump system can expand the microfluidic applications from in-lab use to ubiquitously applicable.

(c) The health monitoring is realized by energy-autonomous backscatter sweat sensor. The change in the conductivity is detected and converted into the modulated backscatter signals. Compared with sensors detecting resonance frequencies, the signals using this topology is easier to be detected with a much longer range (22 m) in an environment with clutters.

3. Glass packaging AiP and SiP designs

   (a) Harvesting energy from broadband 5G signals.

   (b) Package-integrated energy harvesters.

   (c) The broadband AiP design covers 24.5 GHz to 40 GHz with a miniaturized size of 3.05 mm $\times$ 5.56 mm which equals 0.25 $\lambda_0$ $\times$ 0.45 $\lambda_0$ where $\lambda_0$ is the wavelength at 24.25 GHz.

   (d) The AiP design has a steady 4 dBi gain within the operating bandwidth.

   (e) A diplexer can be used to integrate two rectifiers covering 24.5 GHz to 29.5 GHz and 37 GHz to 40 GHz with the proposed AiP design to realize a broadband energy harvester which covers all 5G NR operating bands.

4. Additive manufacturing 3D SiP module

   (a) The first SiP module with embedded energy harvesters harvesting energy from 5G signals is proposed.

(b) The SiP module can be fully powered with the embedded energy harvester so that no exterior boards are required. Therefore, the functional system size is shrunk from the board level to the packaging level.

(c) The output voltage of the energy harvester is 0.9 V at 20 cm away from a 59 dBm EIRP energy source. More than 1 m of operating range is expected with the full-power 75 dBm EIRP 5G signals.

#### 8.2.4 Advancement in Additive Manufacturing Process

1. On-body long-range sensing network

   (a) The inkjet- and 3D-printed flexible AMC is used to reduce the interferences from human body.

   (b) The spacer in the AMC is 3D-printed with customized thickness to achieve the optimized performance.

2. Microfluidic health monitoring system

   (a) A new additive manufacturing process to realize microfluidic channels is proposed.

   (b) The process can realize microfluidic channels with lower cost, shorter time, and more complex structures.

   (c) The sweat sensor is realized with the proposed additive manufacturing process.

3. Glass packaging AiP and SiP designs

   (a) A new low-loss polymer, JSR, is used in the glass packaging process.

   (b) Since the polymer is liquid-type, it is easier to be coated on glass without warpage.

4. Additive manufacturing 3D SiP module

(a) The proof of the superiority of additive manufacturing packaging process over the conventional packaging process is demonstrated. The parasite capacitance from the additive manufacturing packaging is 2.14 times smaller than the conventional packaging while parasite inductance is 1.74 times smaller.

(b) Inkjet printing and 3D printing are integrated together to realize a high-performance packaging process.

(c) The relative dielectric constant and the loss tangent of the 3D printing material is characterized.

(d) The 3D printed structures such as cavities, ramps, and through via are characterized and the best printing receipt is developed.

(e) The surface roughness is improved and the CTE mismatch between the 3D printed material and the inkjet-printed conductive traces is solved by coating a thin layer of SU-8 polymer.

(f) The proposed process is utilized to realize an energy-autonomous SiP module with multi-layer 3D packaging structures.

(g) Low-loss inkjet-printable BCB polymer is developed to improve the proposed additive manufacturing packaging process and push the process to high-performance mm-wave applications.

(h) The printing thickness and via hole resolution of the low-loss BCB polymer is also characterized.

## 8.3 Publications

### 8.3.1 Journals

J1. Tong-Hong Lin, Kimiyuki Kanno, Atom O. Watanabe, Pulugurtha Markondeya Raj, Rao R. Tummala, Madhavan Swaminathan, and Manos M. Tentzeris, "Broadband

and Miniaturized Antenna-in-Package (AiP) Design for 5G Applications," in *IEEE Antennas and Wireless Propagation Letters*, vol. 19, no. 11, pp. 1963-1967, Nov. 2020.

J2. Tong-Hong Lin, Jo Bito, Jimmy Hester, John Kimionis, Ryan A. Bahr, and Manos M. Tentzeris, "On-Body Long-Range Wireless Backscattering Sensing System Using Inkjet-/3-D-Printed Flexible Ambient RF Energy Harvesters Capable of Simultaneous DC and Harmonics Generation," in *IEEE Transactions on Microwave Theory and Techniques*, vol. 65, no. 12, pp. 5389-5400, Dec. 2017.

J3. Atom O. Watanabe, Tong-Hong Lin, Muhammad Ali, Yiteng Wang, Vanessa Smet, Pulugurtha Markondeya Raj, Manos M. Tentzeris, Rao R. Tummala, and Madhavan Swaminathan, "Ultra-Thin Antenna-Integrated Glass-Based Millimeter-Wave Package with Through-Glass Vias," in *IEEE Transactions on Microwave Theory and Techniques*, to be published.

J4. Muhammad Ali, Atom Watanabe, Tong-Hong Lin, Daichi Okamoto, Pulugurtha M. Raj, Manos M. Tentzeris, and Rao. R. Tummala"Package-Integrated, Wideband Power Dividing Networks and Antenna Arrays for 28 GHz 5G New Radio Bands," in *IEEE Transactions on Components, Packaging and Manufacturing Technology*, vol. 10, no. 9, pp. 1515-1523, Sept. 2020.

J5. Aline Eid, Xuanke He, Ryan Bahr, Tong-Hong Lin, Yepu Cui, Ajibayo Adeyeye, Bijan Tehrani and Manos M. Tentzeris, "Inkjet-/3D-/4D-Printed RF and mm-Wave Perpetual Electronics and Modules for 5G+, IoT, Smart Agriculture and Smart Cities Applications," in *IEEE Microwave Magazine*, vol. 21, no. 12, pp. 87-103, Dec. 2020.

J6. Eui M. Jung, Yepu Cui, Tong-Hong Lin, Xuanke He, Aline Eid, Jimmy Hester, Gregory D. Abowd, Thad E. Starner, Wang-Sang Lee, and Manos M. Tentzeris, "A Wide-

band, Quasi-Isotropic, Kilometer-Range FM Energy Harvester for Perpetual IoT," in *IEEE Microwave and Wireless Components Letters*, vol. 30, no. 2, pp. 201-204, Feb. 2020.

J7. Hee-Ran Ahn, Manos M. Tentzeris, Tong-Hong Lin, Bijan Tehrani, and Xuanke He, "Coupled Lines for Wearable Power Dividers: Coupled Transmission-Line Sections for Power Dividers in Wearable and Flexible RF Electronics," in *IEEE Microwave Magazine*, vol. 21, no. 2, pp. 66-87, Feb. 2020.

J8. Soyeon Jeong, Tong-Hong Lin, and M. M. Tentzeris, " Real-Time Range-Adaptive Impedance Matching Utilizing a Machine Learning Strategy Based on Neural Networks for Wireless Power Transfer Systems" in *IEEE Transactions on Microwave Theory and Techniques*, vol. 67, no. 12, pp. 5340-5347, Dec. 2019.

J9. John Kimionis, Wenjing Su, Jimmy Hester, Jo Bito, Xuanke He, Tong-Hong Lin, and Manos M. Tentzeris, "Zero-Power Sensors for Smart Objects: Novel Zero-Power Additively Manufactured Wireless Sensor Modules for IoT Applications," in *IEEE Microwave Magazine*, vol. 19, no. 6, pp. 32-47, Sept.-Oct. 2018.

J10. Ajibayo Adeyeye, Aline Eid, Jimmy Hester, Tong-Hong Lin, Abdullah Nauroze, Bijan Tehrani, and Manos M. Tentzris, "Additively Manufactured Inkjet-/3D-/4D-Printed Wireless Sensors Modules," in *International Journal of High Speed Electronics and Systems*, vol. 27, no. 01n02, pp. 1840012, 2018.

#### 8.3.2 Conference Proceedings

C1. Tong-Hong Lin and Manos M. Tentzeris, "Printed 5G Reconfigurable Wireless Modules Using Additive Manufacturing Techniques," *IEEE International Symposium on Antennas and Propagation and USNC-URSI Radio Science Meeting*, Atlanta, GA, USA, 2019, pp. 1705-1706.

C2. Tong-Hong Lin, Spyridon N. Daskalakis, Apostolos Georgiadis, and M. M. Tentzeris, "Achieving Fully Autonomous System-on-Package Designs: An Embedded-on- Package 5G Energy Harvester within 3D Printed Multilayer Flexible Packaging Structures," *IEEE MTT-S International Microwave Symposium (IMS)*, Boston, MA, USA, 2019, pp. 1375-1378.

C3. Tong-Hong Lin, Aline Eid, Jimmy Hester, Bijan Tehrani, Jo Bito, and Manos M. Tentzeris, "Novel Additively Manufactured Packaging Approaches for 5G/mm-Wave Wireless Modules," *IEEE 69th Electronic Components and Technology Conference (ECTC)*, Las Vegas, NV, USA, 2019, pp. 896-902.

C4. Tong-Hong Lin, Wenjing Su, and Manos M. Tentzeris, "Expand Horizons of Microfluidic Systems: An Inkjet Printed Flexible Energy Autonomous Micropump System for Wearable and IoT Microfluidic Applications," textitIEEE MTT-S International Microwave Symposium (IMS), Philadelphia, PA, 2018, pp. 812-815.

C5. Tong-Hong Lin, Ryan A. Bahr, Manos M. Tentzeris, Pulugurtha M. Raj, Venky Sundaram, and, Rao Tummala, "Novel 3D-/Inkjet-Printed Flexible On-package Antennas, Packaging Structures, and Modules for Broadband 5G Applications," *IEEE 68th Electronic Components and Technology Conference (ECTC)*, San Diego, CA, 2018, pp. 214-220.

C6. Tong-Hong Lin, Pulugurtha M. Raj, Atom Watanabe, Venky Sundaram, Rao Tummala, and Manos M. Tentzeris, "Nanostructured miniaturized artificial magnetic conductors (AMC) for high-performance antennas in 5G, IoT, and smart skin applications," *IEEE 17th International Conference on Nanotechnology (IEEE-NANO)*, Pittsburgh, PA, 2017, pp. 911-915.

C7. Tong-Hong Lin, Jo Bito, and Manos M. Tentzeris, "Wearable inkjet printed energy harvester," *IEEE International Symposium on Antennas and Propagation and*

*USNC/URSI Radio Science Meeting*, San Diego, CA, 2017, pp. 1613-1614.

C8. Tong-Hong Lin, Jo Bito, Jimmy Hester, John Kimionis, Ryan A. Bahr, and Manos M. Tentzeris, "Ambient energy harvesting from two-way talk radio for on-body autonomous wireless sensing network using inkjet and 3D printing," *IEEE MTT-S International Microwave Symposium (IMS)*, Honololu, HI, 2017, pp. 1034-1037.

C9. Soyeon Jeong, Tong-Hong Lin, and Manos M. Tentzeris, "Range-adaptive Impedance Matching of Wireless Power Transfer System Using a Machine Learning Strategy Based on Neural Networks," *IEEE MTT-S International Microwave Symposium (IMS)*, Boston, MA, USA, 2019, pp. 1423-1425.

C10. Muhammad Ali, Atom Watanabe, Tong-Hong Lin, P. M. Raj, M. M. Tentzeris, and Rao Tummala, "3D Glass Package-Integrated, High-Performance Power Dividing Networks for 5G Broadband Antennas," *IEEE 69th Electronic Components and Technology Conference (ECTC)*, Las Vegas, NV, USA, 2019, pp. 960-967.

C11. Muhammad Ali, Atom Watanabe, Tong-Hong Lin, Manos M. Tentzeris, Rao Tummala, and Pulugurtha M. Raj, "Ultra-Wideband, Glass Package-Integrated Power Dividers for 5G and mm-Wave Applications," *IEEE International Symposium on Antennas and Propagation and USNC-URSI Radio Science Meeting*, Atlanta, GA, USA, 2019, pp. 863-864.

C12. Aline Eid, Jimmy Hester, Abdullah Nauroze, Tong-Hong Lin, Joseph Costantine, Youssef Tawk, Ali H. Ramadan, and M. M. Tentzeris, "A Flexible Compact Rectenna for 2.40Hz ISM Energy Harvesting Applications," *IEEE International Symposium on Antennas and Propagation and USNC/URSI Radio Science Meeting*, Boston, MA, 2018, pp. 1887-1888.

C13. Atom Watanabe, Tong-Hong Lin, Pulugurtha M. Raj, Venky Sundaram, Manos M Tentzeris, Rao Tummala, and Tomonori Ogawa, "Leading-Edge and Ultra-Thin 3D

Glass-Polymer 5G Modules with Seamless Antenna-to-Transceiver Signal Transmissions," *IEEE 68th Electronic Components and Technology Conference (ECTC)*, San Diego, CA, 2018, pp. 2026-2031.

C14. Atom Watanabe, Tong-Hong Lin, Tomonori Ogawa, Pulugurtha M. Raj, Venkatesh Sundaram, Manos M. Tentzeris, and Rao Tummala, "Design and demonstration of ultra-thin 3D glass-based 5G modules with low-loss interconnects," *International Conference on Electronics Packaging and iMAPS All Asia Conference (ICEP-IAAC)*, Mie, 2018, pp. 180-183.

#### 8.3.3 Book Chapters

B1. Tong-Hong Lin, Ryan A. Bahr, and Manos M. Tentzeris, "Additive Manufacturing AiP Designs and Applications," in *Antenna-in-Package Technology and Applications*, John Wiley & Sons, Ltd, 2020, Chapter 9, pp. 267–291.

B2. Aline Eid, Tong-Hong Lin, Jimmy G.D. Hester, Yepu Cui, Ajibayo Adeyeye, Bijan Tehrani, Syed A. Nauroze, Manos M. Tentzeris, "Inkjet-/3D-/4D-Printed Nanotechnology-Enabled Radar, Sensing and RFID Modules for Internet of Things, "Smart Skin" and "Zero-Power" Medical Applications," in *Antenna and Sensor Technologies in Modern Medical Applications*, John Wiley & Sons, Ltd, 2020, Chapter 11, to be published.

# REFERENCES


[1] A. Harb, “Energy harvesting: State-of-the-art,” *Renewable Energy*, vol. 36, no. 10, pp. 2641–2654, Oct. 2011.

[2] J. Taneja, J. Jeong, and D. Culler, “Design, Modeling, and Capacity Planning for Micro-solar Power Sensor Networks,” in *2008 International Conference on Information Processing in Sensor Networks (ipsn 2008)*, Apr. 2008, pp. 407–418.

[3] J. P. Carmo, L. M. Goncalves, and J. H. Correia, “Thermoelectric Microconverter for Energy Harvesting Systems,” *IEEE Transactions on Industrial Electronics*, vol. 57, no. 3, pp. 861–867, Mar. 2010.

[4] J. Hagerty, F. Helmbrecht, W. McCalpin, R. Zane, and Z. Popovic, “Recycling ambient microwave energy with broad-band rectenna arrays,” *IEEE Transactions on Microwave Theory and Techniques*, vol. 52, no. 3, pp. 1014–1024, Mar. 2004.

[5] H. Kulah and K. Najafi, “Energy Scavenging From Low-Frequency Vibrations by Using Frequency Up-Conversion for Wireless Sensor Applications,” *IEEE Sensors Journal*, vol. 8, no. 3, pp. 261–268, Mar. 2008.

[6] J. M. Gilbert and F. Balouchi, “Comparison of energy harvesting systems for wireless sensor networks,” *International Journal of Automation and Computing*, vol. 5, no. 4, pp. 334–347, Oct. 2008.

[7] N. Garg and R. Garg, “Energy harvesting in IoT devices: A survey,” in *2017 International Conference on Intelligent Sustainable Systems (ICISS)*, Dec. 2017, pp. 127–131.

[8] J. Paradiso and T. Starner, “Energy scavenging for mobile and wireless electronics,” *IEEE Pervasive Computing*, vol. 4, no. 1, pp. 18–27, Jan. 2005.

[9] A. M. Zungeru, L.-M. Ang, S. R. S. Prabaharan, and K. P. Seng, “Radio Frequency Energy Harvesting and Management for Wireless Sensor Networks,” *ArXiv*, 2012.

[10] X. Zhang and L.-D. Zhao, “Thermoelectric materials: Energy conversion between heat and electricity,” *Journal of Materiomics*, vol. 1, no. 2, pp. 92–105, Jun. 2015.

[11] G. Orecchini, L. Yang, M. M. Tentzeris, and L. Roselli, “Wearable battery-free active paper printed RFID tag with human-energy scavenger,” in *2011 IEEE MTT-S International Microwave Symposium*, Jun. 2011, pp. 1–4.

[12] M. Piñuela, P. D. Mitcheson, and S. Lucyszyn, "Ambient RF Energy Harvesting in Urban and Semi-Urban Environments," *IEEE Transactions on Microwave Theory and Techniques*, vol. 61, no. 7, pp. 2715–2726, Jul. 2013.

[13] W. Brown, "The History of Power Transmission by Radio Waves," *IEEE Transactions on Microwave Theory and Techniques*, vol. 32, no. 9, pp. 1230–1242, Sep. 1984.

[14] W. Lumpkins, "Nikola Tesla's Dream Realized: Wireless power energy harvesting.," *IEEE Consumer Electronics Magazine*, vol. 3, no. 1, pp. 39–42, Jan. 2014.

[15] E. Donchev, J. S. Pang, P. M. Gammon, A. Centeno, F. Xie, P. K. Petrov, J. D. Breeze, M. P. Ryan, D. J. Riley, and N. M. Alford, "The rectenna device: From theory to practice (a review)," *MRS Energy & Sustainability*, vol. 1, 2014.

[16] D. M. Dobkin, in *The RF in RFID*, D. M. Dobkin, Ed., Burlington: Newnes, 2008.

[17] R. J. Vyas, B. B. Cook, Y. Kawahara, and M. M. Tentzeris, "E-WEHP: A Batteryless Embedded Sensor-Platform Wirelessly Powered From Ambient Digital-TV Signals," *IEEE Transactions on Microwave Theory and Techniques*, vol. 61, no. 6, pp. 2491–2505, Jun. 2013.

[18] D. Masotti, A. Costanzo, M. D. Prete, and V. Rizzoli, "Genetic-based design of a tetra-band high-efficiency radio-frequency energy harvesting system," *Antennas Propagation IET Microwaves*, vol. 7, no. 15, pp. 1254–1263, Dec. 2013.

[19] C. R. Valenta and G. D. Durgin, "Harvesting Wireless Power: Survey of Energy-Harvester Conversion Efficiency in Far-Field, Wireless Power Transfer Systems," *IEEE Microwave Magazine*, vol. 15, no. 4, pp. 108–120, Jun. 2014.

[20] S. Hemour and K. Wu, "Radio-Frequency Rectifier for Electromagnetic Energy Harvesting: Development Path and Future Outlook," *Proceedings of the IEEE*, vol. 102, no. 11, pp. 1667–1691, Nov. 2014.

[21] C. H. P. Lorenz, S. Hemour, W. Li, Y. Xie, J. Gauthier, P. Fay, and K. Wu, "Breaking the Efficiency Barrier for Ambient Microwave Power Harvesting With Heterojunction Backward Tunnel Diodes," *IEEE Transactions on Microwave Theory and Techniques*, vol. 63, no. 12, pp. 4544–4555, Dec. 2015.

[22] C. H. P. Lorenz, S. Hemour, W. Li, Y. Xie, J. Gauthier, P. Fay, and K. Wu, "Overcoming the efficiency limitation of low microwave power harvesting with backward tunnel diodes," in *2015 IEEE MTT-S International Microwave Symposium*, May 2015, pp. 1–4.

[23] S. Hemour, Y. Zhao, C. H. P. Lorenz, D. Houssameddine, Y. Gui, C.-M. Hu, and K. Wu, "Towards Low-Power High-Efficiency RF and Microwave Energy Harvesting," *IEEE Transactions on Microwave Theory and Techniques*, vol. 62, no. 4, pp. 965–976, Apr. 2014.

[24] Y. Han, O. Leitermann, D. A. Jackson, J. M. Rivas, and D. J. Perreault, "Resistance Compression Networks for Radio-Frequency Power Conversion," *IEEE Transactions on Power Electronics*, vol. 22, no. 1, pp. 41–53, Jan. 2007.

[25] K. Niotaki, A. Georgiadis, and A. Collado, "Dual-band rectifier based on resistance compression networks," in *2014 IEEE MTT-S International Microwave Symposium (IMS2014)*, Jun. 2014, pp. 1–3.

[26] Y. Huang, N. Shinohara, and T. Mitani, "A Constant Efficiency of Rectifying Circuit in an Extremely Wide Load Range," *IEEE Transactions on Microwave Theory and Techniques*, vol. 62, no. 4, pp. 986–993, Apr. 2014.

[27] Z. Liu, Z. Zhong, and Y.-X. Guo, "Enhanced Dual-Band Ambient RF Energy Harvesting With Ultra-Wide Power Range," *IEEE Microwave and Wireless Components Letters*, vol. 25, no. 9, pp. 630–632, Sep. 2015.

[28] S.-Y. Kim, H. Abbasizadeh, B. S. Rikan, S. J. Oh, B. G. Jang, Y.-J. Park, D. Khan, T. T. K. Nga, K. T. Kang, Y. G. Pu, S.-S. Yoo, S. Lee, S.-C. Lee, M. Lee, K. C. Hwang, Y. Yang, and K.-Y. Lee, "A –20 to 30 dBm Input Power Range Wireless Power System With a MPPT-Based Reconfigurable 48% Efficient RF Energy Harvester and 82% Efficient A4WP Wireless Power Receiver With Open-Loop Delay Compensation," *IEEE Transactions on Power Electronics*, vol. 34, no. 7, pp. 6803–6817, Jul. 2019.

[29] S. Shen, Y. Zhang, C.-Y. Chiu, and R. Murch, "An Ambient RF Energy Harvesting System Where the Number of Antenna Ports is Dependent on Frequency," *IEEE Transactions on Microwave Theory and Techniques*, vol. 67, no. 9, pp. 3821–3832, Sep. 2019.

[30] H. Sun, Y.-x. Guo, M. He, and Z. Zhong, "A Dual-Band Rectenna Using Broadband Yagi Antenna Array for Ambient RF Power Harvesting," *IEEE Antennas and Wireless Propagation Letters*, vol. 12, pp. 918–921, 2013.

[31] Z. Liu, Z. Zhong, and Y.-X. Guo, "High-efficiency triple-band ambient RF energy harvesting for wireless body sensor network," in *2014 IEEE MTT-S International Microwave Workshop Series on RF and Wireless Technologies for Biomedical and Healthcare Applications (IMWS-Bio2014)*, Dec. 2014, pp. 1–3.

[32] C. Song, Y. Huang, P. Carter, J. Zhou, S. Yuan, Q. Xu, and M. Kod, "A Novel Six-Band Dual CP Rectenna Using Improved Impedance Matching Technique for

Ambient RF Energy Harvesting," *IEEE Transactions on Antennas and Propagation*, vol. 64, no. 7, pp. 3160–3171, Jul. 2016.

[33] B. L. Pham and A.-V. Pham, "Triple bands antenna and high efficiency rectifier design for RF energy harvesting at 900, 1900 and 2400 MHz," in *2013 IEEE MTT-S International Microwave Symposium Digest (MTT)*, Jun. 2013, pp. 1–3.

[34] Y.-H. Suh and K. Chang, "A high-efficiency dual-frequency rectenna for 2.45- and 5.8-GHz wireless power transmission," *IEEE Transactions on Microwave Theory and Techniques*, vol. 50, no. 7, pp. 1784–1789, Jul. 2002.

[35] J. Kimionis, A. Collado, M. M. Tentzeris, and A. Georgiadis, "Octave and Decade Printed UWB Rectifiers Based on Nonuniform Transmission Lines for Energy Harvesting," *IEEE Transactions on Microwave Theory and Techniques*, vol. 65, no. 11, pp. 4326–4334, Nov. 2017.

[36] P. Wu, S. Y. Huang, W. Zhou, and C. Liu, "One Octave Bandwidth Rectifier With a Frequency Selective Diode Array," *IEEE Microwave and Wireless Components Letters*, vol. 28, no. 11, pp. 1008–1010, Nov. 2018.

[37] A. Collado and A. Georgiadis, "Conformal Hybrid Solar and Electromagnetic (EM) Energy Harvesting Rectenna," *IEEE Transactions on Circuits and Systems I: Regular Papers*, vol. 60, no. 8, pp. 2225–2234, Aug. 2013.

[38] J. Bito, J. G. Hester, and M. M. Tentzeris, "A fully autonomous ultra-low power hybrid RF/photovoltaic energy harvesting system with –25 dBm sensitivity," in *2017 IEEE Wireless Power Transfer Conference (WPTC)*, May 2017, pp. 1–4.

[39] X. Gu, L. Guo, M. Harouna, S. Hemour, and K. Wu, "Accurate Analytical Model for Hybrid Ambient Thermal and RF Energy Harvester," in *2018 IEEE/MTT-S International Microwave Symposium - IMS*, Jun. 2018, pp. 1122–1125.

[40] C.-L. Chang and T.-C. Lee, "An thermoelectric and RF multi-source energy harvesting system," Jun. 2016, pp. 1–5.

[41] J.-W. Lee and B. Lee, "A Long-Range UHF-Band Passive RFID Tag IC Based on High- $Q$ Design Approach," *IEEE Transactions on Industrial Electronics*, vol. 56, no. 7, pp. 2308–2316, Jul. 2009.

[42] X. Lu, P. Wang, D. Niyato, D. I. Kim, and Z. Han, "Wireless Networks With RF Energy Harvesting: A Contemporary Survey," *IEEE Communications Surveys Tutorials*, vol. 17, no. 2, pp. 757–789, 2015.

[43] M. Philipose, J. Smith, B. Jiang, A. Mamishev, S. Roy, and K. Sundara-Rajan, "Battery-free wireless identification and sensing," *IEEE Pervasive Computing*, vol. 4, no. 1, pp. 37–45, Jan. 2005.

[44] L. Atzori, A. Iera, and G. Morabito, "The Internet of Things: A survey," *Computer Networks*, vol. 54, no. 15, pp. 2787–2805, Oct. 2010.

[45] U. Muncuk, K. Alemdar, J. D. Sarode, and K. R. Chowdhury, "Multiband Ambient RF Energy Harvesting Circuit Design for Enabling Batteryless Sensors and IoT," *IEEE Internet of Things Journal*, vol. 5, no. 4, pp. 2700–2714, Aug. 2018.

[46] C. García Núñez, L. Manjakkal, and R. Dahiya, "Energy autonomous electronic skin," *npj Flexible Electronics*, vol. 3, no. 1, pp. 1–24, Jan. 2019.

[47] Q. Wu, G. Y. Li, W. Chen, D. W. K. Ng, and R. Schober, "An Overview of Sustainable Green 5G Networks," *IEEE Wireless Communications*, vol. 24, no. 4, pp. 72–80, Aug. 2017.

[48] S. E. Hassani, H. E. Hassani, and N. Boutammachte, "RF Energy Harvesting for 5G: An Overview," in *2017 International Renewable and Sustainable Energy Conference (IRSEC)*, Dec. 2017, pp. 1–6.

[49] Y. Huo, X. Dong, and W. Xu, "5G Cellular User Equipment: From Theory to Practical Hardware Design," *IEEE Access*, vol. 5, pp. 13 992–14 010, 2017.

[50] H. Bikas, P. Stavropoulos, and G. Chryssolouris, "Additive manufacturing methods and modelling approaches: A critical review," *The International Journal of Advanced Manufacturing Technology*, vol. 83, no. 1, pp. 389–405, Mar. 2016.

[51] J. G. Hester, S. Kim, J. Bito, T. Le, J. Kimionis, D. Revier, C. Saintsing, W. Su, B. Tehrani, A. Traille, B. S. Cook, and M. M. Tentzeris, "Additively Manufactured Nanotechnology and Origami-Enabled Flexible Microwave Electronics," *Proceedings of the IEEE*, vol. 103, no. 4, pp. 583–606, Apr. 2015.

[52] E. Tekin, P. J. Smith, and U. S. Schubert, "Inkjet printing as a deposition and patterning tool for polymers and inorganic particles," *Soft Matter*, vol. 4, no. 4, pp. 703–713, Mar. 2008.

[53] S. H. Ko, H. Pan, C. P. Grigoropoulos, C. K. Luscombe, J. M. J. Fréchet, and D. Poulikakos, "All-inkjet-printed flexible electronics fabrication on a polymer substrate by low-temperature high-resolution selective laser sintering of metal nanoparticles," *Nanotechnology*, vol. 18, no. 34, p. 345 202, Aug. 2007.

[54] R. Tummala, "SOP: What is it and why? A new microsystem-integration technology paradigm-Moore's law for system integration of miniaturized convergent

systems of the next decade," *IEEE Transactions on Advanced Packaging*, vol. 27, no. 2, pp. 241–249, May 2004.

[55] B. K. Tehrani, B. S. Cook, and M. M. Tentzeris, "Inkjet-printed 3D interconnects for millimeter-wave system-on-package solutions," in *2016 IEEE MTT-S International Microwave Symposium (IMS)*, May 2016, pp. 1–4.

[56] T.-H. Lin, A. Eid, J. Hester, B. Tehrani, J. Bito, and M. M. Tentzeris, "Novel Additively Manufactured Packaging Approaches for 5G/mm-Wave Wireless Modules," in *2019 IEEE 69th Electronic Components and Technology Conference (ECTC)*, ISSN: 2377-5726, May 2019, pp. 896–902.

[57] B. K. Tehrani, R. A. Bahr, W. Su, B. S. Cook, and M. M. Tentzeris, "E-band characterization of 3D-printed dielectrics for fully-printed millimeter-wave wireless system packaging," in *2017 IEEE MTT-S International Microwave Symposium (IMS)*, Jun. 2017, pp. 1756–1759.

[58] P. Calvert, "Inkjet Printing for Materials and Devices," *Chemistry of Materials*, vol. 13, no. 10, pp. 3299–3305, Oct. 2001.

[59] A. Ghannam, C. Viallon, D. Bourrier, and T. Parra, "Dielectric microwave characterization of the SU-8 thick resin used in an above IC process," in *2009 European Microwave Conference (EuMC)*, Sep. 2009, pp. 1041–1044.

[60] G. Di Massa, S. Costanzo, A. Borgia, F. Venneri, and I. Venneri, "Innovative dielectric materials at millimeter-frequencies," in *2010 Conference Proceedings ICECom, 20th International Conference on Applied Electromagnetics and Communications*, Sep. 2010, pp. 1–4.

[61] C. Yang, S.-Y. Wu, C. Glick, Y. S. Choi, W. Hsu, and L. Lin, "3D printed RF passive components by liquid metal filling," in *2015 28th IEEE International Conference on Micro Electro Mechanical Systems (MEMS)*, Jan. 2015, pp. 261–264.

[62] R. Bahr, T. Le, M. M. Tentzeris, S. Moscato, M. Pasian, M. Bozzi, and L. Perregrini, "RF characterization of 3D printed flexible materials - NinjaFlex Filaments," in *2015 European Microwave Conference (EuMC)*, Sep. 2015, pp. 742–745.

[63] I. Zivkovic and A. Murk, "Free-Space Transmission Method for the Characterization of Dielectric and Magnetic Materials at Microwave Frequencies," *Microwave Materials Characterization*, Nov. 2012.

[64] L. Atzori, A. Iera, and G. Morabito, "The Internet of Things: A survey," *Computer Networks*, vol. 54, no. 15, pp. 2787–2805, 2010.

[65] A. Ercan, O. Sunay, and I. F. Akyildiz, "RF Energy Harvesting and Transfer for Spectrum Sharing Cellular IoT Communications in 5G Systems," *IEEE Transactions on Mobile Computing*, vol. 17, no. 7, pp. 1680–1694, 2018.

[66] M. Arrawatia, M. S. Baghini, and G. Kumar, "Broadband Bent Triangular Omnidirectional Antenna for RF Energy Harvesting," *IEEE Antennas Wireless Propagation Letters*, vol. 15, pp. 36–39, 2016.

[67] S. Kim, R. Vyas, J. Bito, K. Niotaki, A. Collado, A. Georgiadis, and M. M. Tentzeris, "Ambient rf energy-harvesting technologies for self-sustainable standalone wireless sensor platforms," *Proceedings of the IEEE*, vol. 102, no. 11, pp. 1649–1666, 2014.

[68] D. De Donno, L. Catarinucci, and L. Tarricone, "An UHF RFID Energy-Harvesting System Enhanced by a DC-DC Charge Pump in Silicon-on-Insulator Technology," *IEEE Microwave and Wireless Components Letters*, vol. 23, no. 6, pp. 315–317, Jun. 2013.

[69] J. Kimionis, A. Bletsas, and J. N. Sahalos, "Increased Range Bistatic Scatter Radio," *IEEE IEEE Transactions on Communications*, vol. 62, no. 3, pp. 1091–1104, 2014.

[70] J. Bito, J. G. Hester, and M. M. Tentzeris, "Ambient RF Energy Harvesting From a Two-Way Talk Radio for Flexible Wearable Wireless Sensor Devices Utilizing Inkjet Printing Technologies," *IEEE Transactions on Microwave Theory and Techniques*, vol. 63, no. 12, pp. 4533–4543, 2015.

[71] A. Feresidis, G. Goussetis, S. Wang, and J. Vardaxoglou, "Artificial magnetic conductor surfaces and their application to low-profile high-gain planar antennas," *IEEE Transactions on Antennas and Propagation*, vol. 53, no. 1, pp. 209–215, 2005.

[72] R. Bahr, T. Le, M. M. Tentzeris, S. Moscato, M. Pasian, M. Bozzi, and L. Perregrini, "RF characterization of 3D printed flexible materials - Ninjaflex Filaments," in *2015 European Microwave Conference (EuMC)*, 2015, pp. 742–745.

[73] E. Kampianakis, J. Kimionis, K. Tountas, C. Konstantopoulos, E. Koutroulis, and A. Bletsas, "Wireless Environmental Sensor Networking With Analog Scatter Radio and Timer Principles," *IEEE Sensors Journal*, vol. 14, no. 10, pp. 3365–3376, 2014.

[74] J. Kimionis and M. M. Tentzeris, "Pulse Shaping: The Missing Piece of Backscatter Radio and RFID," *IEEE Transactions on Microwave Theory and Techniques*, vol. 64, no. 12, pp. 4774–4788, 2016.

[75] E. Bekyarova, M. Davis, T. Burch, M. E. Itkis, B. Zhao, S. Sunshine, and R. C. Haddon, "Chemically Functionalized Single-Walled Carbon Nanotubes as Ammonia Sensors," *Journal of Physical Chemistry B*, vol. 108, pp. 19 717–19 720, 2004.

[76] B. Timmer, W. Olthuis, and A. v. d. Berg, "Ammonia sensors and their applications—a review," *Sensors and Actuators B: Chemical*, vol. 107, no. 2, pp. 666–677, Jun. 2005.

[77] S. Ampuero and J. O. Bosset, "The electronic nose applied to dairy products: A review," *Sensors and Actuators B: Chemical*, vol. 94, no. 1, pp. 1–12, Aug. 2003.

[78] A. A. Kutty, T. Björninen, L. Sydänheimo, and L. Ukkonen, "A novel carbon nanotube loaded passive UHF RFID sensor tag with built-in reference for wireless gas sensing," in *2016 IEEE MTT-S International Microwave Symposium (IMS)*, 2016, pp. 1–4.

[79] G. A. Vera, S. D. Nawale, Y. Duroc, and S. Tedjini, "Read Range Enhancement by Harmonic Energy Harvesting in Passive UHF RFID," *IEEE Microwave and Wireless Components Letters*, vol. 25, no. 9, pp. 627–629, 2015.

[80] J. W. Lee and B. Lee, "A Long-Range UHF-Band Passive RFID Tag IC Based on High- $q$ Design Approach," *IEEE Transactions on Industrial Electronics*, vol. 56, no. 7, pp. 2308–2316, 2009.

[81] A. Popov, S. Dudnikov, and A. Mikhaylov, "Passive UHF RFID Tag with Increased Read Range," in *2008 38th European Microwave Conference*, 2008, pp. 1106–1108.

[82] A. Strobel, C. Carlowitz, R. Wolf, F. Ellinger, and M. Vossiek, "A Millimeter-Wave Low-Power Active Backscatter Tag for FMCW Radar Systems," *IEEE Transactions on Microwave Theory and Techniques*, vol. 61, no. 5, pp. 1964–1972, 2013.

[83] L. M. Ni, Y. Liu, Y. C. Lau, and A. P. Patil, "LANDMARC: Indoor location sensing using active RFID," in *Proceedings of the First IEEE International Conference on Pervasive Computing and Communications, 2003. (PerCom 2003).*, 2003, pp. 407–415.

[84] C. Furse, D. Christensen, C. Durney, and J. Nagel, *Basic Introduction to Bioelectromagnetics, Third Edition*. CRC Press, 2018.

[85] A. K. Skrivervik, M. Bosiljevac, J. Trajkovikj, B. Fuchs, and Z. Sipus, "Design considerations for wearable antennas," in *2016 URSI International Symposium on Electromagnetic Theory (EMTS)*, Aug. 2016, pp. 524–527.

[86] W. Su, B. S. Cook, and M. M. Tentzeris, “Additively Manufactured Microfluidics-Based “Peel-and-Replace” RF Sensors for Wearable Applications,” *IEEE Transactions on Microwave Theory and Techniques*, vol. 64, no. 6, pp. 1928–1936, Jun. 2016.

[87] W. Su, B. S. Cook, Y. Fang, and M. M. Tentzeris, “Fully inkjet-printed microfluidics: A solution to low-cost rapid three-dimensional microfluidics fabrication with numerous electrical and sensing applications,” *Scientific Reports*, vol. 6, no. 1, p. 35 111, Oct. 2016.

[88] C. Mariotti, W. Su, B. S. Cook, L. Roselli, and M. M. Tentzeris, “Development of Low Cost, Wireless, Inkjet Printed Microfluidic RF Systems and Devices for Sensing or Tunable Electronics,” *IEEE Sensors Journal*, vol. 15, no. 6, pp. 3156–3163, Jun. 2015.

[89] K. Entesari and A. P. Saghati, “Fluidics in Microwave Components,” *IEEE Microwave Magazine*, vol. 17, no. 6, pp. 50–75, Jun. 2016.

[90] G. Mumcu, A. Dey, and T. Palomo, “Frequency-Agile Bandpass Filters Using Liquid Metal Tunable Broadside Coupled Split Ring Resonators,” *IEEE Microwave and Wireless Components Letters*, vol. 23, no. 4, pp. 187–189, Apr. 2013.

[91] J. D. Barrera and G. H. Huff, “A Fluidic Loading Mechanism in a Polarization Reconfigurable Antenna With a Comparison to Solid State Approaches,” *IEEE Transactions on Antennas and Propagation*, vol. 62, no. 8, pp. 4008–4014, Aug. 2014.

[92] M. Wang, C. Trlica, M. R. Khan, M. D. Dickey, and J. J. Adams, “A reconfigurable liquid metal antenna driven by electrochemically controlled capillarity,” *Journal of Applied Physics*, vol. 117, no. 19, p. 194 901, May 2015.

[93] T.-H. Lin, J. Bito, J. G. D. Hester, J. Kimionis, R. A. Bahr, and M. M. Tentzeris, “On-Body Long-Range Wireless Backscattering Sensing System Using Inkjet-/3-D-Printed Flexible Ambient RF Energy Harvesters Capable of Simultaneous DC and Harmonics Generation,” *IEEE Transactions on Microwave Theory and Techniques*, vol. 65, no. 12, pp. 5389–5400, Dec. 2017.

[94] T.-H. Lin, J. Bito, and M. M. Tentzeris, “Wearable inkjet printed energy harvester,” in *2017 IEEE International Symposium on Antennas and Propagation USNC/URSI National Radio Science Meeting*, Jul. 2017, pp. 1613–1614.

[95] V. G. Artemov, A. A. Volkov, N. N. Sysoev, and A. A. Volkov, “Conductivity of aqueous HCl, NaOH and NaCl solutions: Is water just a substrate?” *EPL*, vol. 109, no. 2, p. 26 002, Jan. 2015.

[96] G. Liu, C. Ho, N. Slappey, Z. Zhou, S. E. Snelgrove, M. Brown, A. Grabinski, X. Guo, Y. Chen, K. Miller, J. Edwards, and T. Kaya, “A wearable conductivity sensor for wireless real-time sweat monitoring,” *Sensors and Actuators B: Chemical*, vol. 227, pp. 35–42, May 2016.

[97] J. Thompson, X. Ge, H.-C. Wu, R. Irmer, H. Jiang, G. Fettweis, and S. Alamouti, “5G wireless communication systems: Prospects and challenges [Guest Editorial],” *IEEE Communications Magazine*, vol. 52, no. 2, pp. 62–64, Feb. 2014.

[98] D. Liu, X. Gu, C. W. Baks, and A. Valdes-Garcia, “Antenna-in-Package Design Considerations for Ka-Band 5G Communication Applications,” *IEEE Transactions on Antennas and Propagation*, vol. 65, no. 12, pp. 6372–6379, Dec. 2017.

[99] W. Roh, J.-Y. Seol, J. Park, B. Lee, J. Lee, Y. Kim, J. Cho, K. Cheun, and F. Aryanfar, “Millimeter-wave beamforming as an enabling technology for 5G cellular communications: Theoretical feasibility and prototype results,” *IEEE Communications Magazine*, vol. 52, no. 2, pp. 106–113, Feb. 2014.

[100] Y.-W. Lu, B.-S. Fang, H.-H. Mi, and K.-T. Chen, “Mm-Wave Antenna in Package (AiP) Design Applied to 5th Generation (5G) Cellular User Equipment Using Unbalanced Substrate,” in *2018 IEEE 68th Electronic Components and Technology Conference (ECTC)*, May 2018, pp. 208–213.

[101] T.-H. Lin, R. A. Bahr, and M. M. Tentzeris, “Additive Manufacturing AiP Designs and Applications,” in *Antenna-in-Package Technology and Applications*, John Wiley & Sons, Ltd, 2020, pp. 267–291, ISBN: 978-1-119-55667-1.

[102] T.-H. Lin, R. Bahr, M. M. Tentzeris, P. M. Raj, V. Sundaram, and R. Tummala, “Novel 3D-/Inkjet-Printed Flexible On-package Antennas, Packaging Structures, and Modules for Broadband 5G Applications,” in *2018 IEEE 68th Electronic Components and Technology Conference (ECTC)*, May 2018, pp. 214–220.

[103] T.-H. Lin, P. M. Raj, A. Watanabe, V. Sundaram, R. Tummala, and M. M. Tentzeris, “Nanostructured miniaturized artificial magnetic conductors (AMC) for high-performance antennas in 5G, IoT, and smart skin applications,” in *2017 IEEE 17th International Conference on Nanotechnology (IEEE-NANO)*, Jul. 2017, pp. 911–915.

[104] A. O. Watanabe, M. Ali, B. Tehrani, J. Hester, H. Matsuura, T. Ogawa, P. M. Raj, V. Sundaram, M. M. Tentzeris, and R. R. Tummala, “First Demonstration of 28 GHz and 39 GHz Transmission Lines and Antennas on Glass Substrates for 5G Modules,” in *2017 IEEE 67th Electronic Components and Technology Conference (ECTC)*, May 2017, pp. 236–241.

[105] C. Buch, D. Struk, K.-J. Wolter, P. J. Hesketh, V. Sundaram, R. Tummala, C. Shearer, J. Haley, M. Findlay, and M. Papageorge, “Design and Demonstration of

Highly Miniaturized, Low Cost Panel Level Glass Package for MEMS Sensors," in *2017 IEEE 67th Electronic Components and Technology Conference (ECTC)*, May 2017, pp. 1088–1097.

[106] F. Liu, C. Nair, A. Kubo, T. Ando, H. Lu, R. Zhang, H. Chen, K. S. Lee, V. Sundaram, and R. R. Tummala, "Via-in-Trench: A Revolutionary Panel-Based Package RDL Configuration Capable of 200-450 IO/mm/Layer, an Innovation for More-Than-Moore System Integration," in *2017 IEEE 67th Electronic Components and Technology Conference (ECTC)*, May 2017, pp. 2097–2103.

[107] S. Viswanathan, T. Ogawa, K. Demir, T. B. Huang, P. M. Raj, F. Liu, V. Sundaram, and R. Tummala, "High Frequency Electrical Performance and Thermo-Mechanical Reliability of Fine-Pitch, Copper-Metallized Through-Package-Vias (TPVs) in Ultra-Thin Glass Interposers," in *2017 IEEE 67th Electronic Components and Technology Conference (ECTC)*, May 2017, pp. 1510–1516.

[108] H. Ito, K. Kanno, A. Watanabe, R. Tsuyuki, R. Tatara, M. Raj, and R. R. Tummala, "Advanced Low-Loss and High-Density Photosensitive Dielectric Material for RF/Millimeter-Wave Applications," in *2019 International Wafer Level Packaging Conference (IWLPC)*, Oct. 2019, pp. 1–6.

[109] N. Kaneda, W. Deal, Y. Qian, R. Waterhouse, and T. Itoh, "A broadband planar quasi-Yagi antenna," *IEEE Transactions on Antennas and Propagation*, vol. 50, no. 8, pp. 1158–1160, Aug. 2002.

[110] Y.-H. Suh and K. Chang, "A new Millimeter-wave printed dipole phased array antenna using microstrip-fed coplanar stripline tee junctions," *IEEE Transactions on Antennas and Propagation*, vol. 52, no. 8, pp. 2019–2026, Aug. 2004.

[111] I.-J. Hwang, H.-W. Jo, J.-W. Kim, G. Kim, J.-W. Yu, and W.-W. Lee, "Vertically stacked folded dipole antenna using multi-layer for mm-Wave mobile terminals," in *2017 IEEE International Symposium on Antennas and Propagation USNC/URSI National Radio Science Meeting*, Jul. 2017, pp. 2579–2580.

[112] W. El-Halwagy, R. Mirzavand, J. Melzer, M. Hossain, and P. Mousavi, "Investigation of Wideband Substrate-Integrated Vertically-Polarized Electric Dipole Antenna and Arrays for mm-Wave 5G Mobile Devices," *IEEE Access*, vol. 6, pp. 2145–2157, 2018.

[113] S. X. Ta, H. Choo, and I. Park, "Broadband Printed-Dipole Antenna and Its Arrays for 5G Applications," *IEEE Antennas and Wireless Propagation Letters*, vol. 16, pp. 2183–2186, 2017.

[114] H.-T. Kim, B.-S. Park, S.-M. Oh, S.-S. Song, J.-M. Kim, S.-H. Kim, T.-S. Moon, S.-Y. Kim, J.-Y. Chang, S.-W. Kim, W.-S. Kang, S.-Y. Jung, G.-Y. Tak, J.-K. Du,

Y.-S. Suh, and Y.-C. Ho, “A 28GHz CMOS direct conversion transceiver with packaged antenna arrays for 5G cellular system,” in *2017 IEEE Radio Frequency Integrated Circuits Symposium (RFIC)*, Jun. 2017, pp. 69–72.

[115] X. Gu, D. Liu, C. Baks, O. Tageman, B. Sadhu, J. Hallin, L. Rexberg, P. Parida, Y. Kwark, and A. Valdes-Garcia, “Development, Implementation, and Characterization of a 64-Element Dual-Polarized Phased-Array Antenna Module for 28-GHz High-Speed Data Communications,” *IEEE Transactions on Microwave Theory and Techniques*, vol. 67, no. 7, pp. 2975–2984, Jul. 2019.

[116] A. Nafe, M. Sayginer, K. Kibaroglu, and G. M. Rebeiz, “2x64 Dual-Polarized Dual-Beam Single-Aperture 28 GHz Phased Array with High Cross-Polarization Rejection for 5G Polarization MIMO,” in *2019 IEEE MTT-S International Microwave Symposium (IMS)*, Jun. 2019, pp. 484–487.

[117] K. Lim, S. Pinel, M. Davis, A. Sutono, C.-H. Lee, D. Heo, A. Obatoynbo, J. Laskar, E. Tantzeris, and R. Tummala, “RF-system-on-package (SOP) for wireless communications,” *IEEE Microwave Magazine*, vol. 3, no. 1, pp. 88–99, Mar. 2002.

[118] F. Amato, C. W. Peterson, M. B. Akbar, and G. D. Durgin, “Long range and low powered RFID tags with tunnel diode,” in *2015 IEEE International Conference on RFID Technology and Applications (RFID-TA)*, Sep. 2015, pp. 182–187.

[119] T.-H. Lin, W. Su, and M. M. Tentzeris, “Expand Horizons of Microfluidic Systems: An Inkjet Printed Flexible Energy Autonomous Micropump System for Wearable and IoT Microfluidic Applications,” in *2018 IEEE/MTT-S International Microwave Symposium - IMS*, Jun. 2018, pp. 812–815.

[120] B. K. Tehrani, C. Mariotti, B. S. Cook, L. Roselli, and M. M. Tentzeris, “Development, characterization, and processing of thin and thick inkjet-printed dielectric films,” *Organic Electronics*, vol. 29, pp. 135–141, Feb. 2016.

[121] T. Kiuru, J. Mallat, A. V. Raisanen, and T. Narhi, “Schottky Diode Series Resistance and Thermal Resistance Extraction From $S$ -Parameter and Temperature Controlled I–V Measurements,” *IEEE Transactions on Microwave Theory and Techniques*, vol. 59, no. 8, pp. 2108–2116, Aug. 2011.

[122] P. Demestichas, A. Georgakopoulos, D. Karvounas, K. Tsagkaris, V. Stavroulaki, J. Lu, C. Xiong, and J. Yao, “5G on the Horizon: Key Challenges for the Radio-Access Network,” *IEEE Vehicular Technology Magazine*, vol. 8, no. 3, pp. 47–53, Sep. 2013.

[123] X. Gu, D. Liu, C. Baks, O. Tageman, B. Sadhu, J. Hallin, L. Rexberg, and A. Valdes-Garcia, “A multilayer organic package with 64 dual-polarized antennas for

28GHz 5G communication," in *2017 IEEE MTT-S International Microwave Symposium (IMS)*, Jun. 2017, pp. 1899–1901.

[124] N. Ojaroudiparchin, M. Shen, S. Zhang, and G. F. Pedersen, "A Switchable 3-D-Coverage-Phased Array Antenna Package for 5G Mobile Terminals," *IEEE Antennas and Wireless Propagation Letters*, vol. 15, pp. 1747–1750, 2016.

[125] E. Torres and G. A. Rincón-Mora, "Energy-Harvesting System-in-Package ( SiP ) MicroSystem," 2014.

# VITA

The author was born and raised in Kaohsiung, Taiwan. He received the B.S.E.E. and M.S. degree in communication engineering from National Taiwan University, Taipei, Taiwan, R.O.C, in 2011 and 2013. He also received an M.S. degree in computational science and engineering from Georgia Institute of Technology, Atlanta, GA, USA, in 2020.

In 2014, he started working toward the Ph.D. degree in Electrical and Computer Engineering at Georgia Institute of Technology, Atlanta, GA, USA. He joined the Agile Technologies for High-performance Electromagnetic Novel Applications (ATHENA) group at Georgia Institute of Technology as a research assistant advising by Professor Manos M. Tentzeris in 2015. He also did projects in close cooperation with 3D Systems Packaging Research Center at Georgia Institute of Technology leading by Professor Rao R. Tummala and Professor Madhavan Swaminathan.

During his time at Georgia Institute of Technology, he developed inkjet printing and 3D printing fabrication processes for RF and mm-wave components and IC packaging. He also utilized the developed additive manufacturing fabrication processes to realized new wearable and flexible electronics, RF energy harvesting systems, wireless power transfer systems, wireless sensing networks, antenna-in-package design, RF/mm-wave packaging design, system-in-package modules, and glass semi-additive patterning for packaging designs.

He was a recipient of the Student Travel Award of 2018 IEEE Electronic Components and Technology Conference (ECTC). He also worked at Facebook AR/VR Wireless Connectivity (WiConn) team as a research intern at Redmond, WA in 2019. After graduation in 2020, he accepted the offer from Apple as an RF module engineer.